Computational Electromagnetic Modelling of InGaN/GaN Nano-LEDs

Fox, Sophia

Award date:
2017

Awarding institution:
University of Bath

Computational Electromagnetic Modelling of InGaN/GaN Nano-LEDs

submitted by

Sophia Antonia Fox

for the degree of Doctor of Philosophy

of the

University of Bath

Department of Electronic and Electrical Engineering

October 2017

Signature of Author .....

Sophia Antonia Fox

Summary

This work focuses on the development for the electromagnetic optical modelling of a commercial III-nitride vertical LED/nano-LED based on the finite-difference time-domain (FDTD) method. The material properties, boundary conditions and source emission are thoroughly investigated. To achieve a reliable model, results obtained from FDTD using a near-to-far-field transform are compared with those obtained using experimental angular photoluminescence (PL). LED parameters are extracted to quantify the performance of the devices and predict the emission pattern of practically infeasible nanorod arrays on vertical LED structures. It is demonstrated the impact of the shape and dimensions of the nanorods has a significant impact on the light extraction efficiency, however further optimisation is required to significantly increase directionality.

Acknowledgements

I dedicate this to Pierre-Marie Coulon and Kate Cavanagh: meeting you both was the only thing that made any of this worth it. I am also eternally grateful to Peter Richmond for his support.

Oh yeah and I thank myself because I did everything.

Contents

Chapter 1

Introduction

The Climate Change Act 2008 has set a target to reduce the UK's carbon footprint by 50% by 2025 and therefore reduce the country's contribution to global CO_2 emission. Carbon emission production results from any form of energy consumption and therefore reducing the carbon footprint is required for a wide range of different application areas. Advancements in technology of devices and equipment results in an improvement of the energy efficiency which will help to meet this target. One of the easiest applications to reduce the contribution to the carbon footprint is lighting. According to [1] lighting accounts for almost 6% of global CO_2 emissions. A huge advancement in technology for this application is solid state lighting with the invention and development of the light emitting diode (LED).

The LED is an alternative light source which demonstrates low energy usage, longer lifetime, robustness and more environmentally-friendly fabrication and disposal methods relative to other established artificial lighting [2]. For example, LEDs use 90% less energy than incandescent bulbs [3]. The developments of LEDs have led to their implementation in a wide range of high-power applications from household/street lighting to displays through to sterilization processes of medical equipment and water [4]. The wide range of commercial and industrial uses and availability of LEDs was made possible by several breakthroughs in their development.

Development of visible long-wavelength LED devices took place in the 1960s. In 1962, the first patented LEDs were made from gallium arsenide material and emitted light in the near-infrared wavelength range [5]. General Electric invented

the first visible-wavelength emission LED which produced red light and went on to invent the first yellow-emission LED. The application of these devices was limited because of their low output power and it was not until 1976, when the first high brightness LED was developed. These devices however had little use for shorter-wavelength and white light applications.

It was not until the 1990s that the major breakthrough came when Akasaki, Amano and Nakamura of Nichia Corporation invented the first commercially available high-brightness blue-emission LED [6] made from gallium nitride (GaN) and indium (In) material. It was found if the amount of In content was increased, the emission wavelength could be tuned to obtain green light [7]. For this work, they were awarded the Nobel prize in physics in 2014 [8]. With the blue wavelength available, the InGaN-based blue LED can be coated with a phosphor which downconverts the wavelength to produce white light. High brightness white light LED bulbs are now commercially available for a range of colour temperatures. With these devices however, there is a loss of efficiency arising from the down-conversion.

Future research appears to be geared towards developing a similar high-power short-wavelength UV emission device [9]. Such a device could replace UV lamps which contain mercury which is a hazardous material. It is noted there are also developments in the field of polymer-based organic light emitting diodes (OLEDs) [10] to produce white OLEDs.

Several issues exist which limit the efficiency of GaN-based LEDs. A significant issue is the reduction in the LED's efficiency as the input power of the device is increased. This is known as the 'efficiency droop' [11] and it severely limits the LED's suitability for high-power applications. Another undesirable effect is the lower efficiency which is observed for green-yellow emission devices and this is referred to as the 'green-gap'. It limits the realisation of white-emission LEDs without the phosphor downconverter. Significant limitations of the efficiency also arise from the GaN and InGaN material whose crystal structure has a lattice mismatch resulting in strain-induced 'defects' [12] in the crystal which reduce the efficiency of the LED to produce light.

A major issue is the limitation on the amount of light able to escape from within the emitting device due to light trapping arising from GaN's relatively large refractive index. This is referred to as the light extraction of the LED.

In addition, the intensity profile of the light output exhibits poor directionality, making them unsuitable for applications such as high brightness projectors which are an example of an 'etendue-limited system' [13]. The device can be encapsulated in epoxy but at the cost of reducing the overall intensity. This issue limits the applicability of devices in the field of high-brightness lighting such as backlighting.

The light extraction is dependent on the chip design of the LED, and several commercial solutions exist to increase the light output power and LED brightness. These include shaping the chip, using reflectors and roughening the chip's surface. There has been much research into another method of increasing light extraction which uses ordered arrays of nanostructures for both GaN-based LEDs [14] and OLEDs [15]. These are referred to as photonic crystal light emitting diodes (PhC-LEDs) or 'nano-LEDs' as per the title of this thesis. Devices employing these structures have been found to increase both light extraction [16] and the control of directional emission [17]. Additionally, the use of nanostructures have demonstrated theoretically and experimentally more exotic effects on the light mechanisms inside the LED such as photonic bandgaps (PBGs) [18] and microcavities (MCs) [19] which could be exploited to increase the efficiency of the light produced inside the LED.

Nano-LEDs may involve complex processes to fabricate and given the limits of cost, time and material supply, it is impractical to do an optimisation of the light extraction this way. This is where electromagnetic solvers which can model the light extraction of these LEDs becomes extremely useful and brings insight into the light propagation mechanisms which occur inside the device. Furthermore, modelling can be used to simulate for structures that are not yet practically feasible, providing motivation to achieve such devices if they display particularly desirable features.

To demonstrate this, in previous work at the University of Bath, InGaN/GaN-based nano-LEDs were fabricated using a novel process. Modelling of these structures was performed using a numerical electromagnetic solver implementing the finite-difference time-domain (FDTD) method, whereby good agreement with experimental results measured by the author was found. When the diameter of the nanostructures was reduced in the FDTD modelling, the emission profile was calculated to be more directional [20]. This led to an investigation for fabrica-

tion methods to reduce the diameter of the nanostructures [21] because of the potential applications of such devices in etendue-limited systems.

In this thesis, focus is made instead on developing an FDTD model to reliably simulate nanostructures implemented on a commercially available, more cost-effective LED structure provided by Plessey Semiconductors. To achieve an accurate model, the results from FDTD simulations were compared with those obtained from experiment as a method of providing credence to the numerical model. From this, the behaviour i.e., the light extraction and directionality of devices for nanostructured arrays with varying parameters could be predicted including those arrays which are difficult to fabricate practically.

The layout of this thesis is as follows: Chapter 2 will introduce the general theory of LEDs, including important definitions which quantify the performance of the device. A more involved discussion on the current limitations of LED efficiency will be presented with particular focus on light extraction. Examples of commercial solutions which attempt to address the light extraction limitation are reviewed. This will lead to a more detailed discussion of the current research on LEDs employing nanostructures. Chapter 2 finishes with a discussion on the wide use of the finite-difference time-domain (FDTD) method to model such devices.

Chapter 3 will introduce the the FDTD method. This will include its implementation using the Yee algorithm, a detailed discussion of how the model is truncated using the boundary conditions and the modelling of more complicated materials. By developing an understanding of the FDTD method, considerations can be made for its application to LEDs. Finally the reader is introduced to the software used for the implementation of FDTD, called MEEP.

Chapter 4 will present the methods of extracting LED parameters to quantify their performance from results obtained from FDTD simulations. This will include a detailed derivation of the near-to-far-field transform (NFFT) used in antenna theory and to extract the emission profile of the LED modelled using FDTD and its implementation in MATLAB software. The method for quantifying the light extraction and directionality are also detailed. These methods are subsequently applied to the simplest LED structures as a form of validation. The reliability of the extracted parameters (and by proxy the limitation of the FDTD model) are discussed.

In chapter 5 the LED structure to be modelled in FDTD is presented. A brief introduction is made into the fabrication of the nanostructures. Their morphological characterisation is presented for three different devices. Optical characterisation to obtain the emission profiles of the devices is described and from these results, extracted parameters are presented for the commercial device with and without nanostructuring. From these results, a brief comparison and summary is made of their performance.

In chapter 6, the commercial structure without nanostructuring is modelled using the FDTD method. The accurate modelling of the materials and emission inside the device is considered and a final model to provide the base of the nanostructured devices is presented. From the results in FDTD, measures of the light extraction and emission profile are extracted and compared with those obtained from experiment in chapter 5. Discrepancies between FDTD and experiment are discussed.

Chapter 7 extends from chapter 6 by using the final model as a template to simulate the three commercial samples with nanostructuring using the FDTD method. The discrete translational symmetry of the ordered arrays of nanostructures is considered to set up a reliable method of modelling the emission inside the structures. Similarly, measures of the light extraction and emission profile are extracted and compared with those obtained experimentally in chapter 5. Results displaying the light propagation mechanisms inside the LEDs are also presented and discussed. Finally the reliability and accuracy of the FDTD model is summarised.

In chapter 8, provided the FDTD model developed for the modelling of the commercial structure is in good agreement with experimental results, several parameters of the nanostructure array employed on the commercial device are varied. The subsequent light extraction and emission profiles are extracted and the light propagation mechanisms inside the structures are presented. From this simulation campaign, a discussion is made on the motivation to achieving these structures.

This thesis is concluded in chapter 9 with a discussion on the FDTD model developed, and the key findings from nanostructuring of commercial devices. A discussion is also made on the contribution of this work to the technological advancement of LEDs and suggestions for future work are presented.

Chapter 2

Light Emitting Diodes (LEDs)

The group III-Nitrides are semiconductor alloys composed of elements in group III of the periodic table and Nitrogen. They can form binary alloys such as Gallium Nitride (GaN), Indium Nitride (InN) and Aluminium Nitride (AlN). Tertiary and quaternary alloys can made from combinations of these such as InGaN and InAlGaN. They exhibit many useful electronic, optical and physical properties for light-emitting diodes (LEDs) especially their large direct bandgap ranging from $0.7 - 6.2$ eV (for InN and AlN), enabling at least in principle emission wavelengths from the infrared to the deep UV. Their interesting properties arise from the electronic bandstructure which in turn depends on the crystal lattice structure. To further this discussion, important and general definitions from solid state theory will now be introduced[1]. This will include the LED parameters and their limitations, a review of commercial solutions and how they address these limitations and finally a discussion of the use of FDTD to model LEDs.

2.1 General Theory

The atoms of a semiconductor material are arranged in a crystal lattice which results in a band structure like that shown by the energy diagram in figure 2-1 due to the periodic potential in the crystal. There is a valence band having a maximum energy E_V and conduction band with a minimum energy E_C separated by an energy gap, E_G. Electrons (with carrier density n) in the valence band are

[1]For more information the reader is referred to Schubert [22] or for the most comprehensive guide, Kittel [23].

bound to atoms and require a minimum energy E_G to become a conduction band electron, i.e. $E_G = E_C - E_V$. When this occurs the electron leaves an empty state in the valence band termed a hole (represented by carrier density p) which is treated as a positive charge moving in the opposite direction to an electron: the electrons and holes are termed carriers. The Fermi energy level E_F is defined as the energy which has a 50% probability of being occupied by an electron at equilibrium.

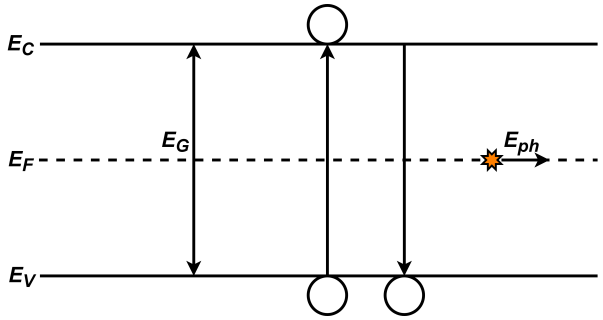

Figure 2-1: *Energy diagram for intrinsic semiconductor where electron at E_V jumps to E_C and then recombines, emitting a photon of energy hf.*

The electron can return to its lower energy state and recombine radiatively with a hole releasing a photon which has an energy, E_{ph} given by:

$$E_{ph} = \frac{hc}{\lambda} \tag{2.1.1}$$

$h =$ Planck's constant
$c =$ Speed of light in vacuum
$\lambda =$ Emission wavelength

This recombination process is spontaneous emission which is the dominant mechanism of light emission in light-emitting diodes (LEDs). Electron-hole recombination can be accurately modelled by an electric dipole point source oscillating at a frequency (energy) equal to the transition frequency (band gap) [24]. The spontaneous emission rate, R_{rad} for bulk semiconductor can be written as a bimolecular rate equation [22]:

$$R_{rad} = Bnp \tag{2.1.2}$$

B = Spontaneous emission coefficient
n = Electron carrier density
p = Hole carrier density

It can be shown that the spontaneous lifetime of each state is $1/B$: this finite lifetime results in the spectrum of the emitted radiation but spread usually over a small frequency range. This is also the case for absorption.

An important property of the bandgap for optical emission applications is whether the semiconductor has a direct or an indirect bandgap. Carriers have an associated crystal momentum arising from De Broglie's hypothesis in wave-particle duality and this must always be conserved. For direct bandgap material an electron can jump from the valence band to the conduction band with zero momentum change which can be achieved by absorbing a photon which has near zero momentum. When the electron recombines with the hole a photon is emitted. For indirect bandgap material an electron cannot jump from the conduction band directly and must simultaneously undergo another transition to gain (or lose) momentum i.e. absorb (or emit) a phonon. Phonon-assisted transfer is much less likely to occur in time and so the radiative recombination is much slower in indirect bandgap material making it less suitable for applications in LEDs. An example of an indirect bandgap semiconductor is silicon.
To increase the number of free carriers within the valence band and conduction band the intrinsic i.e. pure semiconductor is doped with impurity atoms which become ionized and either release an electron into the conduction band (donors) or receive an electron from the valence band (acceptors): these are termed n-type and p-type doping respectively.

When p-type and n-type material are joined a pn junction is formed as shown in figure 2-2(a). Here electrons in the n-type diffuse to the p-type where they recombine with holes and vice versa. An equilibrium is reached whereby the electric field of fixed dopant ions prevent further diffusion of carriers. This can be observed in figure 2-2(a) where the matching of the Fermi levels forces the E_C and E_V bands to bend forming an energy barrier which can be quantified by a threshold voltage, V_D. Upon applying a forward bias, the energy barrier is reduced as shown in figure 2-2(b) and carriers are able to diffuse across where they recombine and emit a photon.

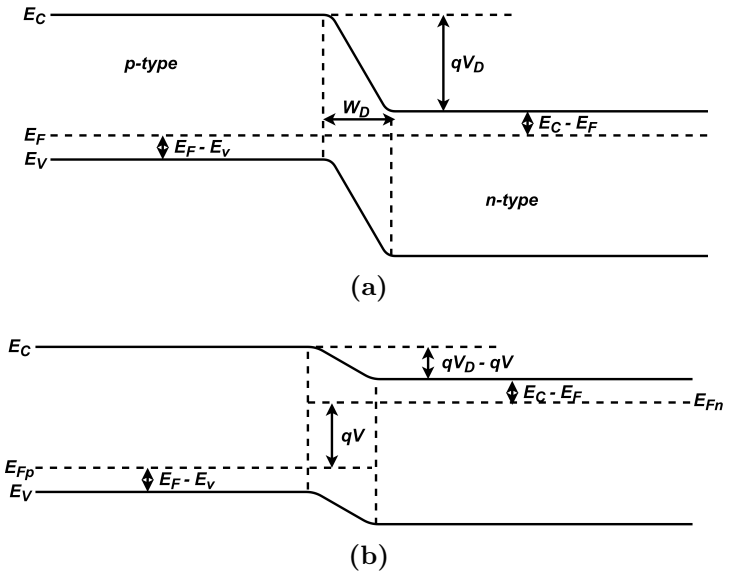

Figure 2-2: *pn junction under (a) zero bias and (b) forward bias. Adapted from [22]*

Thus a LED is a *pn*-junction which emits light when the voltage applied exceeds the threshold voltage of the device.

Quantum Wells

From equation (2.1.2), the radiative spontaneous emission rate is proportional to the concentration of electrons and holes. Thus higher carrier concentrations are needed to increase the emission rate. This is achieved by confining carriers inside a small region forming a potential well. This well is achieved by a double heterostructure which is shown in figure 2-3(a) and shows the active region of width W_{DH} sandwiched between two larger bandgap barrier regions that are *n*-type and *p*-type. The bandgap of the barriers should exceed the photon energy to reduce optical absorption.

When the well is made thin enough i.e. a few nanometers, quantisation effects occur whereby the electron and hole wavefunctions take discrete energy values due to the boundary condition[2] and the double heterostructure is termed a quantum well (QW) [22] as shown in figure 2-3(b).

[2]The carriers are bounded in one dimension. Confinement in two or three dimensions correspond to quantum wires or quantum dots respectively.

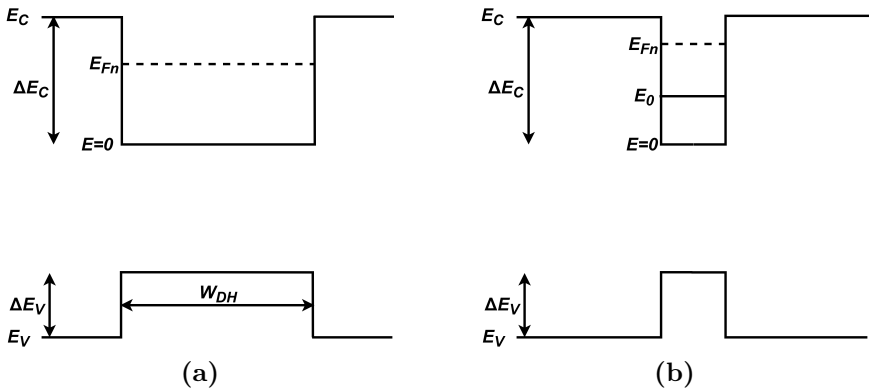

Figure 2-3: *Energy band diagrams with Fermi level, E_{Fn} of (a) double heterostructure of width W_{DH} and (b) quantum well structure with discrete subband levels e.g. first allowed energy E_1. Adapted from [22].*

In quantum mechanics, Fermi's golden rule gives the transition rate, p_r of a carrier (in this context, an electron) going from energy level 2 to energy level 1 as the following:

$$p_r \propto |M_T(E_{21})|^2 \rho_f \tag{2.1.3}$$

M_T = Transition matrix element
ρ_f = Density of final states

The term M_T is a measure of the coupling between the initial and final state. The radiative recombination rate increases for a larger transition matrix element which in turn depends on the coupling between carriers. This coupling is proportional to the overlap of the wavefunctions for each carrier which increases for thinner QWs. However for thin QWs at high injection currents carriers escape from the QW which is called carrier overflow and this saturates the optical intensity. This can be alleviated by implementing multiple quantum well (MQW) structures. The region where emission takes place and so where the QWs are situated in the LED is often termed the active region.

Properties of III-Nitrides

GaN, InN and AlN are commonly arranged in an hexagonal wurtzite structure as shown in figure 2-4 for a unit cell where a and c are the defining axes of the hexagonal unit cell. Figure 2-4 also shows four planes of the crystal namely the

c-, a-, m- and r- planes. For such structures, Bravais-Miller indices with four integers [25] are used to denote the orientation of crystal planes with each integer quantifying how the corresponding plane intersects the main axes of the crystal.

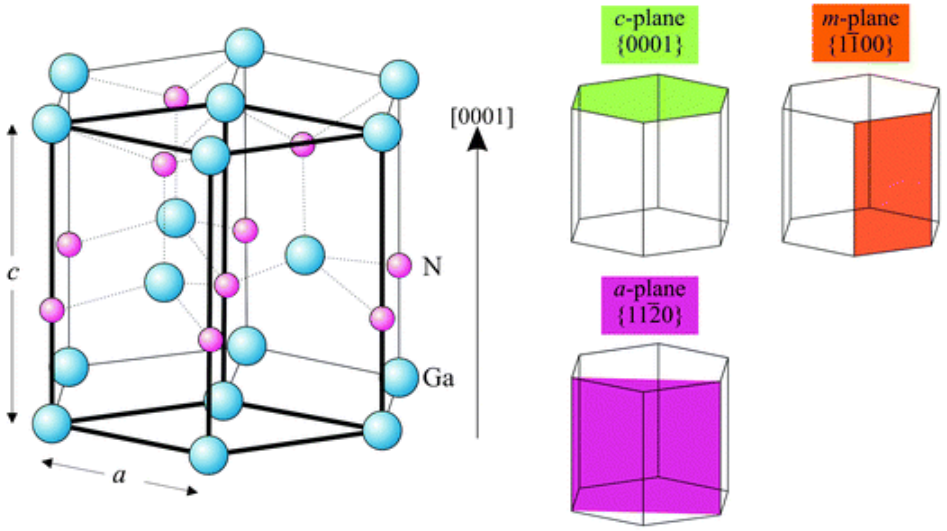

Figure 2-4: *Wurtzite unit cell highlighted in bold with the a- and c-axes labelled. The c-, a-, and m-planes are shown left. Taken from [26].*

For bulk wurtzite material the crystal is typically grown along the c-direction or [0001] direction. Wurtzite GaN has spontaneous polarisation [27] which arises from a net displacement of the electrons held in chemical bonds aligned parallel to the c-axis towards the N atoms[3] [28]. Since the c-plane comprises only Ga and N atoms there is no net polarisation in the direction orthogonal to the c-axis. This polarisation accounts for the uniaxial optical behaviour of GaN (direction dependent refractive index) and its relatively large linear electrooptic coefficients, which are a measure of the change in refractive index in proportion to an applied electric field (known as the Pockel's effect).

The wurtzite structure of III-nitrides results in a bandstructure whereby the spontaneous emission is polarized. The effect is due to the valence band splitting into three subbands [29] resulting in important selection rules which determine the angular momentum distribution between the electron and hole. The projection

[3]In the ideal wurtzite the shift between cation and anion atoms is always 3/8 however in GaN this is 0.377. Spontaneous polarization increases when this value deviates further from the ideal wurtzite structure

of the angular momentum of photons on the direction of propagation indicates the polarization of the light [30]

InN, GaN and AlN have direct bandgaps ranging from 0.7 eV to 3.4 eV to 6.2 eV respectively. The particularly large direct bandgaps of GaN and AlN make these materials suitable for blue and UV emission. Carrier concentrations in intrinsic GaN can be increased via doping with impurities like magnesium or silicon to create *p*- or *n*-type GaN respectively.
MQWs in GaN typically have indium (In) incorporation to form InGaN QWs and GaN barriers (QBs). For higher indium composition the emission wavelength is longer allowing for tunable emission of GaN-based devices. For blue emission InGaN/GaN MQWs the electric field of the emission is dominantly polarised perpendicular to the *c*-axis and this is often called transverse electric (TE) emission in literature [29]. UV wavelength emission AlInGaN alloys using high Al content can produce emission with the electric field polarised parallel to the *c*-axis and is termed transverse magnetic (TM) emission [31] [32].

2.2 LED Parameters

In this section the fundamental parameters used to characterise the performance of an LED will be defined.

Internal Quantum Efficiency

The internal quantum efficiency, η_{iqe} is defined as the ratio of photons generated by carriers recombining in the active region to the number of carriers injected into the LED [22] which may be expressed as:

$$\eta_{iqe} = \frac{P_{int}/E_{ph}}{I/q}$$

P_{int} = Optical power emitted from active region
I = Injection current
q = Charge of an electron

η_{iqe} is dependent on the degree of radiative and non-radiative recombination and there are two major types of non-radiative recombination namely: (i)

Shockley-Read-Hall (SRH) and (ii) Auger recombination which becomes more probable at high injection currents. The former is caused by trap levels inside the bandgap that present lower energy nonradiative recombination centers to carriers and arise from defects and/or impurities in the crystal. The latter dominates at high injection currents because in this process an electron and hole recombine and transfer energy and momentum to a second electron instead of emitting a photon: thus three carriers are involved which manifests in the recombination rate having a cubic dependence on carrier density. η_{iqe} depends on the crystal quality and structure. Typical values for blue emission LEDs have reached more than 70% [33].

External Quantum Efficiency

The external quantum efficiency, η_{eqe} is defined as the ratio of photons emitted into free space to the number of electrons injected into the LED. It can be expressed as:

$$\eta_{eqe} = \frac{P_{rad}/E_{ph}}{I/q} \tag{2.2.1}$$

P_{rad} = Optical power emitted into free space

Light Extraction Efficiency

The light extraction efficiency, η_{lee} of an LED is defined as the ratio of photons escaping from the structure to the photons generated by electron-hole pairs in the active region. It can be expressed as:

$$\eta_{lee} = \frac{\eta_{eqe}}{\eta_{iqe}} \tag{2.2.2}$$

It is therefore dependent on the extent of photon absorption inside the structure and the design geometry [34]. Equation (2.2.2) may also be written as:

$$\eta_{lee} = \frac{P_{rad}}{P_{int}} \tag{2.2.3}$$

Wall Plug Efficiency

The wall plug efficiency, η_{wp} is defined as the ratio of the light output power to the electrical input power:

$$\eta_{wp} = \frac{P_{rad}}{IV} \tag{2.2.4}$$

Where V is the voltage applied to the LED and I is the current through it. The wall plug efficiency is a figure of merit of an LED device while the previous parameters are used to optimise η_{wp}.

2.3 Efficiency Limitations

In this section, various limitations of LEDs will be presented, with particular focus on the limitations of light extraction efficiency and directionality of light emission as these represent the core topic of this thesis.

2.3.1 Other Efficiency Limitations

Polarization Effects of Wurtzite Structures

When an InGaN QW is grown in c-plane GaN, the larger lattice constant of InGaN compared with that of GaN causes the QW to be under compressive strain which deforms the crystal resulting in an additional piezoelectric polarisation, P_{pz}, which acts in the opposite direction to P_{sp}. The strain induced polarisation will effect the bandstructure of an InGaN QW sandwiched between GaN bulk grown along the [0001] direction [35]. This is illustrated in figure 2-5 which shows the resultant bandstructure of the QW in an LED under forward bias. In figure 2-5 it is observed the electrons in the conduction band shift to lower energy and the holes in the valence band shift to higher energies. Furthermore, the electron and hole wavefunction overlap is reduced which will decrease the spontaneous emission rate in accordance to Fermi's golden rule. The former effect is referred to as the quantum confined Stark effect (QCSE) and this is an issue for the realisation of longer wavelength GaN-based devices.

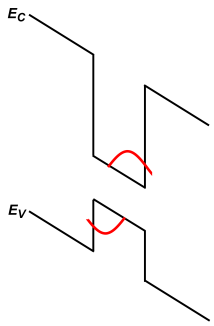

Figure 2-5: *Impact of polarisation on energy bands of planar forward biased QW.*

In addition to QCSE, the deformation of the crystal in lattice mismatching with sapphire can result in dislocation defects and a large thermal expansion mismatch of GaN with substrates like silicon can even cause cracking.

Efficiency Droop

A major limitation of GaN/InGaN LEDs for high power applications is an effect known as efficiency droop which describes the decrease in η_{iqe} with increasing injection current density. The origin of droop is still in debate but is most likely due to or a combination of phonon/defect-assisted Auger recombination [36]. Other factors however also increase the efficiency droop effect including the QCSE [37], non-uniform carrier distribution and carrier overflow [38].

Green Gap

The green gap refers to the relatively lower efficiency of green-yellow emission LEDs which is a major issue to achieving high brightness white emission without the use of a phosphor converter. AlInGaP and AlInGaN are existing materials used for green light devices however the former has reduced carrier confinement. The latter system requires high indium content for longer wavelengths resulting in larger piezoelectric polarisation due to the lattice mismatch and higher dislocation densities thus reducing η_{iqe}.

2.3.2 Light Extraction Efficiency

To provide the reader the tools to understand the following chapter, the relevant electromagnetic plane wave propagation theory and definitions will be presented. These concepts are important for understanding light extraction limitation and they will be applied to the case of III-nitride semiconductors.

The light extraction efficiency, η_{lee} is dependent on the design geometry and this is a major limiting factor for planar structures whereby light is unable to escape and remains trapped inside. To be able to demonstrate this a brief review will be made of basic electromagnetic theory and definitions.

Electromagnetic Review

The laws governing electromagnetic propagation are described Maxwell's equations. Using the MKS unit system and in differential form they are given below:

$$\nabla \times \mathbf{E} = -\frac{\partial \mathbf{B}}{\partial t} + \mathbf{M} \tag{2.3.1a}$$

$$\nabla \times \mathbf{H} = \frac{\partial \mathbf{D}}{\partial t} + \mathbf{J} \tag{2.3.1b}$$

$$\nabla \cdot \mathbf{D} = \rho_v \tag{2.3.1c}$$

$$\nabla \cdot \mathbf{B} = 0 \tag{2.3.1d}$$

$\mathbf{E}$ = Electric field (V m^{-1})
$\mathbf{H}$ = Magnetic field (A m^{-1})
$\mathbf{D}$ = Electric displacement (C m^{-2})
$\mathbf{B}$ = Magnetic induction (Wb m^{-2})
$\mathbf{J}$ = Electric current density (A m^{-2})
$\mathbf{M}$ = Equivalent magnetic current density (V m^{-2})
ρ_v = Charge volume density (C m^{-3})

The constitutive relations are required to account for the effect on the fields due to the material properties. In optical materials such as GaN the relative permeability, μ_r, linking $\mathbf{H}$ to $\mathbf{B}$ is approximately unity. The constitutive relations

are written as:

$$\mathbf{D} = \epsilon_0 \epsilon_r \mathbf{E} \tag{2.3.2a}$$

$$\mathbf{B} = \mu_0 \mu_r \mathbf{H} \tag{2.3.2b}$$

ϵ_0 = Vacuum permittivity
ϵ_r = Relative permittivity
μ_0 = Vacuun permeability
μ_r = Relative permeability

For a general medium ϵ_r (μ_r) is a tensor of rank 2 to represent the anisotropy of the material so that $\mathbf{E}$ and $\mathbf{D}$ ($\mathbf{H}$ and $\mathbf{B}$) are not in the same direction. Additionally ϵ_r (μ_r) may depend on the strength of applied electric (magnetic) field and the frequency leading to non-linear optical effects and dispersion. For the sake of clarity, an isotropic, non-dispersive and linear material is assumed in this work unless otherwise stated. Furthermore, assuming the region of interest is source free i.e. $\mathbf{J}, \mathbf{M}$ and $\rho_v = 0$ and assuming harmonic time dependence i.e. $E(t) = e^{j\omega t}$ it can be shown using equations 2.3.1a, 2.3.1b and 2.3.2, one obtains the Helmholtz wave equation which for the electric field is:

$$\nabla^2 \mathbf{E} + k^2 \mathbf{E} = \frac{\partial^2 \mathbf{E}}{\partial x^2} + \frac{\partial^2 \mathbf{E}}{\partial y^2} + \frac{\partial^2 \mathbf{E}}{\partial z^2} + k^2 \mathbf{E} = 0 \tag{2.3.3}$$

The magnetic field also satisfies wave equation of the same form. The constant k is called the wavenumber and can be expressed as:

$$k = \frac{2\pi n}{\lambda_0} = k_0 n \tag{2.3.4}$$

Where λ_0 is the free space wavelength and n is the refractive index of the medium. Equation 2.3.3 holds for each component of the field and can be solved using the separation of variables method [39]. Solutions to the wave equation are termed modes and are waves of the form[4]

$$\mathbf{E} = \mathbf{E}_0 e^{-j\mathbf{k}\cdot\mathbf{r}} \tag{2.3.5}$$

[4]Strictly speaking there is both a forward and reverse travelling wave, but only the forward travelling wave is considered for now.

Where $\mathbf{E}_0$ is the amplitude and using equation (2.3.1)(c) this is perpendicular to $\mathbf{k}$. The term $\mathbf{k}$ is the propagation vector whose magnitude is given by equation (2.3.4) and is in the direction of the wave, given by:

$$\mathbf{k} = \hat{\mathbf{x}}k_x + \hat{\mathbf{y}}k_y + \hat{\mathbf{z}}k_z \tag{2.3.6}$$

And $\mathbf{r}$ is the position vector:

$$\mathbf{r} = \hat{\mathbf{x}}x + \hat{\mathbf{y}}y + \hat{\mathbf{z}}z \tag{2.3.7}$$

Therefore:

$$\mathbf{k} \cdot \mathbf{r} = k_x\hat{\mathbf{x}} + k_y\hat{\mathbf{y}} + k_z\hat{\mathbf{z}} = \text{constant} \tag{2.3.8}$$

Equation (2.3.5) describes a uniform plane wave because (2.3.8) is a plane normal to $\mathbf{k}$ and is termed a wavefront which travels at a phase velocity with an associated power. The time-average rate of energy flow per unit area is termed the Poynting vector, $\mathbf{S}$ and is given by:

$$\mathbf{S} = \frac{1}{2}\text{Re}(\mathbf{E} \times \mathbf{H}^*) \tag{2.3.9}$$

Where * signifies the complex conjugate. The E and H fields of a plane wave are perpendicular to each other and the direction of propagation hence this wave is called transverse electromagnetic (TEM).

Total Internal Reflection (TIR)

Consider an interface at $x = 0$ separating air and a non-absorbing, isotropic and homogeneous semiconductor in figure 2-6 with refractive indices n_1 and n_2 respectively. An electromagnetic TEM plane wave propagates in the direction of $\mathbf{k}_i$ and strikes the interface at an angle θ_i. Part of the light is reflected back into the semiconductor, denoted by $\mathbf{k}_r$ and part is transmitted at a refracted angle, θ_t and propagates in the direction $\mathbf{k}_t$ as shown in figure 2-6(a). The axis is oriented as such that $\mathbf{k}_i$ lies in the xz-plane defined as the plane of incidence.

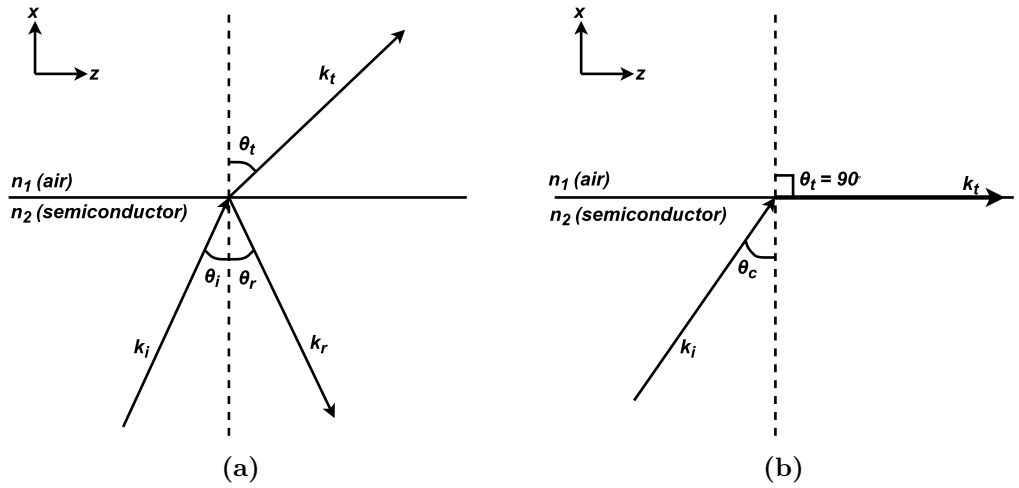

Figure 2-6: *Diagram representing the wavevector of an incident plane wave, k_i in semiconductor striking an interface with air at an angle (a) θ_i with respect to the normal where part is reflected and transmitted and (b) at θ_c when condition for TIR is met.*

The boundary conditions between the two media may be derived from Maxwell's equations and state that the tangential electric and magnetic field components are continuous across the interface at $x = 0$ for all values of z and y which is only possible if the propagation phase constant parallel along z i.e. k_z is the same for all waves. Thus:

$$k_0 n_2 \sin(\theta_i) = k_0 n_2 \sin(\theta_r) = k_0 n_1 \sin(\theta_t) \tag{2.3.10a}$$

$$\therefore \theta_i = \theta_r \tag{2.3.10b}$$

$$\text{and} \qquad n_2 \sin(\theta_i) = n_1 \sin(\theta_t) \tag{2.3.10c}$$

Equation (2.3.10c) is called Snell's law. The solutions for determining the amount of reflection and transmission at the interface are given by the Fresnel equations. If $n_1 < n_2$, the critical angle for total internal reflection (TIR) when $\theta_t = 90^\circ$ is:

$$\theta_c = \theta_i = \sin^{-1}\left(\frac{n_1}{n_2}\right) \tag{2.3.11}$$

At $\theta_i > \theta_c$ the wave propagates along the interface and is evanescent in air so no energy is transferred in the direction perpendicular to the interface and it is

completely reflected, that is the Poynting vector in the direction of x is zero. The critical angle in turn defines the internal light escape cone of solid angle, $\Omega_c = 2\pi(1 - \cos\theta_c)$: any light not emitted within this cone remains trapped inside the semiconductor by TIR.

Returning to the definition of η_{lee} in section 2.3.2, if one assumes isotropic emission of the source as is the case for a double heterostructure the light extraction efficiency can be approximated by [40]:

$$\eta_{lee} = \frac{1}{4n_2^2} \tag{2.3.12}$$

To demonstrate the limitation of the light extraction efficiency for GaN-based planar structures we take GaN in air, from which we obtain a critical angle of 24° (assuming $n_{GaN} \approx 2.5$ for blue-green emission). This indicates most of the light emitted inside the epitaxy will undergo total internal reflection. From equation (2.3.12) η_{lee} is just 4%.
Note that for InGaN QWs the emission is not isotropic but instead the electric field emits preferentially perpendicular to the c-axis which may result in slightly better coupling into the escape cone [40].

Slab Waveguide Effect

The simple model discussed in the previous section ignored the lower interface where typically one has a substrate or reflector below the semiconductor. It is now assumed the previous model includes a substrate of refractive index, n_3 where $n_2 > n_3 > n_1$ and the lateral size i.e. size along z and y is infinite as shown in figure 2-7(a) with the addition that the variation of the field is uniform along y. This can be approximated as an asymmetric slab waveguide whereby the substrate and air form the lower and upper cladding layers respectively and the semiconductor forms the core. If the light strikes the upper and lower interfaces at an angle larger than the critical angle (for both the air and substrate interfaces) it will undergo TIR and remain trapped and guided along the core or along z.

A more rigorous analysis is achieved by considering the electromagnetic field solutions to the slab waveguide which can be found from Maxwell's equations. These fields are set to be oscillatory plane waves in the core with $e^{-j(k_z z + k_y y)}$ propagation dependence and decaying waves in the cladding. It can be shown

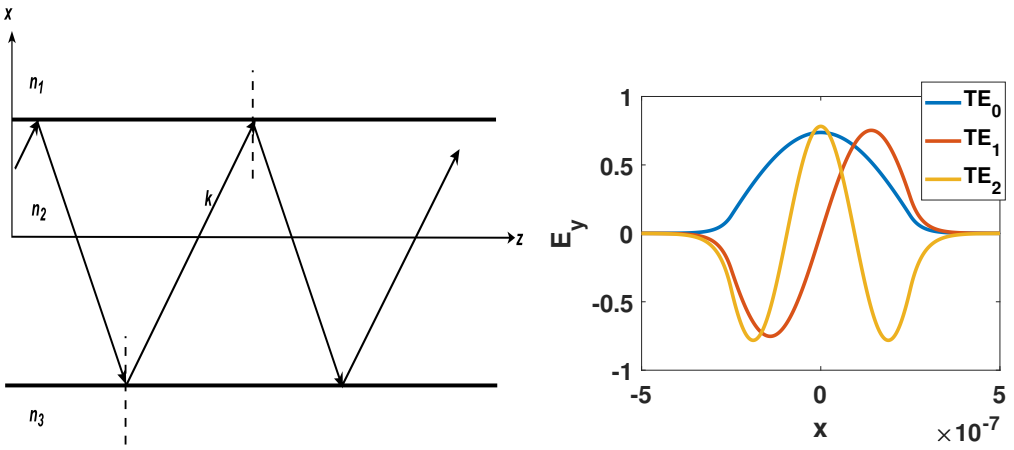

Figure 2-7: *(a) Diagram showing plane wave propagation via TIR inside asymmetric slab waveguide. (b) The three TE_m mode profiles for normalised E_y field component across slab waveguide of width 500 nm, $n_1 = n_3 = 1, n_2 = 2.5$ and $\lambda_0 = 450$ nm.*

there are a finite number of allowed solutions in the waveguide called the guided modes. The guided modes of figure 2-7(a) can be separated into two sets of linearly polarised modes: one set with the field components H_x, E_y and H_z which are termed transverse electric (TE$|_z$) modes and the other with field components E_x, H_y and E_z termed transverse magnetic (TM$|_z$) modes[5]. The power of each mode can be found from the integral of equation (2.3.9) and is proportional to the field amplitude squared[6] i.e. for a TE mode, $P \propto |E_y|^2$.

The field distribution profiles of several modes are shown in figure 2-7(b) where it has been assumed that $n_1 = n_3 = 1$ and $n_2 = 2.5$. Each guided mode has an associated $k_{z,m}$ which will be renamed β_m where $m = 0, 1, 2...$ and an effective refractive index, n_{eff} given by:

$$n_2 > n_{eff,m} = \beta_m / k_0 \tag{2.3.13}$$

If $\beta < kn_1$ the solutions have oscillatory field profiles in the cladding and form a continuum of radiation modes and the light escapes the waveguide. It is also possible for the field profiles to be oscillatory in just the substrate layer where

[5] TE$|_z$ means transverse electric with respect to the z-axis.

[6] This is for the S_z component. It is interesting to note that for TM modes, the power is also dependent on the refractive index.

$k_0 n_3 > \beta > k_0 n_1$ which results in substrate radiation modes whose energy is usually lost in the substrate from the core. Any arbitrary field profile inside the waveguide can be expressed as the weighted sum of the guided modes and radiation modes.

When the slab is made thinner or the wavelength is increased higher order modes are cut-off which is equivalent to increasing the amount of light which radiates. Furthermore, the guided modes have field profiles which extend more into the cladding.

It is desirable to have thinner planar LEDs to increase the amount of light escaping the device and consequently increase η_{lee}. The short wavelength of blue-green emission (400-550 nm) requires such devices to be very thin if one wishes to limit the number of modes to a few low orders. Such commercial solutions will be discussed in section 2.4.

It should finally be noted that when spontaneous emission in the form of a dipole occurs inside the waveguide, fractions of this emission will couple to guided modes. The power launched into the m^{th} mode, $P_m \propto |a_m E_{y,m}|^2$ assuming TE modes and a_m is the coupling coefficient which is essentially a measure of the correlation between the guided mode and the source i.e.

$$A_m \propto \int_{-\infty}^{\infty} E_{y,m} \times sourcefield$$

From figure 2-7(a) if a dipole was placed at a point inside the waveguide, the amplitude of some modes at the emission location are higher than others. In terms of Fermi's Golden rule in equation (2.1.3) this corresponds to the transition matrix element of some modes larger than for others [40]. Thus the coupling of spontaneous emission into guided modes is position dependent [41] [42] and placing the source in the region of maximum field strength i.e. an antinode of a mode will increase coupling to that mode.

2.3.3 Etendue

In addition to the reduced light extraction of planar devices from TIR, the observed emission pattern in the far-field has poor directionality. It can be shown for a dipole emitting inside the semiconductor near the planar surface that the

far-field emission pattern is given by [22]:

$$I_{air} = \frac{P_{src}}{4\pi r^2} \frac{n_{air}^2}{n_s^2} \cos\theta_2 \tag{2.3.14}$$

P_{src} = Total source power
r = Radius of sphere centered at position of source
n_{air} = Refractive index of air
n_s = Refractive index of semiconductor
θ_2 = Angle of refracted ray with respect to normal

From equation (2.3.14) it can be seen that maximum emission occurs at $\theta_2 = 0°$ and is at 50% of this value at $\theta_2 = 60°$. This is known as Lambertian emission and there is no significant preferential emission.

This is an issue for high brightness applications such as projectors and back-lighting where directional far-field emission is desirable if not essential and these are referred to as entendue-limited systems [13, 43–45]. Etendue, E, is a measure of the flux gathering (emitting) capability of an optical system defined by:

$$E = A\Omega \tag{2.3.15}$$

A = Area of emission (collection)
Ω = Projected (collected) solid angle

For an optical system like that shown in figure 2-8 of a simplified high-brightness projector, it can be shown for maximum power transfer the etendue of the display must match the etendue of the LED.

Using equation (2.3.15) this means that:

$$A_{LED}\Omega_{LED} = A_{disp.}\Omega_{disp.} \tag{2.3.16}$$

Thus if the solid angle of the LED is more narrow then more LEDs can be used to satisfy (2.3.16). By using more LEDs, more light output power is transferred and the gain of the optical system is increased.

Encapsulating the LED with a lens, whilst increases the η_{lee} due to the reduced refractive index contrast, reduces the luminance and increases the etendue of

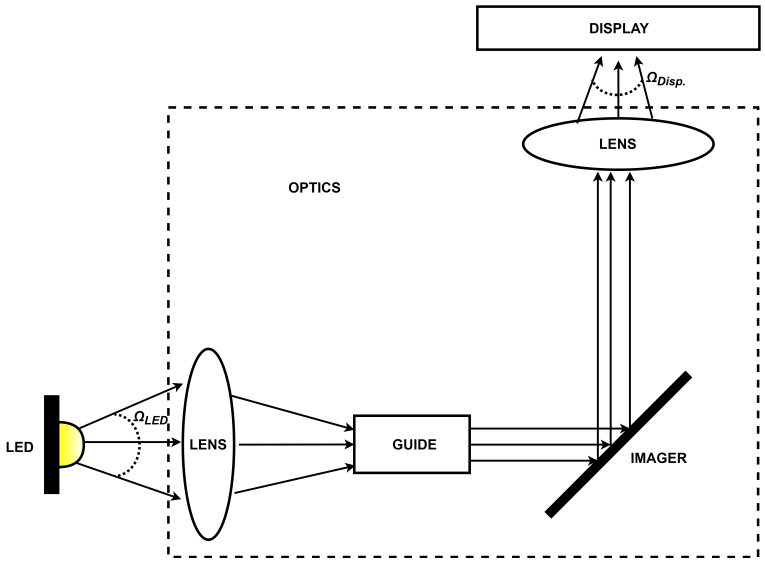

Figure 2-8: *Simplified high brightness projector system.*

the device. It is often more desirable to use unencapsulated devices for such applications. For example, implementing ordered arrays of nanostructures on the surface of devices have been experimentally shown to improve directionality in the vertical direction [46] [47].

2.3.4 Summary

To summarise, it has been shown that unencapsulated planar GaN devices have low light extraction efficiency of around 4% arising from the large refractive index contrast between GaN and air which reduces the critical angle so most of the light undergoes TIR. For thick structures we observe a large number of guided modes that are trapped and do not contribute to the η_{lee}, including modes radiating into the substrate and dissipating energy. There is also the addition of poor directionality making planar structures unsuitable for high power etendue-limited applications. The next section will discuss some typical commercial solutions that are implemented and attempt to alleviate these issues and increase light extraction efficiency.

2.4 Commercial Solutions

Currently there are several standard LED designs and typically, as with everything in life, there is a compromise between complexity (and therefore generally cost) of LED fabrication and the optimisation of LED parameters. Some typical designs are presented in figure 2-9 and show a:

(a) Lateral chip GaN-on-substrate device

(b) Flip-chip device

(c) Vertical structure with conductive substrate

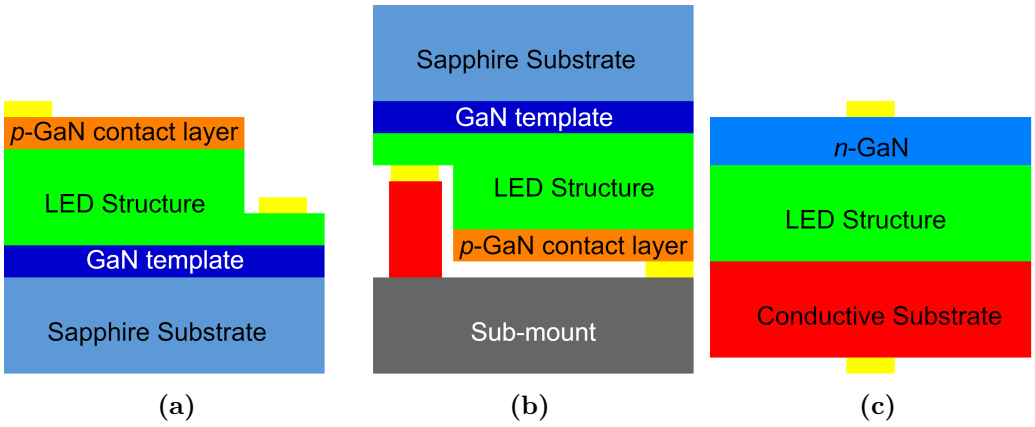

Figure 2-9: *Schematic of three typical commercial GaN-based LED structures employing (a) GaN-on-substrate, (b) flip-chip and (c) vertical arrangement. Adapted from www.soft-epi.com/overview.php*

Substrates are used for the growth of epitaxy and in 2012 it was reported that almost 100% of blue emission LEDs were produced on insulating substrates with 90% grown on sapphire [48]. Sapphire has the advantages of being transparent to UV-blue-green emission and being more stable in terms of thermal, chemical and mechanical properties. It is however more costly compared with materials like silicon. Additionally it has a lattice and thermal mismatch with GaN which introduces strain and causes an increase in defects thus reducing efficiency. This means it is difficult to achieve high quality sapphire substrates at large wafer sizes [49] greater than 2-4 inches in diameter, reducing yield. For larger substrate

sizes it is desirable to replace sapphire with silicon which is cheaper and silicon is far easier to remove which simplifies the achievability of different LED structures [50]. When GaN is grown on silicon substrates the lattice mismatch causes tensile strain resulting in cracking. Early commercial high power GaN-on-silicon LEDs were fabricated by OSRAM on 6 inch wafers [51] in 2013. From figure 2-9(a), GaN-on-substrate devices require a current spreading layer to improve electrical properties but these layers are optically absorbing.

Flip-chip devices like that shown in figure 2-9(b) tend to be implemented for high power applications. The LED structure is grown on sapphire and then flipped over. The light escapes through the transparent substrate and is not absorbed/reflected off the contacts and current spreading layer. These devices can be made larger and light can be reflected from the contact, provided its reflectivity is very high as the light extraction efficiency is sensitive to this. Silver is typically implemented and when its absorption properties were accounted for in modelling was found to reduce LEE by 5% [52]

Vertical devices in figure 2-9(c) are so called due to the vertical current flow. The materials used for the substrate need a larger electrical conductivity than sapphire, such as silicon carbide. Alternatively the substrate can also be removed completely: commercial thin film vertical LED technology has been well established by OSRAM [53] who remove the substrate using a laser lift-off technique. Such devices can be made very thin and so reduce the number of guided modes trapped inside the structure. The contact arrangement of vertical devices can reduce light extraction however by obstructing the light.

For all of these presented structures the issue of light trapping remains due to the planar surface and presence of guided and substrate radiation modes. Several methods to alleviate these effects and increase light extraction can be employed and are presented in the following section.

2.4.1 Geometrical Shaping

In this method, the shape of the device is modified to increase the probability of light escaping as shown in figure 2-10 [54]. Typically the devices are angled at the sidewalls to be shaped like a prism. The resulting deflection of the light vertically has resulted in enhancement factors of around 2 and 4.65 [55] [56] reported com-

pared with a rectangular shaped die. They can also be shaped into polygons to increase sidewall emission whereby, if a light strikes an interface and undergoes TIR, its incident angle will be different when it strikes the next interface if it is not parallel to the previous. It has been shown for a range of different polygons, the rectangular structure displayed the lowest LEE by around 10-15% [57] compared with 21% light enhancement observed for prisms due to increased light extraction from the sidewalls [58]. Circular shaped devices also displayed similar enhancements by about 19% [59]. The shaping is usually achieved via laser micromachining [60] however growth methods also exist [58].

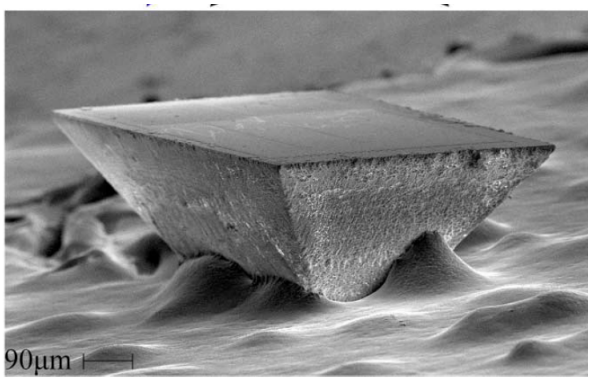

Figure 2-10: *Image of prism shaped LED die. Taken from [54].*

2.4.2 Surface Roughening

In this method the surface of the LED is roughened using a wet chemical etching process which has the advantage of being an easy and cheap way to increase light extraction. The resulting roughened surface consists of random, densely arranged small facets as shown in figure 2-11 [61]. The size of these features can vary from 100 nm to 2 μm. It has been shown that roughening the surface of an LED randomises the light trajectories [62] [63], increasing the probability of light striking the surface at an angle less than the critical angle for TIR, leading to light escaping into air. This technique has been shown to increase the wall plug efficiency by 62% [64]. For GaN-on-substrate structures the extraction efficiency was increased by a factor of 2-4 [61] [65] compared to a planar structure. Applied to thin-film vertical LEDs, surface roughening increased the η_{lee} by about 50% [66]. One drawback of this approach is the little theoretical work which has

been done on surface roughening. Due to the ergodicity of light propagation (i.e. the independence of the final state on its initial state) it can be challenging to model and have any control over the directionality of the light emission.

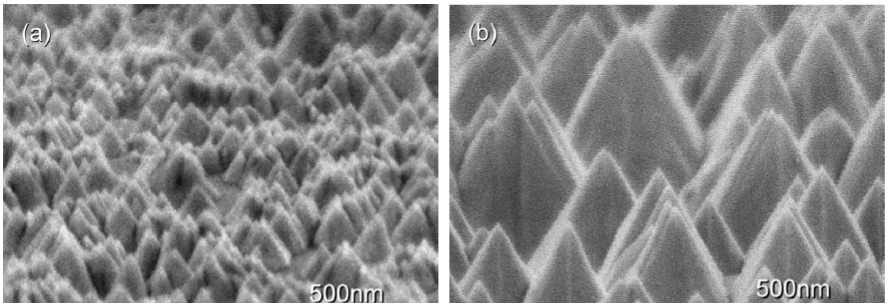

Figure 2-11: *Surface etched GaN. Taken from [61].*

2.4.3 Resonant Cavity LEDs

Resonant Cavity LEDs (RCLEDs) make use of cavities whereby the resonance conditions are satisfied and the transmission is maximum for a particular wavelength. For the sake of physical insight the most simple form of planar cavity is considered with a thickness, L, which is of the order of the wavelength and formed by a highly reflective mirror at the bottom and a partially reflective mirror above. The cavity is filled with a refractive index n. Such a structure may be termed a Fabry-Perot interferometer and its principle of operation is shown in figure 2-12 for three layers.

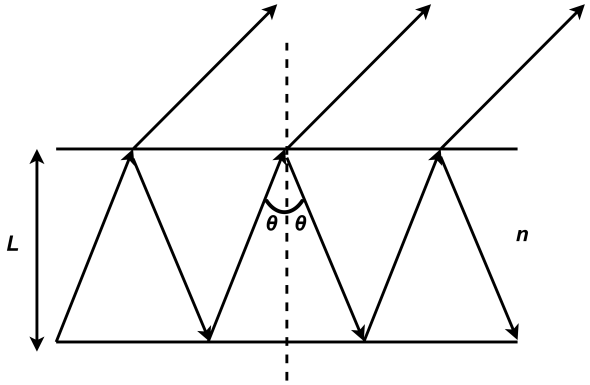

Figure 2-12: *Fabry-Perot interferometer.*

In accordance to Snell's law, a beam of light strikes one interface and is partially transmitted and reflected. The reflected beam then strikes the other interface where it is also reflected and transmitted and so on. The amount of reflection and transmission at the interface are given by the Fresnel equations. The total upward transmitted light is found by summing up the multiple beams and it can be shown for maximum transmission:

$$k_0 nL\cos(\theta) = m\pi \tag{2.4.1}$$

This means the beams constructively interfere. Hence for a given wavelength, the far field will consist of concentric rings at discrete angles which are often termed Fabry-Perot (FP) modes or resonances: resonances with angles, $\theta > \theta_c$ are truly guided modes [41]. This approximation has also been applied to planar GaN-on-substrates being modelled as a cavity [67]. Placing the active region at antinodes of the FP modes enhances the coupling between the QW emission and resonance modes, thus increasing η_{lee}.

For cavities where $L >> \lambda$ one can obtain a gain of factor two and $\eta_{lee} \approx 8\%$ due to the bottom reflector [41]. If however the thickness is made so small of the order of the wavelength, one has a microcavity (MC) [68]. Here the cavity is thin enough so that quantum effects occur whereby ρ_f in equation (2.1.3) is altered and is maximum at the same frequency as the cavity mode. This will modify the spontanous emission rate and thus affect η_{iqe}. This is known as the Purcell effect [69]. Recent simulation work showed spontaneous emission rate enhancements of 1.9 of blue emission LEDs using metamaterials [70].

RCLEDs have the advantage of being highly directional and more spectrally 'pure', i.e. a narrower spectrum whose width is determined by the Q-factor of the cavity. Early RCLEDs had $\eta_{eqe} \approx 23-28\%$ [71–73] for wavelengths of around 980 nm but this value can reduce to 7% at 650 nm [74], demonstrating the difficulty in achieving shorter wavelength emission RCLEDs. Nevertheless recently blue RCLEDs have displayed η_{eqe} of 15% (at low injection currents) and 26% light output power increase compared to conventional LEDs [75] by using distributed Bragg reflectors (DBRs) instead of metal mirrors for high reflectivity, with the lower loss factor of dieletric materials contributing to this improvement. DBRs were shown to increase conventional RCLED light output power by a factor of

three [76].

2.4.4 Micro/Nano-texturing

Investigation has been made into the use of ordered arrays of micro or nanostructures. The latter are often termed two dimensional 'photonic crystals' (PhCs) because much literature adopts the same analysis used for semiconductor crystals when the period of the array is of the order of the optical wavelength, and the array is periodic in two dimensions. Many of these structures are implemented as diffraction gratings whereby the active region is located below the array. The grating has the effect of coupling the guided modes to radiation modes via the grating vector $|K| = \frac{2\pi}{\Lambda}$ where Λ is the pitch of the array. Mathematically this can be represented by:

$$\beta_m + i\mathbf{K} < kn_1 \tag{2.4.2}$$

Where i is an integer and represents the order of diffraction. If the pitch of the array is made larger, more diffraction orders are observed in the 'far-field' which is the infinite distance from the array but as a rule of thumb is usually around 8-10 wavelengths.

Nano/microstructures are typically formed via a dry etching technique called reactive ion etching (RIE) whereby accelerated ions are directed onto the device and etch away parts of the semiconductor. By placing the active region below the array one avoids etching the active region (and p-type GaN). By etching these regions there is the risk of damage to the emissive QWs and degraded electrical properties from etching the p-GaN, hence the reason the diffraction grating method is adopted.

For this reason early GaN-on-sapphire devices were shallow etched i.e. less than a wavelength depth on the surface to form the nanostructures. Such devices have shown light output enhancements of 1.3-1.6 for blue (460 nm wavelength) emission [77] [78] and 2-2.5 for UV (340 nm) emission [78] [79] achieved by etching holes in a 2D hexagonal arrangement. An immediate advantage of implementing such structures is the potential of improved control of the light extraction by changing the many parameters of the array such as the pitch, lattice arrangement and diameter. In terms of the arrangement, [80] it was found the reflectivity decreased as the height of pyramids arranged in hexagonal arrays increased. For

close packing of pyramids where the bases touched, the reflectivity was calculated to reduce exponentially with increasing height. For cones, where the perimeter of the bases did not touch around the whole perimeter, the reflectivity saturated with increasing height. It has been experimentally observed that the pitch has a strong impact on the enhancement of the light output: enhancements reached a factor of 4.4 when optimising the pitch of 2D square lattice arrangements of holes [81]. It has also been observed that the angular far-field emission pattern included higher diffraction orders when the pitch was increased [82] demonstrating control of directionality. Directional emission was enhanced by a factor of 3.5 by varying the pitch and $\eta_{lee} \approx 50\%$ [17]. However there is a limit to increasing the pitch due to diffraction into the substrate [81].

Shallow etching results in the etched surface having poor interaction with all of the guided modes as shown in figure 2-13 [14] where several guided mode field profiles are shown inside a thin-film vertical LED structure with a shallow etched PhC on the surface. Note that low order modes have poor interaction with the PhC because just the tails of the profiles overlap the PhC, reducing the coupling efficiency. From the discussion of the slab waveguide earlier the position of the active region will result in larger overlap of the active region with the mode envelope and therefore greater coupling strength and so will remain trapped inside the LED because of their poor interaction with the PhC.

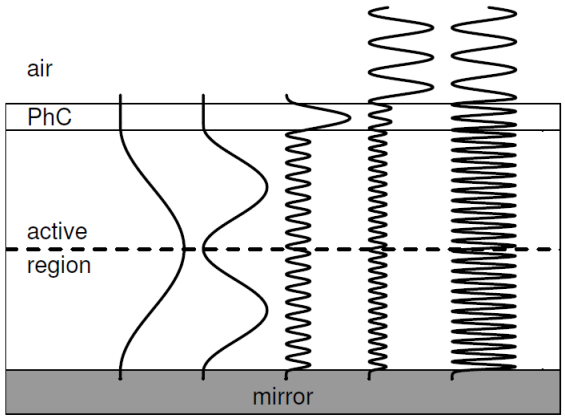

Figure 2-13: *Schematic of thin-film vertical structure LED with PhC and several guided mode field profiles in increasing order from left to right. Taken from [14].*

It is desirable to have larger etch depths to extract more guided modes out

of the structure. Deep etching of dense arrays of nanorods is hard to achieve and so alternative designs have been proposed to extract more guided modes. Some are shown in figure 2-14. In the design of 2-14(a) a tunnel junction was inserted which spreads the injection current and places the PhC closer to the active region, thus increasing the coupling of emission to the PhC. A reported extraction enhancement of 1.5 and directionality enhancement of 1.75 [46] was obtained.

In 2-14(b) David *et al.* [83] implemented tailored guided mode distribution whereby a lower index AlGaN cladding layer was inserted near and below the active region to force low order modes below where they are not excited. In the layer above the cladding one observes cap-layer modes (CLMs) and for very thin layers a single CLM can be well extracted as it overlaps strongly with both the active region and PhC. Such structures reported enhancements of 1.7-2 and $\eta_{lee} = 20\%$.

The design of 2-14(c) implemented embedded PhCs whereby a GaN coalescence layer is grown over the nanostructure which is located below the active region. Such a structure can ensure low order modes have good overlap with the PhC. This is achieved by the PhC forming a lower refractive index medium which traps low order modes above, where they have strong overlap with the active region and below where they will be less likely excited. If the thickness of the overgrown layer is thin enough a single CLM can be supported which has strong interaction with the PhC. Increased directionality was reported [84] [85] and η_{lee} of up to 94% was experimentally observed after optimizing the coalesced layer and PhC thickness [85].

A significant issue with such structures are the inferior electrical properties in the form of higher turn on voltages: for example the structure in figure 2-14(a) reported turn on values of 4-5.5 V compared to 3.5 V for conventional LEDs. The structure of 2-14(b) required etching into the active region and p-GaN and in fact no electrical characterisation could be made. The structure in figure 2-14(c) however avoids any etching of the active region and additionally due to the planar surface contact arrangement, is greatly simplified consequently little degradation in the electrical properties was found [85]. Nevertheless the additional nanofabrication adds cost to the device manufacturing.

PhCs made up of nanostructured arrays have also been etched onto the surface

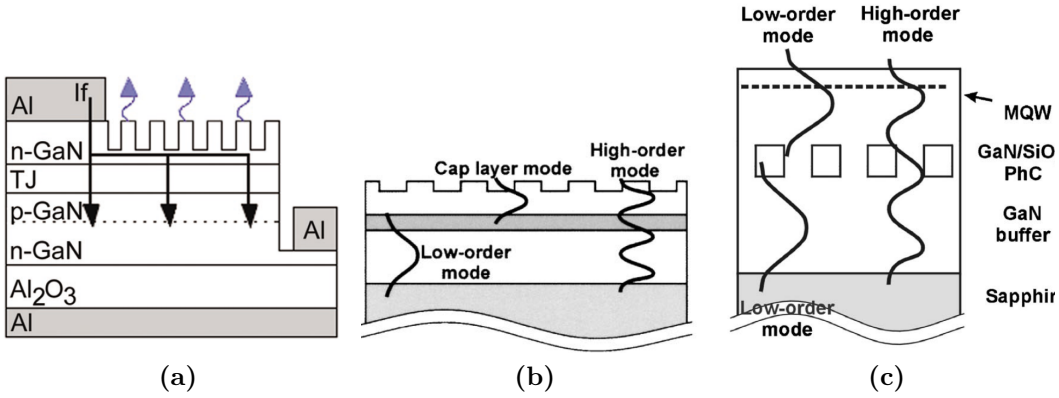

Figure 2-14: *Methods of extracting guided modes using PhCs by (a) using a tunnel junction [46], (b) implementing a lower index cladding layer just belowe the active region [83] and (c) embedding the PhCs below the active region [84].*

of thin-film vertical and MC-RCLED devices. Due to fewer guided modes, a reduced dependence of the light extraction efficiency on the ability to extract a large range of guided modes would be expected. The first case of a superior vertical thin-film (700 nm thick) blue emission device using a PhC with $\eta_{lee} = 73\%$ was reported after optimising parameters including the pitch, etch depth and PhC arrangement [86]. Other studies have shown little dependence of the thickness of the epitaxy below the etched structures on the light output power and far-field emission. Nevertheless large enhancements of light output power of 4.5 were still reported [47] compared to unetched structures and higher intensity in the vertical emission (directionality). The directionality is also dependent on the position of the active region due to the reflector and increasing etch depth [16] allowing for more degrees of freedom for optimisation. MC structures with PhC etching on the surface have displayed light output power enhancement factors of 1.8 [87] and 2.5 [88] which, for the latter, displayed a directional far-field with 50% of the intensity within an angle of 17°. A new problem arises with this approach in the form of absorption losses from the metal contacts [89] for which silver is superior to metals like gold [47].

In summary it can be seen that nano/microstructures etched into the surface of conventional structures significantly increases the light output power and by changing parameters of the array and the epitaxy thickness below one achieves good control of η_{lee} and directionality in the far-field emission patterns, particu-

larly the pitch and etch depth. The degrees of freedom allow for optimisation of such structures in terms of achieving maximum η_{lee} and directionality.

2.4.5 Summary

Three typical commercial structures have been presented namely (i) GaN-on-substrate, (ii) flip-chip and (iii) vertical devices. To address the issue of limited light extraction due to light trapping, several methods have been discussed to alleviate this effect and they are: (i) geometrical shaping, (ii) surface roughening, (iii) resonant cavities and (iv) micro/nanotexturing. For the method of (iv) the use of ordered arrays has the potential of controlling the directionality of emission.

The complicated fabrication and limited supply of material and cost to make these structures means numerical or analytical modelling is required to perform optimisation. Additionally modelling allows one to test or predict the output of new structures. A method widely used to model the emission of LED structures is finite difference time domain (FDTD) which is a numerical electromagnetic solver. We will discuss its use in the application of LEDs particularly structures which implement periodic arrays of nano/monostructures.

2.5 The Use of FDTD for Modelling LEDs

Electromagnetic solvers are extremely useful tools to design and optimise the light extraction and overall emission of LED devices. In section 2.4.4, several of the references initially used modelling to validate and design LEDs with high light extraction efficiency.

The finite-difference time-domain (FDTD) method [90] numerically solves Maxwell's equations to find the electromagnetic propagation within a given a structure defined by the refractive index profile. This method has the following advantages for LED modelling:

(i) Structures with very complicated material optical properties and complex geometry can be simulated.

(ii) FDTD is a time-domain solver and so can simulate over a wide frequency range. This makes the method ideal for modelling spontaneous emission and looking for resonances over a larger frequency range.

(iii) The method is intuitive and straightforward in the sense that a user need only to input the structure to observe the fields evolve over time.

(iv) Fields can be measured at any position at any time directly from the simulation which can be used to calculate LED parameters such as η_{lee} and far-field emission patterns as will be shown later.

(v) Other methods used before FDTD (e.g. the plane wave expansion (PWE) method and rigorous coupled wave analysis (RCWA)) require solving many simultaneous equations which becomes practically difficult and easily unstable for complicated structures, compared with FDTD which is a very robust method.

FDTD is computationally expensive in terms of running time and processor capability relative to other methods. Consequently it was not used frequently, and only for one/two-dimensional simulations, until the 1990s when computer capability accelerated. Furthermore the uniform Cartesian grid structure of FDTD can limit this method's ability to model small structures and reduce numerical errors. However implementations of non-uniform gridding have allowed for FDTD to be used to simulate demanding features such as surface roughening [91] and resonances without the huge computational resources required otherwise. Now non-uniform resolution is readily available in commercial FDTD software like Lumerical [92]. FDTD is a common method for calculating η_{lee} and far-field emission of LEDs. It may also be used to look at the field distributions inside the structure i.e. near-field measurements and thus identify issues (or benefits) associated with light trapping.

Because FDTD can easily model complex geometry relative to other methods it is often used to simulate PhC arrangements. The potential of photonic crystals for increasing the light extraction efficiency was first investigated using FDTD in 1997 [93] whereby a simple dielectric slab perforated with air holes arranged in a two-dimensional hexagonal array displayed a light extraction efficiency of 70% and peaking at 90% for certain wavelengths. Here η_{lee} was defined as the ratio of light output power outside the structure to the total emitted power from the source acting as spontaneous emission which was placed in the middle of the PhC as per equation (2.2.3). Early FDTD simulations which demonstrated the feasibility of PhCs for LEDs were made on similar structures. The impact of the

etch depth on η_{lee} was investigated and it was observed that this increases when the hole depth is increased, and reaches maximum with fully etched holes through the entire structure [94]. This is in agreement with experimental observations of increasing etch depth increasing light output and furthermore demonstrates the potential enhancement if the active region is not degraded from etching. Such deep etching is difficult to achieve experimentally.

The same study also found the relative η_{lee} decreased to 80% when a cladding layer was placed below the fully etched PhC. FDTD simulations of GaN-on-sapphire devices with arrays of holes etched into the surface found increased η_{lee} for increased etch depth [95] with η_{lee} of almost 20% compared to 9% for the unetched structure.

All of these early studies demonstrated how FDTD can be used to optimise light extraction as a function of the known parameters of PhCs. It also allows for modelling of extreme pattern geometry i.e small pitch, small diameter and large etch depth which can be difficult to achieve in the actual fabrication process technology especially at large scale. The previous study in [95] also used FDTD to obtain η_{lee} as a function of the lattice constant where the optimum value of 700 nm was hard to achieve practically at the time. Ichikawa [96] performed two-dimensional FDTD simulations to optimise the pitch of shallow PhCs etched into vertical LEDs, as shown in figure 2-15(a), and found enhancement factors of almost 3 could be reached. Comparison with experiment was in relatively good agreement for smaller pitches. Good agreement with experiment was also found in [97] for GaN-on-sapphire structures shallow etched with square arrays of varying pitch with an enhancement factor of 2.3 reached. The same group modelled thin-film GaN-based vertical devices with PhCs [98] [99] where it was shown that η_{lee} saturated at large etch depths and the output enhancement was increased for a larger refractive index contrast in the PhC. The far-field emission patterns obtained from FDTD and experiment of high aspect ratio nanorod arrays etched on vertical structures were also found to be in excellent agreement and showed increased directivity with the nanorods [100] as shown in figure 2-16(a).

FDTD can model more 'exotic' PhC arrangements. A different type of PhC called photonic quasi-crystals whereby the array has local disorder but long range order are of interest because of their unique optical properties such as potential for more uniform far-field emission. Charlton *et al.* [101] modelled photonic quasi-

crystals etched on the surface of thin flip-chip GaN LEDs and obtained far-field emission patterns which demonstrated this feature. FDTD has also been used to investigate Anderson localization [102] in more random arrays [103]. More recently FDTD has been used to demonstrate increased light extraction efficiency and uniform emission can be achieved with amorphous PhCs of GaN-based thin-film flip-chip LEDs [104] as shown in figure 2-15(b).

Xu *et al.* [105] used FDTD to simulate more complicated LED structures using 'double PhCs' in a vertical structure as shown in figure 2-15(c). Here the effect of the pitch, hole diameter and height of the second PhC were varied and enhancement was increased by a factor of 1.39 compared to a structure employing a single PhC at the surface for practically feasible parameter values of the arrays.

The motivation of embedded PhCs was provided in FDTD simulations by Long *et al.* [106] by comparing results for a PhC etched on the surface of a GaN-on-sapphire device and a PhC placed below the active region. From near-field measurements, the mechanism of embedded PhCs could be identified whereby the PhC acted to 'decouple' light from the substrate where it was lost in the case of the PhC etched on the surface to the substrate. Both structures were optimised by varying the pitch, the ratio of hole diameter to pitch, the PhC thickness and for the embedded PhC the distance from the PhC to the active region. For the latter it was found η_{lee} decreased as the the distance from the PhC to the active region increased (t_2 in figure 2-14(c)) and the thickness of the embedded PhC displayed maximum enhancement at an optimum value unlike for the surface PhC. The structure employing the embedded PhC displayed a value of $\eta_{lee} = 71\%$ compared to 63% for the top PhC. It was also found that employing both a top and bottom PhC did not significantly increase η_{lee} enough to justify the complicated and expensive fabrication process that would be required. The same study found the shape of the holes had little effect and predicted that light extraction was dependent only on the density of holes and area occupied by them implying the main mechanism for increased η_{lee} of surface PhCs was scattering of light.

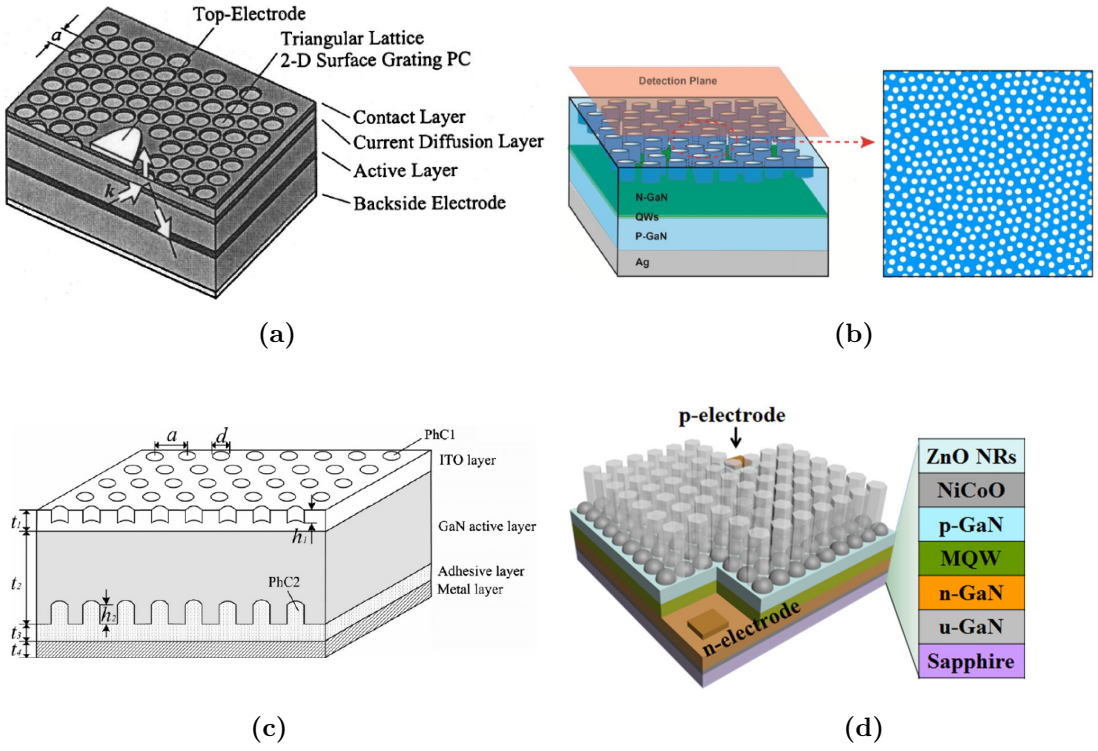

Figure 2-15: *Several PhC structures which have been simulated in FDTD: (a)Vertical LED with surface grating PhC [96]. (b) Thin-film flip-chip LED with amorphous PhC [104] (c) vertical structure employing a double PhC [105]. (d) GaN-on-substrate devices with ZnO nanorod arrays on NiCoO hemisphere lenses [107].*

FDTD has also been implemented as a method of modelling organic LEDs (OLEDs). Early FDTD results showed that more than 40% of the total emitted light is trapped inside the structure [108] of planar devices despite the smaller refractive index contrast between the organic polymer and air compared with inorganic LEDs. Thus, similarly to GaN-based LEDs, PhCs have been used to increase η_{lee}. Values of 60% were obtained for PhC-OLEDs after optimising the rod radius, depth and lattice constant using FDTD and good agreement between simulated and measured far-field emission patterns was achieved [109] as shown in figure 2-16(b).

FDTD has been used to calculate the light extraction efficiency of spherical shaped microtextured devices which are often more practically feasible: Zhao *et al.* [110] [111] modelled thin-film vertical devices with GaN microdomes and

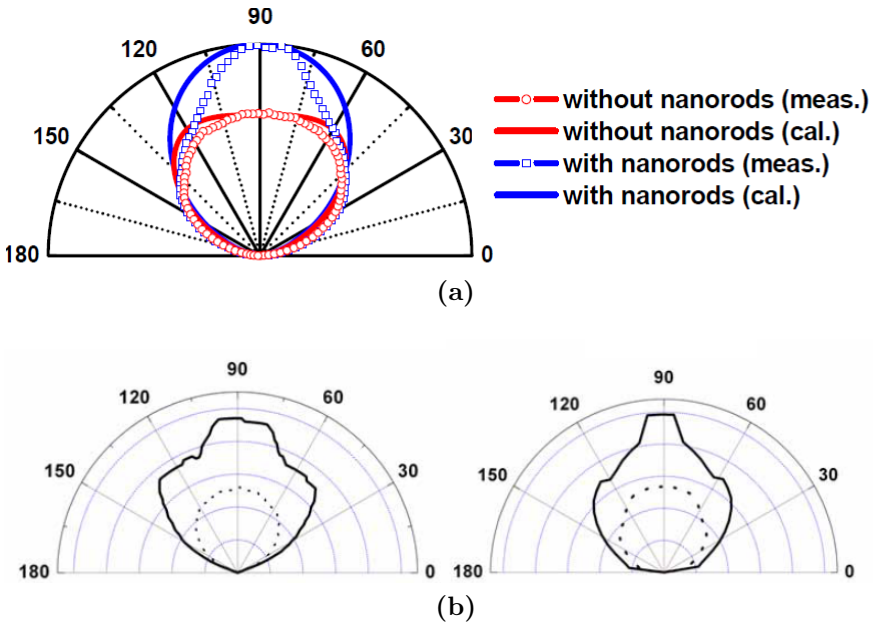

Figure 2-16: *Comparison of FDTD with experimental results obtained for the far-field emission patterns (a) Vertical injection GaN-LED with nanorod arrays [100]. (b) OLED with PhC of pitch=500 nm where left is measured and right is FDTD [109].*

obtained η_{lee} enhancements of 2.5-2.7 after optimising the height and width of the microdomes. The same group used FDTD to extend the application of microdomes to deep-UV wavelength (230-270 nm) emission devices [112] where TM polarised light is more dominant in the spontaneous emission. Achieving efficient deep-UV devices is a subject of much research. After optimising the position of the active region and microdome height and diameter the light extraction efficiency was enhanced by a factor of 7.3 compared to conventional devices. Furthermore, far-field emission patterns were obtained from FDTD showing the enhancement due to the microdomes. Zhu *et al.* [113] simulated microspheres on the surface of GaN-on-sapphire structures made of SiO_2 and TiO_2 (which is index matched to GaN) and found enhancements in η_{lee} of 1.9 and 2.2 respectively after optimising the diameter of the spheres. The increased enhancement of the latter was attributed to the refractive index matching of TiO_2 and GaN and this was also found from FDTD simulations for nanodomes structures in another study where η_{lee} enhancement factor of 5.7 was predicted [114]. The TiO_2 microspheres also demonstrated increased directionality as observed in simulated

far-field emission patterns which increased for a larger diameter of microsphere. The same group applied TiO_2 microsphere arrays on thin-film flip-chip structures in FDTD simulations [115] and the extraction efficiency was optimised as a function of the array arrangement and number of layers of spheres to produce a 3.6 fold enhancement. The number of layers also had a strong effect on the directionality of the far-field emission pattern.

FDTD is often used to model the complex properties of metals and their alloys on a nanoscale making it a useful tool to investigate plasmonic effects by looking at near-field distributions and methods of texturing the surface of contacts. Aluminium nanoparticles were simulated and investigated using FDTD and their plasmonic effects where found to increase η_{lee} of deep-UV LEDs by extracting more of the TM-polarised spontaneous emission [116]. More recently randomly distributed indium tin oxide (ITO) nanodots and silver nanowires were modelled on contacts as a method to increase light output power of UV LEDs and where it was observed that silver nanowires increased scattering [117]. Modelling of ZnO rods and ZnO nanorods on NiCoO hemispherical lens arrays on the surface of GaN-on-sapphire structures, as shown in figure 2-14(d) gave results that were consistent with experimental work [107]. ZnO nanorods were also simulated whereby the near-field distributions as a function of the tilt angle of the nanorods [118] were obtained to investigate the broader emission that was observed experimentally.

Photonic Bandgaps

The current discussion has been on PhCs implemented as diffraction gratings or scatterers to outcouple light to air. There exists another use of PhCs which exploit the photonic bandgap (PBG) effect [119] whereby light within a range of frequencies cannot propagate inside the periodic refractive index medium: this is analogous to a semiconductor crystal where the periodic variation of the potential causes an energy gap, hence the term photonic crystal. The PBG becomes wider for larger refractive index contrast and in practice exploiting a large omnidirectional PBG for visible wavelength LEDs is difficult to achieve.

In fact the initial justification for the study in [93] was to investigate the PBG effect. For LEDs, a PBG could have the effect of inhibiting spontaneous emission for frequencies within that gap so no optical modes are available for spontaneous

emission in accordance to Fermi's golden rule thus creating the potential to control the number of modes. Early modelling used the PWE method to solve for the modes of such structures [120–124] and observe PBGs however good agreement has been observed between FDTD and PWE [108].

An issue was simulating the placement of defects within the PhC in the form of say a larger hole in an array of smaller holes: this can result in strongly localised modes inside the gap and therefore one obtains a microcavity. The PWE method becomes very time consuming and often unstable when modelling defect modes but FDTD is ideal. Defect modes were first demonstrated from FDTD simulations of periodic dielectric waveguides containing defects and high Q-factors were obtained [125]. FDTD is now widely used for modelling PBG materials with defects [126] [127] in the microwave wavelength range. More recently enhancements in spontaneous emission have been calculated using FDTD by designing nanodisk arrays where η_{iqe} was increased by a factor of 88% for green wavelength emission [128] thus the potential for bridging the so called green gap.

Summary

A brief discussion has been presented of several studies whereby FDTD modelling was used to simulate and optimise the light extraction, far-field emission and in some cases spontaneous emission of a range of different and complex LEDs. In Particular the comparison with experimental results has proven that FDTD is a reliable and flexible method. The next chapter will go into the details of FDTD and its algorithm in order to develop the simulation set-up used to model the devices in chapter 7 and extract parameters to provide a quantitative comparison.

Chapter 3

Finite-Difference Time-Domain (FDTD) Method

The finite-difference time-domain (FDTD) method allows complicated structures to be mapped onto a discrete spatial grid, often termed the computational cell and the electromagnetic fields are evolved over time on this spatial grid. Provided the sampling in space and time is high enough i.e. on a sub-wavelength scale, the method is robust and accurate. Additionally, it can be easily implemented as a parallel process on computational machines.

In this chapter a rigorous discussion and overview of the FDTD method and its implementation is given. For a comprehensive literary source the reader is referred to [129] and much of the initial discussion has been summarised from this work. Subsequently the considerations to be made for the modelling of LEDs is discussed and an introduction to the software used for implementing FDTD called MEEP is presented.

This chapter begins with the Yee algorithm which established the crux of the FDTD method for the case of a linear, isotropic and nondispersive medium. It is the intention that by reviewing a simple example the salient features of FDTD will be clearly identified.

3.1 Yee Algorithm

The FDTD method [90] is a numerical method that approximates Maxwell's curl equations with finite difference expressions to model the propagation of elec-

tromagnetic radiation. For convenience these and the constitutive relations in section 2.3.2 are rewritten here:

$$\nabla \times \mathbf{E} = -\frac{\partial \mathbf{B}}{\partial t} + \mathbf{M} \tag{3.1.1a}$$

$$\nabla \times \mathbf{H} = \frac{\partial \mathbf{D}}{\partial t} + \mathbf{J} \tag{3.1.1b}$$

$$\mathbf{D} = \epsilon_0 \epsilon_r \mathbf{E} \tag{3.1.1c}$$

$$\mathbf{B} = \mu_0 \mu_r \mathbf{H} \tag{3.1.1d}$$

It is assumed that the material properties are linear (field-independent), isotropic (direction-independent) and nondispersive (frequency-independent) so that ϵ_r and μ_r reduce to scalar values as in equations 3.1.1c and 3.1.1d.

The terms $\mathbf{J}$ and $\mathbf{M}$ are made up of two parts: one part is due to sources independent of the applied fields and the second part is due to dissipation of energy from free charges inside the material moving under the applied field for which we have assumed is linear. They may be written as:

$$\mathbf{J} = \mathbf{J_s} + \sigma \mathbf{E} \tag{3.1.2a}$$

$$\mathbf{M} = \mathbf{M_s} + \sigma^\star \mathbf{H} \tag{3.1.2b}$$

σ = Electrical conductivity (S m^{-1})
$\sigma^\star$ = Equivalent magnetic loss (H m^{-1})
$\mathbf{J_s}$ = Source current density (A m^{-2})
$\mathbf{M_s}$ = Equivalent source magnetic density (V m^{-2})

Substituting equations 3.1.1c, 3.1.1d and 3.1.2 into 3.1.1a and 3.1.1b and with some rearrangement one obtains:

$$\frac{\partial \mathbf{H}}{\partial t} = -\frac{1}{\mu_0 \mu_r} \nabla \times \mathbf{E} - \frac{1}{\mu_0 \mu_0} (\mathbf{M_s} + \sigma^\star \mathbf{H}) \tag{3.1.3a}$$

$$\frac{\partial \mathbf{E}}{\partial t} = \frac{1}{\epsilon_0 \epsilon_r} \nabla \times \mathbf{H} - \frac{1}{\epsilon_0 \epsilon_r} (\mathbf{J_s} + \sigma \mathbf{E}) \tag{3.1.3b}$$

The three-dimensional vector fields, $\mathbf{E}$, $\mathbf{H}$, and source densities, $\mathbf{J_s}$, $\mathbf{M_s}$ may be

expressed in terms of their vector field components as:

$$\mathbf{E} = \hat{\mathbf{x}}E_x + \hat{\mathbf{y}}E_y + \hat{\mathbf{z}}E_z \tag{3.1.4a}$$

$$\mathbf{H} = \hat{\mathbf{x}}H_x + \hat{\mathbf{y}}H_y + \hat{\mathbf{z}}H_z \tag{3.1.4b}$$

$$\mathbf{J_s} = \hat{\mathbf{x}}J_{s,x} + \hat{\mathbf{y}}J_{s,y} + \hat{\mathbf{z}}J_{s,z} \tag{3.1.4c}$$

$$\mathbf{M_s} = \hat{\mathbf{x}}M_{s,x} + \hat{\mathbf{y}}M_{s,y} + \hat{\mathbf{z}}M_{s,z} \tag{3.1.4d}$$

Here the time dependence has not been included which generally the fields will be a function of as well. After applying the curl operations in equations 3.1.3, they can be expressed for each vector component of the field and one obtains six coupled equations. For the sake of brevity a single one is expressed for the E_x field component:

$$\frac{\partial E_x}{\partial t} = \frac{1}{\epsilon_0 \epsilon_r}\left[\frac{\partial H_z}{\partial y} - \frac{\partial H_y}{\partial z} - (J_{s,x} + \sigma E_x)\right] \tag{3.1.5}$$

Yee [130] showed that each of the six coupled equations can be approximated in discrete form derived from Taylor series as a finite difference equation[1]. As a reminder Taylor series is a series expansion of a function $u(x)$ about a point $x = a$ given by:

$$u(x) = u(a) + u'(a)(x-a) + \frac{f''(a)}{2!}(x-a)^2 + \dots \tag{3.1.6}$$

By setting $x - x_i = \Delta x$ so that

$$x = x_i + \Delta x \tag{3.1.7}$$

And substituting this into 3.1.6:

$$u(x_i + \Delta x) = u(x_i) + u'(x_i)\Delta x + \frac{u''(x_i)}{2!}(\Delta x)^2 + \dots \tag{3.1.8}$$

[1]The method of using finite differences to approximate partial derivatives was first tested by Courant *et al.* [131] to approximate the wave equation to 2^{nd} order accuracy in one and two dimensions.

Similarly for $u(x_i - \Delta x)$:

$$u(x_i - \Delta x) = u(x_i) - u'(x_i)\Delta x + \frac{u''(x_i)}{2!}(\Delta x)^2 - \dots \tag{3.1.9}$$

Subtracting 3.1.9 from 3.1.8 and upon rearranging, the partial derivative can be expressed as a finite-difference expression:

$$\left.\frac{\partial u}{\partial x}\right|_{x_i} = \frac{u(x_i + \Delta x) - u(x_i - \Delta x)}{2\Delta x} + O[(\Delta x)^2] \tag{3.1.10}$$

Where $O[(\Delta x)^2]$ is the remainder term which represents the error caused by approximating the partial derivative.

Yee devised an algorithm to implement finite-difference expressions for the partial derivatives to 2$^{\text{nd}}$ order accuracy by representing the structure as a spatial grid or lattice made up of individual Yee cells as shown in figure 3-1 in three-dimensional space. The six electric and magnetic field components are represented at positions of the cell as such that each electric and magnetic field component has four circulating magnetic and electric field components respectively to represent the curl operations of Maxwell's equations. The divergence laws of Maxwell's equations are implicitly satisfied at each cell.

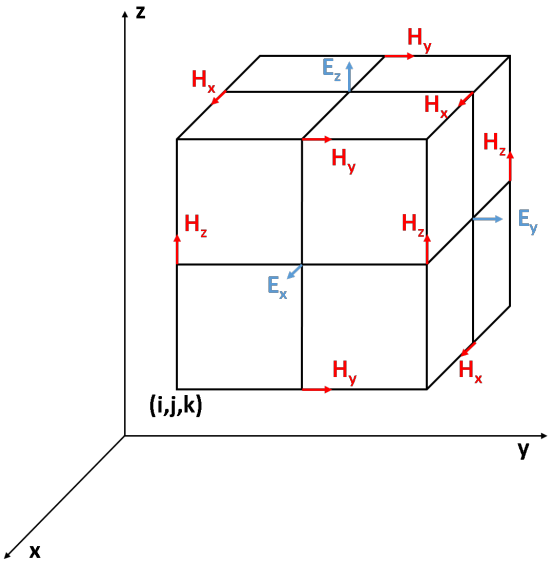

Figure 3-1: *Position of the electric (blue) and magnetic (red) field components on a three dimensional unit Yee cell. Modified from [129].*

From figure 3-1, the space point (i, j, k) is defined as:

$$(i, j, k) = (i\Delta x, j\Delta y, k\Delta z) \tag{3.1.11}$$

Where the terms Δx,Δy and Δz denote the three spatial increments along x, y and z. The function u represents a field component at a point in time and space and can be rewritten as:

$$u(i\Delta x, j\Delta y, k\Delta z, n\Delta t) = u^n_{i,j,k} \tag{3.1.12}$$

Where n is an integer and Δt is the time increment. The difference between equation (3.1.10) and Yee's finite difference approximation of the partial derivatives was the substitution of $\Delta x/2$ so that the space finite difference was over $\pm\Delta x/2$. Using the notation in (3.1.12) and assuming the time step is at $n\Delta t$, the partial derivative of u in the x-direction may be expressed as:

$$\left.\frac{\partial u}{\partial x}\right|^n_{i,j,k} = \frac{u^n_{i+1/2,j,k} - u^n_{i-1/2,j,k}}{\Delta x} + O\big[(\Delta x)^2\big] \tag{3.1.13}$$

Partial derivatives with respect to y, z (if applicable) or t can be expressed in a similar manner by incrementing the corresponding step by 1/2 e.g. $\pm\Delta t/2$. Defining the finite difference as 1/2 shifts the electric and magnetic fields by a half Yee cell and results in an overlapping 'leapfrog' scheme which is probably best described by applying the algorithm to a 1D example:

(i) Electric field components are calculated at $t = 0$, i.e. an initial value problem is defined for all positions $x = 0, \Delta x, 2\Delta x, 3\Delta x$ etc. These are stored in memory.

(ii) Magnetic field components are calculated from previously stored electric field values at next time step $t = 1/2\Delta t$ at all positions midway between the electric field components i.e. $x = \frac{\Delta x}{2}, \frac{3\Delta x}{2}, \frac{5\Delta x}{2}$ etc. These are stored in memory.

(iii) The process repeats for next time step at $t = \Delta t$: electric field updated using previous stored magnetic field and so on.

(iv) The process finishes when all time steps have expired which occurs at steady state or late-time when the fields have decayed sufficiently.

To see how the finite differences are applied to Maxwell's equations this notation and the form of (3.1.13) is applied to the vector component in equation (3.1.5) at for example $(i+1/2, j, k+1/2, n)$ in figure 3-1. One obtains:

$$\frac{E_x\big|^{n+1/2}_{i+1/2,j,k+1/2} - E_x\big|^{n-1/2}_{i+1/2,j,k+1/2}}{\Delta t} = \frac{1}{\epsilon_0\epsilon_r\big|_{r,i+1/2,j,k+1/2}}\left(\frac{H_z\big|^n_{i+1/2,j+1/2,k+1/2} - H_z\big|^n_{i+1/2,j-1/2,k+1/2}}{\Delta y} - \frac{H_y\big|^n_{i+1/2,j,k+1} - H_y\big|^n_{i+1/2,j,k}}{\Delta z} - J_{s,x}\big|^n_{i+1/2,j,k+1/2} - \sigma\big|_{i+1/2,j,k+1/2} E_x\big|^n_{i+1/2,j,k+1/2}\right) \tag{3.1.14}$$

Because the fields are measured half a timestep apart, E_x at timestep n is estimated using semi-implicit approximation:

$$E_x\Big|^n_{i+1/2,j,k+1/2} = \frac{E_x\Big|^{n+1/2}_{i+1/2,j,k+1/2} + E_x\Big|^{n-1/2}_{i+1/2,j,k+1/2}}{2} \tag{3.1.15}$$

Substituting (3.1.15) into (3.1.5) and after some rearrangement one obtains the

explicit time step expression for $E_x\big|^{n+1/2}_{i+1/2,j,k+1/2}$:

$$E_x\big|^{n+1/2}_{i+1/2,j,k+1/2} = \left(\frac{1 - \frac{\sigma\big|_{i+1/2,j,k+1/2}\Delta t}{2\epsilon_0\epsilon_r\big|_{i+1/2,j,k+1/2}}}{1 + \frac{\sigma\big|_{i+1/2,j,k+1/2}\Delta t}{2\epsilon_0\epsilon_r\big|_{i+1/2,j,k+1/2}}} \right) E_x\big|^{n-1/2}_{i+1/2,j,k+1/2}$$

$$+ \left(\frac{\frac{\Delta t}{\epsilon_0\epsilon_r\big|_{i+1/2,j,k+1/2}}}{1 + \frac{\sigma\big|_{i+1/2,j,k+1/2}\Delta t}{2\epsilon_0\epsilon_r\big|_{i+1/2,j,k+1/2}}} \right) \left(\frac{H_z\big|^n_{i+1/2,j+1/2,k+1/2} - H_z\big|^n_{i+1/2,j-1/2,k+1/2}}{\Delta y} \right.$$

$$\left. - \frac{H_y\big|^n_{i+1/2,j,k+1} - H_y\big|^n_{i+1/2,j,k}}{\Delta z} - J_{s,x}\big|^n_{i+1/2,j,k+1/2} \right) \quad (3.1.16)$$

Similar finite-difference expressions can be found for the other field components. Therefore, new field value can be computed from previous field values, the field values at adjacent points and the known sources. This highlights an advantage of the method namely it can be ran as a parallel process and the spatial grid can be divided into sub-cells with each sub-cell ran on a processor for each time step. It is finally noted that for one- and two-dimensional simulations the structure and field are uniform and of infinite extent in the other two or one directions respectively.

In order to obtain reliable and stable results in FDTD the lattice increments, $\Delta x, \Delta y$ and Δz which are related to Δt need to be small enough so that the fields do not diverge and result in an instability where the fields blow up over time. Additionally the propagation of the fields through the discretized grid can result in non-physical phenomenon whereby the numerical phase velocity of waves is different to the physical phase velocity. This will now be discussed in more detail.

3.2 Stability and Numerical Dispersion

When the simulation is unstable the solution does not converge and the strength of the fields tends to infinity as time is advanced. It can be shown via complex-frequency analysis that, for stability in three-dimensions [129], Δt must be bounded as:

$$\Delta t < \frac{1}{c\sqrt{\frac{1}{(\Delta x)^2} + \frac{1}{(\Delta y)^2} + \frac{1}{(\Delta z)^2}}} \tag{3.2.1}$$

By setting the spatial increment e.g. Δx one is also setting Δt. This is known as the Courant-Fridrichs-Lewy condition [132]. If the lattice is cubic by setting the spatial increment to be $\Delta x = \Delta y = \Delta z$ one can define the Courant factor, S as:

$$S = \frac{c\Delta t}{\Delta x} \tag{3.2.2}$$

For stability in a three-dimensional Yee lattice, $S < 1/\sqrt{3}$.

In addition to instability, a more frequently encountered issue is numerical dispersion. This arises due to the discretization of the grid and causes non-physical effects in electromagnetic wave propagation such that the phase velocity varies with sample spacing, direction of propagation in the grid and wavelength. To better demonstrate this the wave equation from section 2.3.2 is repeated here for the electric field:

$$\nabla^2\mathbf{E} + k^2\mathbf{E} = \frac{\partial^2\mathbf{E}}{\partial x^2} + \frac{\partial^2\mathbf{E}}{\partial y^2} + \frac{\partial^2\mathbf{E}}{\partial z^2} + k^2\mathbf{E} = 0 \tag{3.2.3}$$

In equation (3.2.3) it is assumed the sources $\mathbf{J}$ and $\mathbf{M} = 0$ and harmonic time dependence $E(t) = e^{j\omega t}$. Solutions to (3.2.3) are of the form:

$$\mathbf{E} = \mathbf{E_0}e^{j(\omega t - k_x x - k_y y - k_z z)} \tag{3.2.4}$$

Where

$$k^2 = \epsilon_r\mu_r\left(\frac{\omega}{c}\right)^2 = (k_x)^2 + (k_y)^2 + (k_z)^2 \tag{3.2.5}$$

Equation (3.2.5) is termed the dispersion relation for a physical three-dimensional plane wave propagating in a lossless, isotropic medium. Applying the FDTD notation discussed so far to this plane wave solution in (3.2.4) for each field

component and substituting into the numerical forms of the six coupled partial derivative equations in equation (3.1.14) and after several steps the equivalent numerical dispersion becomes:

$$\left[\frac{\sqrt{\epsilon_r\mu_r}}{c\Delta t}\sin\left(\frac{\omega\Delta t}{2}\right)\right]^2 = \left[\frac{1}{\Delta x}\sin\left(\frac{k'_x\Delta x}{2}\right)\right]^2 + \left[\frac{1}{\Delta y}\sin\left(\frac{k'_y\Delta y}{2}\right)\right]^2 + \left[\frac{1}{\Delta z}\sin\left(\frac{k'_z\Delta z}{2}\right)\right]^2 \tag{3.2.6}$$

Where k'_x, k'_y and k'_z are the x, y and z components of the numerical wavevector. If $\Delta x, \Delta y, \Delta z$ and $\Delta t \to 0$ equation (3.2.6) is identical to (3.2.5). Therefore the dispersion relation now depends on the resolution.

In three-dimensions, the dispersion relation is a transcendental equation. For propagation along one dimension, e.g. x, it can be solved analytically. Defining the phase velocity of the numerical wave as $v'_p = \omega/k'$ and defining the grid sampling resolution, N_λ:

$$N_\lambda = \frac{\lambda}{\Delta x} \tag{3.2.7}$$

And using equation (3.2.2), the ratio of v'_p to the physical wave velocity, v_p can be expressed as:

$$\frac{v'_p}{v_p} = \frac{\pi\sqrt{\epsilon_r\mu_r}}{N_\lambda \sin^{-1}\left[\frac{\sqrt{\epsilon_r\mu_r}}{S}\sin\left(\frac{\pi S}{N_\lambda}\right)\right]} \tag{3.2.8}$$

If $S = 1$, $v'_p = v_p$ thus the larger S is the closer the solution becomes to the ideal case, with less dispersion. A large value of S implies Δt is larger which also enables the simulation to run more quickly, but this is limited by the Nyquist theorem. For two/three-dimensions however, $S < 1$ to ensure numerical stability and so there will be a degree of numerical dispersion. Pulses will contain a range of frequencies whereby each frequency will propagate at different speeds. Additionally due to the cumulative nature of FDTD, numerical dispersion will become more pronounced for larger cell sizes. These effects can be reduced quadratically by increasing resolution.

3.3 Boundary Conditions

The computational cell containing the structure to be simulated must be bounded to limit the amount of memory required. Several boundary conditions can be used to limit the size of the computation. To have more of an understanding of these, the boundary conditions that arise from Maxwell's equations are considered for the interface of two different media as shown in figure 3-2.

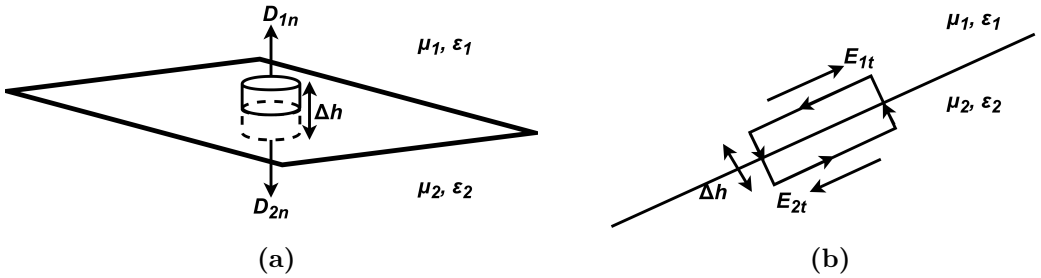

Figure 3-2: *Interface of two media. Boundary conditions are derived by applying surface integral in (a) and line integral in (b) where* $\Delta h \to 0$

These can be summarised as:

$$D_{2n} - D_{1n} = \rho_v \tag{3.3.1a}$$

$$B_{2n} = B_{1n} \tag{3.3.1b}$$

$$\mathbf{E}_{2t} = \mathbf{E}_{1t} \tag{3.3.1c}$$

$$\mathbf{H}_{2t} - \mathbf{H}_{1t} = \mathbf{J} \tag{3.3.1d}$$

Here the subscripts n and t refer to the components that are normal and tangential to the interface. The boundary conditions result in reflection and transmission of a TEM wave at the interface. Again referring to the discussion in section 2.3.2 this is redrawn in figure 3-3. The variation along x and y is zero and by orienting the axis as such that the plane of incidence is the xz-plane. It can be shown the solutions may be decoupled into two special cases where the E-field is (i) parallel to the plane of incidence and (ii) perpendicular to it. They are termed parallel (or TM) and perpendicular (or TE) polarisation respectively and the equations governing their reflection and transmission are different for each polarisation. From figure 3-3 a perpendicular polarised wave with H_x, E_y, H_z field

components is considered.

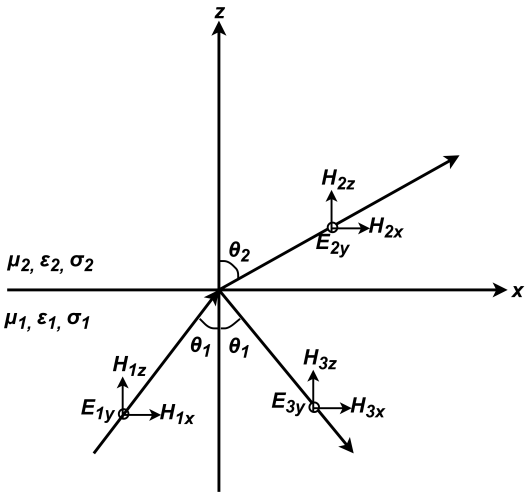

Figure 3-3: *Perpendicular (TE) polarised plane wave incident on interface at angle θ_1 where it is reflected and refracted at angle θ_2.*

The reflection coefficient, Γ is defined as:

$$\Gamma = \frac{E_2}{E_1} \tag{3.3.2}$$

The transmission coefficient, T, is:

$$T = \frac{E_3}{E_1} \tag{3.3.3}$$

From the boundary conditions listed in equations (3.3.1), the Fresnel reflection and transmission coefficients for perpendicular polarisation are:

$$\Gamma = \frac{\eta_1 \cos(\theta_1) - \eta_2 \cos(\theta_2)}{\eta_1 \cos(\theta_1) + \eta_2 \cos(\theta_2)} \tag{3.3.4a}$$

$$T = \frac{2\eta_1 \cos(\theta_1)}{\eta_1 \cos(\theta_1) + \eta_2 \cos(\theta_2)} \tag{3.3.4b}$$

Where η is the wave impedance given by:

$$\eta_i = \sqrt{\frac{\mu_i}{\epsilon_i}} \qquad i = 1, 2 \tag{3.3.5}$$

Here the notation from Taflove and Hagness [129] has been used to remain consistent with the previous discussion of FDTD. The relevant boundary conditions implemented in FDTD will now be discussed with particular focus on perfectly matched layers.

3.3.1 Perfect Electric Conductor (PEC)

The perfect electric conductor (PEC) boundary condition is the most simple whereby the user sets the tangential electric fields to be zero at the boundary.

If one includes conductivity for region 2 in figure 3-3, this alters equation (3.3.5) to:

$$\eta_2 = \sqrt{\frac{\mu_2 \left(1 + \frac{\sigma^\star}{j\omega\mu_2}\right)}{\epsilon_2 \left(1 + \frac{\sigma}{j\omega\epsilon_2)}\right)}} \tag{3.3.6}$$

The PEC by definition has infinite conductivity and from equation (3.3.6) will appear as a short circuit with zero impedance. From (3.3.4) this results in $\Gamma = 1$ so all of the light is reflected. PECs can be useful for simulating resonators however cannot be used if one wishes to simulate a structure in which return reflections would corrupt the results. A similar case arises for the perfect magnetic conductor (PMC) boundary condition where the tangential magnetic fields are set as zero at the boundary.

3.3.2 Perfectly Matched Layer (PML)

From equations (3.3.4) and (3.3.6), it is possible to achieve $\Gamma = 0$, i.e. a reflection-less interface for normal incidence, by impedance matching the media $\epsilon_1 = \epsilon_2$ and $\mu_1 = \mu_2$ and enforcing conditions on the conductivity namely $\sigma^\star = \sigma\eta_1^2$. In these conditions the amplitude of the wave in region 2 will decay exponentially. In general however waves will be incident on the interface at all angles for which this set-up would still yield very large return reflections.

The perfectly matched layer (PML) [133] addresses this issue and is theoretically reflection-less for all angles of incidence, frequencies and polarisations. It is an artificial material placed on the inside of the computational cell which technically does not make it a boundary condition [134]. A PEC is placed at the outer edge of the computational cell and it is reasoned that the wave is almost

completely attenuated by the time it enters the PML and reflects off an outermost PEC and travels through the PML again, as shown in figure 3-4.

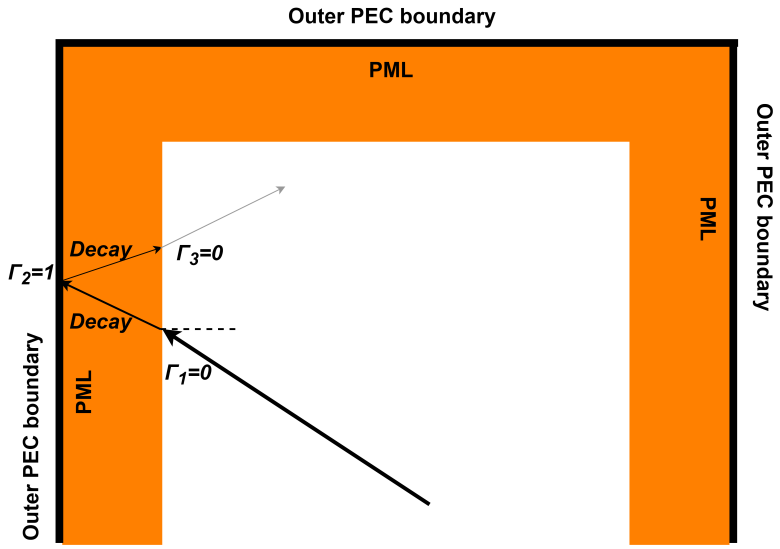

Figure 3-4: *Application of PML whereby wave is incident on PML with zero reflection strikes the PEC and returns heavily attenuated.*

Similarly the PML is designed to be impedance matched to the medium adjacent to it but instead of scalar conductivities alone, the PML incorporates anisotropy whereby ϵ_r and μ_r are tensors of rank three of the form:

$$[\epsilon_r] = \begin{bmatrix} \epsilon_{xx} & 0 & 0 \\ 0 & \epsilon_{yy} & 0 \\ 0 & 0 & \epsilon_{zz} \end{bmatrix} \qquad [\mu_r] = \begin{bmatrix} \mu_{xx} & 0 & 0 \\ 0 & \mu_{yy} & 0 \\ 0 & 0 & \mu_{zz} \end{bmatrix} \tag{3.3.7}$$

Referring to figure 3-3 a plane wave is incident from air onto the PML interface. A straightforward method to ensure impedance matching everywhere is:

$$[s] = [\mu_r] = [\epsilon_r] = \begin{bmatrix} a & 0 & 0 \\ 0 & b & 0 \\ 0 & 0 & c \end{bmatrix} \tag{3.3.8}$$

It can be shown that Snell's law for anisotropic media is modified and given by:

$$\sin(\theta_1) = \sqrt{bc}\sin(\theta_2) \tag{3.3.9}$$

For both perpendicular and parallel polarisations the reflection coefficients are respectively [135]:

$$\Gamma_{par.} = \frac{\sqrt{a}\cos(\theta_1) - \sqrt{b}\cos(\theta_2)}{\sqrt{a}\cos(\theta_1) + \sqrt{b}\cos(\theta_2)} \tag{3.3.10a}$$

$$\Gamma_{per.} = \frac{-\sqrt{a}\cos(\theta_1) + \sqrt{b}\cos(\theta_2)}{\sqrt{a}\cos(\theta_1) + \sqrt{b}\cos(\theta_2)} \tag{3.3.10b}$$

If $\sqrt{bc} = 1$ equations (3.3.9) and (3.3.10) reduce to:

$$\sin(\theta_1) = \sin(\theta_2) \therefore \theta_1 = \theta_2 \tag{3.3.11}$$

And:

$$\Gamma_{par.} = \frac{\sqrt{a} - \sqrt{b}}{\sqrt{a} + \sqrt{b}} \tag{3.3.12a}$$

$$\Gamma_{per.} = \frac{-\sqrt{a} + \sqrt{b}}{\sqrt{a} + \sqrt{b}} \tag{3.3.12b}$$

As can be seen, the reflection coefficients are no longer a function of angle and setting $a = b$ makes the reflection zero. If $a = b = 1/c$ the PML can be written as a tensor containing just one variable:

$$[s_z] = \begin{bmatrix} s_z & 0 & 0 \\ 0 & s_z & 0 \\ 0 & 0 & s_z^{-1} \end{bmatrix} \tag{3.3.13}$$

The subscript z refers to a wave travelling in the $+z$ direction that hits a PML boundary that is limiting the z-axis. Similar matrices exist for s_x and s_y for a three-dimensional simulation and may be combined to obtain a single parameter, s:

$$[s] = \begin{bmatrix} \frac{s_y s_z}{s_x} & 0 & 0 \\ 0 & \frac{s_x s_z}{s_y} & 0 \\ 0 & 0 & \frac{s_x s_y}{s_z} \end{bmatrix} \tag{3.3.14}$$

This is known as the uniaxial PML (UPML) [136] because (3.3.13) describes an

uniaxial anisotropic medium. Figure 3-5(a) visualizes the PML and how the $s_{x,y,z}$ parameters are varying only for the relevant direction. For example, s_x of the PML boundary which terminates the x-axis is set to a value other than one and with $s_y = s_z = 1$ inside this layer. It should also be noted that at the edges and corners in the three-dimensional cell the PML overlaps and for these regions the tensor must be modified to include contributions in the other directions.

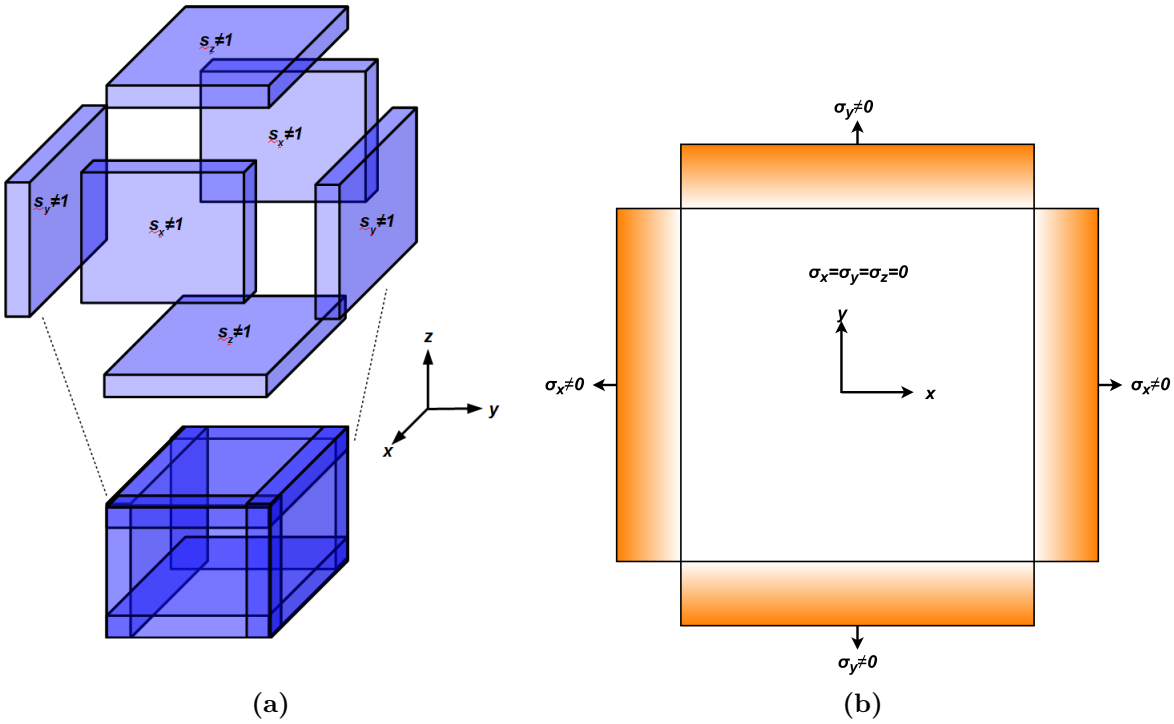

Figure 3-5: *(a) 3D visualization of UPML and the s_x, s_y, s_z parameters for each boundary terminating the corresponding axis are set to not equal one. (b) xy-plane of PML and the σ_x and σ_y parameters for the corresponding boundary. Adapted from [137].*

The elements of s must be complex to incorporate loss inside the PML and attenuate the wave so that there are no reflections from the outer edge of the computational cell which is typically a PEC. This is achieved by defining the elements of s as the following:

$$s_x = 1 + \frac{\sigma_x}{j\omega\epsilon_0} \qquad s_y = 1 + \frac{\sigma_y}{j\omega\epsilon_0} \qquad s_z = 1 + \frac{\sigma_z}{j\omega\epsilon_0} \tag{3.3.15}$$

Where $\sigma_{x,y,z}$ is the PML conductivity that is only spatially varying along the

corresponding axis. Figure 3-5(b) shows how $\sigma_x \neq 0$ and $\sigma_y \neq 0$ for the corresponding x and y PML boundary. In the frequency domain where harmonic time dependence is assumed, the UPML is incorporated into Maxwell's equations (3.1.1b) and (3.1.1a) (assuming $\mathbf{J_s}$ and $\mathbf{M_s}$ as zero):

$$\nabla \times \mathbf{E}(\omega) = -j\omega\mu_0[\mu_r][s]\mathbf{H}(\omega) \tag{3.3.16a}$$

$$\nabla \times \mathbf{H}(\omega) = j\omega\epsilon_0[\epsilon_r][s]\mathbf{E}(\omega) \tag{3.3.16b}$$

For implementation of an UPML in FDTD, equations (3.3.16) are Fourier-transformed into the time domain and then discretized. The final expressions become very extensive and are omitted here but may be found in [129].

In continuous space the PML is theoretically reflectionless. However in discrete space, the PML no longer obeys an analytical formulation and the boundary between the PML and medium are no longer perfectly reflectionless. A critical parameter for the effectiveness of the PML is the conductivity profile. This needs to be turned on gradually, as shown in figure 3-5(b) by the graduation in colour, over the length of the PML to prevent numerical reflections which arise from the discretization of the absorbing layer. Furthermore, from figure 3-4, there are round-trip reflections from waves incident upon the PML, reflecting off the PEC boundary and then returning into the inner domain. The strength of the conductivity needs to be large enough that the wave is (almost) completely attenuated by the PML before it returns. Taking $\sigma_x(x)$ as the conductivity inside the x-PML this is chosen as:

$$\sigma_x(x) = \sigma_0 f\left(\frac{x}{L}\right) \tag{3.3.17}$$

The term σ_0 is the strength and increasing this will reduce the round-trip reflections but at the cost of increasing numerical reflections. L is the length of the PML and for a thicker PML, σ_x is more gradual because the profile shape is more stretched out, however this requires increased computational memory. Additionally if L is too thin, round-trip reflections from the PEC are more dominant. The term $f(u)$ is the conductivity profile whose argument $u = x/L$ and starts from zero at the PML interface to 1 at the end of the PML. Figure 3-6 [138] shows how if the profile is turned on too fast the numerical reflections from the discretization are increased by discretizing the profiles for polynomial grading $f(u) = u^d$.

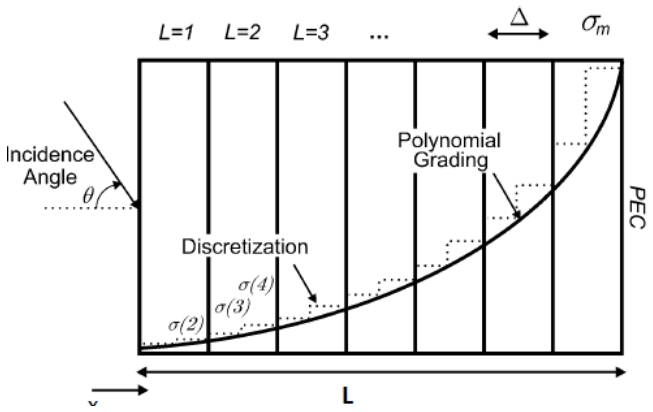

Figure 3-6: *Discretization of polynomial graded PML profile with PEC boundary at end. Taken from [138].*

As the order, d of $f(u) = u^d$ is increased, the reflections from the PML interface are reduced for the same thickness, L [139]. Once again however there is a trade-off as one can see from figure 3-6 where for larger d the discretization error near the PEC is larger because the decay is more rapid: it is assumed that deeper in the PML these reflections will contribute less because of the increased attenuation. There have been many studies to optimize the PML profile [139] and the most frequently used is polynomial grading with d usually between 2-4 [140] [138].

In some situations the concept of the PML fails such as for periodic media whereby the refractive index profile is periodic. Even for infinite resolution the PML is not reflectionless. This can be explained by considering equations (3.3.16) where the PML tensor is multiplied with the material permittivity and permeability. If $[s]$ is moved to the other side it can be linked to the curl operator. Assuming a wave travelling along z incident upon a PML boundary terminating the z-axis ($s_x = s_y = 1$) one obtains:

$$[s]^{-1}\nabla\times = \begin{bmatrix} 0 & -\frac{1}{s_z}\frac{\partial}{\partial z} & \frac{1}{s_y}\frac{\partial}{\partial y} \\ \frac{1}{s_z}\frac{\partial}{\partial z} & 0 & -\frac{1}{s_x}\frac{\partial}{\partial x} \\ -\frac{1}{s_y}\frac{\partial}{\partial y} & \frac{1}{s_x}\frac{\partial}{\partial x} & 0 \end{bmatrix} \tag{3.3.18}$$

For each non-zero term it can be seen that ∂z is being multiplied by s_z, ∂y by s_y and ∂x by s_x. Effectively s_x, s_y and s_z, which are complex numbers, are stretching the coordinates into complex space [141]. This is known as the stretched coor-

dinate PML (SC-PML) [134, 142, 143]. Thus if a wave is incident on the PML it is continued analytically inside the PML but decays because of the complex coordinates and it still solves the same wave equation. For a wave propagating in the z-direction the PML will work so long as the medium is homogeneous in the direction perpendicular to the PML, because the wave equation is set for all z. For periodic media this condition is no longer satisfied and the PML can only act as a quasi-PML whose effectiveness now depends on its use as an adiabatic absorber [139]. The turn-on of the PML conductivity must be so gradual and smooth that one approaches a reflectionless limit. To achieve this the PML is both made very thick and with higher order polynomial grading, although functions like $f(u) = e^{1-1/u}$ have been found to improve the rate of absorption [139]. Other methods include increasing the distance between the PML [144] and the periodic media or replacing the PML with a simple absorber with scalar values of σ and $\sigma^\star$, which is less computationally expensive.

3.3.3 Periodic Boundary Condition (PBC)

An alternative boundary condition that a user may feel is more intuitive to simulate periodic media are periodic boundary conditions (PBCs) which will now be discussed.

Periodic media have a permittivity profile which repeats periodically along one or more dimension (assuming $\mu_r = 1$ for optical materials). An example of a two-dimensional periodic lattice in a square arrangement is shown in figure 3-7(a) and from this one can construct a unit cell which is the simplest repeating unit. The unit cell can be constructed by drawing bisectors across lines joining the nearest neighbouring repeated structure: this is sometimes termed a Wigner-Seitz cell, adopting the nomenclature of solid state crystals. The permittivity at any point in the infinite periodic medium can now be described by $\epsilon(\mathbf{r}) = \epsilon(\mathbf{r}+\mathbf{R})$ where $\mathbf{R} = m_1\mathbf{\Lambda_x} + n_2\mathbf{\Lambda_y}$. Here m_1 and m_2 are integers and $\mathbf{\Lambda_x}$ and $\mathbf{\Lambda_y}$ are the primitive lattice vectors in the $x-$ and y-axis respectively and are also shown in figure 3-7(a).

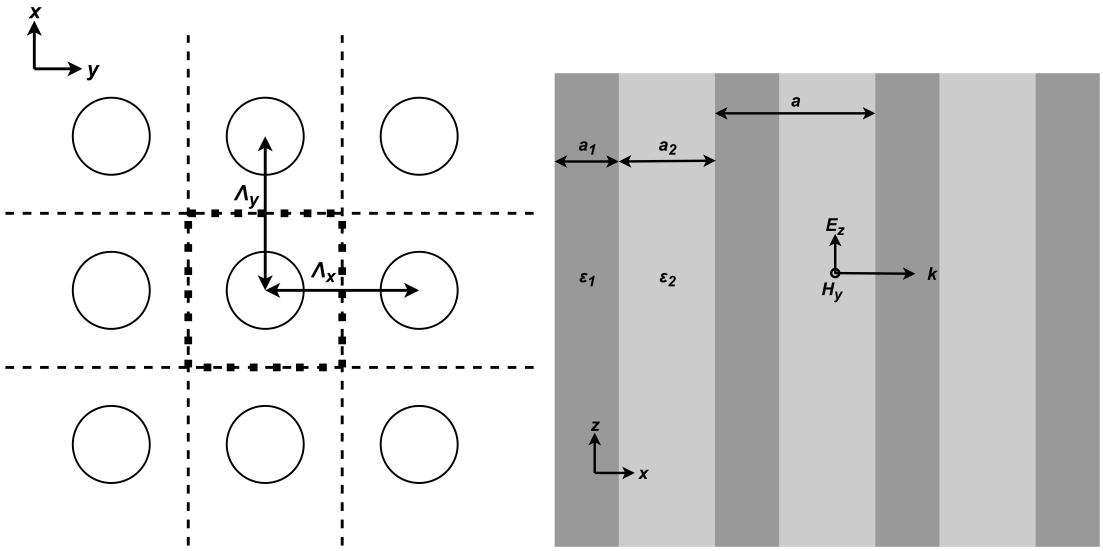

Figure 3-7: *(a) Two-dimensional square lattice with primitive lattice vectors, Λ_x and Λ_y. Dashed lines showing the bisectors used to form the unit cell in bold dashed line. (b) One-dimensional periodic multiple slab waveguide. Adapted from [145].*

Periodic boundary conditions (PBCs) repeat the computational cell to simulate an infinite periodic structure so when using PBCs, one only needs to simulate the unit cell. In addition to the geometry, the fields are also repeated. This is achieved by setting the fields on the right side of the unit cell to be the same as the left[2]. This also means that if sources are placed inside the unit cell, they are repeated.

To better understand how the fields are repeated consider a very simple one-dimensional example of the slab waveguide repeated periodically as shown in figure 3-7(b) with alternating permittivities ϵ_1 and ϵ_2 and widths a_1 and a_2 respectively. It is assumed there is no variation of the fields along z and y. From section 2.3.2 the solutions can be decoupled into two linear polarisations and figure 3-7(b) considers the $TM|_z$ modes. It can be shown that according to the Floquet theorem the $E_z(x)$ mode solutions for the infinitely repeating structure are plane waves multiplied by an amplitude function, $\mathbf{u}(x)$ which has the same

[2]The PEC boundary condition could be thought of as a special type of PBC where the fields are set as zero on either side provided the source is at the center of the cell.

periodicity as the structure:

$$E_z(x) = \mathbf{u}(x)e^{jk_x x} \tag{3.3.19}$$

Where:

$$\mathbf{u}(x) = \mathbf{u}(x + m\Lambda_x)$$

The solutions in equation (3.3.19) are often termed Bloch modes [146]. From this theorem the fields on the other side of the unit cell can be found i.e.

$$\begin{aligned} E_z(x \pm \Lambda_x) &= \mathbf{u}(x \pm \Lambda_x)e^{jk_x(x\pm\Lambda_x)} \\ &= [\mathbf{u}(x)e^{jk_x x}]e^{\pm jk_x\Lambda_x} \\ &= \mathbf{E_z}(x)e^{\pm jk_x\Lambda_x} \end{aligned} \tag{3.3.20}$$

Therefore the field at a point outside the unit cell is equal to the field inside the unit cell multiplied by a transverse field term across the grid. This phase appears as a time delay when Fourier transforming equation (3.3.20) to the time domain for FDTD. A serious issue arises if one is simulating incident fields at an angle ($k_x \neq 0$) because on one side of the unit cell boundary the field values from the future are required. Several methods exist to alleviate this such as the sine-cosine and angled-update methods [129].

From equation (3.3.19) a value of k_x is set for PBCs in FDTD. In section 3.2.5 the dispersion relation for the three-dimensional plane wave was introduced in equation (3.2.5). For one dimension and assuming propagation in air this is reduced to:

$$k^2 = \left(\frac{\omega}{c}\right) = k_x^2 \tag{3.3.21}$$

Equation (3.3.21) demonstrates that by setting an arbitrary value of k_x one may obtain the resonance frequencies, ω for that structure.

3.4 Modelling Dispersive Material

The previous sections have demonstrated FDTD concepts for nondispersive i.e. frequency independent media however one can also easily implement structures with dispersive properties which is a major advantage of FDTD. To further understand how this is achieved a brief discussion on the relevant theory follows,

specifically the Lorentz and Drude models.

The dielectric will be made up of atoms in which the electrons are bound to the nucleus. When an electric field travels through the medium, the electrons will be displaced from their equilibrium positions and induce a microscopic dipole moment which polarises the atoms. To convert this to an approximate macroscopic effect all of the dipole moments are summed to obtain a polarisation field, $\mathbf{P}$. This is accounted for in Maxwell's equations by expanding the constitutive relation (3.1.1c):

$$\mathbf{D} = \epsilon_0 \epsilon_\infty \mathbf{E} + \mathbf{P} \tag{3.4.1}$$

Where ϵ_∞ is the permittivity at infinite frequency and

$$\mathbf{P} = \epsilon_0 \chi \mathbf{E} \tag{3.4.2}$$

The term χ is the electric susceptibility, which makes $\epsilon_r = 1 + \chi$ where χ accounts for the summed dipole moments. In classical physics one can approximate the electrons oscillating elastically at a resonant frequency in a simple harmonic oscillator system whose response will be represented by a Lorentzian function. Generally there are M resonances and it can be shown that the permittivity may be represented by:

$$\epsilon_r(\omega) = \epsilon_\infty + \sum_{m=1}^{M} \frac{\sigma_m \omega_m^2}{\omega_m^2 - \omega^2 + 2j\omega\gamma_m} \tag{3.4.3}$$

$\sigma_m =$ Oscillator strength of m^{th} harmonic
$\gamma_m =$ Damping frequency of m^{th} harmonic

This is known as the Lorentz model. For metals the presence of free electrons means there is no restoring force which is included by setting $\omega_m = 0$. The permittivity is now given by the Drude model:

$$\epsilon_r(\omega) = \epsilon_\infty - \sum_{m=1}^{M} \frac{\omega_m^2}{\omega^2 - j\omega\gamma_m} \tag{3.4.4}$$

In FDTD the Lorentz and Drude dispersion of materials are included using the auxiliary differential equation (ADE) method [147] [148]. Here a polarisation

current, $\mathbf{J_{p,m}} = \frac{\partial \mathbf{P}}{\partial t}$ associated with each resonance is defined as the ADE to be solved. For the Lorentzian model and after applying an inverse Fourier transform one obtains:

$$\omega_m^2 + 2\gamma_m \frac{\partial \mathbf{J_{p,m}}}{\partial t} + \frac{\partial^2 \mathbf{J_{p,m}}}{\partial t^2} = \epsilon_0 \sigma_m \omega_m^2 \frac{\partial \mathbf{E}}{\partial t} \tag{3.4.5}$$

This expression can be written in finite-differences and solved for $\mathbf{J_{p,m}}^{n+1}$. The procedure is as follows:

(i) Calculate $\mathbf{E}^{n+1}$ given $\mathbf{E}^n, \mathbf{J_{p,m}}^n$ and $\mathbf{H}^{n+1/2}$

(ii) Find the new $\mathbf{J_{p,m}}^{n+1}$

(iii) Calculate $\mathbf{H}^{n+3/2}$ given $\mathbf{H}^{n+1/2}$ and $\mathbf{E}^{n+1}$ and repeat process

A similar method is use to implement the Drude model in FDTD. From this it is seen that $\mathbf{J_{p,m}}$ is calculated synchronously with Maxwell's curl equations.

It is observed that if a material has many polarisations more values need to be stored in computer memory. Furthermore if ω_m is too large to be sampled for a given Δt the simulation will become unstable.

3.5 MEEP

For this work a free open-source software package called MEEP (MIT Electromagnetic Equation Propagation) [149] is used to implement the FDTD algorithm. In this thesis the parallel version of MEEP is used to efficiently divide the computational cell over several processors so that large three-dimensional models can be simulated via message passing interfacing (mpi). An advantage of MEEP over other FDTD software is the access to source code which provides flexibility to adapt simulations for specific models. MEEP has low level Java and C^{++} interfaces and a higher level interface based on Scheme syntax. Additionally there are libraries with built in-functions specific to FDTD. This higher level interface will be used for the modelling described in this thesis.

Everything specified for the model is written to a control (ctl) file, whose format and ability to be executed is due to the library 'libctl'. This ctl file includes the geometry, boundary conditions, material properties, sources, fields to output etc. The general layout and syntax is demonstrated in the pseudocode below:

```
---Define Optical Properties---
(define Material (make dielectric (index val1)))
...
---Define Parameters---
(define-param param1 value1)
...
(define-param a value2);define normalization unit, 'a'
---Normalize Parameters---
(define-param norm_param1 (/ param1 a));normalize parameters
...
---Set Computational Cell---
(set! geometry-lattice (make lattice (size x y z)))
---Set Geometry---
(set! geometry
...)
---Set Sources---
(set! sources (list (make source
...)
---Set PML and Resolution---
(set! pml-layers (list (make pml
...)
(set! resolution res)
---Symmetry Exploitation---
(set! symmetries (list (make mirror-sym
...)
---Run Simulation---
(run-sources+
...
(to-appended "filename" output-field_component)
...
)
```

The position of the geometry defined by the user is set up with reference to the center of the computational cell as shown in figure 3-8.

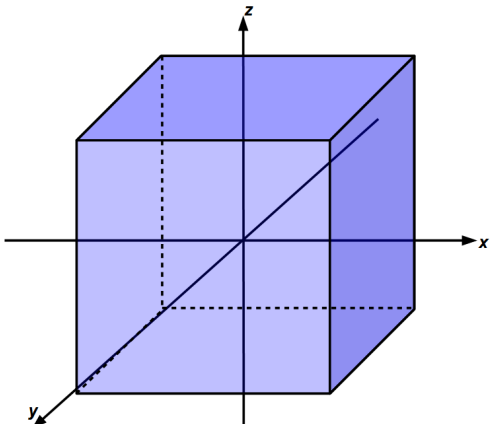

Figure 3-8: *Coordinate system of computational cell in MEEP*

MEEP is only compatible with Unix-based operating systems[3] and so the software and ctl file may be invoked from the terminal command line. For example to run the file 'led.ctl' from the command line one would enter:

```
1  mpi meep-mpi led.ctl>led.out &
```

The output file `led.out` contains the log of the simulation. Field outputs defined by the user are saved in HDF5 format which is a file type optimised for very large data files and can be manipulated in MATLAB [150] for post-processing.

MEEP supports the modelling of anisotropic, dispersive and nonlinear electric and magnetic materials. It also implements PML, PEC, PBC and absorber boundary conditions. There are several subtle differences between MEEP and the FDTD concepts described so far which need to be considered when modelling in MEEP. For example, in the pseudocode above the user needs to define a unit of distance a and all distances are defined in terms of it. From lines 23-25 of the above pseudocode, one can exploit mirror symmetry in MEEP and reduce the computation time. These and some other relevant features of MEEP will now be discussed.

3.5.1 Units in MEEP

MEEP uses dimensionless units whereby constants like μ_0, ϵ_0 and c have the value of unity. The justification for this is because it highlights the scale invariance of

[3]There are workarounds to run MEEP on windows-based operating systems using cygwin

Maxwell's equations [146].

The user defines an arbitrary base unit of distance, a, and all subsequent distances and dimensions are in units of a. If $c = 1$ then a is also the base unit of time. From the following definition of frequency:

$$f = c/\lambda_0$$

The frequency in Meep, f_m, is therefore defined as:

$$f_m = \frac{1}{\lambda_0/a}$$

And so the transformation is:

$$f = f_m * \frac{c}{a}$$

For example if $a = 100\ nm$ and $\lambda_0 = 450\ nm$ then this corresponds to a MEEP wavelength and frequency of 4.5 and 0.222 respectively.

There appears to be confusing information regarding the base unit of current that are set in MEEP. Although not explicitly stated it appears that MEEP's unit system are Natural Units because the parameters c, ϵ_0, μ_0 are unity. By setting $\epsilon_0 = 1$ the unit of charge is set via the fine-structure constant, α, defined in SI units as:

$$\alpha = \frac{1}{4\pi\epsilon_0}\frac{q^2}{\hbar c} \approx \frac{1}{137} \tag{3.5.1}$$

The term α is dimensionless and has the same value for all unit systems, thus the charge of an electron, q has the value 0.303 in Natural Units ($\hbar = 1$) and corresponds to $1.609 \times 10^{-19}\ C$. This therefore corresponds to a current of $0.303/a$ in Natural Units. The base unit of mass can be found in a similar way.

3.5.2 Exploiting Symmetry in MEEP

In MEEP the user can exploit any mirror symmetry present in the structure *and* the sources, thus reducing the computation by half. Particular care is required depending if the source is an electric or magnetic charge current. To demonstrate this, figures 3-9(a) and (b) shows the two types of charge current polarised with E_y and H_y field components respectively.

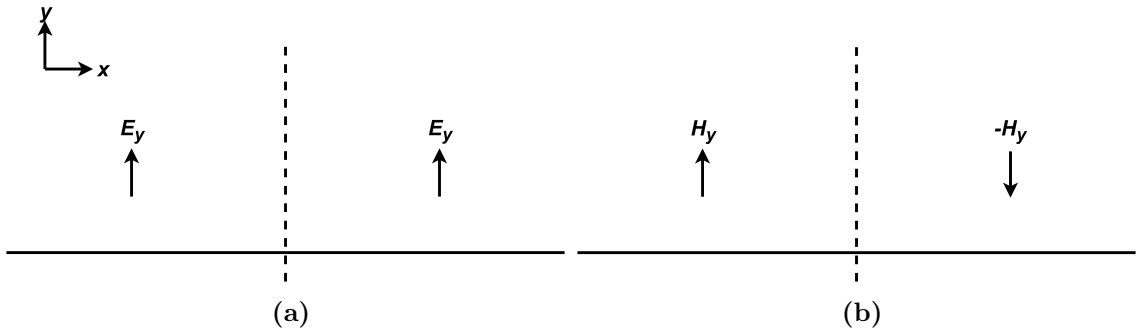

Figure 3-9: *Mirror symmetry operation represented by dashed line applied to an (a) E_y -polarised and (b) H_y-polarised source.*

If a mirror symmetry transform is applied at $x = 0$ the E_y field is unchanged. In MEEP, the user would specify:

```
(set! symmetries
        (list
                (make mirror-sym
                        (direction Y) (phase 1)
                )))
```

However as shown the H_y component is inverted after the transform so that $H_y = -H_y$ and this is the definition of a pseudovector [151]. To account for this inversion the user writes the following:

```
(set! symmetries
        (list
                (make mirror-sym
                        (direction Y) (phase -1)
                )))
```

In this way only half the computational cell needs to be simulated and the other half is obtained by applying the mirror transforms to the calculated values.

3.5.3 Illusion of Continuity

There are two coordinate systems in MEEP: one is the discrete Yee grid that has been discussed and the other is a continuous one which is generally where the user will specify their geometry, source positions and where to measure field values.

The aim of the continuous interface is to decouple the user from the discretized grid and create the illusion of continuity.

Figure 3-10 demonstrates how this is achieved. From figure 3-10(a) the field output value, f, at any point specified by the user can be found using bilinear interpolation over the two dimensional discrete Yee grid. In three dimensions the linear interpolation would be over three directions. Figure 3-10(b) shows the reverse process [152] where in this case the user positions a point dipole current source **J** at an arbitrary position on the continuous grid and this is converted to four weighted values at the discrete points. From this there may be a possible issue from having a point source at an exact grid point i.e. (0,0) because the size of **J** will be smaller.

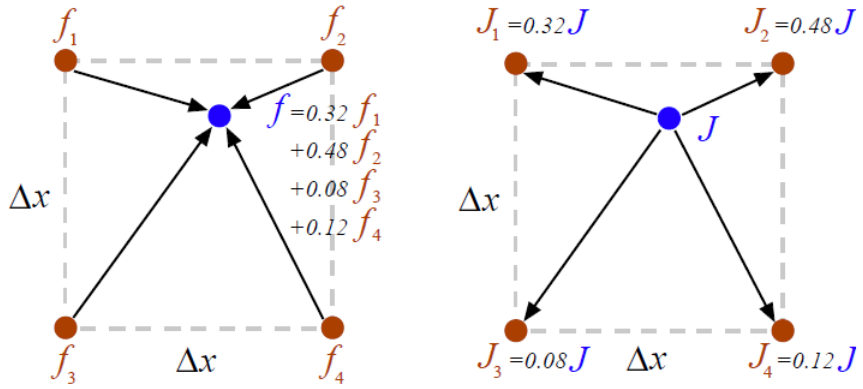

Figure 3-10: *(a) Interpolation of field values f_1, f_2, f_3, f_4 on the Yee grid to f value in continuous grid. (b) Reverse process where user specifies current source J at arbitrary position and its conversion to the Yee grid. Taken from [149].*

Similarly an arbitrary size of structure will not contain an integer number of Yee unit cells. This becomes an especially important issue when modelling curved structures and results in a staircase distribution which will result in artificial reflections. To address this MEEP uses subpixel smoothing of ϵ and μ whereby a special averaging technique [153] is used to create a continuous transition over a Yee cell. In [149] it was shown that subpixel smoothing provided better convergence for the same resolution and so a coarser grid can be used.

3.6 Summary

A brief introduction of FDTD concepts has been presented: it has been shown that FDTD in essence approximates the curl expressions in Maxwell's equations as 2^{nd} order finite-differences. The Yee method implements this by dividing the model into a grid of Yee cells whereby the electric and magnetic fields are calculated at different positions in a leapfrog scheme. If the resolution of this grid is too coarse one may observe numerical dispersion or instability when the condition in (3.2.2) is not satisfied and the fields will diverge with time.

Three methods of terminating the computational cell have been discussed: (i) perfect electrical conductor (PEC), (ii) uniaxial perfectly matched layer (UPML) and (iii) periodic boundary condition (PBC). The author concludes it would appear that for the modelling of PhC LED emission, PBCs are not suitable despite the favourable geometry because they do not represent the spontaneous emission. A PML may also be compromised when modelling periodic media because Maxwell's equations do not continue analytically into the PML. A brief introduction to the auxiliary differential equation (ADE) method was given for modelling dispersive media.

The software used to implement FDTD for the remainder of this thesis is parallel MEEP (meep-mpi). It has several advantages:

- It can divide large 3D simulations over several processors.
- It is free and open-source and so provides flexibility to customise simulations.
- It's Scheme programming language is easy to learn.
- It can model anisotropic, dispersive and non-linear media.
- It can exploit mirror symmetry to reduce computation by half or a quarter.
- It incorporates subpixel smoothing which allows for coarser resolution and therefore reduction in computation time

It is now possible to set-up reliable models for the simulation of LED structures. In addition, it is possible to discuss in more detail how to obtain LED parameter values from FDTD as discussed in literature (see section 2.3.2) namely (i)

the far-field emission pattern, (ii) light extraction efficiency, η_{lee} and (iii) directionality. Because of the Unix-based compatibility of MEEP, this software does not automatically plot/visualise fields. Fields are instead stored in large HDF5 files which can be manipulated in MATLAB. The next section details the post-processing of these files to obtain the listed parameters required for determining the performance of LEDs.

Chapter 4

Post-Processing of FDTD Results

MEEP outputs any field component for any defined point, plane or volume. There are features of MEEP that allow the user to output transmission and reflection spectra and output resonant modes of a structure including the frequency, decay rate and Q-factor. These are obtained by performing an internal Fourier transform on the fields in response to a pulse, the latter using a filter diagonalization method [154]. Because of the nature of FDTD the direct output will be field components as a function of time. The user can input a sinusoidal monochromatic source of time dependence[1] $e^{-j\omega t}$ and observe the fields evolve with time: when the field distribution inside the structure no longer changes this is the steady state solution. To observe the response to many frequencies this would require repeating the simulation for many sinusoid sources of different frequencies. It is easier to input a pulse of finite spectral width and apply a Fourier transform to the fields and obtain them as a function of frequency so that only one simulation is required instead of many. The pulse shape can be set to be spectrally Gaussian to make it representative of the emission from the active region of LEDs.

It is not straightforward to extract the Fourier-transformed fields from MEEP's internal calculations for transmission and reflection spectra giving rise to the need to implement a Fourier-transform on the time-domain fields. These fields are output from MEEP as HDF5 files which can be processed easily using MATLAB by applying a discrete Fourier transform (DFT) to obtain the spectrally resolved field distributions at any point or over the entire structure. Such near-field distributions can provide information on the internal light trapping and coupling effects

[1] MEEP uses $e^{-j\omega t}$ convention.

inside different LED structures [107] [116] [118] [128] [155]. However, there is limited quantitative information indicative of an LED's performance from the near-fields and direct comparison with experimental measurements.

As was discussed in section 2.5, FDTD may be used to obtain the angular far-field emission pattern and the light extraction efficiency of LED devices. The former is the intensity distribution of the light emission as a function of the azimuth(ϕ) and elevation(θ) angles at a large distance from the LED. By obtaining the far-field emission in FDTD one can determine the directionality of the emission. Additionally a direct comparison with experimental results obtained from photoluminescence (PL) and electroluminescence (EL) can be made. In these experiments a laser beam or current injection is used to activate the LED and a probe is used to measure the intensity of the emission as a function of position. It will be shown that the angular far-field emission can be calculated from the near-fields generated by MEEP via a near-to-far-field transform (NFFT). This method is more efficient because it avoids extending the computational cell to measure the far-fields directly and has been used in previous studies where comparisons with experimental PL/EL were made [100] [109] [115].

As was also shown in these studies, the light extraction efficiency, η_{lee}, can be extracted from the far-field emission by integrating the intensity over all solid angle to obtain the total emitted power and dividing this by the power emitted from a dipole. Other studies have taken the total emitted power just above the surface of the LED to calculate η_{lee} from FDTD simulations. Another measure of the light extraction used for LEDs with surface texturing e.g. PhCs, is the enhancement factor which is often much easier to calculate by simply dividing the emitted power of a textured LED by that of the planar device and as with the angular far-field, a direct comparison with experiment can be made [118].

The next section details the post-processing and methods to obtain (i) the far-field emission patterns, (ii) light extraction efficiency, η_{lee}, (iii) enhancement factor, F, and (iv) directionality, D, using the time-domain fields obtained from MEEP modelling of LED devices.

4.1 Near-to-Far Field Transform

From diffraction theory it can be shown that in general the far-field of a radiating aperture is the Fourier transform of the field distribution across the aperture. This can be demonstrated by considering an abrupt interface at $z = 0$ between two media of refractive indices n_a and n_b in the xz-plane as shown in figure 4-1.

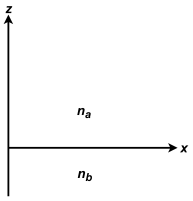

Figure 4-1: *Interface of two media in xy-plane.*

It is assumed the structure and fields do not vary along the y-axis so that $\partial y = 0$ to make the wave equation for a field component, F_a, in region a become:

$$\left[\frac{\partial^2}{\partial x^2} + \frac{\partial^2}{\partial z^2} + k_0^2 n_a^2\right] F_a(x, z) = 0 \tag{4.1.1}$$

It is further assumed the media in the half plane $z > 0$ is homogeneous so that n_a is constant for all (x, z). It follows that the wave equation in (4.1.1) is satisfied by a solution of the form:

$$F_a(x, z) = Ae^{-j(\kappa_a x + \beta_a z)} \tag{4.1.2}$$

Where the constants β_a and κ_a must satisfy:

$$\beta_a^2 + \kappa_a^2 = k_0^2 n_a^2$$

Note that $F_a(x, z)$ is a solution for any $\kappa_a = constant$ and so correspondingly:

$$\beta_a = \beta_a(\kappa_a) = \pm\sqrt{k_0^2 n_a^2 - \kappa_a^2}$$

In general the amplitude term A in (4.1.2) can have different (constant) values for different κ_a i.e.

$$F_a(x, z) = A(\kappa_a)e^{-j(\kappa_a x + \beta_a z)} \tag{4.1.3}$$

A more general solution would be composed of a summation or more accurately an integration of all κ_a. Generally:

$$F_a(x,z) = \int_{-\infty}^{\infty} A(\kappa_a) e^{-j(\kappa_a x + \beta_a z)} \, \mathrm{d}\kappa_a \tag{4.1.4}$$

One may define the source field distribution, f_s as:

$$f_s(x) = F_a(x, z = 0)$$

And so at $z = 0$ equation (4.1.4) reduces to:

$$F_a(x, z = 0) = f_s(x) = \int_{-\infty}^{\infty} A(\kappa_a) e^{-j\kappa_a x} \, \mathrm{d}\kappa_a \tag{4.1.5}$$

This is recognised as a Fourier transform operation. Therefore:

$$A(\kappa_a) = \frac{1}{2\pi} \int_{-\infty}^{\infty} f_s(x) e^{j\kappa_a x} \, \mathrm{d}x \tag{4.1.6}$$

Equation (4.1.6) shows for a given field distribution, f_s, one can obtain $A(\kappa_a)$ and from equation (4.1.4) $F_a(x,z)$ for all (x,z) in the half plane $z > 0$. This indicates that the field at a distant point can be represented as the superposition of a continuum (or discrete) set of plane waves with different directions and amplitudes as defined by the term $A(\kappa_a)$ which is called the angular plane wave spectrum. This analysis highlights the general principle of how the intensity of the far-field is determined by the constructive and destructive interferences of the fields from the source plane. For constructive interference the fields must be in phase, hence this is called the phase matching condition.

As an example Snell's law can be derived by considering the incident plane wave at $z = 0$ as the source field distribution:

$$F_b(x,z) = A e^{-j(\kappa_b x + \beta_b z)}$$
$$\therefore F_b(x, z = 0) = f_s(x) = A e^{-j\kappa_b x}$$

Where

$$\beta_b^2 = k_0^2 n_b^2 - \kappa_b^2 \tag{4.1.7}$$

The field amplitude, A, for a plane wave is constant for all x. Inserting the above into (4.1.6) then from equation (4.1.2) results in:

$$F_a(x,z) = Ae^{-j(\kappa_b x + \beta_a z)}$$

Where

$$\beta_a^2 = k_0^2 n_a^2 - \kappa_b^2 \tag{4.1.8}$$

This is a plane wave in region a. Equating (4.1.7) and (4.1.8) and after some algebra Snell's Law is obtained:

$$n_b \sin(\theta_1) = n_a \sin(\theta_2) \tag{4.1.9}$$

Another example that provides insight is a plane wave incident upon a diffraction grating. Consider a binary grating consisting of a PEC with N number of slits shown in figure 4-2(a). This is also termed an amplitude grating because the source field, $f_s(x)$, is a pulse-train waveform of the field's amplitude shown inset. The resulting plane wave spectrum is found by applying the operation in equation (4.1.6) on the pulse train.

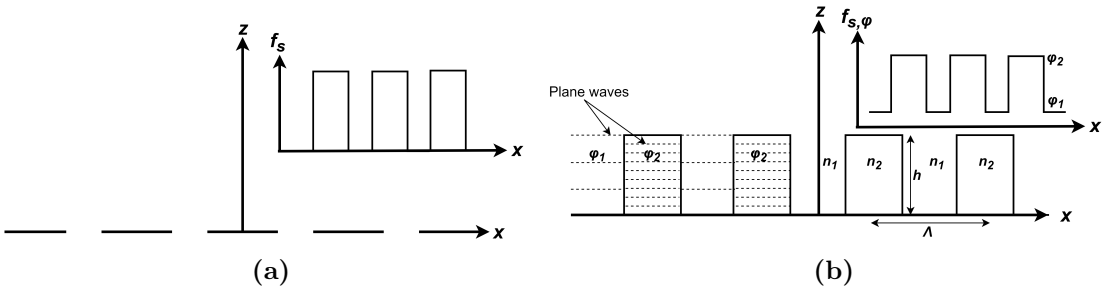

Figure 4-2: *Schematic and corresponding $f_s(x)$ distributions for (a) amplitude grating and (b) binary phase grating of refractive indices n_1 and n_2 and height, h.*

The other type of grating is the phase grating which may be separated into two categories. The first is the thin-phase where the wavelength of light is much larger than the thickness of grating, h, and less than the pitch, Λ. The second category are thick-phase gratings where $\Lambda \approx \lambda$ and $\lambda < h$, as shown in figure 4-2(b). It is approximated that in each grating element a plane wave propagates

with a phase, ϕ related to the corresponding refractive index. It is important to note that $f_s(x)$ will also include a periodic phase as a function of x as shown in the inset of figure 4-2(b). The phases in each grating element are:

$$\phi_1 = \frac{2\pi h n_1}{\lambda} \qquad \phi_2 = \frac{2\pi h n_2}{\lambda} \tag{4.1.10}$$

The resultant diffraction is often termed Raman-Nath diffraction. The larger value of h in the thick phase grating restricts further the number of allowed constructive interferences in the far-field because not only must the scattering from the periodic interface be in phase but so too must the scattering within the grating element.

For LED structures the source field, f_s, which will be defined at the interface between the surface of the LED and air, will not be an analytic function. Further, since three-dimensional simulations of the LED structures will be performed, f_s will be defined across a plane i.e. $f_s(x, y)$. Also, for the most general case it is intended to apply the transform of (4.1.6) on all tangential field components measured in the plane.

4.1.1 Extension to Generalized 2D-Plane

The previous derivations in section 4.1 extend and in a way deviate from the previous simple analysis to a two-dimensional xy-plane at $z = 0$ as shown in figure 4-3. This will be the top surface of the LED device being simulated. Here it is treated as a flat rectangular aperture which defines an arbitrary source field distribution over the surface area, A.

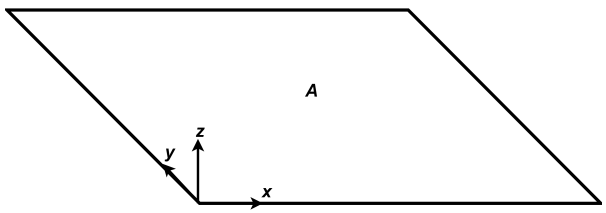

Figure 4-3: *Two-dimensional plane of area, A, representing source plane.*

This derivation of the near-to-far field transform has been taken from Balanis [156] and Orfanidis [157] for a dielectric aperture antenna. This has the following advantages:

(i) The near-to-far field transform in antenna theory is used on measured or calculated near-fields that are sampled over an antenna using a probe. Thus, this transform can be easily applied to the sampled near-field data returned by FDTD.

(ii) It can be applied to any arbitrary near-field distribution across the surface of the LED and obtain the practical far-field radiation intensity which can be directly compared with similar experimental results.

(iii) The transform is expressed in spherical coordinates so that angular dependent properties such as the far-field pattern and directionality can be easily found.

(iv) It is mathematically straightforward to implement for a planar surface and is suitable for applying the efficient Fast Fourier Transform (FFT).

(v) Is compatible with the discrete and Cartesian nature of MEEP's FDTD method.

For the general case there will be the aperture fields $\mathbf{E}_a$ and $\mathbf{H}_a$. It can be shown from the field equivalence principle that the fields across the aperture may be replaced by equivalent electric and magnetic current densities, $\mathbf{J_s}$ and $\mathbf{M_s}$, defined as:

$$\mathbf{J_s} = \hat{\mathbf{z}} \times \mathbf{H}_a \qquad \mathbf{M_s} = -\hat{\mathbf{z}} \times \mathbf{E}_a \tag{4.1.11}$$

The electric and magnetic far-fields of these source currents are determined by using the corresponding auxiliary vector potential functions, $\mathbf{A}$ and $\mathbf{A_m}$. These are used to solve the inhomogeneous (i.e. with sources) vector wave equations:

$$\nabla^2 \mathbf{A} + k^2 \mathbf{A} = -\mu \mathbf{J_s} \tag{4.1.12a}$$

$$\nabla^2 \mathbf{A_m} + k^2 \mathbf{A_m} = -\epsilon \mathbf{M_s} \tag{4.1.12b}$$

The fields radiated by the aperture antenna are spherical waves and so the vector potential functions are written in terms of spherical components. In the far-field this expression can be further simplified. Taking the vector potential due to $\mathbf{J_s}$

this is expressed as:

$$\begin{aligned}\mathbf{A} &= \hat{\mathbf{r}}A_r(r,\theta,\phi) + \hat{\theta}A_\theta(r,\theta,\phi) + \hat{\phi}A_\phi(r,\theta,\phi) \\ &\approx \left[\hat{\mathbf{r}}A_r(\theta,\phi) + \hat{\theta}A_\theta(\theta,\phi) + \hat{\phi}A_\phi(\theta,\phi)\right]\frac{e^{-jkr}}{r}\end{aligned} \tag{4.1.13}$$

It can be shown that the electric and magnetic fields due to the vector potential $\mathbf{A}$ are given by [156]:

$$\mathbf{E_A} = -j\omega\mathbf{A} - j\frac{1}{\omega\mu\epsilon}\nabla(\nabla\cdot\mathbf{A}) \qquad \mathbf{H_A} = \frac{1}{\mu}\nabla\times\mathbf{A} \tag{4.1.14}$$

Substituting (4.1.13) into (4.1.14) and equating components, also noting in the far-field that the radial field components are negligible, the electric and magnetic fields due to $\mathbf{A}$ simplify to:

$$E_r \approx 0, \quad E_\theta \approx -j\omega A_\theta, \quad E_\phi \approx -j\omega A\phi \tag{4.1.15}$$

$$H_r \approx 0, \quad H_\theta \approx \frac{j\omega}{Z_0}A_\phi = -\frac{E_\phi}{Z_0}, \quad H_\phi \approx -\frac{j\omega}{Z_0}A_\phi = \frac{E_\theta}{Z_0} \tag{4.1.16}$$

Similar expressions can be derived for the field components due to $\mathbf{M_s}$ using the vector potential $\mathbf{A_m}$ using the duality theorem. The following summarises in vector form below:

$$\mathbf{E_A} \approx -j\omega\mathbf{A} \qquad \mathbf{H_A} \approx \frac{-j\omega}{Z_0}\hat{\mathbf{r}}\times\mathbf{A} \tag{4.1.17a}$$

$$\mathbf{H_{Am}} \approx -j\omega\mathbf{A_m} \qquad \mathbf{E_{Am}} \approx j\omega Z_0\hat{\mathbf{r}}\times\mathbf{A_m} \tag{4.1.17b}$$

Therefore the vector potential functions are required which can be rewritten in terms of the fields over the aperture. The solutions to the wave equations in equation (4.1.12a) are:

$$\mathbf{A}(\mathbf{r}) = \frac{\mu e^{-jkr}}{4\pi r}\int_A \mathbf{J}_s(\mathbf{r}')e^{j\mathbf{k}\cdot\mathbf{r}'}\mathrm{d}S' \tag{4.1.18a}$$

$$\mathbf{A_m}(\mathbf{r}) = \frac{\epsilon e^{-jkr}}{4\pi r}\int_A \mathbf{J}_m(\mathbf{r}')e^{j\mathbf{k}\cdot\mathbf{r}'}\mathrm{d}S' \tag{4.1.18b}$$

Here the primes indicate the space occupied by the $\mathbf{J_s}$ and $\mathbf{M_s}$ sources over

which the integration is performed which is the plane region of the aperture. The unprimed terms indicate a distant point in the far-field. Equation (4.1.18) is rewritten as:

$$\mathbf{A} = \frac{\mu e^{-jkr}}{4\pi r}\mathbf{F}(\theta,\phi) \tag{4.1.19a}$$

$$\mathbf{A_m} = \frac{\epsilon e^{-jkr}}{4\pi r}\mathbf{F_m}(\theta,\phi) \tag{4.1.19b}$$

Where

$$\mathbf{F}(\theta,\phi) = \int_A \mathbf{J}_s(\mathbf{r}')e^{j\mathbf{k}\cdot\mathbf{r}'}\mathrm{d}S' \tag{4.1.20a}$$

$$\mathbf{F_m}(\theta,\phi) = \int_A \mathbf{M}_s(\mathbf{r}')e^{j\mathbf{k}\cdot\mathbf{r}'}\mathrm{d}S' \tag{4.1.20b}$$

And so it can be shown by combining equations (4.1.17) and (4.1.19), the electric and magnetic far-field components are approximated as:

$$E_r \approx 0, \quad E_\theta \approx -\frac{jke^{-jkr}}{4\pi r}\left(F_{m\phi} + Z_0F_\theta\right), \quad E_\phi \approx \frac{jke^{-jkr}}{4\pi r}\left(F_{m\theta} - Z_0F_\phi\right) \tag{4.1.21a}$$

$$H_r \approx 0, \quad H_\theta \approx \frac{jke^{-jkr}}{4\pi r}\left(F_\theta - \frac{F_{m\theta}}{Z_0}\right), \quad H_\phi \approx -\frac{jke^{-jkr}}{4\pi r}\left(F_\theta + \frac{F_{m\phi}}{Z_0}\right) \tag{4.1.21b}$$

In equations (4.1.21)(a) and (b), use has been made of the fact that $\mathbf{F}$ and $\mathbf{F_m}$ can be resolved into their spherical components and in the far-field the θ and ϕ angular components are dominant. Using the definitions given in (4.1.11), the equations in (4.1.20) may be rewritten as:

$$\mathbf{F}(\theta,\phi) = \hat{\mathbf{z}} \times \int_A \mathbf{H}(\mathbf{r}')e^{j\mathbf{k}\cdot\mathbf{r}'}\mathrm{d}S' \tag{4.1.22a}$$

$$\mathbf{F_m}(\theta,\phi) = -\hat{\mathbf{z}} \times \int_A \mathbf{E}(\mathbf{r}')e^{j\mathbf{k}\cdot\mathbf{r}'}\mathrm{d}S' \tag{4.1.22b}$$

The integrals in equation (4.1.22) are the Fourier transform operations on the near-fields E_a and H_a which can be resolved into their tangential Cartesian com-

ponents, E_{ax}, E_{ay}, H_{ax} and H_{ay} as:

$$\mathbf{E}_a = \hat{\mathbf{x}} E_{ax} + \hat{\mathbf{y}} E_{ay} \tag{4.1.23a}$$

$$\mathbf{H}_a = \hat{\mathbf{x}} H_{ax} + \hat{\mathbf{y}} H_{ay} \tag{4.1.23b}$$

Applying the Fourier transform for each field component at $z = 0$ over the aperture will give the corresponding angular plane wave spectrum respectively given by the following:

$$f_x(k_x, k_y) = \int_A E_{ax}(x, y, z = 0) e^{-j(k_x x + k_y y)} \mathrm{d}S' \tag{4.1.24a}$$

$$f_y(k_x, k_y) = \int_A E_{ay}(x, y, z = 0) e^{-j(k_x x + k_y y)} \mathrm{d}S' \tag{4.1.24b}$$

$$g_x(k_x, k_y) = \int_A H_{ax}(x, y, z = 0) e^{-j(k_x x + k_y y)} \mathrm{d}S' \tag{4.1.24c}$$

$$g_y(k_x, k_y) = \int_A H_{ax}(x, y, z = 0) e^{-j(k_x x + k_y y)} \mathrm{d}S' \tag{4.1.24d}$$

It is noted that the relation between Cartesian and spherical coordinates in the wavevectors is given by:

$$k_x = k_0 \cos(\phi) \sin(\theta) \qquad k_y = k_0 \sin(\phi) \sin(\theta) \tag{4.1.25}$$

The equations in (4.1.22) may therefore be written as:

$$\mathbf{F} = \hat{\mathbf{z}} \times \mathbf{g} = \hat{\mathbf{z}} \times (\hat{\mathbf{x}} g_x + \hat{\mathbf{y}} g_y) = \hat{\mathbf{y}} g_x - \hat{\mathbf{x}} g_y \tag{4.1.26a}$$

$$\mathbf{F_m} = -\hat{\mathbf{z}} \times \mathbf{f} = -\hat{\mathbf{z}} \times (\hat{\mathbf{x}} f_x + \hat{\mathbf{y}} f_y) = \hat{\mathbf{x}} f_y - \hat{\mathbf{y}} f_x \tag{4.1.26b}$$

To obtain the spherical components of $\mathbf{F}$ and $\mathbf{F_m}$ a Cartesian to spherical coordinate transform is applied to obtain the following:

$$F_\theta = -\cos(\theta)(g_y \cos(\phi) - g_x \sin(\phi)) \tag{4.1.27a}$$

$$F_\phi = g_x \cos(\phi) + g_y \sin(\phi) \tag{4.1.27b}$$

$$F_{m\theta} = \cos(\theta)(f_y \cos(\phi) - f_x \sin(\phi)) \tag{4.1.27c}$$

$$F_{m\phi} = -(f_x \cos(\phi) + f_y \sin(\phi)) \tag{4.1.27d}$$

The far-field radiation intensity $U(\theta, \phi)$, is defined as the power radiated per unit solid angle and may be written as the magnitude of the time-averaged Poynting vector defined in section 2.3.2 and which is repeated here:

$$\mathbf{S} = \frac{1}{2}\mathrm{Re}\left(\mathbf{E} \times \mathbf{H}^{\star}\right) \tag{4.1.28}$$

From equations (4.1.21)(a) and (b) the magnetic field is related to the electric field via the following:

$$H_{\theta} = -\frac{1}{Z_0}E_{\phi}, \qquad H_{\phi} = \frac{1}{Z_0}E_{\theta} \tag{4.1.29}$$

Therefore the far-field radiation pattern is:

$$\begin{aligned} U(\theta, \phi) &= \frac{1}{2}\mathrm{Re}\left[(E_{\theta} + E_{\phi}) \times (H_{\theta} + H_{\phi})^{\star}\right] \\ &= \frac{1}{2Z_0}\left(|E_{\theta}|^2 + |E_{\phi}|^2\right) \end{aligned} \tag{4.1.30}$$

To summarise, the far-field radiation pattern will be calculated from the fields collected across the surface of the LED by using the following procedure:

(i) Determine E_x, E_y, H_x and H_y tangential field components across the top radiating surface of the LED from FDTD simulations.

(ii) Apply Fourier transform operations to the tangential field components to find f_x, f_y, g_x and g_y as per equations (4.1.24)(a-d).

(iii) Find $F_{\theta}, F_{\phi}, F_{m\theta}$ and $F_{m\phi}$ from equations (4.1.27)(a-d).

(iv) Find E_{θ} and E_{ϕ} from the expressions in equations (4.1.21)(a).

(v) Find $U(\theta, \phi)$ using equation (4.1.30).

The implementation of this procedure will now be discussed using the method described in chapter 17.2.4 of Balanis [156]. This method has been used in previous FDTD work of LEDs [109] [113] [115].

4.1.2 Implementation

In antenna experiments one is physically measuring the near-field components of a test antenna using a measurement probe to sample the fields over a rectangular grid. The probe is placed a distance z_{nf} above the antenna to avoid the reactive near-fields coupling to the probe and perturbing the measurement. The measured data is then transformed to the far-field. The exact same technique can be applied to the fields collected in FDTD simulations. The square xy grid is defined as shown in figure 4-4 with sample spacing[2] of Δx and dimensions of $a \times b$.

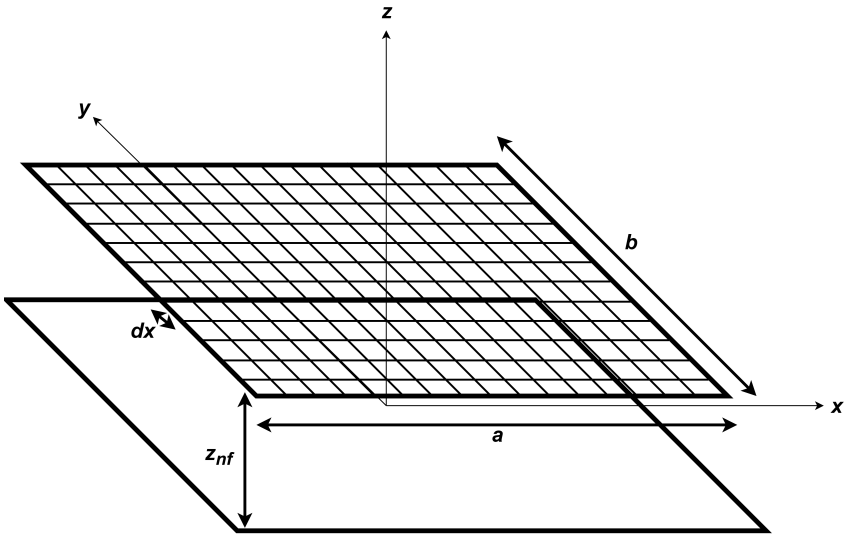

Figure 4-4: *Two-dimensional plane of area, $a \times b$, divided into a grid of spacing dx positioned z_{nf} above LED surface where the tangential electric and magnetic fields are measured.*

At each point on the grid the tangential electric and magnetic fields are measured at regular time intervals, dt. The derivation of the near-to-far-field transform in the previous section assumed the fields were in the frequency domain. It is also the intention to input a pulsed source to exploit FDTD's advantage of running a single simulation and obtain results for several frequencies. The measured field components e.g. $E_x(x, y, t)$ will be Fourier transformed to obtain $E_x(x, y, \omega)$. To achieve this, a Gaussian pulsed dipole source is used to represent the spontaneous emission. The fields will be measured at a point on the aperture plane until they have sufficiently decayed away, to ensure any resonances left after

[2]MEEP does not support non-uniform resolution i.e. $\Delta x = \Delta y = \Delta z$

the source have turned off and do not effect the Fourier transform. In MEEP the simulation is set to finish when the intensity of the field has decayed to 10^{-5} of the maximum value measured which should be sufficient and is typically used for LED devices with nanostructuring [158].

An immediate issue is that in FDTD the E and H fields are offset by half a time step because of the leapfrog algorithm and so reducing the accuracy of Poynting vector calculations. MEEP overcomes this problem with a feature called 'synchronized-magnetic' which synchronizes the electric fields with the magnetic fields in time albeit at the cost of extra time and memory.

From equations (4.1.24)(a-d) the plane wave spectrum for each field component is given by by the following Fourier transform operations:

$$f_x(k_x, k_y) = \int_{-a/2}^{a/2} \int_{-b/2}^{b/2} E_{ax}(x, y, z = 0) e^{-j(k_x x + k_y y)} \mathrm{d}x\mathrm{d}y \tag{4.1.31a}$$

$$f_y(k_x, k_y) = \int_{-a/2}^{a/2} \int_{-b/2}^{b/2} E_{ay}(x, y, z = 0) e^{-j(k_x x + k_y y)} \mathrm{d}x\mathrm{d}y \tag{4.1.31b}$$

$$g_x(k_x, k_y) = \int_{-a/2}^{a/2} \int_{-b/2}^{b/2} H_{ax}(x, y, z = 0) e^{-j(k_x x + k_y y)} \mathrm{d}x\mathrm{d}y \tag{4.1.31c}$$

$$g_y(k_x, k_y) = \int_{-a/2}^{a/2} \int_{-b/2}^{b/2} H_{ax}(x, y, z = 0) e^{-j(k_x x + k_y y)} \mathrm{d}x\mathrm{d}y \tag{4.1.31d}$$

The dimensions of the plane correspond to a rectangular grid of $M \times N$ points spaced Δx apart. Any point on the grid is defined by $(m\Delta x, n\Delta x, 0)$. These are related by the following:

$$M - 1 = \frac{a}{\Delta x}; \qquad N - 1 = \frac{b}{\Delta y} \tag{4.1.32}$$

In sampled space, the discrete Fourier transform (DFT) is implemented. Equa-

tions (4.1.31)(a-d) become:

$$f_x(k_x,k_y)=\sum_{n=-\frac{N}{2}}^{\frac{N}{2}-1}\sum_{m=-\frac{M}{2}}^{\frac{M}{2}-1}E_{ax}(m\Delta x,n\Delta x,0)e^{-j(k_xm\Delta x+k_yn\Delta y)} \tag{4.1.33a}$$

$$f_y(k_x,k_y)=\sum_{n=-\frac{N}{2}}^{\frac{N}{2}-1}\sum_{m=-\frac{M}{2}}^{\frac{M}{2}-1}E_{ay}(m\Delta x,n\Delta x,0)e^{-j(k_xm\Delta x+k_yn\Delta y)} \tag{4.1.33b}$$

$$g_x(k_x,k_y)=\sum_{n=-\frac{N}{2}}^{\frac{N}{2}-1}\sum_{m=-\frac{M}{2}}^{\frac{M}{2}-1}H_{ax}(m\Delta x,n\Delta x,0)e^{-j(k_xm\Delta x+k_yn\Delta y)} \tag{4.1.33c}$$

$$g_y(k_x,k_y)=\sum_{n=-\frac{N}{2}}^{\frac{N}{2}-1}\sum_{m=-\frac{M}{2}}^{\frac{M}{2}-1}H_{ay}(m\Delta x,n\Delta x,0)e^{-j(k_xm\Delta x+k_yn\Delta y)} \tag{4.1.33d}$$

Where the wavenumbers are defined as:

$$k_x=\frac{2\pi m}{M\Delta x} \qquad \frac{M}{2}\leq m\leq\frac{M}{2}-1 \tag{4.1.34a}$$

$$k_y=\frac{2\pi n}{N\Delta x} \qquad \frac{N}{2}\leq n\leq\frac{N}{2}-1 \tag{4.1.34b}$$

Equations (4.1.33)(a-d) can be implemented using two-dimensional fast Fourier transforms (FFTs). Specifically in MATLAB the two-dimensional FFT function 'fft2' is used. It should be noted that in this case the MATLAB function 'fftshift' is also required because the fundamental is located at the center of the matrix, not at the first element. Additionally the FFTs need to be scaled to account for the finite grid. Referring to [159], the DFT is implemented in MATLAB as:

```
fftshift((fft2(fftshift(data))).*delta^2;
```

The plane wave spectra need to be translated onto a hemisphere so as to obtain the spherical far-field pattern. This is achieved by first defining the angular range for a hemisphere for the elevation, $\theta=-\frac{\pi}{2}:\Delta\theta:\frac{\pi}{2}$, and azimuth, $\phi=-\pi:\Delta\phi:\pi$. Then using the relations in equation (4.1.25), the values of f_x, f_y, g_x and g_y are interpolated onto points specified by the value of θ and ϕ. This is easily implemented in MATLAB using the 'interp2' function.

There are several issues that must be considered when using this method: the first is the restriction of the angular span that can be dealt with increasing the cell

size. This comes at the cost of computation time and memory. Another issue is visually resolving spikes in the far-field pattern which can be present for example for diffraction grating structures. The effect cannot be alleviated by increasing the number of sampling points in the near-field but by increasing the length of the measurement. This is achieved by padding the near-field data with zeros before it has been Fourier transformed: 'zero padding' in real space is equivalent to interpolation in wave vector space. To preserve original data, the number of added zeros to the grid will be an integer multiple of the original $M \times N$ length.

The complete procedure is summarised by the flow chart in figure 4-5. The fields are output as a subset of an HDF5 file containing $M \times N \times Q$ data points where Q is the total number of time steps and the field at a specific time step is at $q\Delta t$, where q is an integer. MATLAB has functions which can read this file format and extract the fields directly with the use of the function 'h5read'.

This method will now be applied to compute the far-field emission pattern of cases whereby the solution is analytically known to validate the model and any limitations that arise from the limited lateral size of the computational cell. The effect of the position of the near-field monitor and PML thickness is also investigated to determine suitable initial values for these parameters.

4.1.3 Modelling of Planar LED device

A simple planar GaN surface LED in ambient air was modelled and the set-up is shown in figure 4-6(a) for the xz-plane. The z dimension or thickness of GaN is denoted t_{GaN} and its optical properties were modelled as a simple dielectric with a non-dispersive refractive index, n_{GaN}, of 2.5. The PML of thickness t_{PML} overlapped the structure along all three dimensions and the lateral dimensions of the GaN geometry is set as infinite. It was reasoned that with thick layers of GaN and sapphire substrate there would be negligible return reflections from the base back into the GaN. The tangential electric and magnetic near-field components were measured in an xy-plane at a distance z_{nf} above the dielectric and a single dipole source with a Gaussian spectrum centered at 450 nm wavelength and half-width of around 60 nm was placed at $x = y = 0$ and a vertical distance z_{src} above the interface between the GaN and the PML. To model isotropic incoherent emission three separate simulations were run for an electric field dipole

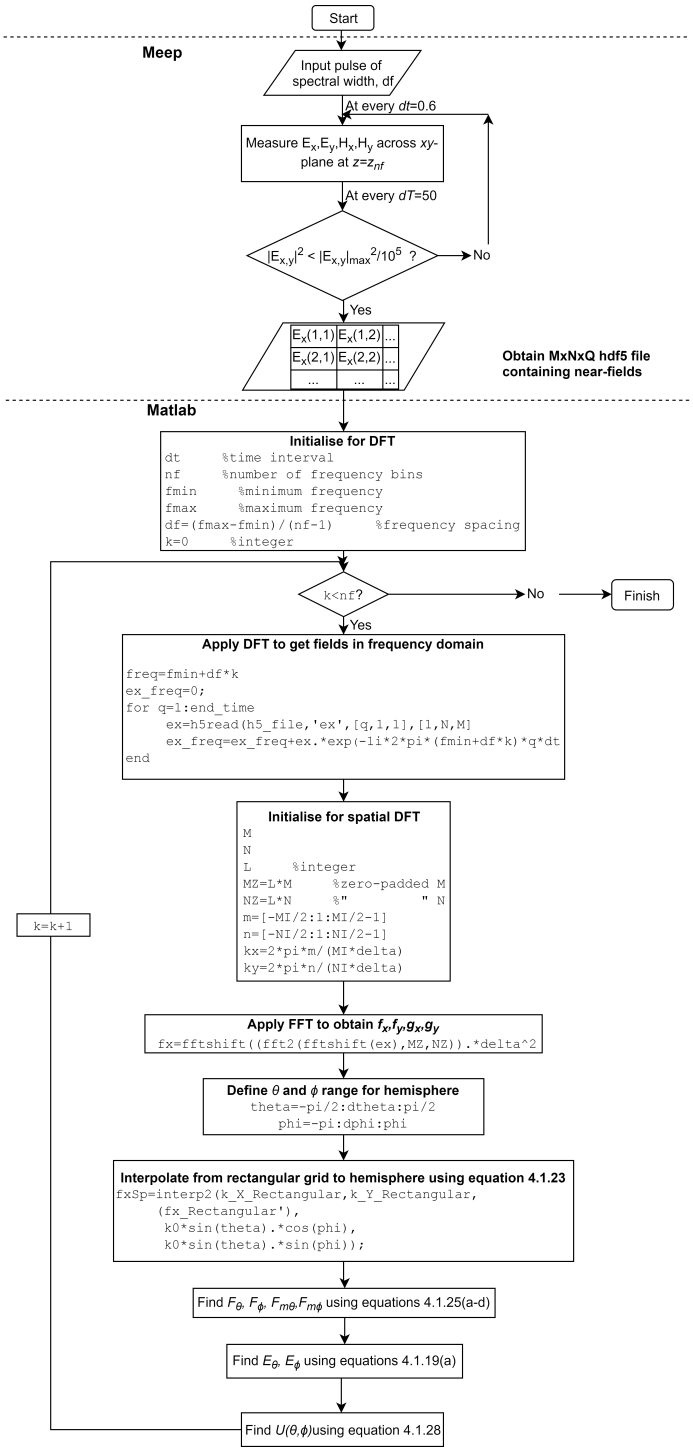

Figure 4-5: *Flow-chart summarising near-to-far-field transform procedure of near-fields measured in MEEP.*

polarised along the three orthogonal directions with E_x, E_y and E_z polarisations. It should be noted for an InGaN QW grown along the c-axis, the emission will dominantly have the electric field polarised perpendicular to the crystal's c-axis which is aligned along the z-axis. Therefore one could simplify the emission by running separate simulations for an E_x and E_y polarised dipole only. The far-field radiation intensities for the three dipoles were then summed and averaged as follows [19]:

$$U = \frac{U_{E_x} + U_{E_y} + U_{E_z}}{3} \tag{4.1.35}$$

The computational cell was extended along the z-axis by a distance z_{pad} in air to reduce the effect of reflections from the PML in the $+z$-plane on measurements made at the near-field monitor position. As was discussed in section 2.3.2, a Lambertian emission pattern is expected in the angular far-field.

Figure 4-6(b) shows the normalised far-field intensity pattern for $t_{GaN} = 5$ μm, $t_{PML} = 1$ μm, $z_{nf} = 200$ nm, $z_{src} = 2.5$ μm and $z_{pad} = 4$ μm for emission wavelength of 450 nm and fixed azimuth. The lateral dimensions of the computational cell were limited to 6×6 μm and the resolution was set to 20 nm per Yee cell. The theoretical Lambertian pattern (in black) described by equation (2.3.14) in section 2.3.2 has been overlayed on the same plot for comparison and shows a good fit: the FDTD result has maximum intensity at 0° and this is 50% of the maximum value at 60°. Figure 4-6(c) shows the three-dimensional hemispherical far-field intensity pattern.

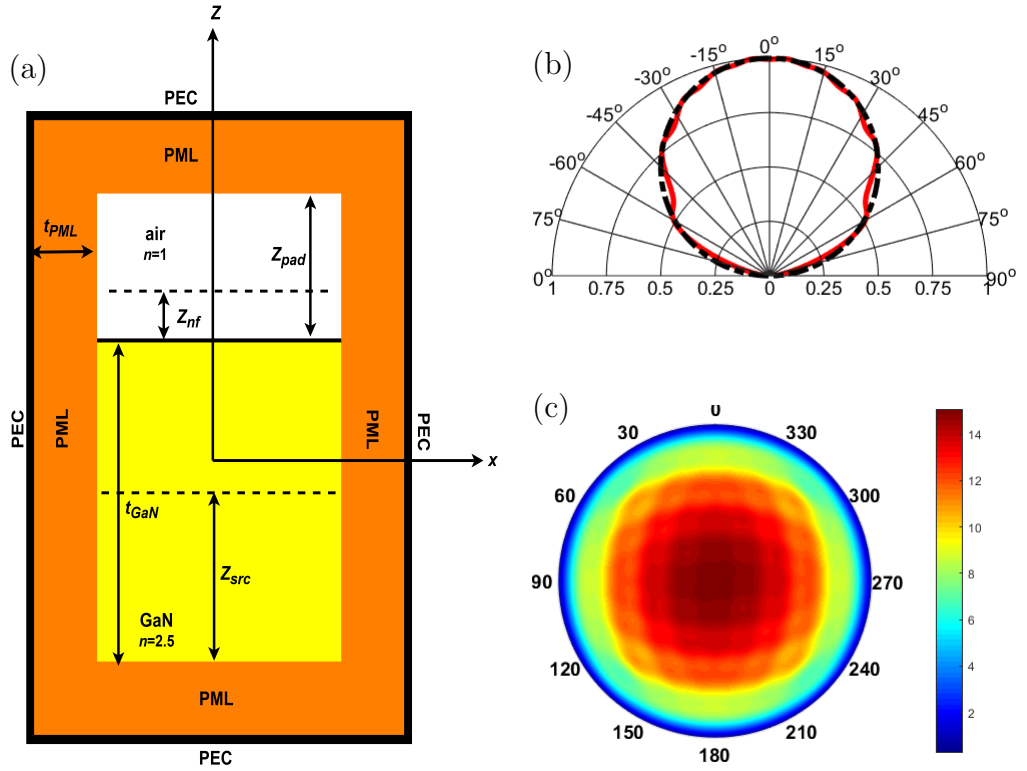

Figure 4-6: *(a) Schematic of dielectric block structure modelled in FDTD in xz-plane. (b) Comparison of normalised far-field radiation intensity obtained from FDTD (red) and Lambertian emission described by equation* (2.3.14) *(black) of planar LED. (c) Three-dimensional representation of far-field radiation intensity of structure in (a). Both (b) and (c) are spectrally resolved at 450 nm wavelength and fixed azimuth.*

Some small oscillatory variation or 'rippling' can be observed from figure 4-6(b) in the FDTD plot. After changing each model parameter separately, this effect was found to be most strongly alleviated when the PML thickness was increased from $1\mu m$ to $3\mu m$ as shown in figure 4-7(a). It was also observed that when there was a difference of around 5-6 μm between the lateral and vertical size of the computational cell, significant Fabry-Perot cavity effects occurred. Figure 4-7(b) shows broad lobes arise in the far-field for w_{GaN} reduced to 3 μm. When w_{GaN} (or t_{GaN}) was increased the lobes become narrower due to the increase in cavity size. The optimum was achieved with a square simulation cell where $w_{GaN} \approx t_{GaN}$.

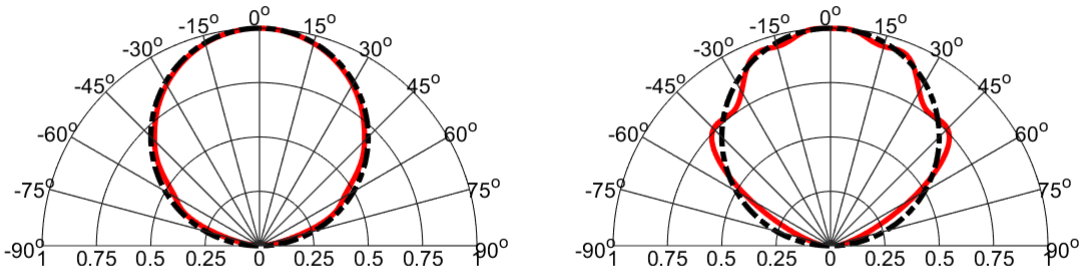

Figure 4-7: *(a) Comparison of normalised far-field radiation intensity obtained from FDTD (red) and Lambertian emission described by equation* (2.3.14) *(black) of planar LED for (a) $t_{PML} = 3\mu m$ and (b) $w_{GaN} = 3\mu m$ spectrally resolved at 450 nm wavelength and fixed azimuth.*

It has been shown for a planar GaN LED a reduced lateral size is sufficient to obtain the correct results over the angular range in the far-field. However, if one is simulating a structure which produces a wide angular ranged far-field, there are limitations to increasing the width of the cell because of available computer memory and time. This results in a trade-off when increasing the transverse size of the computational cell to capture more energy and wider observation angles in the far-field. To demonstrate the limitations of the NFFT the problem of a horizontal dipole placed a distance $z = h$ above a ground plane was considered and is shown in figure 4-8(a). The solution can be derived analytically using image theory whereby the PEC is replaced with an image dipole positioned at $z = -h$. The total field at a distant point, P, is the sum of the direct ray from the real dipole and that of the image dipole. The electric far-field components of a dipole are:

$$E_\theta = \frac{-j\omega\mu I_0 l e^{-jkr}}{4\pi r}\cos(\theta)\sin(\phi)$$
$$E_\phi = \frac{-j\omega\mu I_0 l e^{-jkr}}{4\pi r}\cos(\phi)$$

In the far-field, $r_1 \approx r_2 \approx r$ and so the total electric far-field [156] components,

E^T, are:

$$E_\theta^T = 2E_\theta \times AF \tag{4.1.36}$$

$$E_\phi^T = 2E_\phi \times AF \tag{4.1.37}$$

Where

$$AF = j\sin[kh\cos(\theta)] \tag{4.1.38}$$

When h is increased the far-field develops more side lobes at extreme angles. This was simulated in FDTD by placing an E_x polarised dipole above a PEC boundary condition with emission wavelength 450 nm. The near-fields were measured 100 nm above the dipole and the size of the computational cell was $5 \times 5 \times 5$ μm. For $h < \lambda$ the far-field patterns obtained from FDTD and equation (4.1.36) were in excellent agreement. For larger values of h where the far-field will have more sidelobes, the NFFT could not capture these extreme angular sidelobes. This is shown in figure 4-8(b) for $h = 900$ nm. A planar near-field system is inherently limited at wider observation angles because it cannot practically capture the energy since it is sampling on a finite grid. Figure 4-8(c) shows the effect of increasing the lateral size of the cell from 5 μm to 40 μm where it was observed more of the side lobes are captured. A planar NFFT needs theoretically to capture a planar grid out to infinity to obtain the far-field at $\theta \pm 90°$ which is not possible. Nevertheless, the FDTD simulations reproduced with good accuracy within $\pm 45°$ for relatively small cell sizes.

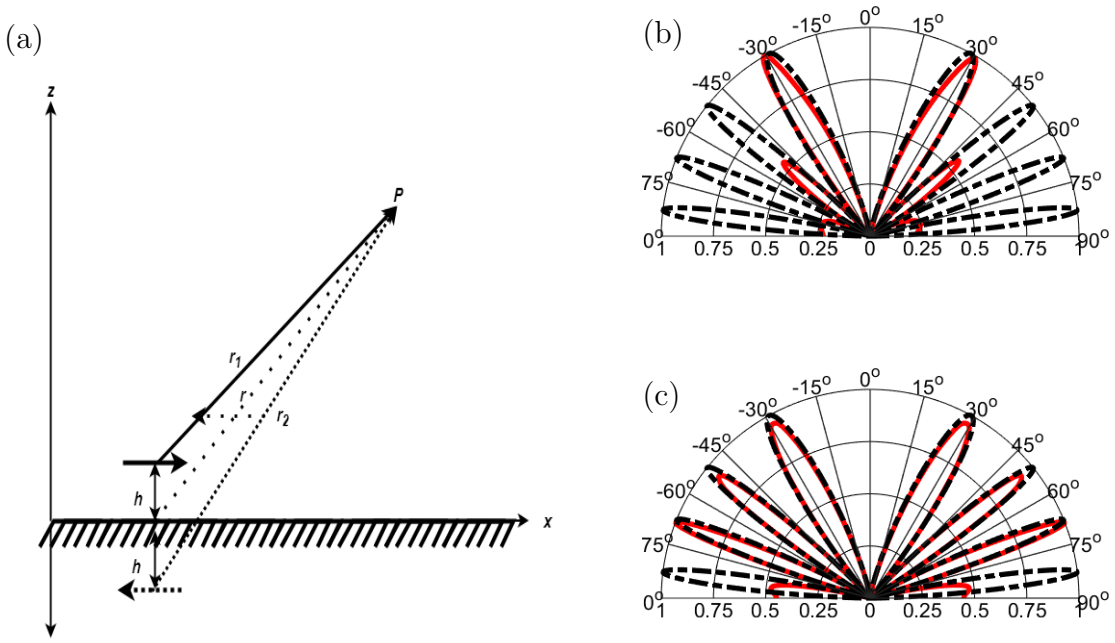

Figure 4-8: *(a) Horizontal dipole above ground plane. (b) Comparison of normalised far-field radiation intensity obtained from FDTD (red) and analytic solution obtained from equation* (4.1.36) *(black) of E_x dipole above ground plane for lateral cell size of 5μm and (c) 40μm. Both (b) and (c) are spectrally resolved at 450 nm wavelength and fixed azimuth.*

Finally the choice of the position of the near-field monitor, z_{nf}, is considered. In experiment one is physically measuring the near-field components of a test antenna using a measurement probe. Ideally the fields should be measured as close to the aperture as possible because as the wave spreads further and further away, a larger measurement area is needed to capture the energy effectively with a near-field system. This needs to be done at a 'safe region' which is typically dictated as the radiative near-field at a distance when the reactive near-field has little effect on the probe perturbing the measurement and coupling to the aperture. Taking the simple derivation and its notation from section 4.1 it was assumed the source or aperture plane was at $z = 0$. However the source field, f_s, can be specified for any z: for example for a field distribution at $z = z_a$, $F(x, y, z = z_a) = f_{sa}(x, y)$, and so the field can be obtained for any point where $F(x, y, z > z_a)$. The near-field distribution will likely be different at different z-positions and diverge with z. There are two extremes:

(i) $f_{sa}(x, y)$ is the field of a perfect planewave propagating purely along z-axis

and so there is no divergence as $f_{sa}(x, y) = constant$ with z

(ii) Point (Dirac) function source which changes rapidly with z

As the waves propagate away from the aperture it spreads and goes through a near-/far-field transition. Equation (4.1.5) takes the infinite sum of planewaves can be taken at any location and will approach an infinite bound, i.e. the far-field, thus the z-position of what is taken as the aperture plane is irrelevant so long as the amplitude and phase of the fields are being measured.

For the FDTD simulation of the horizontal dipole above the ground plane the far-field pattern was unchanged as z_{nf} was increased[3]. In the case of the GaN planar LED structure, increasing z_{nf} to 300 nm and above however resulted in oscillations in the far-field emission pattern. It is likely as the waves propagate from the surface of the LED they become more absorbed by the PML affecting the final measurement. In the literature for a free space wavelength of 450-500 nm, $z_{nf} \approx 180 - 300$ nm [113] [115] and a rule of thumb is $z_{nf} = \lambda/n$ [98]. However unlike experiment there appears no obvious reason not to have $z_{nf} = 0$ nm unless there are charges present. To apply the NFFT on any source plane $z_{nf} = 100$ nm is used because this provided the closest result to the theoretical Lambertian for the modelling of the planar structure.

4.2 Light Extraction Efficiency

The light extraction efficiency, η_{lee} is defined in equation (2.3.2) but will be repeated here for convenience:

$$\eta_{lee} = \frac{P_{ext}}{P_{in}} \tag{4.2.1}$$

To find the LEE from FDTD simulations the total power emitted from the dipole, P_{in}, modelling the active region and the power that escapes from the top surface of the LED, P_{ext} are required. The power is defined as the integral of the Poynting vector over the volume, surface or line of interest. For a dipole, P_{in} is given by:

$$P_{in} = \int_V \mathbf{S} \, \mathrm{d}V \tag{4.2.2}$$

[3]One cannot measure a dipole's near-field at the dipole because FDTD does not include charge dynamics: charges are considered to be infinitely massive and do not move

FDTD uses a Cartesian space and to find the total power radiated by the dipole it is surrounded by six faces which represent monitors to measure the Poynting vector component perpendicular to the face [158] [160] [114]. This set-up is shown in figure 4-9(a). The power for each face can then be calculated by summing the Poynting vector over the area of the face for example:

$$P_{x1} = \int_{y_1}^{y_2} \int_{z_1}^{z_2} S_x \, \mathrm{d}y \, \mathrm{d}z \tag{4.2.3}$$

The total power becomes:

$$P_{in} = P_{x1} + P_{x2} + P_{y1} + P_{y2} + P_{z1} + P_{z2} \tag{4.2.4}$$

MEEP can output the Poynting vector as a function of time, but it would be incorrect to input a pulse, measure $\mathbf{S}(t)$ and then Fourier-transform to obtain $\mathbf{S}(\omega)$ and $P_{in}(\omega)$. This is because the Poynting vector equation in (4.1.28) requires the fields to be Fourier transformed and the Poynting vector is not a linear function of the fields. To compute $P_{in}(\omega)$ the tangential field components $E(t)$ and $H(t)$ are taken from FDTD and a DFT is applied to find $E(\omega)$ and $H(\omega)$. Using equation (4.1.28) the normal component of the Poynting vector can be calculated and then summed over the area to find the power. In its most general form equation (4.2.3) is written as:

$$P_{x1}(\omega) = \int_{y_1}^{y_2} \int_{z_1}^{z_2} \left[\frac{1}{2} \mathrm{Re} \left(E_y(y,z,\omega) H_z^\star(y,z,\omega) - E_z(y,z,\omega) H_y^\star(y,z,\omega) \right) \right] \mathrm{d}y \, \mathrm{d}z \tag{4.2.5}$$

Similar expressions may be found for the other components and are summarised below:

$$
\begin{aligned}
P_{x2}(\omega) &= \int_{y_1}^{y_2}\int_{z_1}^{z_2}\left[\frac{1}{2}\mathrm{Re}\left(E_z(y,z,\omega)H_y^\star(y,z,\omega) - E_y(y,z,\omega)H_z^\star(y,z,\omega)\right)\right]\,\mathrm{d}y\,\mathrm{d}z \\
P_{y1}(\omega) &= \int_{x_1}^{x_2}\int_{z_1}^{z_2}\left[\frac{1}{2}\mathrm{Re}\left(E_z(x,z,\omega)H_x^\star(x,z,\omega) - E_x(x,z,\omega)H_z^\star(x,z,\omega)\right)\right]\,\mathrm{d}x\,\mathrm{d}z \\
P_{y2}(\omega) &= \int_{x_1}^{x_2}\int_{z_1}^{z_2}\left[\frac{1}{2}\mathrm{Re}\left(E_x(x,z,\omega)H_z^\star(x,z,\omega) - E_z(x,z,\omega)H_x^\star(x,z,\omega)\right)\right]\,\mathrm{d}x\,\mathrm{d}z \\
P_{z1}(\omega) &= \int_{x_1}^{x_2}\int_{y_1}^{y_2}\left[\frac{1}{2}\mathrm{Re}\left(E_x(x,y,\omega)H_y^\star(x,y,\omega) - E_y(x,y,\omega)H_x^\star(x,y,\omega)\right)\right]\,\mathrm{d}x\,\mathrm{d}y \\
P_{z2}(\omega) &= \int_{x_1}^{x_2}\int_{y_1}^{y_2}\left[\frac{1}{2}\mathrm{Re}\left(E_y(x,y,\omega)H_x^\star(x,y,\omega) - E_x(x,y,\omega)H_y^\star(x,y,\omega)\right)\right]\,\mathrm{d}x\,\mathrm{d}y
\end{aligned}
\tag{4.2.6}
$$

It should be noted when the FDTD simulation containing only the dipole source is made, the entire cell must be made up of the medium that the dipole is placed because the radiated power depends on refractive index.

To calculate the extracted power two equivalent methods have been used in literature. The first is finding the perpendicular Poynting vector just above the surface of the LED which was first done in [93]. The extracted power is then given by:

$$
P_{ext} = \int_{-\frac{a}{2}}^{\frac{a}{2}}\int_{-\frac{b}{2}}^{\frac{b}{2}}\left[\frac{1}{2}\mathrm{Re}\left(E_x(x,y)H_y^\star(x,y) - E_y(x,y)H_x^\star(x,y)\right)\right]\,\mathrm{d}x\,\mathrm{d}y \tag{4.2.7}
$$

An obvious issue arises from the limited lateral size of the simulation cell relative to the actual size of of the device and so less light output is measured in the simulation. Wiessman [158] found η_{lee} was dependent on the lateral size of the computational cell when modelling LEDs with surface PhC arrays. This was attributed to guided modes with poor interaction with the PhC and get absorbed by the PML before being diffracted. The same study found η_{lee} saturated at very large lateral simulation sizes of around $80 \times 80\ \mu m$, which is generally impractical, and shows complete light extraction could not be achieved for normal simulation sizes. This issue was addressed by running several simulations of the

same structure but for different smaller lateral dimensions and then extrapolating η_{lee} from a trend line of η_{lee} vs. lateral computational size. The study in [94] found η_{lee} increased by 5-10% when the array was increased from 7×7 to 9×9 implying a degree of sensitivity of η_{lee} on lateral simulation size. Another method of addressing this issue was the use of PBCs and PECs as shown in figure 4-9(b).

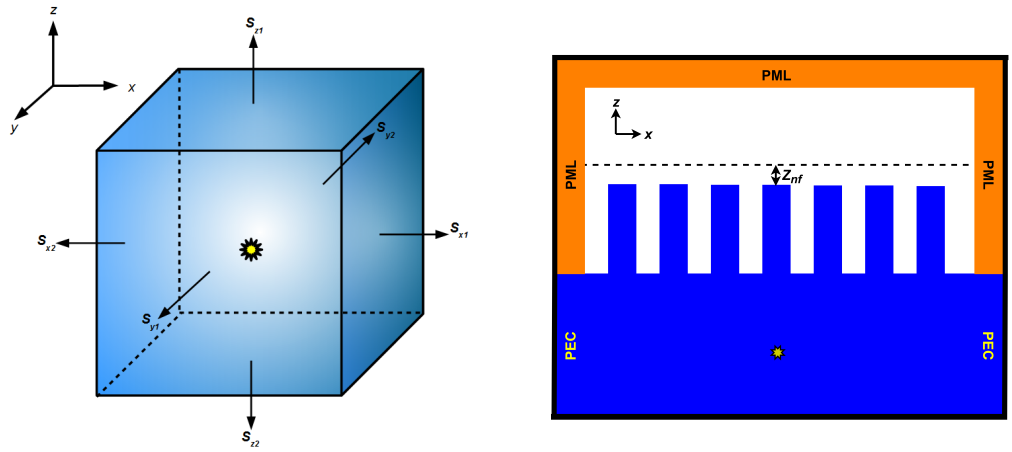

(a) **(b)**

Figure 4-9: *(a) Set-up in FDTD to measure total radiated power of a dipole. (b) Method used by [98] [95, 97, 99, 105, 106] for calculation of* η_{lee}.

The aim of the PEC arrangement in figure 4-9 is to ensure all of the light escapes through the top of the LED and obtain a complete value of η_{lee}. Cho *et al.* [95] used this method to justify using small lateral sizes of the computational cell and it was reasoned that the dipoles which were placed in the middle of the MQW region at (0,0) were far enough from the boundaries that reflections were negligible in the far-field emission pattern. The same group also used this method for other PhC LED structures [98] [99]. Interestingly no far-field emission results were presented and unfortunately such a set-up cannot be implemented in MEEP to check the effect of the lateral PECs on the far-field emission. This method of obtaining maximum η_{lee} appears to have been referenced in other work: Long *et al.* [106] also surrounded their structure with PECs stating that such an arrangement gave the same result as an infinite structure not unlike PBCs. However, this could only be applicable because the source was placed at the center of the computational cell and the phase at the edge of the cell set as zero. Zhao *et al.* [110] used the PEC set-up in figure 4-9(b) in their simulations to

calculate η_{lee} but interestingly the group replaced the PECs with PMLs in future work [112] where they presented both far-field emission patterns and values of η_{lee}.

The other position to measure the light output power was by integrating the far-field radiation intensity over all solid angle of the hemisphere [115] [113] [16] [96]. This is expressed as:

$$P_{ext} = \int_0^{2\pi} \int_0^{\frac{\pi}{2}} U(\theta, \phi) \sin(\theta) \, \mathrm{d}\phi \, \mathrm{d}\theta \tag{4.2.8}$$

For both cases there remains the issue of limited cell size: for the latter case and with a planar near-field collection system, the range of the angular far-field pattern is limited as was previously discussed in section 4.1.3.

Taking the planar GaN LED structure from the previous section, it is known that $\eta_{lee} \approx 4\%$ from the discussion in section 2.3.2. Implementing the method to find P_{ext} was found to be more convenient by using the near-fields measured for the NFFT. A value of $\eta_{lee} = 4.04\%$ was obtained. It should be noted however when the lateral size of the block was increased to 10×10 μm, η_{lee} reduced to 1.6%. A similar effect was observed in [161] where it was attributed it to a waveguide effect in the overall computational cell whereby the much larger lateral size promoted wave propagation into the PML rather than directed upwards. This is also indicated in the far-field emission pattern in figure 4-7(b).

4.3 Enhancement Factor

Another parameter which is used to compare different structures is the enhancement factor, F, which is defined as the ratio of the light extraction efficiency for two different structures. When quantifying light extraction for structures with PhC arrays etched on the surface of an LED one typically divides the light extraction efficiency of the PhC-LED with that of the planar surface version [104] [114]:

$$F = \frac{\eta_{lee}|_{PhC}}{\eta_{lee}|_{pla.}} \tag{4.3.1}$$

4.4 Directionality

Using the method in [47] the directionality of LEDs with PhCs is found by normalising the extracted power to be $P_{ext} = 1$ and dividing this by the normalised Lambertian emission. In this work the directionality of a patterned device is defined as the ratio of the normalised P_{ext} to the normalised P_{ext} of Lambertian emission within $\pm 15°$ elevation emission cone from the normal and integrated over azimuth, ϕ:

$$D = \frac{\int_0^{360} \int_0^{15} \bar{U}|_{PhC}(\theta, \phi) \sin(\theta) \, \mathrm{d}\phi \, \mathrm{d}\theta}{\int_0^{360} \int_0^{15} \bar{U}|_{pla.}(\theta, \phi) \sin(\theta) \, \mathrm{d}\phi \, \mathrm{d}\theta} \tag{4.4.1}$$

4.5 Summary

Implementation and validation of the procedures was made for the calculation of the parameters referred to in literature which quantify the light extraction of LED structures using measurements obtained from MEEP's FDTD software. These parameters are:

(i) Far-field emission pattern, $U(\theta, \phi)$

(ii) Light extraction efficiency, η_{lee}

(iii) Enhancement factor, F

(iv) Directionality, D

Excellent agreement was found for the planar GaN LED structure from the values obtained for the far-field emission pattern and η_{lee}, the latter when the computational cell was suitably sized. Applying the NFFT to the extreme case of a horizontal dipole displayed good agreement within the angular range of $\theta = \pm 45°$ for small cell sizes, thus demonstrating the limitation of the planar NFFT for far-field patterns with extreme sidelobes. This effect can be alleviated by increasing the lateral size of the cell width at the cost of increased computational time. For planar structures it was observed that there is a cavity effect when the lateral dimensions are made much larger relative to the vertical length by around $5 - 6\mu m$. Similarly the value of η_{lee} decreased from the theoretical 4% to 1.6%. This is likely due to waveguiding effects where the light tends to be guided towards the PML where it is absorbed.

A literature review has been made on the measurement of η_{lee} from FDTD simulations where it has been shown there is a sensitivity of η_{lee} on the lateral size of the computational cell. This value saturates for extremely large dimensions which are impractical to simulate. Therefore the values calculated should be taken with consideration and are likely underestimating the actual η_{lee}.

To further observe the effect of patterning the surface of planar LEDs with PhC arrays, a proposed method for calculating F and D has been presented to obtain a further LED parameter values for comparing the results for different structures in order to obtain a more reliable measure of the light extraction.

Now that the tools to measure LED light extraction from FDTD simulations have been established, LED models can be developed to determine the effect of changing certain LED parameters without the need to fabricate actual samples. To develop a reliable model it needs to be validated with experimental measurements. The parameters $U(\theta, \phi)$, F and D are independent of the radiated power of the active region and can be compared with experimental photoluminescence (PL) results. The next chapter will present experimental results including PL which can be used to compare with FDTD and information on the complicated structure of the samples to accurately set up the FDTD model.

Chapter 5

Experimental Results of NR Array Etched onto Vertical LED Structure

This chapter presents the LED structures studied as per the subject of this thesis. Here focus will be on the nanotexturing of the LED structures from their fabrication to their morphological characterisation. Finally optical characterisation on the structures will be presented. From this, comparison can be made between the performance of the original device, several nanostructured devices and with surface roughening.

5.1 Texturing of LEDs

The LED wafer material was provided by Plessey Semiconductors. It has a vertical structure layout whereby the semiconductor epitaxy is grown on a silicon substrate and then flipped over. A reflecting metal contact is first formed on the upper *p*-side epitaxy and bonded to a conductive substrate wafer. Next the sapphire growth substrate is removed. The epitaxial layers including the active region are grown along the [0001] direction i.e. the *c*-axis. They include a graded AlGaN layer which is used to alleviate the tensile strain between the GaN and sapphire substrate during the growth process, reducing the number of defects and possibility of cracking.

5.1.1 Plessey LED structure

Figure 5-1 is a schematic of the Plessey LED vertical structure after wafer bonding.

Label	Composition	Thickness
AlN		200±20nm
AlGaN1	88-61% Al linear grade	200±20nm
AlGaN2	61-24% Al linear grade	320±32nm
AlGaN3	24%±1 %Al	130±13nm
U:GaN	Mg:GaN	300±30nm
U:GaN	GaN	130nm
Si:GaN	GaN	850±50nm
Si:GaN	GaN	228±30nm
Active region	InGaN/GaN 6QW/QB	112nm
EBL	Mg:AlGaN 20±1 %Al	22±2nm
P-GaN	Mg:GaN	170±7nm
Ag Mirror		
Bonding Materials		
Si Handle		

Figure 5-1: *Schematic of Plessey LED vertical structure after wafer bonding.*

The full fabrication process involves first depositing metals onto the p-GaN to form a mirror contact which improves electrical contacting and maximises the reflection of light. It also acts to dissipate heat to the conductive silicon substrate for large injection currents. The active region is 112 nm thick and made up of six InGaN quantum wells (QWs), each separated by a GaN quantum barrier (QB). However, no information has been provided on the thickness of the QWs. Typically they range between $2-5$ nm with $7-13$ nm QBs. A p-type AlGaN electron blocking layer (EBL) of 20% Al composition is used to prevent electrons escaping into the p-GaN and recombining, reducing the η_{IQE} of the QWs. This is a standard commercially available structure for high power applications. The

total thickness of the epitaxial layers is 2662 ± 204 nm.

5.1.2 Nanorod Fabrication

Nanorod arrays were fabricated on the surface of the structure in figure 5-1 at the University of Bath's NanoFab facility by Szymon Lis. This process is described by figure 5-2.

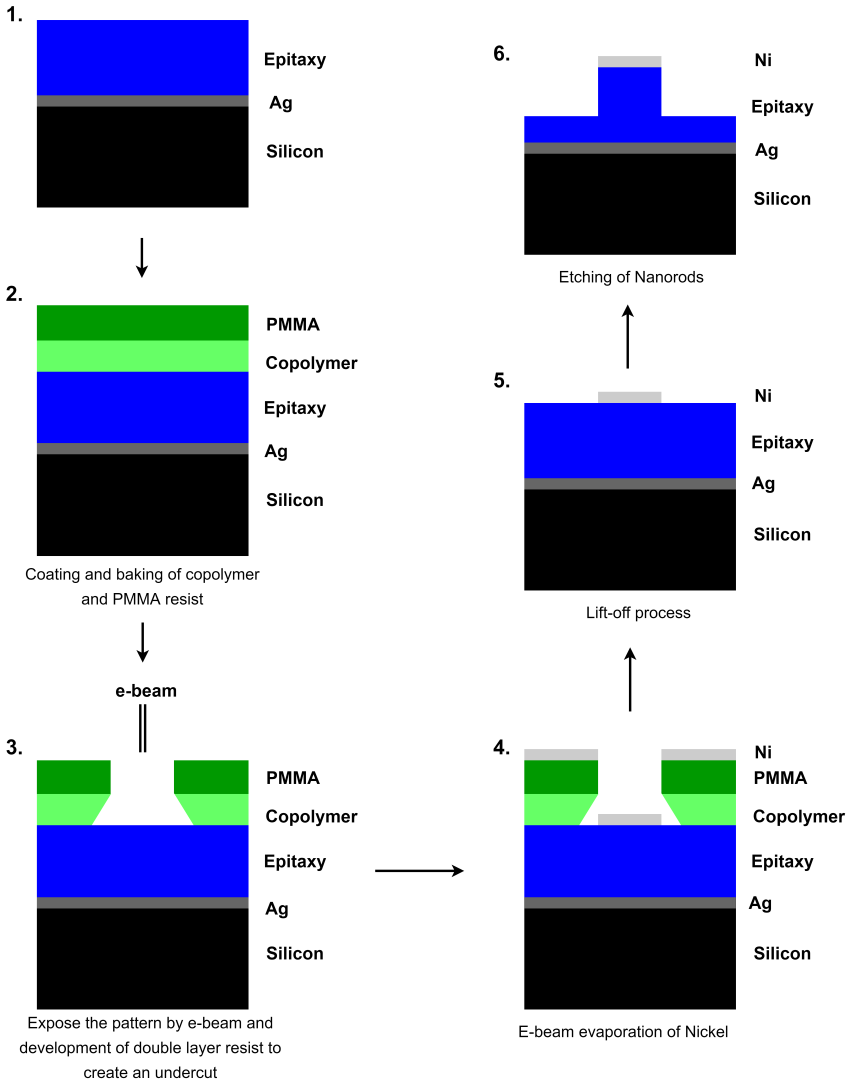

Figure 5-2: *Diagram of nanorod fabrication process.*

The fabrication of nanorods was achieved by a method called electron beam lithography (EBL). The following lists and briefly describes steps 2-6 of the pro-

cess in figure 5-2. The grown semiconductor layers of the Plessey structure are grouped as epitaxy for the sake of brevity:

2. First, a double-layer of photo-resist is spin-coated onto the surface of the Plessey structure. The sample is then baked to set the resist. The double-layer resist consists of copolymer and Polymethyl methacrylate (PMMA)-495 and is used to allow effective lift-off later to occur.

3. An electron beam within a scanning electron microscope (SEM) is used to pattern the PMMA. The pattern is set by the user using software. The configuration of the array was hexagonal and three 100×100 μm different patterns were designed for this study which are:

   - Pitch= 1200 nm, diameter= 400 nm
   - Pitch= 800 nm, diameter= 300 nm
   - Pitch= 600 nm, diameter=200 nm

   The electron beam will break the bonds of the resist in areas that it illuminates so when the sample is placed in resist developer, the exposed areas will be removed. The resist developer used was 1:3 of Methyl Isobutyl Ketone (MIBK):Isopropanol (IPA) which allows a greater control in the formation of the undercut profile in the copolymer layer.

4. Nickel is deposited on top with a typical thickness of 50 nm using electron beam vacuum evaporation.

5. The double-layer resist is removed in a lift-off process of 3 minute ultrasonic bath in acetone. Note that the undercut acts to decouple the nickel on the epitaxy from the nickel on the double-layer resist so that only the nickel in direct contact with epitaxy remains. The result is an hexagonal array of nickel dots which act as an etch mask.

6. Nanorods are etched using inductively-coupled plasma (ICP) etching using a chlorine based chemistry. ICP is an anisotropic etching process and the etch rate will be much higher vertically than laterally. Chlorine plasma is commonly used to etch III-nitride material. Nickel acts as a hard etch mask due to its good selectivity for III-nitride.

The nanorod arrangement was in an hexagonal layout to achieve close packing and greater symmetry. Increasing the number of directions for periodicity will correspondingly promote more omnidirectional light extraction.

5.1.3 Nanorod Morphology

In order to measure the dimensions of the nanostructures and observe the morphology, the three samples were placed in a scanning electron microscope (SEM). SEM imaging was performed in collaboration with Szymon Lis. Figures 5-3, 5-4 and 5-5 show the SEM images of the top and side views of the etched samples at 25k magnification for an array pitch, Λ = 1200 nm, 800 nm and 600 nm respectively.

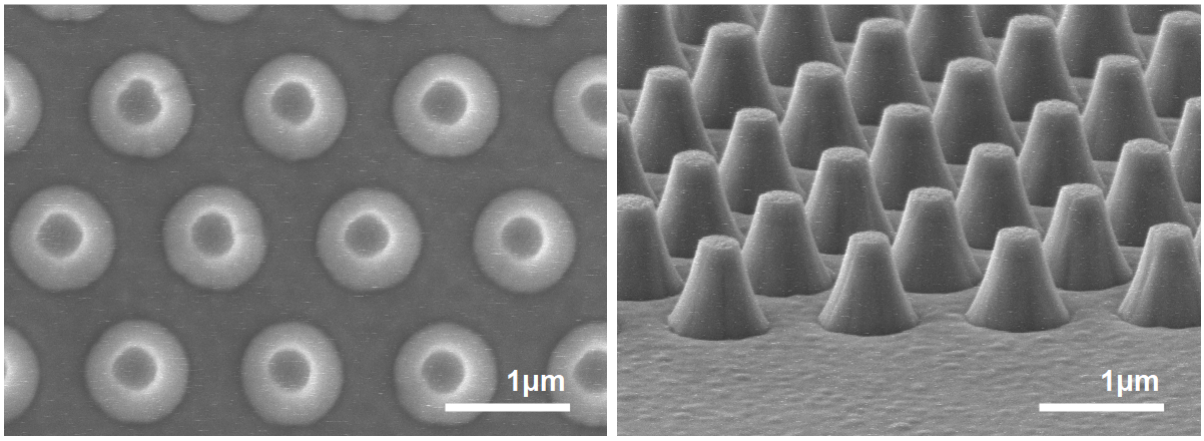

(a) **(b)**

Figure 5-3: *SEM image of (a) top and (b) side-angle view of sample with* $\Lambda = 1200$ *nm at magnification* $\times 25k$.

As can be seen from the SEM images the nanorods are cones. This is because the ICP etch conditions lead to forming a tapered profile of the rods rather than vertical sidewalls. One needs to tune the plasma properties, i.e. chemistry, pressure, temperature and power to achieve vertical sidewalls but this optimisation was out of the scope of this thesis. The conical shape of the nanorods will need to be accounted for in the simulations of their electromagnetic properties.

From the SEM images, the top and base diameters, D_{top} and D_{bottom}, of the nanorods could be obtained for each sample. In order to avoid damaging the nanorod array, the height, h, could not be extracted from a direct cross sectional

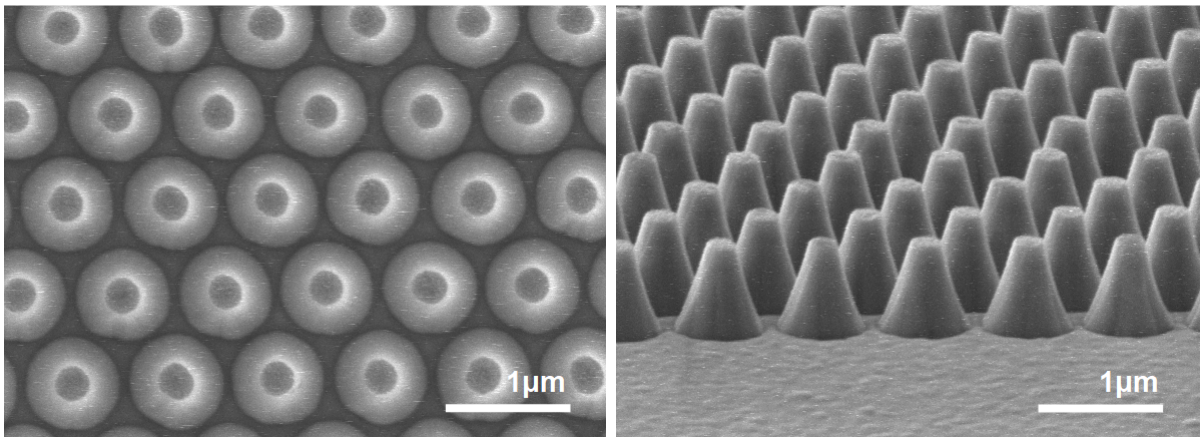

(a) **(b)**

Figure 5-4: *SEM image of (a) top and (b) side-angle view of sample with* $\Lambda = 800$ *nm at magnification* $\times 25k$.

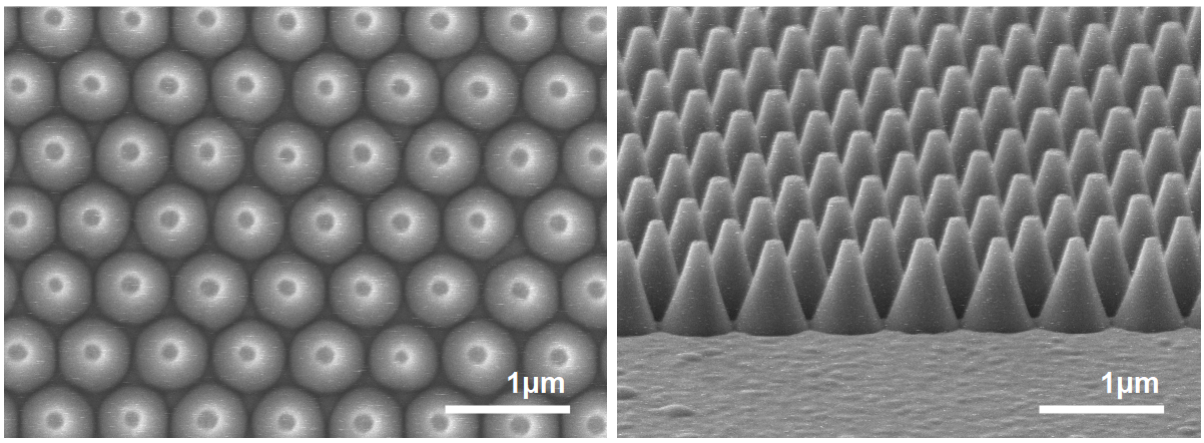

(a) **(b)**

Figure 5-5: *SEM image of (a) top and (b) side-angle view of sample with* $\Lambda = 600$ *nm at magnification* $\times 25k$.

side view. Instead it was extrapolated from the slope angle, D_{top} and D_{bottom} as shown in figure 5-6.

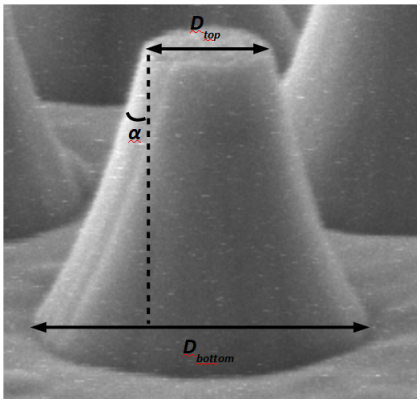

Figure 5-6: *Method of extrapolating height of nanorod from side-angled SEM imaging.*

Table 5.1 summarises the dimensions for each sample: D_{top} should correspond

$\boldsymbol{\Lambda}$ (nm)	$\boldsymbol{D}_{top}$ (nm)	$\boldsymbol{D}_{bottom}$ (nm)	$\boldsymbol{h}$ (nm)
1200	355	845	690
800	275	620	705
600	140	600	730

Table 5.1: Summary of sample's nanorod dimensions

to the mask diameter set for the EBL but as can be seen, the measured values are reduced in practice. This is due to the way the nickel is deposited, as more rounded at the edges than uniformly across the exposed epitaxy. The ICP etch therefore etched the edge of the nickel faster due to the reduced thickness and ultimately erodes the epitaxy around the edge. Note also there is a slight fluctuation in diameter from rod to rod for all the samples studied.

5.2 Angular Photoluminescence

Optical characterisation was performed on all three nanorod samples and the original Plessey structure using angular photoluminescence (PL). The angular PL was performed in collaboration with Szymon Lis. In this process, electrons and holes are excited directly in the active region by a laser light whose photons have greater energy than the bandgap of the QWs. These charge carriers then recombine radiatively and the emission of the device is measured for different

emission angles. This differs from electroluminescence (EL) where the carriers are produced by current injection and so EL is only performed on contacted devices.

PL is still representative of the optical properties of the structure and can be used to compare with FDTD, whereas EL also includes effects due to the electrical characteristics of devices such as the contacts and the injected carriers transporting to the active region.

Angular PL was performed in collaboration Szymon Lis.

5.2.1 Experimental Set-up

The experimental set-up of the angular PL system is shown in figure 5-7(a)[1] and the concept of operation is shown in figure 5-7(b). Here the sample is placed on a stand and illuminated by a laser beam of wavelength 405 nm. An optical fibre is used as the probe to measure the emission from the sample at a point in the far-field. The position of the probe is varied as a function of elevation (θ) and azimuth (ϕ) in increments of $\Delta\theta$ and $\Delta\phi$ respectively, hence the term angular PL. The potential angular range is over a hemisphere around the sample. This is achieved using two separate stepping motors so one can measure the intensity at any point over any range.

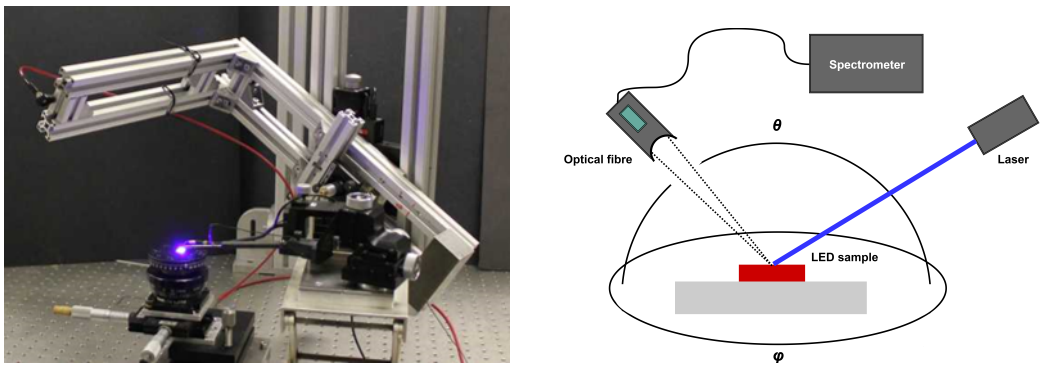

(a) **(b)**

Figure 5-7: *(a) Experimental set-up of angular PL system. (b) Concept of operation.*

[1]It should be noted that the experiment in the photograph is EL where probes are used to contact the sample. PL is a contactless process, making the probes redundant.

For angular PL measurements on the etched samples, the azimuth was fixed for two angles: $\phi = 60°$ and $\phi = 90°$ as shown in figure 5-8. The elevation was then varied as $\theta = -90° : 90°$ in increments of $0.1°$. Running three-dimensional angular ranged PL is extremely time consuming given the requirement for very high resolution, and this is why angular PL measurements where taken for two single slices. The choice of azimuth angles $\phi = 60$ and $\phi = 90$ is because they are along the fundamental symmetry axes of the hexagonal array as shown in figure 5-8.

To determine the alignment of the sample so that the elevation slices were taken at the correct azimuth, the sample was illuminated with the laser and a piece of white paper was placed above the sample. Making use of the concepts introduced in chapter 4, the diffracted pattern projected onto the paper will be to a first order approximation the Fourier transform of the hexagonal arrays of the nanorods. This is a crude approximation in which the hexagonal array is treated like a two dimensional amplitude diffraction grating with an hexagonal array of field distribution. Figure 5-8 shows the hexagonal array in blue circles and the Fourier transform of this is the array shown by the red circles. This is often termed reciprocal space and is what was very faintly observed in practice on the paper. A red laser beam at $\phi = 90°$ was used for the alignment by moving the sample with micro-positioners until the red beam coincided with $\phi = 90°$ on the paper.

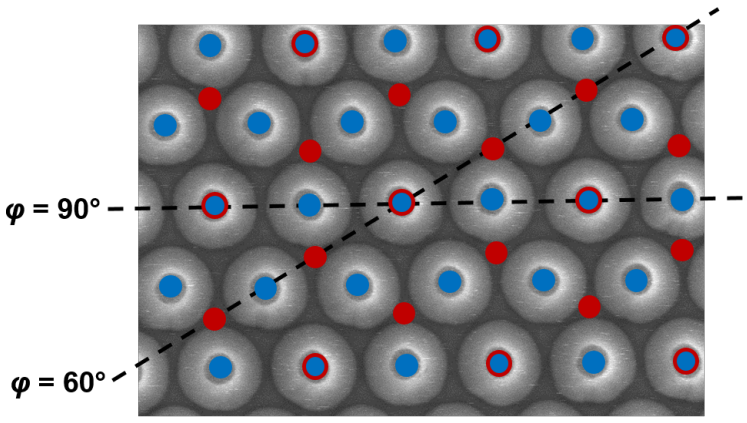

Figure 5-8: *Method of aligning sample by aligning a red beam at $\phi = 90°$ to the reciprocal array that will be observed on a piece of white paper placed above sample.*

The spectrum was measured at each θ position using a spectrometer which was set with an exposure time of 0.1 seconds and slit width of 20 μm. The slit width determines the spectral resolution of the PL measurement. The wavelength range was 414-552 nm with a spectral resolution of 0.1343 nm.

5.2.2 Results of Planar Structure

Figure 5-9 shows the spectrum of the planar structure at $\theta = 0°$. The emission spectrum of the active region was found by fitting the spectrum obtained from PL in figure 5-9 to a Gaussian waveform from which values for center wavelength, $\lambda_{cen} = 450$ nm, and half maximum width, $\Delta\lambda = 60$ nm were obtained.

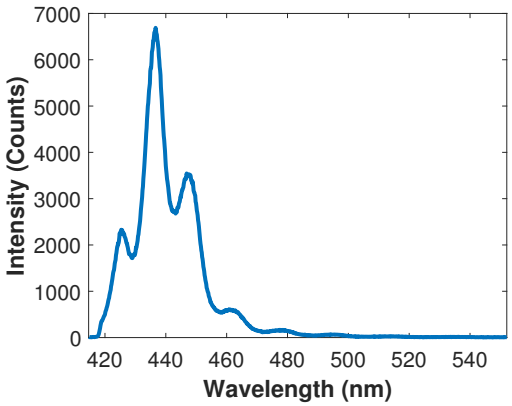

Figure 5-9: *Emission spectrum of planar structure at* $\theta = 60°$.

Figures 5-10(a) and (b) show the normalised angular far-field emission intensity obtained from PL for $\theta = -90° - 90°$ spectrally resolved at 450 nm and integrated over the width of the emission band respectively.

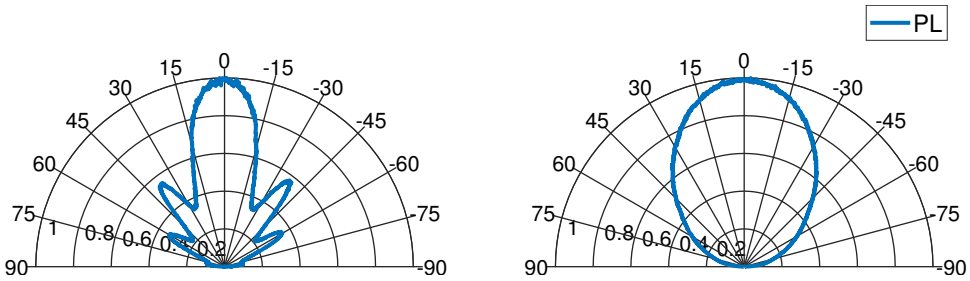

(a) (b)

Figure 5-10: *Normalised angular PL results for (a) spectrally resolved at* 450 *nm and (b) integrated emission of planar structure.*

The plots have been normalised such that:

$$\bar{U}(\theta) = \frac{U(\theta)}{U(\theta)|_{max}} \tag{5.2.1}$$

Where U is the intensity measured from the spectrometer in arbitrary units of counts.

Taking the Lambertian emission pattern for GaN in air this is normalised as such that the total power (for a single azimuth) and that of the Plessey planar structure are both unity. The directionality, D, is then defined for the planar structure within the emission angle $\theta = \pm 15°$ as:

$$D = \frac{\int_0^{15} \bar{U}|_{pla.}(\theta)\ \mathrm{d}\theta}{\int_0^{15} \bar{U}|_{lam.}(\theta)\ \mathrm{d}\theta} \tag{5.2.2}$$

$\bar{U}|_{pla.}$ = Measured intensity of planar structure normalised so integration over all θ is unity

$\bar{U}|_{lam.}$ = Theoretical intensity of Lambertian emission normalised so integration over all θ is unity

The range $\theta = \pm 15°$ is a figure of merit defined by the author. It has also been used for defining directionality in previous work [16]. From equation (5.2.2) values of $D = 1.18$ over the integrated emission wavelength and $D = 1.47$ at 450 nm emission wavelength were obtained. It is likely the larger relative directionality with respect to Lambertian is mainly due to the silver reflector.

5.2.3 Results of Surface Roughened Structure

In addition to the nanorod samples, angular PL was performed on the planar structure with surface roughening. The roughening was achieved using potassium hydroxide. As was discussed in section 2.4.2, this is a common way to increase the light extraction of LEDs.

Figure 5-11 shows the normalised angular far-field emission intensity obtained from PL for $\theta = -90° : 90°$ for a fixed azimuth. Here the emission was integrated over the width of the emission band.

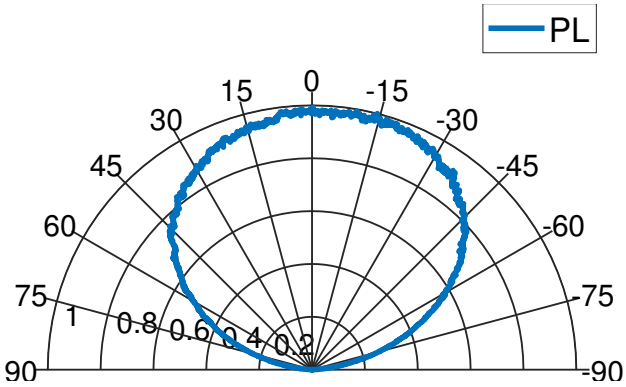

Figure 5-11: *Normalised angular PL results for integrated emission of planar structure with surface roughening.*

From equation (5.2.2), $D = 0.93$ was calculated which indicates the emission of the roughened structure is very similar to Lambertian. Spectrally resolved PL results have been omitted as they were unchanged from the integrated emission pattern: for an emission wavelength of 450 nm, $D = 0.95$. The independence of the far-field pattern on wavelength was further demonstrated by observing the spectra as a function of θ. For comparison, figures 5-12(a) and (b) display the ϕ slice of the planar structure and roughened structure respectively.

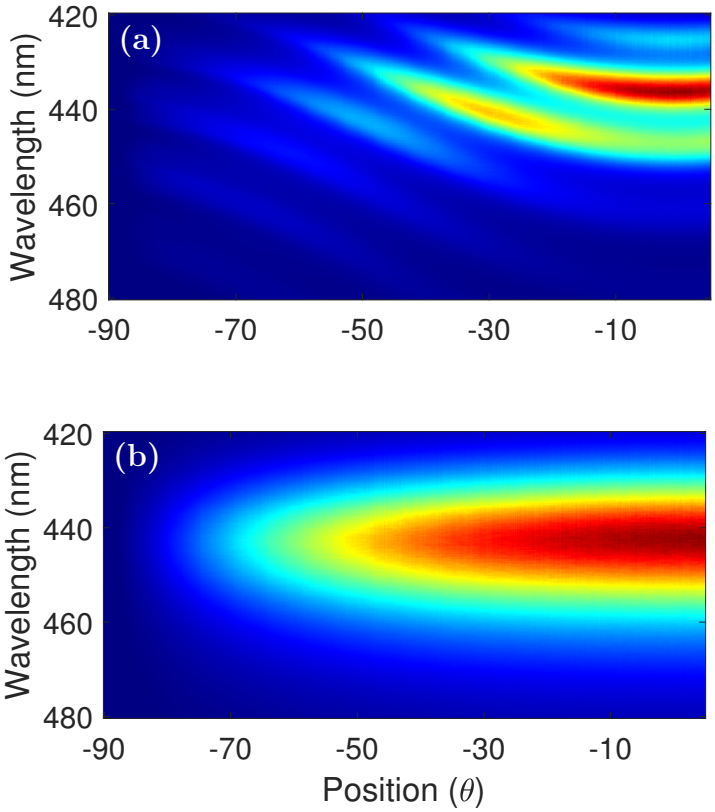

Figure 5-12: *Wavelength vs. elevation angle, θ of angular PL results obtained for (a) planar structure and (b) roughened structure.*

In figure 5-12(a) Fabry-Perot fringing is observed for the planar structure with strong relative intensity around 430nm for normal emission. It is also seen that the fringes rapidly decay as $\theta \rightarrow -90°$ indicating strong light trapping inside the LED. In figure 5-12(b) the fringes have been removed and the emission is strongly Lambertian-like due to the random scattering of light extracted from the structure. This highlights the issue of directionality loss from surface roughening discussed in section 2.4.2.

5.2.4 Results of Etched Nanorod Structures

Figure 5-13 shows the unnormalised angular far-field emission intensity obtained from PL for θ=$-90° - 90°$ at a fixed azimuth, $\phi = 90°$: (a) is integrated over emission and (b) is spectrally resolved at 450 nm for the three hexagonal array pitches considered.

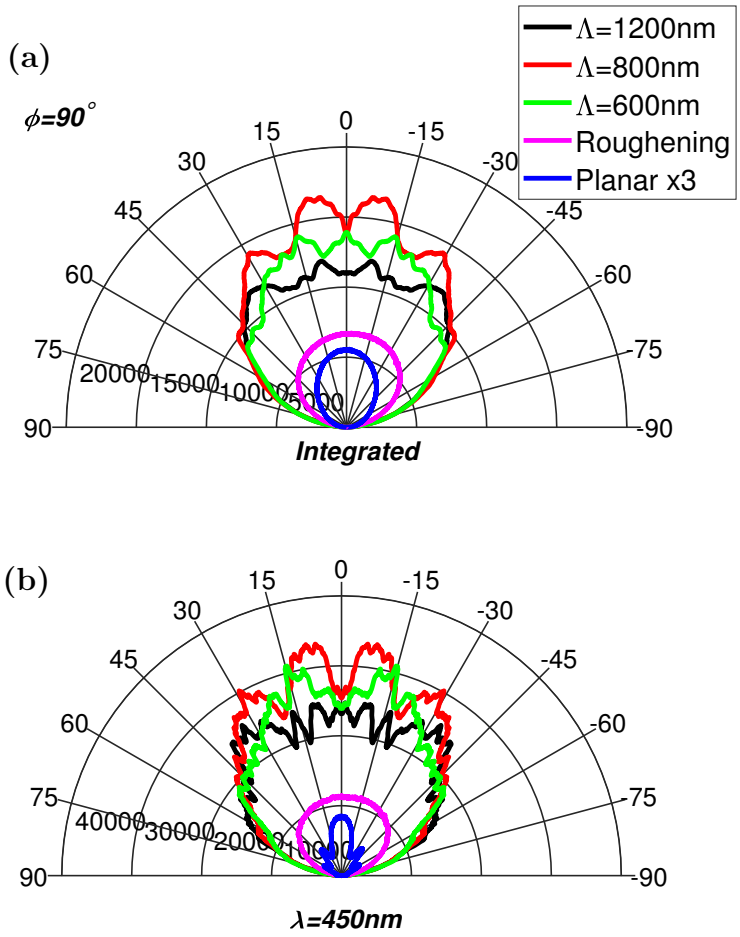

Figure 5-13: *Comparison of unnormalised angular PL results for (a) integrated emission and (b) spectrally resolved at* 450 *nm for fixed* $\phi = 90°$ *of NR structures, surface roughened structure and planar structure.*

Figures 5-14(a) and (b) are the corresponding results for $\phi = 60°$.

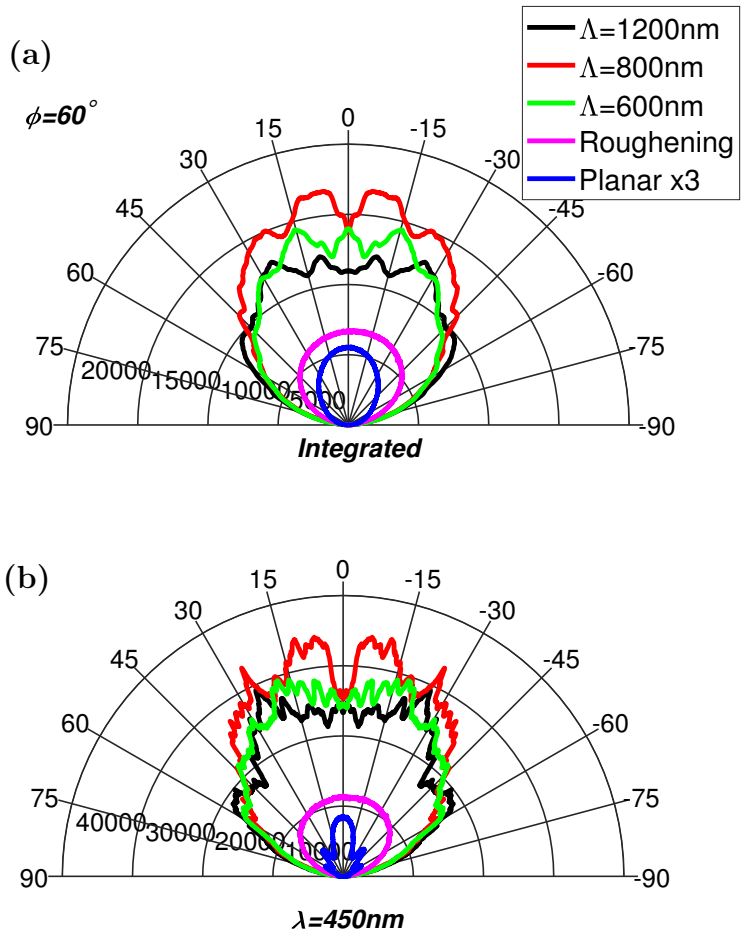

Figure 5-14: *Comparison of unnormalised angular PL results for (a) integrated emission and (b) spectrally resolved at* 450 *nm for fixed* $\phi = 60°$ *of NR structures, surface roughened structure and planar structure.*

The plots are unnormalised and include the unnormalised results for the planar structure and structure with surface roughening to demonstrate the relative enhancement displayed from the nanorod samples. The PL results of the planar structure have been magnified by a factor of three in figures 5-13 and 5-14 to appear more visible to the reader.

In order to quantify this enhancement, the enhancement factor, F, is defined with respect to the planar structure as:

$$F = \frac{\int_0^{\frac{\pi}{2}} U(\theta)\ \mathrm{d}\theta}{\int_0^{\frac{\pi}{2}} U|_{pla.}(\theta)\ \mathrm{d}\theta} \tag{5.2.3}$$

U = Measured intensity of etched structure

$U|_{pla.}$ = Measured intensity of planar structure

Table 5.2 summarises the enhancement factors for each structure using equation (5.2.3) for integrated emission.

Sample	$\boldsymbol{F}$ $(\phi = 90°)$	$\boldsymbol{F}$ $(\phi = 60°)$
$\Lambda = 1200$ nm	8.62	8.39
$\Lambda = 800$ nm	9.80	9.91
$\Lambda = 600$ nm	8.76	8.80
Roughened	4.60	x

Table 5.2: *Summary of enhancement factors, F, for etched structures relative to planar structure using equation* (5.2.3).

What is immediately apparent in figures 5-13 and 5-14 is the extremely large enhancement arising from nanostructuring the surface and secondly, the changes in the directionality of the emission from the nanostructured surface. The large enhancement of the nanorod samples relative to the roughened structure may be due to the deeper etching of the rods: in section 2.4.4 it was found in literature that increased etch depths resulted in stronger coupling of guided modes to the array. The sharp fringes observed in the spectrally resolved PL in figures 5-13(b) and 5-14(b) indicate diffraction.

It is important to note that the numbers in table 5.2 should be considered with caution. With PL, any absolute enhancement will result in an increase in in-coupling as well as light extraction. That is, the light from the PL laser will have a different intensity when it reaches the active region due to the geometry of the structure. Consequently the MQWs will re-emit at a different intensity which compromises the absolute value of F. In the next chapter it will be observed whether the trend of F will be similar in FDTD modelling of these structures.

Table 5.3 summarises the directionality, D, for each nanorod structure using equation (5.2.2) for both integrated emission and emission resolved at 450 nm wavelength. The results are for both azimuths, $\phi = 90°$ and $\phi = 60°$.

From table 5.3, the directionality is largest for the nanorod sample of $\Lambda = 800nm$ albeit only 6% greater than Lambertian emission. The nanorod sample of $\Lambda = 600nm$ displayed directionality extremely similar to Lambertian, deviating by a per cent. This suggests that scattering is the dominant mechanism of light

	$\phi = 90°$		$\phi = 60°$	
Sample	$\boldsymbol{D}$ (Integrated)	$\boldsymbol{D}$ ($\lambda = 450$ nm)	$\boldsymbol{D}$ (Integrated)	$\boldsymbol{D}$ ($\lambda = 450$ nm)
$\Lambda = 1200$ nm	0.87	0.89	0.89	0.88
$\Lambda = 800$ nm	1.06	1.05	1.07	1.05
$\Lambda = 600$ nm	0.99	1.01	0.99	0.96

Table 5.3: *Summary of directionality, D, values for nanorod etched structures relative to Lambertian using equation* (5.2.2).

extraction as these values of D are similar to those obtained from the surface roughened sample. The lowest directionality was obtained for $\Lambda = 1200nm$ with an average value of $D = 0.875$ for integrated emission. Comparison of the SEM images in figure 5-3 with those of figure 5-4 and 5-5 show the nanorods of the $\Lambda = 1200nm$ sample are not closely packed with large facet separation. It is therefore likely that the scattering for the nanorod samples of $\Lambda = 800$ nm and 600 nm arises from the very small spacing between nanorods and their tapered profile. The scattering of the $\Lambda = 1200$ nm may be reduced because of the larger separation/increased order which would impose a larger limitation on the available constructive interferences. The facets between the nanorods would also reduce the light extraction because the light would be reflected back inside the epitaxy. This could explain the reduced enhancement factor observed for the 1200 nm sample in table 5.2.

For further comparison, the spectra of the nanorod samples were plotted as a function of θ for $\phi = 90°$ and $\phi = 60°$ as per figure 5-12. Figures 5-15(a), (b) and (c) display the labelled ϕ slices of the three nanorod samples of $\Lambda = 1200$ nm, $\Lambda = 800$ nm and $\Lambda = 600$ nm respectively.

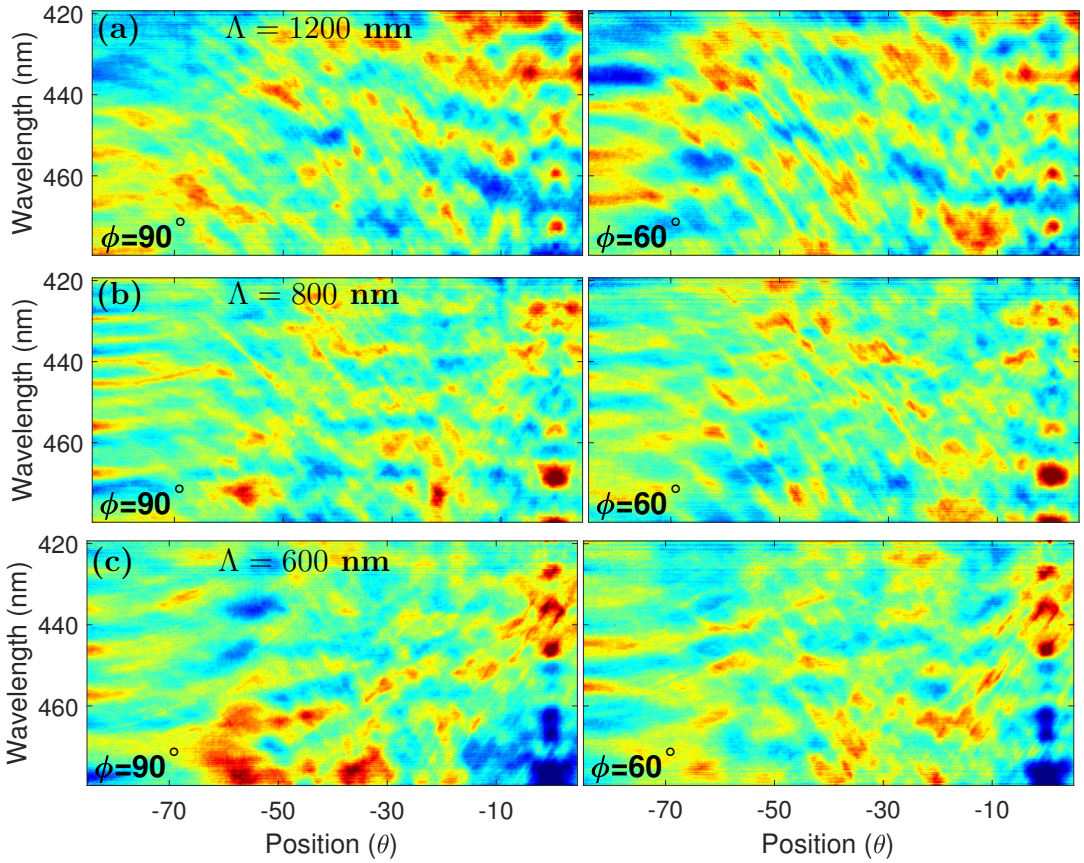

Figure 5-15: *Wavelength vs. elevation angle, θ of angular PL results for fixed $\phi = 90°$ (right) and $\phi = 60°$ (left) obtained for nanorod structure of (a) $\Lambda = 1200$ nm, (b) $\Lambda = 800$ nm and (c) $\Lambda = 600$ nm.*

All of the plots in figure 5-15 are strikingly different to both the planar and roughened structures in figure 5-12. The Fabry-Perot effect is very weak and the emission contains sharp bands of high intensity. These represent diffracted guided modes [14] [16] [17]. There are areas of particular high intensity occurring at 0° for certain wavelengths, which are particularly intense for the $\Lambda = 800$ nm sample. They also appear for the nanorod samples of $\Lambda = 800$ nm and $\Lambda = 600$ nm at around 470 nm wavelength for $\phi = 90°$ in the range $\theta \approx -15° - -60°$. The wavelength separation of these 'hotspots' at 0° indicate they may be due to extracted guided modes coinciding with Fabry-Perot modes resulting in the increased intensity. In figure 5-15(c), the diffraction lines are relatively less sharp for the $\Lambda = 600$ nm which is likely due to more random scattering arising from the increased close packing arrangement and tapered profile of the nanorods.

5.3 Summary

The vertical structure LED device provided by Plessey Semiconductors was presented. Various nanorod arrays were etched onto the surface of the LED using EBL and ICP etching techniques. The morphology of three nanorod etched samples of different pitches, $\Lambda = 1200nm, 800nm, 600nm$ were examined using SEM imaging. From this, the dimensions of the nanostructures could be obtained as listed in table 5.1 and these varied depending on the processing and etching conditions.

Optical characterisation was performed on the planar structure, the structure with surface roughening and the three nanorod-structures identified by the three different pitches. This was achieved by angular PL from which the far-field emission results were obtained for fixed azimuths and varying elevation. Using equations (5.2.2) and (5.2.3), values of directionality, D and enhancement factor, F, could be obtained. The latter value should be considered with caution due to in-coupling in the PL measurement.

The nanorod samples displayed massive enhancement factors relative to the planar structure with values of F ranging 8.62 for $\Lambda = 1200$ nm to 9.80 for $\Lambda = 800$ nm. Maximum directionality was achieved for the nanorod sample of $\Lambda = 800$ nm and which is likely due to strong overlap of diffracted guided modes and Fabry-Perot modes. A dominant behaviour in the nanorod samples is likely due to the scattering of light from the nanostructures, arising from their close packing. This is supported by the lower value of D observed for the $\Lambda = 1200$ nm sample whereby the nanorods had larger separation in the array. The increased spacing may also result in the reduced enhancement factor observed in table 5.2.

In the next chapter this optical characterisation will be used to validate an FDTD model. The model will be set up using the methods discussed in chapter 4. The morphological characterisation obtained from SEM imaging will be used to set up the accurate dimensions of the FDTD structures. Upon developing a reliable model it will be used to further investigate the light propagation mechanisms inside the structures and confirm if effects such as light scattering are responsible for the emission observed in angular PL results.

Chapter 6

FDTD Modelling of Planar Vertical LED Structure

From the previous chapter, obtaining values of the directionality, D, and enhancement factor, F, for different structures is an involved and lengthy process. In the fabrication process for example, obtaining vertical nanorods is not straightforward. Furthermore, there is unreliability from the absolute values of F obtained from PL experiments. Given the many parameters of the nanorod array which can be changed, practically it is not feasible to fabricate a large number of samples to investigate the subsequent effect on D and F.

Modelling the devices with FDTD instead saves time and resources used for fabrication and measuring emission. It can also be used to simulate nanorod structures not practically feasible in the fabrication process and determine if these structures are worth the complexity required to achieve. Absolute values of F and light extraction efficiency, η_{lee} can be obtained because the intensity of the dipole emission in all of the simulated structures will be the same.

In order to develop an FDTD model which accurately predicts the emission, it needs to be corroborated in some way. This can be achieved by comparing experimental results with those obtained from FDTD on the same structures. Discrepancies may be addressed by including more accurate modelling of the materials, more dipole sources and appropriate boundary conditions. This is the subject of the next two chapters where MEEP will be used to simulate the planar and etched structures described in chapter 5. Here, the following will be discussed:

- Simulation which reliably reproduces the PL far-field emission pattern of the planar structure (this chapter).
- Simulation which reliably reproduces the PL far-field emission pattern of the nanorod structures identified by pitch, $\Lambda = 600$ nm, $\Lambda = 800$ nm and $\Lambda = 1200$ nm (chapter 7).

There will likely be discrepancies arising from the differences between the FDTD model and the physical samples, for example the uniformity of nanorod geometry, physical size of the sample compared with simulation size etc. Nevertheless, if an approximate model can be developed which reproduces the overall shape of the emission pattern, the model will still provide much information on the light extraction and light propagation mechanisms occurring inside the structures.

6.1 Modelling of Planar Structure

The unetched vertical structure layout was presented in the previous chapter in figure 5-1 and this was used as the reference to set up an equivalent model in FDTD.

To get the total radiation of the active region, many dipoles of different polarisations and positions within the active region must be simulated individually and then summed. This is a very time-consuming process and can be simplified. From figure 5-1, the active region was 112 nm thick which makes the range of the vertical position of a single dipole source from the silver reflector, z_{src}, to be between 192 and 304 nm, not including the error range in measurement. In previous work on FDTD modelling of vertical LEDs, multiple vertical dipole positions were not considered. Typically a single dipole was placed at the center of the MQW region [98, 99, 104, 105]. However, the presence of the silver reflector will result in the far-field being very sensitive to the vertical position of the source. This can be seen from the array factor in equation (4.1.38) for a horizontal dipole above a ground plane which was briefly introduced in section 4.1.3. No information was provided on the exact positions on the QWs. Given that six InGaN QWs were present with a typical thickness of around 2 to 4 nm thick [162], the QBs were estimated to have a thickness of around 20 nm. Therefore, simulations with dipoles placed at 20 nm increments were made however,

summing the results over the six positions did not result in an improvement of the correlation between the FDTD and experimental PL results. The sensitivity of the far-field on z_{src} is demonstrated in figure 6-1(a) and 6-1(b) which displays the 450 nm spectrally-resolved far-field emission patterns for $z_{src} = 260$ nm and 270 nm respectively.

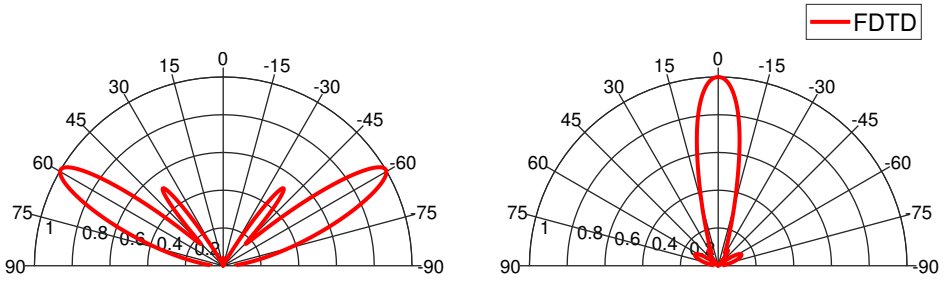

(a) **(b)**

Figure 6-1: *Normalised far-field emission patterns spectrally-resolved at 450 nm for vertical dipole position above reflector, (a) $z_{src} = 260$ nm and (b) $z_{src} = 270$ nm.*

The abrupt change in the far-field emission by incrementing z_{src} by 10 nm indicated that for a justified and reliable model of the emission, more information was required to know the exact dipole locations. Given this and the variation in the dimensions of the layers, three vertical positions of the dipole set as $z_{src} = 190, 250$ and 300 nm which corresponded to the bottom, middle and top of the active region range. It has been reported that for current injection into InGaN QWs, the QW nearest to the *p*-GaN exhibited more light emission because holes have a lower mobility and so there is a tendency for them to accumulate there [163]. For PL however it can be assumed that all of the QWs are excited equally.

The emission of wurtzite InGaN QWs grown along the *c*-axis of the Plessey structure is preferentially polarised in the plane of the QW [32] and so two polarised dipoles perpendicular to the *c*-axis were considered. By setting the *c*-axis to be parallel to the *z*-axis in FDTD, simulations were run for E_x and E_y polarised dipoles. The total radiation intensity, U, was averaged over the two dipoles:

$$U = \frac{U_{E_x} + U_{Ey}}{2} \tag{6.1.1}$$

It is noted that such an assumption has been justified in previous work [164], [165], [97]. Therefore a total of six separate simulations, corresponding to the two polarised dipoles at the three different values of z_{src}, were used to model the incoherent spontaneous emission.

For blue wavelength emission, the center wavelength of the Gaussian emission spectrum, λ_{cen} was set as 450 nm with the half width at half maximum, $\Delta\lambda = 60$ nm in the FDTD model. By setting the normalisation parameter, $a = 100$ nm, λ_{cen} corresponded to a MEEP wavelength and frequency of 4.5 and 0.222 respectively. In order to check the accuracy of the model, comparison of the normalised spectrally-resolved far-field patterns of the experimental PL and simulated FDTD results was made. That is, comparison of the shape of the far-field patterns rather than the absolute intensity. Due to the 10 nm wavelength discrepancy of λ_{cen} between the FDTD and PL (where $\lambda_{cen} = 440$ nm) emission spectra, there will likely be a discrepancy between the integrated wavelength far-field emission patterns of the PL and FDTD.

The FDTD model of the planar structure gradually took into account more complex modelling of the refractive index profile of the planar structure. Figure 6-2(a) shows the initial simulation model in the xz-plane. This was the most simple structure whereby the entire epitaxy was modelled as real dielectric with refractive index, $n = 2.5$ which may be considered the refractive index value of GaN at $\lambda = 450$ nm [166]. The silver reflector was modelled as a PEC boundary condition, the total thickness of the GaN, t_{GaN}, was taken as 2.65 μm and PML thickness was $t_{PML} = 1$ μm. The lateral size of the computational cell was set to be 6×6 μm. The tangential fields were measured at $z_{nf} = 100$ nm above the structure for the near-to-far-field transform (NFFT) and checked every 50 time units for the fields to decay to 1×10^{-5} at this position. The distance from the top of the structure to the $+z$-PML, z_{pad}, was set as 2 μm which was more than sufficient for good absorption from the $+z$-directed PML. The resolution was set as $\Delta x = 20$ nm per Yee cell.

The far-field emission patterns were obtained by applying the NFFT developed in chapter 4 on the tangential near-fields measured in FDTD at position $z = z_{nf}$. Comparison was made of the normalised spectrally resolved experimental PL and FDTD far-field emission patterns between the wavelengths 420 to 480 nm in 5 nm increments.

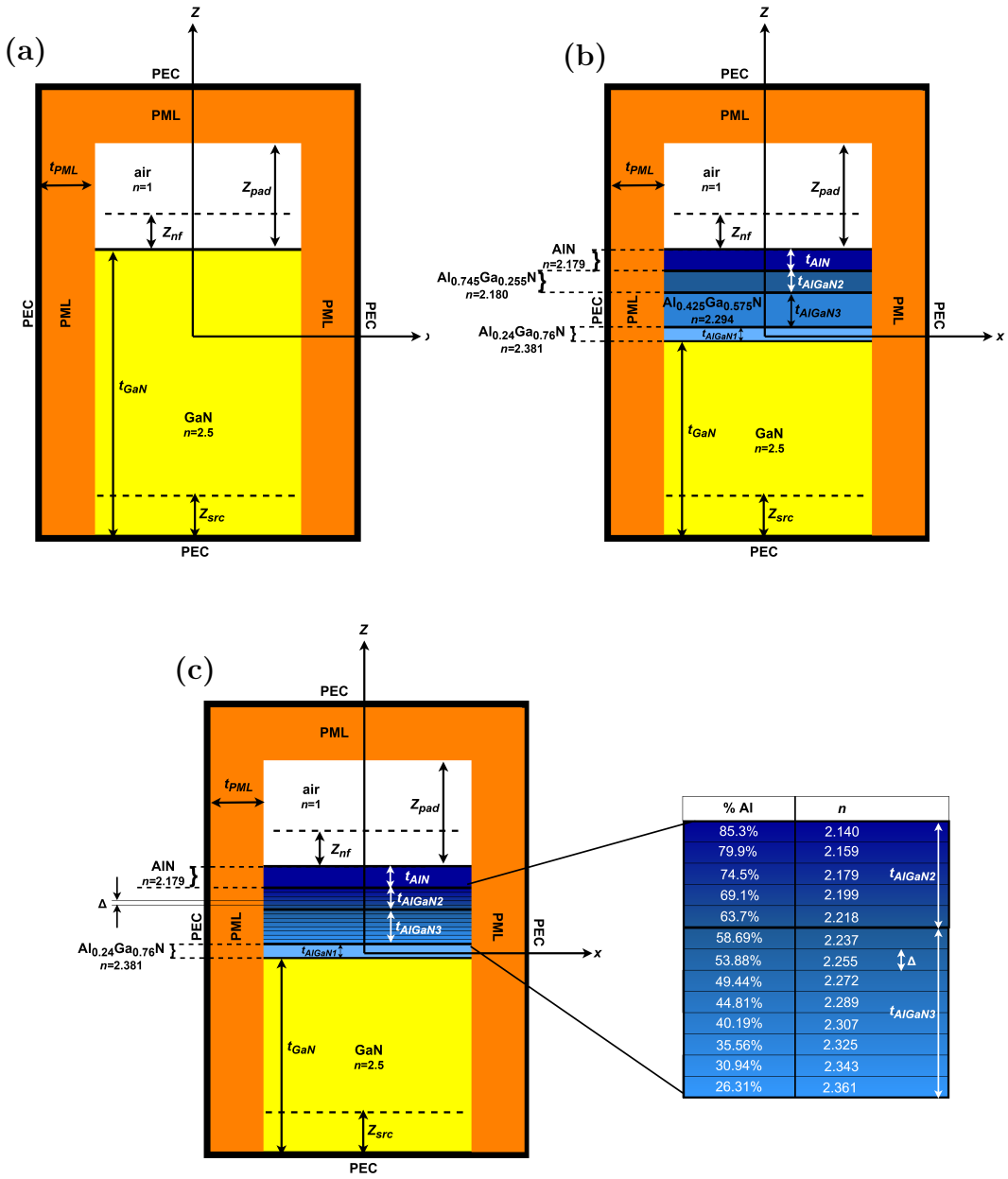

Figure 6-2: *Development of FDTD model of planar vertical structure using real dielectrics. In (a) all of the epitaxy was modelled using an average $n = 2.5$. In (b) the AlGaN and AlN refractive index layers were included, averaging the graded AlGaN. In (c) the graded AlGaN was subdivided into smaller layers of thickness $\Delta = 40nm$.*

For the next iteration, the model shown in figure 6-2(b) was simulated. Here, the refractive indices of the AlGaN and AlN layers were included, again modelled by real dielectrics. The optical properties of AlGaN will vary with Al composition. For the linear graded AlGaN layers of the structure in figure 5-1, the average Al mole fraction was taken for the calculation of the refractive index value. Thus the 61-24% graded AlGaN was approximated as 42.5% and for the 88-61% grading, an average of 74.5% Al content was used. The 24% Al composition layer is not graded. The model in [167] was taken to calculate the refractive index:

$$n(\lambda) = \sqrt{A + \frac{\lambda^2}{\lambda^2 - B}} \tag{6.1.2}$$

Where λ is assumed to be in units of μm. The parameters A and B are a function of the fraction of Al, x, in the $Al_xGa_{1-x}N$ alloy and are given by:

$$A(x) = 4.27 - 1.07x \tag{6.1.3a}$$

$$B(x) = 0.092 - 1.065x \tag{6.1.3b}$$

Assuming $\lambda = 450$ nm, values of $n = 2.381, 2.294$ and 2.180 for the layers with 24%, 42.5% and 74.5% respectively were obtained. The vertical dimensions of the three layers were set as $t_{AlGaN1} = 130$ nm, $t_{AlGaN2} = 320$ nm and $t_{AlGaN3} = 200$ nm respectively. The refractive index of AlN was taken from [168] for $\lambda = 450$ nm and its thickness set as $t_{AlGaN} = 200$ nm.

For the third iteration, the model shown in figure 6-2(c) was simulated. Here, the linear graded AlGaN layers were subdivided into smaller layers of length $\Delta = 40$ nm to provide a more accurate modelling of the grading. Each sub-layer was modelled as a real dielectric of refractive index value obtained from equation (6.1.2), assuming 450 nm wavelength. A list of the values of n for each sublayer and the Al mole fraction assumed is included in figure 6-2(c).

For the models in figure 6-2(a-c), no correlation between the far-field results obtained from FDTD and PL was found. Additional simulations taking into account the error in measured thickness of the layers were performed but with no success. It appeared a more accurate dielectric profile of the layers was required.

6.1.1 Including Dispersion Properties

To accurately model the dispersive optical properties of GaN, reference [169] was used to simulate the ordinary ray of GaN where the real part of the permittivity is described in terms of the energy, E in units of electron-volts:

$$\epsilon_r(E) = 1 + \frac{2}{\pi}\left(\frac{A_0}{2}\ln\frac{E_1^2 - E^2}{E_0^2 - E^2} + \frac{A_1 E_1}{E_1^2 - E^2}\right) \tag{6.1.4}$$

$A_0 = 1.837$
$E_0 = 3.450\text{eV}$
$A_1 = 40.65\text{eV}$
$E_1 = 8.175\text{eV}$

In MEEP, the Lorentz model is written slightly differently than in section 3.4 as the following:

$$\epsilon = \left(1 + \frac{j\sigma_D}{\omega}\right)\left[\epsilon_\infty + \sum_m \frac{\sigma_m \omega_m^2}{\omega_m^2 - \omega^2 - j\omega\gamma_m}\right] \tag{6.1.5}$$

Where σ_D is the electrical conductivity.

To convert equation (6.1.4) to the MEEP format, the real part of equation (6.1.5) was fitted to equation (6.1.4) using Matlab. A single Lorentzian function ($m = 1$) was sufficient to model GaN dispersion. To find the real part of equation (6.1.5) the following was performed:

$$\epsilon = \epsilon_\infty + \frac{\sigma_1\omega_1^2}{\omega_1^2 - \omega^2 - j\omega\gamma_1} + \frac{j\sigma_D}{\omega}\left(\epsilon_\infty + \frac{\sigma_1\omega_1^2}{\omega_1^2 - \omega^2 - j\omega\gamma_1}\right)$$

Excluding terms multiplied by j and multiplying the denominator of the second term by the complex conjugate, after some algebra:

$$\begin{aligned}\epsilon_r &= \epsilon_\infty + \frac{\sigma_1\omega_1^2\left(\omega^2 - \omega_1^2\right)}{\omega^4 + \omega^2\left(\gamma_1^2 - 2\omega_1^2\right) + \omega_1^4} \\ &= \epsilon_\infty + \frac{a(b-x)}{x^2 + (c-2b)x + b^2}\end{aligned} \tag{6.1.6}$$

Where:

$$a = \sigma_1 \omega_1^2; \qquad b = \omega_1^2; \qquad c = \gamma_1^2; \qquad x = \omega^2 \tag{6.1.7}$$

Figure 6-3 shows the curve fit of equation (6.1.6) to (6.1.4) from which values of a, b, c and ϵ_∞ were obtained. Using the relations in equation (6.1.7) values of σ_D, σ_1, γ_1 and ω_1 were extracted. Note the values of the frequencies are in units of electron volts. To convert to MEEP units, these were first expressed in angular frequency and then divided by $\frac{2\pi c}{a}$ as was discussed in section 3.5.1. The table in figure 6-3 lists the extracted values both in SI and MEEP units for the parameters describing the dispersion of GaN.

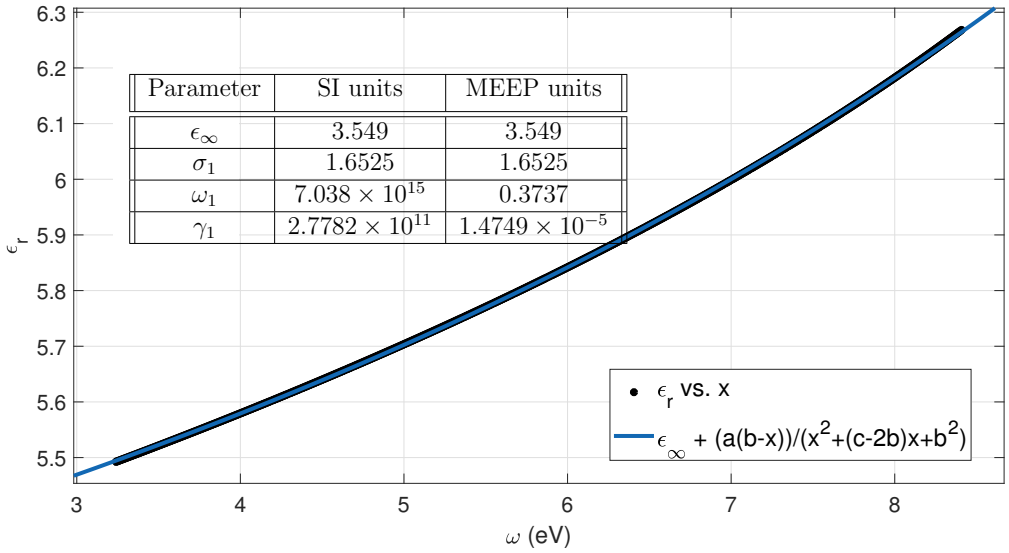

Parameter	SI units	MEEP units
ϵ_∞	3.549	3.549
σ_1	1.6525	1.6525
ω_1	7.038×10^{15}	0.3737
γ_1	2.7782×10^{11}	1.4749×10^{-5}

Figure 6-3: *Fitting of equation* (6.1.6) *(blue) to the GaN dispersion relation in* (6.1.4) *(black) taken from [169]. The table inset lists the Lorentzian paramters in SI units and MEEP units*

The simulation campaign was repeated by modelling the entire epitaxy as dispersive GaN with a PEC in place of the silver reflector which is shown in figure 6-4.

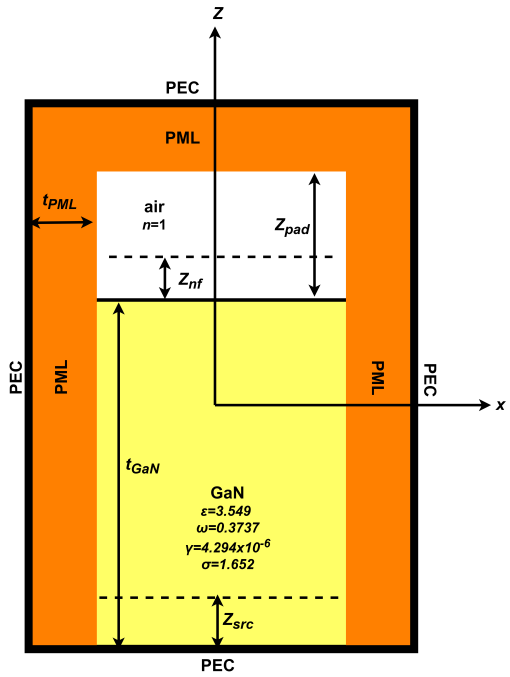

Figure 6-4: *(a) Simulation model where the model in figure 6-2(a) included the dispersive properties of GaN using [169].*

Using the same dimensions as those used in figure 6-2(a) no obvious correlation between the emission patterns obtained from PL and FDTD could be observed. When the thickness of the GaN, t_{GaN} was increased from 2.65 μm to 2.7 μm however, the fit between the simulation and experiment was improved for short wavelengths. This is shown in figure 6-5 which compares the normalised spectrally-resolved far-field emission patterns and the integrated emission from 420 nm to 480 nm in 5 nm increments.

From figure 6-5, far-field emission patterns obtained from FDTD and experimental PL are in very good agreement for emission wavelengths 420 to 445 nm. For these wavelengths, the overall emission pattern is obtained. At 450 nm wavelength, the main lobe observed at 0° in the PL measurement is suppressed in the FDTD simulation. For longer emission wavelengths, the correlation drops suddenly. This manifests in the integrated far-field emission of the FDTD simulation not reproducing the vertical emission observed for the PL result.

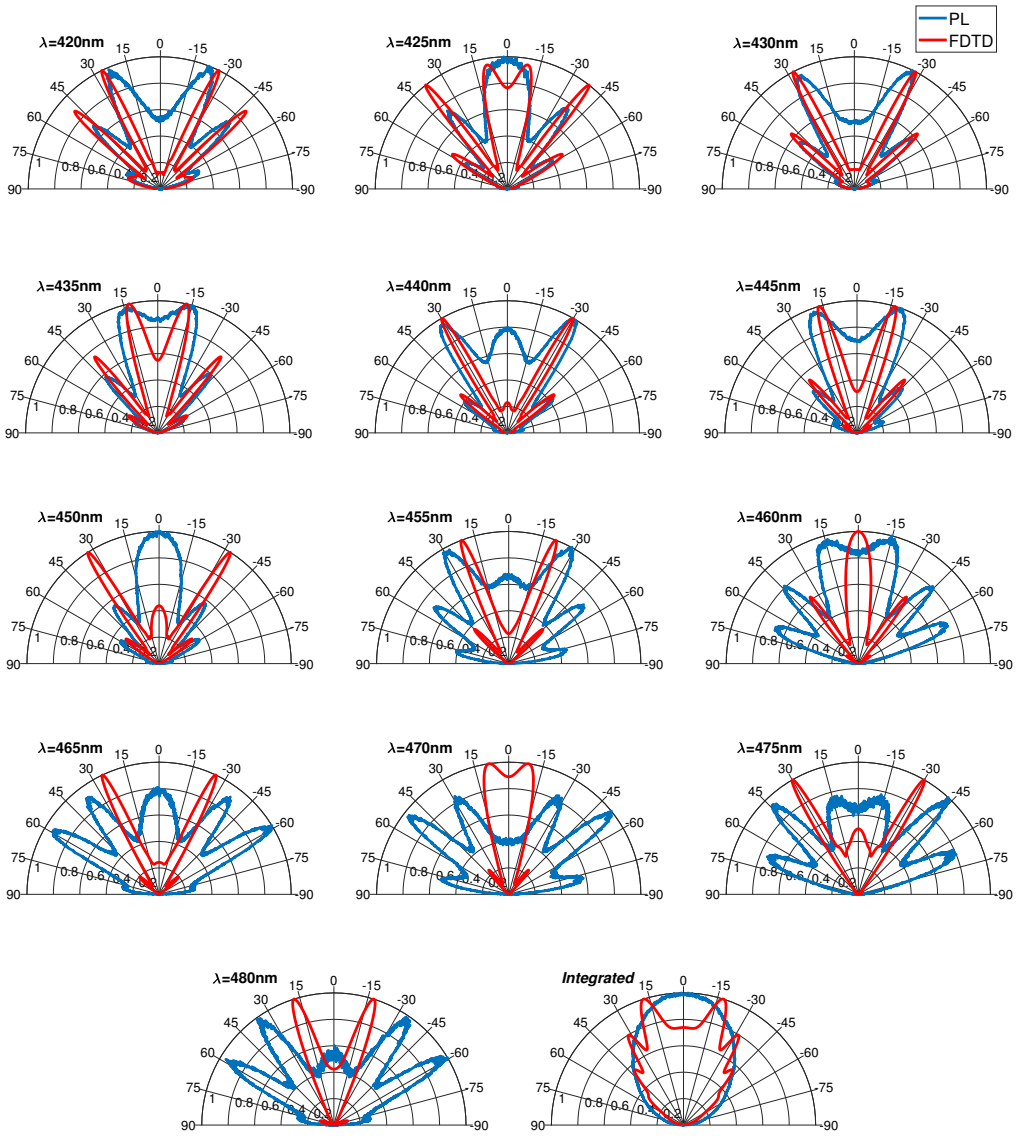

Figure 6-5: *Comparison of PL and FDTD normalised far-field emission patterns obtained from the model in figure 6-4 for spectrally-resolved wavelengths and integrated over emission.*

Due to the abrupt decline of the fits between the far-field emission patterns obtained from FDTD and PL, some further investigation appeared to show a possible 35 nm wavelength discrepancy between FDTD simulation and PL experiment. This is made clearer in figure 6-6 where the angular PL results spectrally resolved at λ_{PL} are compared with simulated FDTD resolved at $\lambda_{PL} + 35$ nm.

Here it is observed that the 35 nm shift allows accurate prediction of the far-field emission pattern. Due to the limitation of the emission spectrum width, comparison for the other wavelengths could not be made. The thickness of the GaN was increased within the estimates of the dimensions from figure 5-1 to $2.5 - 2.9$ μm which reduced the discrepancy to 30 nm.

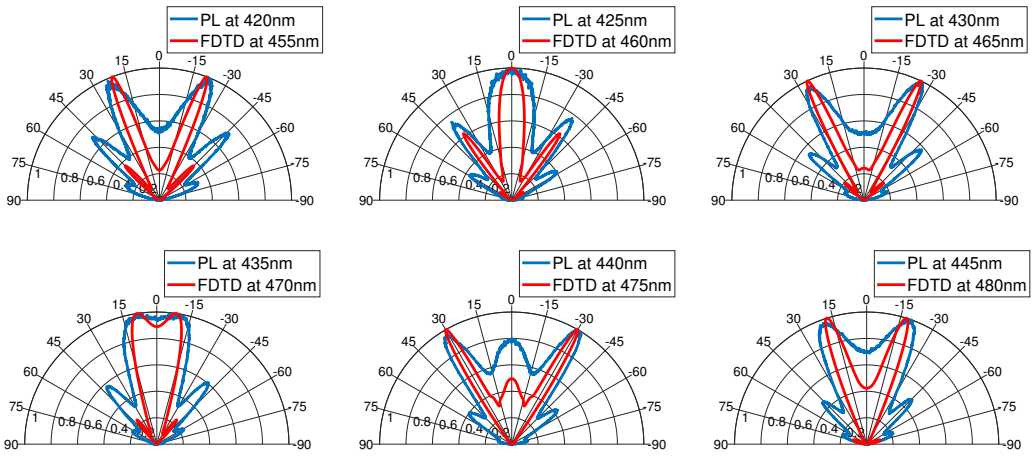

Figure 6-6: *Comparison of PL and FDTD normalised far-field emission patterns obtained from the model in figure 6-4 demonstrating a 35nm discrepancy between PL and FDTD emission wavelength.*

To more accurately model the optical thickness of the structure, the different refractive indices of the AlGaN layers had to be taken into account.

For the next iteration the dispersive properties of AlGaN were modelled using the equations (6.1.2) and (6.1.3) [167]. Taking the same method for modelling the dispersion of GaN, equation (6.1.2) was fitted to equation (6.1.6) after converting from wavelength in μm to electron volts. The average Al % composition for the graded AlGaN layers was used as the value of x for the A and B parameters of equation (6.1.3). Table 6.1 summarises the Lorentizian parameters extracted using the relations of (6.1.7) for the layers of $Al_{0.24}Ga_{0.76}N$, $Al_{0.425}Ga_{0.575}N$ and $Al_{0.745}Ga_{0.255}$. They are expressed in both SI and MEEP units.

The FDTD set-up which incorporates the AlGaN dispersive model is shown in figure 6.1.3(a).

$Al_{0.24}Ga_{0.76}N$			$Al_{0.425}Ga_{0.575}N$		$Al_{0.745}Ga_{0.255}$	
Parameter	SI units	MEEP units	SI units	MEEP units	SI units	MEEP units
ϵ_∞	4.013	4.013	3.815	3.815	3.473	3.473
σ_1	1	1	1	1	1	1
ω_1	6.815×10^{15}	0.3618	7.424×10^{15}	0.3941	9.025×10^{15}	0.4791
γ_1	3.014×10^{11}	1.601×10^{-5}	4.677×10^{12}	2.483×10^{-4}	5.802×10^{11}	3.08×10^{-5}

Table 6.1: *Summary of parameters used for the modelling of the dispersive properties of the AlGaN layers using [167] expressed in SI units and MEEP units.*

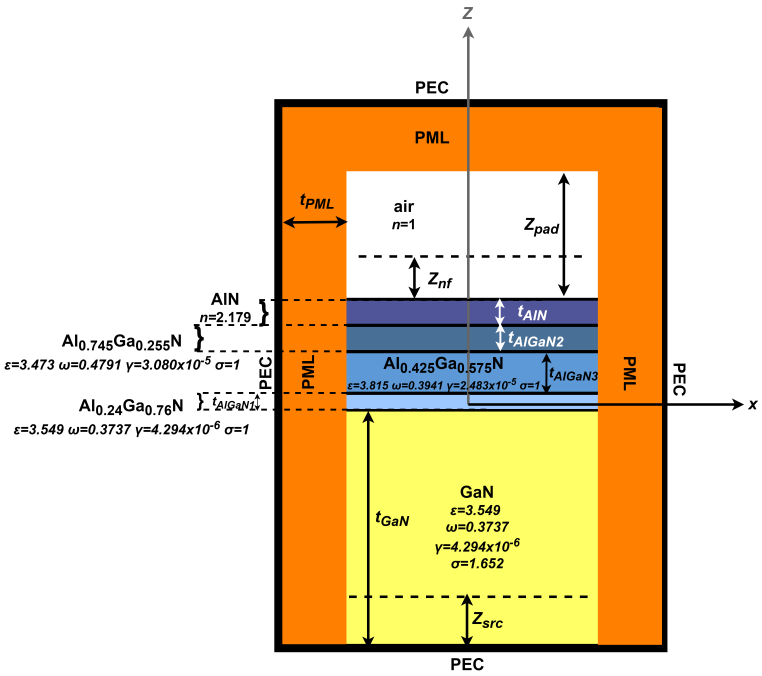

Figure 6-7: *(a) Simulation model where the model in figure 6-4 included AlN and the dispersive properties of AlN and the dispersive properties of AlGaN using [167].*

Including these layers appeared to reduce the discrepancy in wavelength between the FDTD and PL far-field patterns to 5 nm. However, at longer wavelengths greater than 460 nm the patterns deviated further. From the discussion on the slab waveguide in section 2.3.2, for a fixed thickness of the slab, as the wavelength of the guided mode is increased the mode approaches cut-off. The deviation of the simulated and measured results at longer wavelength may be due to the simulated structure thickness being less than the actual thickness of the sample. As a result it is possible that a mode may be approaching cut-off

in the FDTD which would not occur in the experiment. The total thickness of the epitaxy was increased by 50 nm which is within the error range of the physical sample's dimensions. The subsequent FDTD emission patterns displayed improved fits with those obtained from PL measurement. Figure 6-8 compare the normalised spectrally-resolved far-field emission patterns and the integrated emission from 420 nm to 480 nm in 5 nm increments. From these it is observed that there is fairly good reproduction of the PL emission pattern obtained by FDTD. There is still some deviation for wavelengths at 470 nm and longer, particularly at $\lambda = 475$ nm. Integrated emission shows a similarly good fit given the discrepancy in λ_{cen}, however some rippling can be observed in the FDTD results.

In all of the previous simulations the silver was modelled as a PEC boundary condition. To investigate the effect of including its dispersive properties, the parameters from [170] were taken. Here the model of silver is described by five Lorentzian components and one Drude component which are directly provided so a straightforward conversion into MEEP units is required.

The thickness of the silver was set to be 100 nm which was found to be the smallest value in which all of the light was reflected. A significant issue of taking into account silver's disperision properties was the massive increase in computation time due to the inclusion of the six polarisations and increase in resolution from 20 nm to 8 nm per Yee cell. This higher resolution was required to ensure a small enough Δt for the high frequency component in silver's dispersion model and prevent instabilities. It was found that simulation time increased from around 39 minutes to almost 2.5 days for a single run.

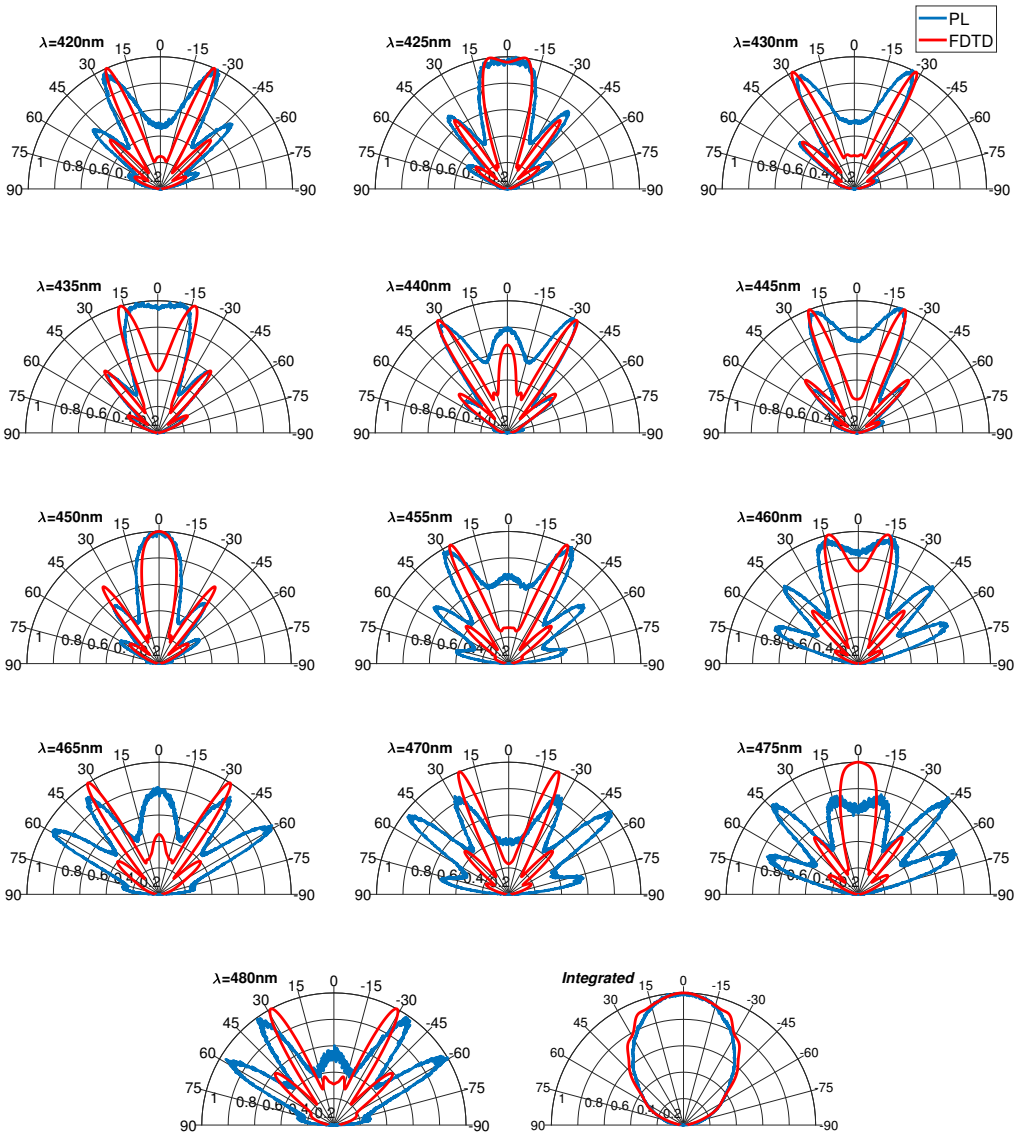

Figure 6-8: *Comparison of PL and FDTD normalised far-field emission patterns obtained from the model in figure 6-7 for spectrally-resolved wavelengths and integrated over emission.*

Moreover and most importantly, the comparison between the far-field emission patterns of PL and FDTD was not improved and in fact was worsened. This is exhibited by the spectrally-resolved far-field emission patterns in figure 6-9 where the integrated emission is also included. Here, the results were obtained by including the dispersion properties of AlGaN and GaN. Consequently silver

was not modelled or further investigated in future simulations.

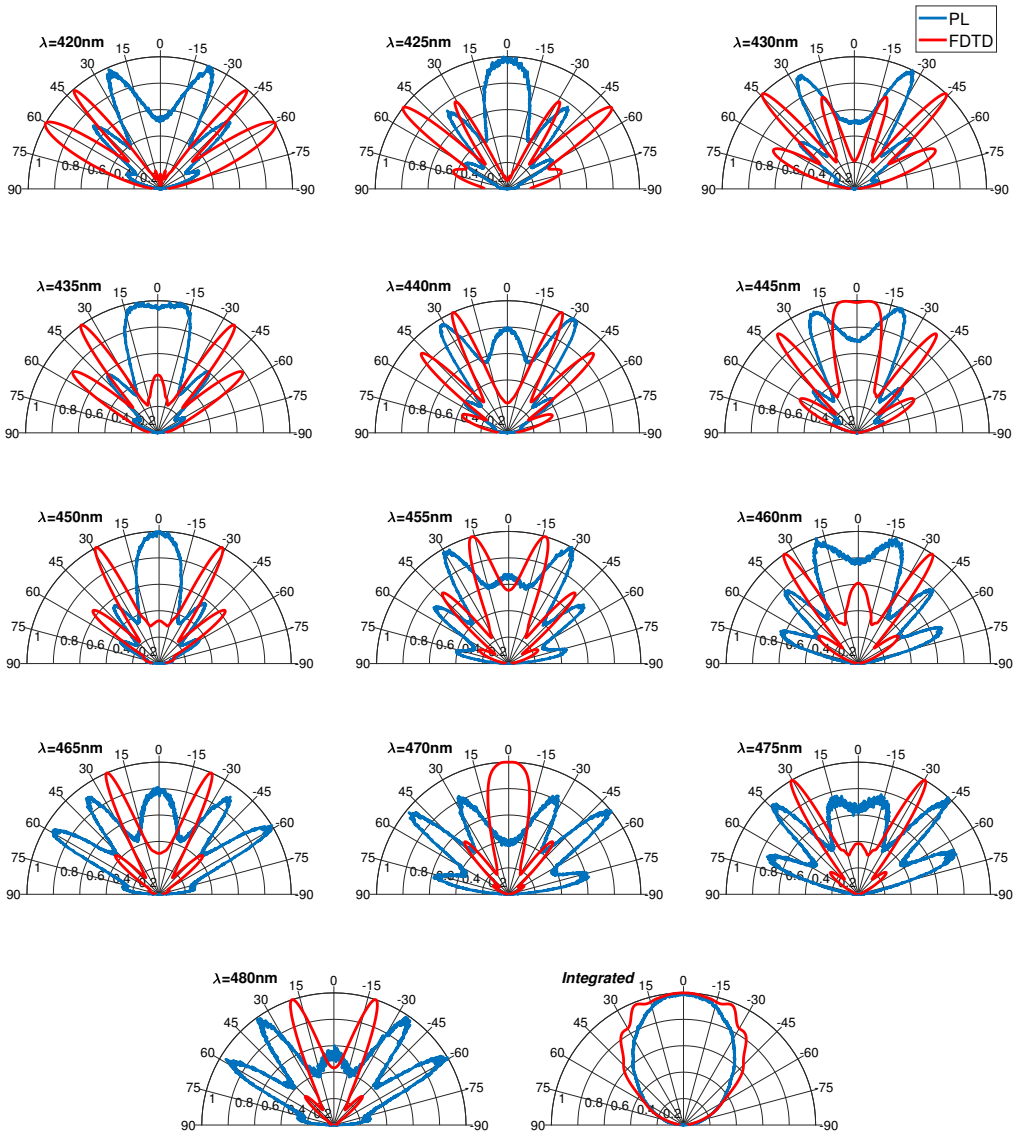

Figure 6-9: *Comparison of PL and FDTD normalised far-field emission patterns obtained from the model in figure 6-7 and including the dispersive properties of silver using the method in [170] for spectrally-resolved wavelengths and integrated over emission.*

6.1.2 PML Issues

Initially it was found that when the entire epitaxy was modelled as dispersive GaN in figure 6-4(a) there were large fields strongly localised inside the PML of thickness, $t_{PML} = 1$ μm. This can be observed in figure 6-10(a) which shows the real part of the E_x field distribution spectrally resolved at 450 nm for a quadrant in the xy-plane taken at $z = z_{nf}$. The near-fields were plotted on a decibel scale $20 \log |E_x(x, y, \omega)|$. This demonstrates that the PML is not working as intended. The effect was not realised until observation of the near-fields because the PML was not included in the xy-plane spatial range input to the near-to-far-field transform.

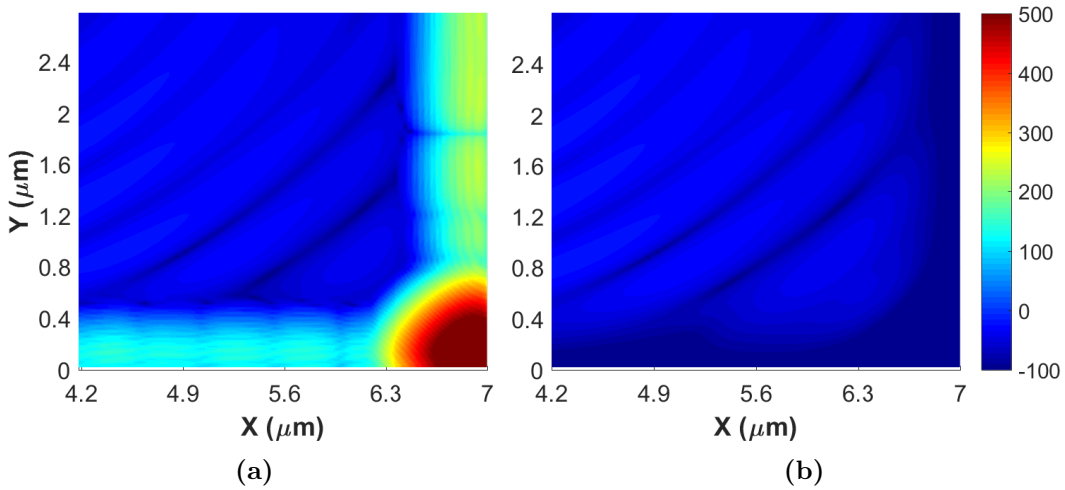

Figure 6-10: *xy-plane quadrant of near-field distribution of real part of E_x field at $z = z_{nf}$ for PML strength of (a) 1.0 and (b) 0.5 spectrally resolved at 450 nm wavelength.*

It has been stated that instabilities can occur when the PML overlaps dispersive media in MEEP (MEEP FAQs 2013) and the field diverges inside the PML. From figure 6-10(a), the divergence appears strongly localised inside the corners of the computational cell: the magnitude of the field inside the PML is around 100 dB but at the corners this is around 470 dB. Any one of the following actions appeared to removed the effect in figure 6-10(a):

- Reducing the strength of the PML from 1.0 (default) to 0.5

- Increasing PML thickness to 1.6 μm
- Increasing resolution from 20 nm/cell to 10 nm/cell
- Replacing the PML with an absorber of same thickness and using same resolution

By changing any one of the first three parameters accordingly, the PML is being 'turned on' more slowly. The effect was alleviated by shifting the dipole source off center by several nanometers. Figure 6-10(b) shows how the effect is removed by reducing the PML strength from 1.0 to 0.5.

It has been found that for the uniaxial PML (UPML) discussed in section 3.3.2, a long time linear growth of the fields can occur inside the PML. In reference [171] the fields remain localised inside the PML and no energy can exit normally into the interior non-PML region. The energy propagates along the PML and is absorbed at the corners which is what is observed in figure 6-10(a). In reference [172] the same long-time behaviour is observed but the fields leak into the interior. It was suggested in the study of [171] that this was because the Yee scheme in [172] did not follow a discrete form of Poynting's theorem [173]. The growth inside the PML was postponed by increasing the resolution which indicates truncation errors contribute to the divergence of the fields inside the PML. The instability could also be alleviated by having the σ profile of the PML as constant but this caused reflections in the simulation which manifested in the far-field emission patterns.

From [171], the divergence occurs when, as $t \to \infty$, the fields inside the PML are constant such that the transverse derivatives are zero. Referring to figure 6-10, taking a wave with an H_y field component which is transverse to the x-directed PML and using the notation of [171] one can write:

$$\partial_y^2 H_z = 0$$

This has the linear solution, $H_z = -H_z y + C$ and so a linear growth will be observed. The linear growth as $t \to \infty$ is removed by including an additional term, $\alpha > 0$, in the implementation of the PML (see section 3.3.2):

$$s_x = 1 + \frac{\sigma_x(z)}{\alpha - j\omega}$$

MEEP however does not appear to support this implementation and so there is the possibility of late-time instability for any type of material. Due to the localised nature of the instability, it was ensured the PML was not included in the NFFT. A PML thickness of 1 μm and strength of 0.5 was used as a compromise between accuracy (PML being less reflective than an absorber) and computation time (using a thinner PML).

6.1.3 Final Model

To observe if an improved fit could be obtained from modelling the graded AlGaN, the model for these layers in the previous simulation in figure 6-2(c) was taken and combined with the modelling of dispersive GaN in figure 6-4. This set up is shown in figure 6-11.

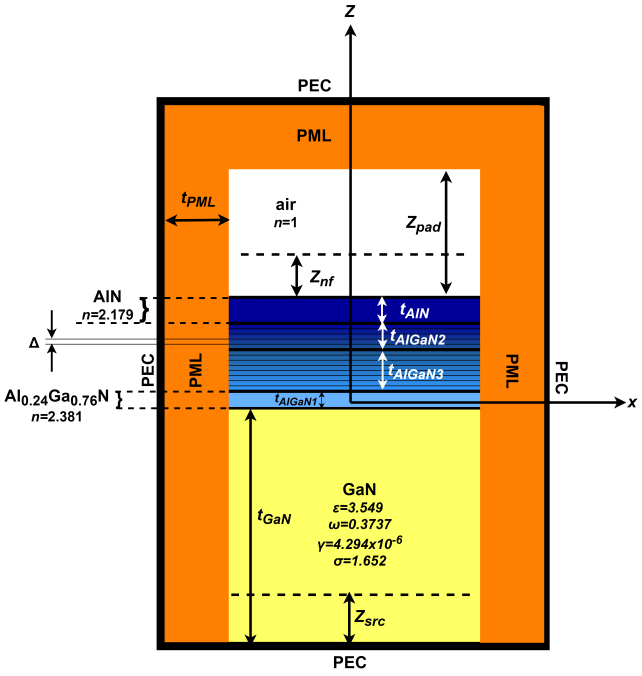

Figure 6-11: *(a) Final simulation model which combined graded AlGaN layers modelled in figure 6-2(c) and dispersive GaN in figure 6-4.*

Figure 6-12 show the spectrally-resolved far-field emission patterns comparing experimental PL and the FDTD results obtained from the simulation of the model in figure 6-11. The integrated emission is also included. From these, there is relatively little difference to the results presented in figure 6-8 of the model in

figure 6-7 where the dispersive properties of AlGaN are included. However, when the FDTD modelling included both the dispersive nature of AlGaN with three layers and alloy grading, the simulated far-fields showed improved fits for $\lambda = 475$ nm and 480 nm in the angular region $\pm 15^{\circ}$ from the vertical. It is also noted in figure 6-12, the emission at $\lambda = 440$ nm for the model in figure 6-11 is reproduced almost perfectly. Discrepancies are likely due to the limited lateral size of the FDTD model which restricted the angular range of the far-field emission pattern. For the longer wavelengths in figure 6-12, the more extreme sidelobes in the emission patterns are not modelled as accurately. It is possible the accuracy of the dispersion relations modelling the dielectrics breaks down for longer wavelengths and the NFFT which is not optmised for capturing extreme sidelobe emission (see section 4.1.3). Furthermore, it was observed the wavelength discrepancy between FDTD and PL was removed by increasing the total thickness of the epitaxy from 2.65 μm to 2.7 μm, indicating sensitivity of the far-field emission on the geometry of the structure. Given the error range in the dimensions of the layers in the Plessey structure in figure 5-1 presented in section 5.1.1, this is another likely cause in the error observed between the PL and FDTD emission results.

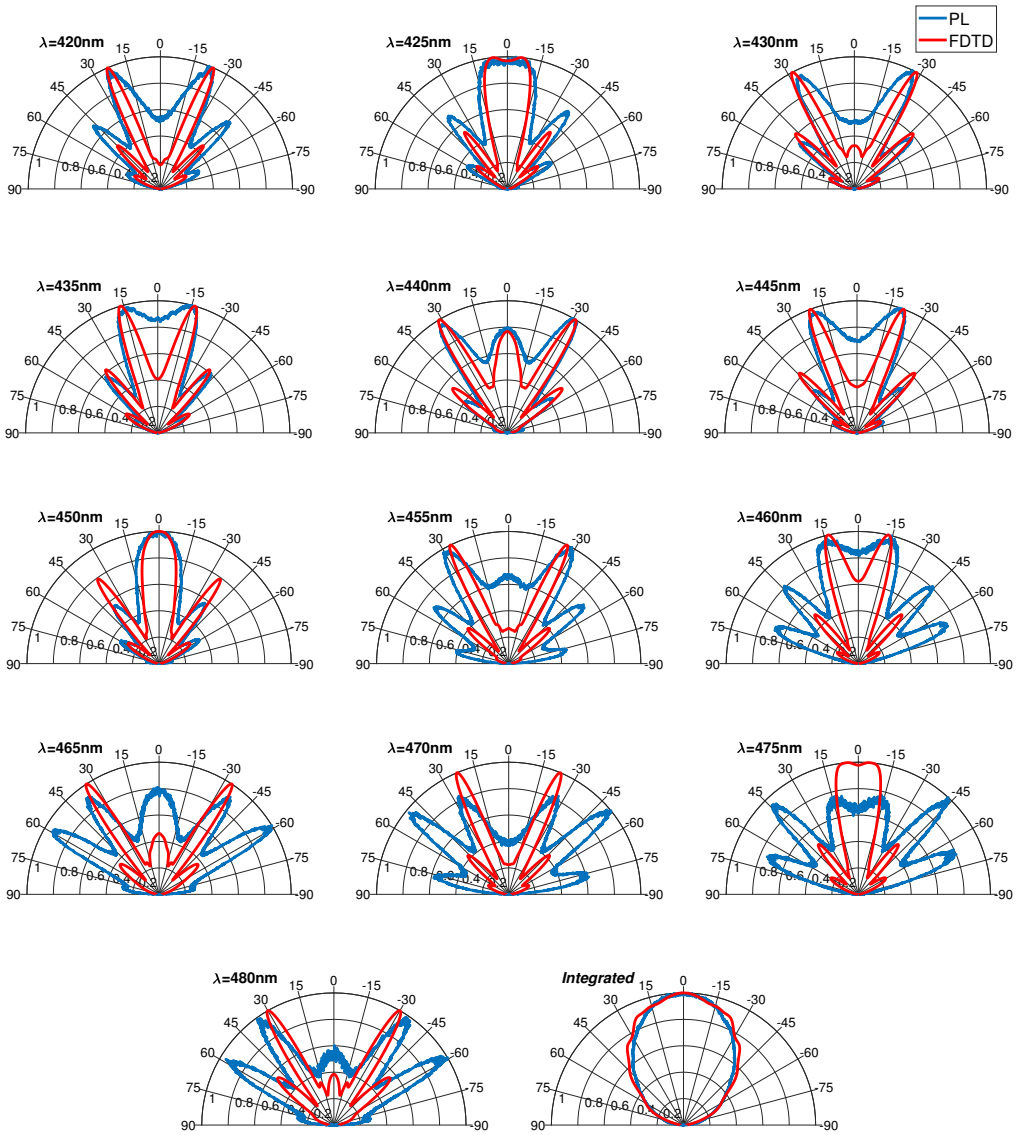

Figure 6-12: *Comparison of PL and FDTD normalised far-field emission patterns obtained from the model in figure 6-11 for spectrally-resolved wavelengths and integrated over emission.*

Therefore, after various optimizations presented, the set-up of figure 6-11 was selected as the final model to represent the planar structure in figure 5-1.

Equation (5.2.2) was used to calculate the directionality, D, of the FDTD emission pattern relative to Lambertian emission for a fixed azimuth, $\phi = 90°$

and this is repeated below:

$$D = \frac{\int_0^{15} \bar{U}|_{pla.}(\theta)\ \mathrm{d}\theta}{\int_0^{15} \bar{U}|_{lam.}(\theta)\ \mathrm{d}\theta} \tag{6.1.8}$$

From equation (6.1.8), D is defined within $\pm 15°$. Table 6.2 gives the value of D as a function of the three vertical dipole positions, z_{src} = 190 nm, 250 nm and 300 nm, and the sum of them is also indicated. The values obtained from experimental PL are included for comparison.

FDTD				**PL**	
$\boldsymbol{z_{src}}(nm)$	$\boldsymbol{D}$ (Integrated)	$\boldsymbol{D}$ ($\lambda = 450nm$)	$\boldsymbol{\eta_{lee}}(\%)$	$\boldsymbol{D}$ (Integrated)	$\boldsymbol{D}$ ($\lambda = 450nm$)
190	1.54	2.17	2.11	x	x
250	0.47	0.48	4.35	x	x
300	1.25	1.76	6.34	x	x
Sum	1.14	1.44	4.27	1.18	1.47

Table 6.2: *Comparison of directionality, D, for planar structure modelled in FDTD (figure 6-11) for the three vertical dipole positions, z_{nf}, and the sum, and those obtained from PL using equation* (6.1.8).

From table 6.2, the sensitivity of D on the vertical height of the dipole above the reflector was clearly observed. Excellent agreement between simulated and measured directionality at both 450 nm and integrated wavelength are due to the FDTD model reproducing the emission patterns shown in figure 6-12. The slight discrepancy between the integrated emission obtained from the PL and FDTD is due to the small 'rippling' effect observed for the integrated emission in figure 6-12.

In the NFFT, a full hemispherical far-field emission pattern was obtained. Figures 6-13(a) and 6-13(b) display the unnormalised three-dimensional far-field emission patterns of the planar structure spectrally-resolved at 450 nm and integrated over wavelength emission respectively.

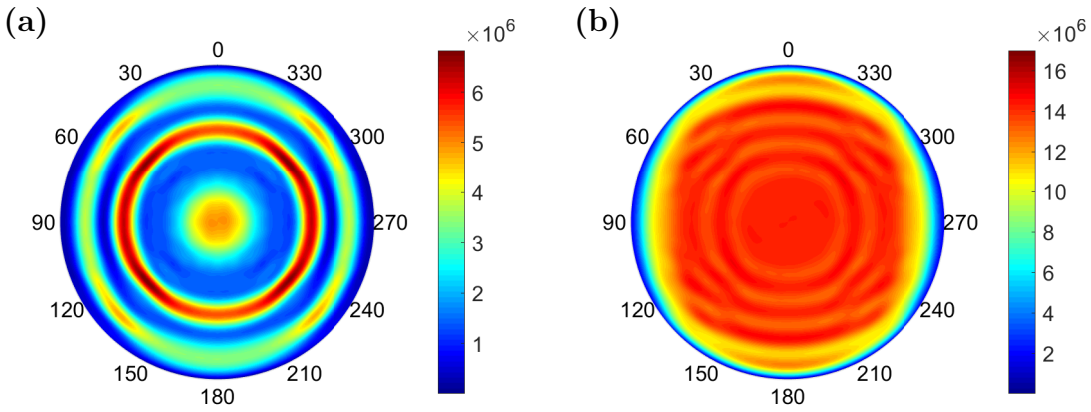

Figure 6-13: *3D unnormalised hemispherical far-field emission patterns spectrally resolved at (a) 450nm and (b) integrated over wavelength for planar structure.*

At 450 nm emission wavelength in figure 6-13(a) concentric rings can be observed indicating Fabry-Perot resonances where strong constructive interference occurs. For the integrated emission, this effect is relatively weak. For the integrated wavelength emission patterns in figure 6-12 comparing FDTD simulation and experimental PL, this effect is not observed in the PL emission results which indicates this effect may be due to reflections in the computational cell.

By integrating all or part of the hemisphere in figure 6-13 over solid angle, power values can be calculated. The definition of directionality in section 4.4 is repeated here as:

$$D = \frac{\int_0^{360}\int_0^{15} \bar{U}|_{PhC}(\theta,\phi)\sin(\theta)\ \mathrm{d}\phi\,\mathrm{d}\theta}{\int_0^{360}\int_0^{15} \bar{U}|_{pla.}(\theta,\phi)\sin(\theta)\ \mathrm{d}\phi\,\mathrm{d}\theta} \tag{6.1.9}$$

Equation (6.1.9) gives the ratio of the normalised P_{ext} to the normalised P_{ext} of Lambertian emission within $\pm 15°$ elevation emission cone from the normal and integrated over azimuth, ϕ.

Using equation (6.1.9) values of $D = 1.14$ for integrated emission and $D = 1.54$ at 450 nm wavelength relative to Lambertian emission were calculated. In terms of the enhancement dependence on z_{src} it was found that the maximum light output power was obtained for $z_{src} = 300$ nm where the power was a factor of 2.57 greater than $z_{src} = 190$ nm and 1.48 greater than $z_{src} = 250$ nm for integrated wavelength emission. The light output power for the dipole at $z_{src} = 300$ nm

contributed to 48% of the total light output of the three vertical dipole positions.

The light extraction efficiency, η_{lee} is also listed in table 6.2 and was calculated using equation (4.2.1) in section 4.2 which is rewritten here:

$$\eta_{lee} = \frac{P_{ext}}{P_{in}} \tag{6.1.10}$$

The dipole power, P_{in}, was calculated using the method decribed in section 4.2. The extracted power P_{ext} was calculated from the tangential fields measured at $z = z_{nf}$ in the NFFT.

When the dipole was placed at $z_{src} = 300$ nm, the value of η_{lee} was three times greater than for the dipole at $z_{src} = 190$ nm. The average $\eta_{lee} = 4.27\%$ was obtained which indicated that most of the light remains trapped inside the device.

Figures 6-14(a-c) show the real part of the E_x field distribution in the xz-plane for a single dipole placed at $z_{nf} = 190$ nm, 250 nm and 300 nm respectively, spectrally resolved at 450 nm. Figures 6-14(d-e) show the corresponding xy-plane at $z = z_{nf}$ above the planar structure. From the xz-planes the interference of the reflection from the PEC mirror and the dipole can be clearly seen to be a function of z_{src}. These fields are modulated by many closely spaced fringes which are often termed Fabry-Perot fringes as per the discussion in section 2.4.3. From the number of fringes at normal incidence inside the cavity, the average refractive index was calculated to be around 2.33. The xy-planes display the concentric rings characteristic of a Fabry-Perot interferometer. These appear relatively more intense for $s_{zrc} = 300$ nm in figure 6-14(f). In the corresponding xy-plane in figure 6-14(c) the constructive interference between the dipole and reflected fields normal to the x-axis is present. From the array factor of a horizontal dipole above a ground plane in section 4.1.3, this is maximum when z_{src} is an integer number of quarter wavelengths inside the medium. The relatively large field intensity incident at zero degrees contributes to the much higher extraction efficiency because it is less than the critical angle. This explains the reduced light extraction for $z_{src} = 250$ nm where there is destructive interference at normal incidence inside the epitaxy. The lowest η_{lee} for $z_{src} = 190$ nm which shows a narrower and less intense beam at normal incidence and the majority of the direct light at the larger incidence angle is reflected.

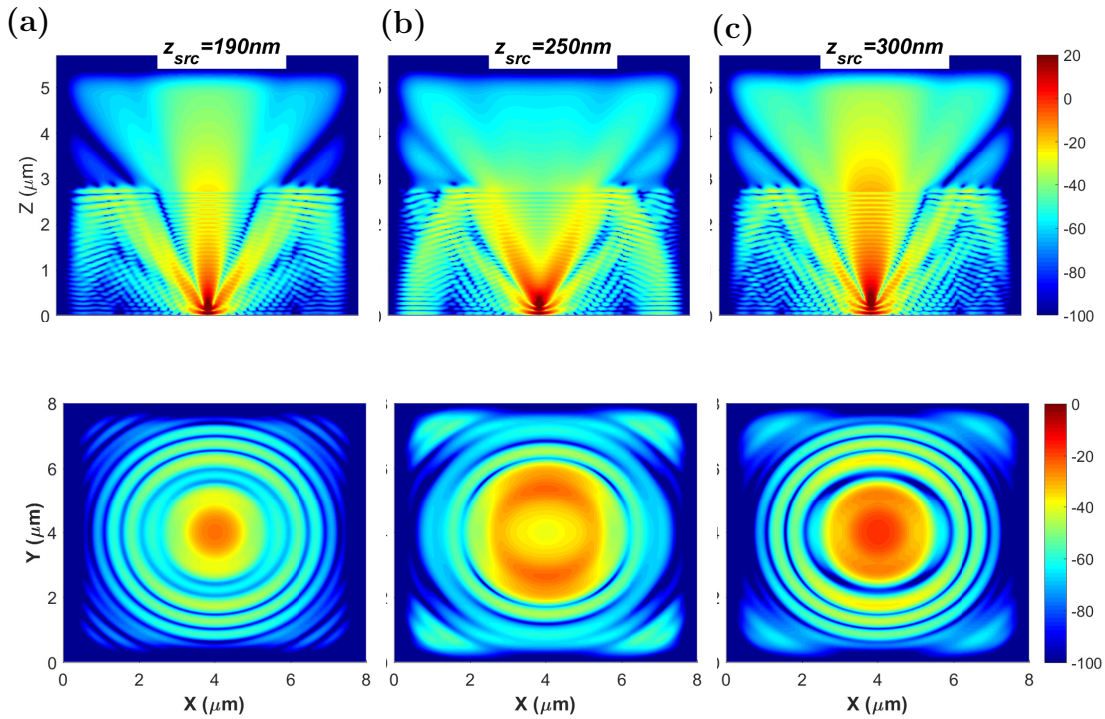

Figure 6-14: *(top) xz-plane of near-field distribution of real part of E_x field spectrally resolved at 450 nm for (a) $z_{src} = 190$ nm, (b) $z_{src} = 250$ nm and (c) $z_{src} = 300$ nm. (bottom) corresponding xy-planes in (d-f) at $z = z_{nf}$ above the reflector.*

6.1.4 Summary

An FDTD model was set up for the planar vertical LED sample shown in figure 5-1. The final FDTD model is presented in figure 6-11(a) where the dispersion of GaN was modelled using a Lorentz model and the graded AlGaN was modelled as sublayers of real dielectric. Far-field emission patterns obtained from applying the near-to-far-field transform (NFFT) on results from FDTD simulations were found to be in acceptable agreement with experimental PL on the same structure for most of the wavelength range, thus providing credance for the model. The discrepancy between the emission patterns obtained from FDTD and PL for longer wavelengths can be due to (i) the lateral limits of the computational cell containing the FDTD structure which restricts the angular range in the NFFT, (ii) the error in the positions and thickness values, provided by Plessey, of the structure and (iii) the exact vertical dipole position.

The multiple quantum well (MQW) region was modelled using three dipoles

placed at vertical positions from the reflector. A strong sensitivity was observed of the light output power and directionality, D, on the vertical dipole position, z_{nf} relative to the reflector. For $z_{nf} = 300$ nm, the light output power obtained for this dipole contributed to almost half of the total emission. Near-fields showed light trapping at the epitaxy/air interface and Fabry-Perot behaviour inside the structures. This explains the large contribution to the total light output power.

Having demonstrated good correlation of FDTD simulation with PL experiment for the planar structure, the model was applied to the simulation of the nanorod samples. This is the subject of the next chapter.

Chapter 7

FDTD Modelling of Nanorod Array Etched onto Vertical LED Structure

7.1 Modelling Nanorod Array

The three nanorod samples discussed in chapter 5, identified by their pitches $\Lambda = 1200\ nm, 800$ nm and 600 nm, were modelled. The dimensions measured from SEM imaging of the nanorod samples and summarised in table 5.1 were used as the reference for the modelling of the nanorod geometry in the FDTD model.

7.1.1 Simulation Set-up

The set up in FDTD is shown in figure 7-1. PMLs of thickness, $t_{PML} = 1\ \mu$m, and strength of 0.5, were used to terminate a cell containing a finite number of nanorods. This set up is commonly used for modelling nanorod arrays [14] [113].

As shown in figure 7-1, the nanostructures are considered to be truncated cones of height, h, base diameter, d_1 and top diameter, d_2, etched into the graded AlGaN layers. The thickness of the GaN epitaxy below the nanorods was $t_{GaN}(nm) = 2700 - h$. It was found no increase in resolution was necessary for simulation convergence and the same value used for modelling the planar

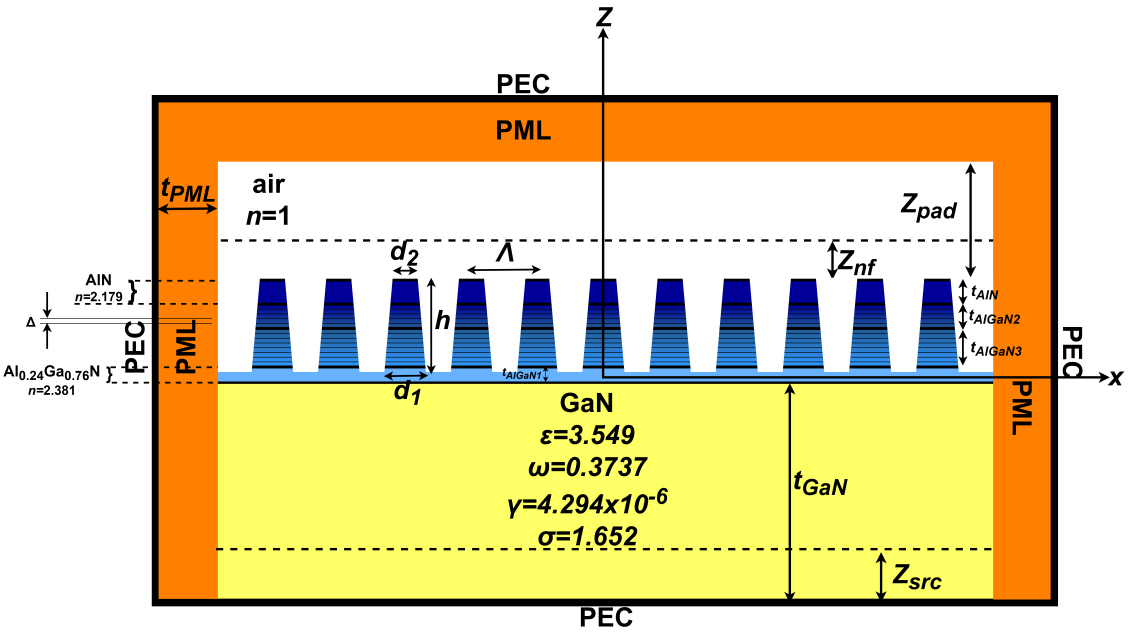

Figure 7-1: *FDTD model for simulation of nanorod samples in xz-plane.*

structure, $\Delta x = 20$ nm was used.

The tangential fields for the near-to-far-field transform (NFFT) were measured at the vertical position $z = z_{nf} = 100$ nm. Simulations were run for the three vertical dipole positions, $z_{src} = 190$ nm, 250 nm and 300 nm corresponding the the edges and center of the multiple quantum well (MQW) structure. Due to computational limitations it was impractical to simulate large arrays of nanorods, which subsequently limited the accuracy of the FDTD model by limiting the resolution of the far-field emission pattern. By simulating an $N \times N$ size structure where N is the number of nanorods, the smallest possible lateral size of the computational cell was determined empirically as when the far-field emission pattern did not significantly change. For the nanorod sample of pitch $\Lambda = 800$ nm, $N = 11$ was observed to be sufficient to contain all of the main lobes and features in the far-field. To demonstrate this, figure 7-2 displays the far-field emission patterns obtained in FDTD for $x_{src} = y_{src} = 0$ nm and $z_{nf} = 300$ nm for $N = 7, 9, 11, 13$ and 15. For $N = 11$ the lateral dimensions of the interior computational cell were $11\Lambda \times 11\frac{\sqrt{3}}{2}\Lambda \approx 8800 \times 7620$ nm.

For the nanorod sample of smaller pitch, $\Lambda = 600$ nm, a larger number of periods was required and $N = 15$ was used, which resulted in a lateral size of

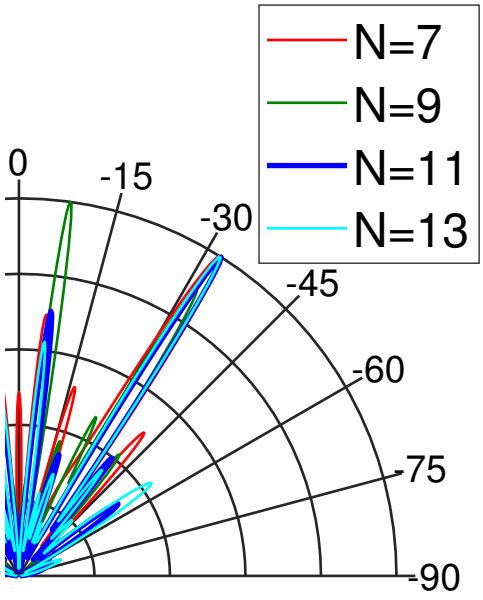

Figure 7-2: *Normalised far-field emission patterns at fixed $\phi = 90°$ of nanorod sample with $\Lambda = 800$ nm for $N \times N$ nanorod array.*

9×7.8 μm. For the sample of pitch, $\Lambda = 1200$ nm, an 11×11 array was used and resulted in a lateral size of 13.2×11.43 μm. Thus, there was a variation of the lateral size between samples and so values obtained for η_{lee} in the following sections, should be considered with caution. It should be noted that in literature the range of the lateral size for PhC arrays has varied from 5.5×5.5 μm [115], 10×10 μm [112] [108] to 25×25 μm [101] for similar emission wavelengths.

7.1.2 Lateral Dipole Position

For the planar structure, the lateral position of the source does not matter, at least theoretically because of the continuous translational symmetry of the structure. For the nanorod arrays however, there is a discrete translational symmetry and so the result for one dipole position will likely not be the same as for another placed at a different lateral position within the unit cell of the array. It was determined in reference [14] for their simulation of similar hexagonal array structures that if the dipole is a large distance from the array (greater than 5-8λ), the dependence of the results on the lateral position of the dipole can be ignored. The author assumed this approximation was justified because the light hitting the array was

almost a plane wave. In the same study, for the case where the dipole was closer to the array, simulations were run for the dipole directly below the center nanorod and halfway between two nanorods separated by the pitch, Λ.

However, for the vertical structure, the reflector will cause a variation of the fields when they strike the array. Note for the horizontal dipole above the ground plane mentioned in section 4.1.3, the far-field has an angular dependence with the effect that the lateral position of the dipole may affect the amount of power coupling into the nanorods. Therefore, dipoles were placed at several positions within a region where they were unique and simulations were run for each dipole separately. The far-field radiation intensities from these dipoles would then be summed incoherently.

The region within which the lateral dipole positions would be unique is the unit cell of the hexagonal array. This was constructed as shown in figure 7-3 which shows part of the array of the simulated nanorod sample identified by $\Lambda = 800$ nm visualised in the xy-plane using a software called Paraview [174]. To do this, lines were first drawn to all nearest neighbouring rods as indicated in blue and then at the midpoint of each line a second line (in orange) was drawn perpendicular to the first. The unit cell is enclosed by the lines in orange. The unit cell was reduced further to the region shaded in cyan: any position could be represented by a translation and rotation of the corresponding point inside the cyan region. For example the position labelled $2a$ is the same as position 2 but rotated 60°.

Seven dipoles were placed at lateral positions, (x_{src}, y_{src}), marked as 1 to 7 in figure 7-3 with their lateral positions listed in the accompanying table.

To determine if the far-field emission due to a point outside the cyan region can be translated back inside the region, separate simulations were run for a dipole placed at position 2 and position $2a$ in figure 7-3 for $z_{src} = 300$ nm.

It was found that the three-dimensional far-field emission patterns over the hemisphere enabled clear observation of the effect of translation. Figure 7-4 compares the results obtained for the dipole at position $2a$ with the far-field from the dipole at position 2 but rotated azimuthally by $\phi = 60°$. These were spectrally resolved at 440 nm because at this wavelength there are distinct opposing sidelobes which act as a marker for the rotation.

Comparison of figures 7-4(a) and 7-4(b) are in relative agreement in terms of

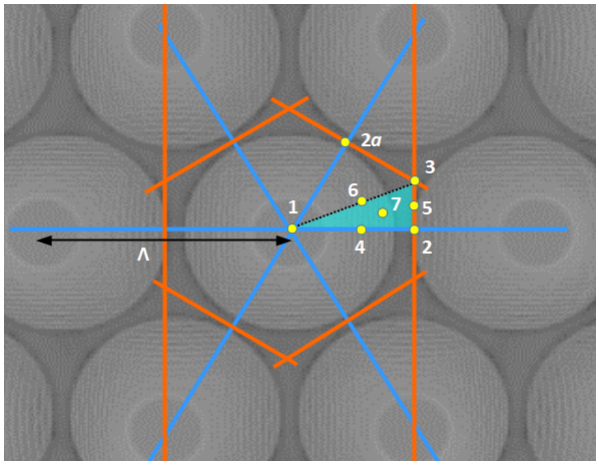

Position	x_{src}	y_{src}
1	0	0
2	0	0.5Λ
3	0.5Λ	$\frac{\Lambda}{2\sqrt{3}}$
4	0.25Λ	0
5	0.5Λ	$\frac{\Lambda}{4\sqrt{3}}$
6	0.25Λ	$\frac{\Lambda}{4\sqrt{3}}$
7	0.33Λ	$\frac{\Lambda}{8\sqrt{3}}$

Figure 7-3: *xy-plane of nanorod array with $\Lambda = 800nm$ indicating lateral dipole source positions 1-7 within the region shaded in cyan. The unit cell is constructed by the lines in orange and blue. The table lists the lateral dipole positions.*

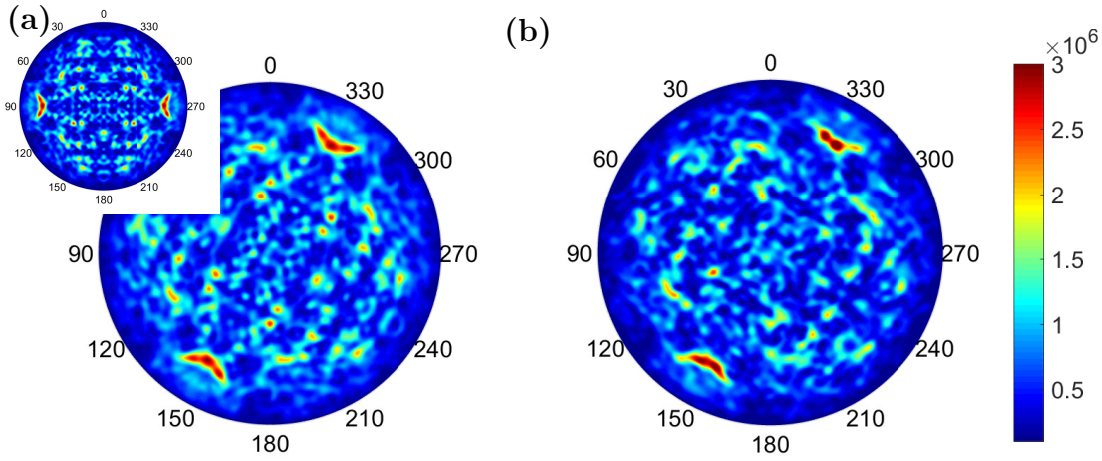

Figure 7-4: *Three-dimensional hemispherical far-field emission patterns for (a) position 2 (inset) rotated 60° and (b) position 2a. These are spectrally resolved at 440 nm wavelength.*

reproducing the main intensity peaks. Position $2a$ in figure 7-4(b) displays some asymmetry of the main lobes at $\phi = 330°$ where the lobe is less well formed, and the intensity peaks for position $2a$ are less pronounced than the emission from position 2 in figure 7-4(a). The cause of this is likely due to position $2a$ being nearer to the PML directed along the y-axis. Consequently more of the fields will be absorbed by this PML resulting in the slight asymmetry of the main lobes in

figure 7-4(b).

Based on figure 7-4(b) it was now possible to take the far-field emissions corresponding to the dipole position, and cumulatively sum their emission patterns after rotating by $m \times 60°$ where $m = 0 : 5$:

$$U_{tot,i} = \frac{1}{6} \sum_{m=0}^{5} U_i \left(\theta, \phi + m\frac{\pi}{3} \right) \tag{7.1.1}$$

Where i refers to the i^{th} position denoted in the table in figure 7-3. In this way the far-field emission patterns for the whole unit cell could be obtained.

The choice of the positions in figure 7-3 were focused at the symmetry points except for position 7 which was set to be more random and therefore less likely to excite any particular modes arising from symmetry of the computational cell and array. An issue was realised for the dipoles at positions 5 and 7 with the rotation and summation operation in equation (7.1.1). From figure 7-3 the far-fields corresponding to positions 5 and 7 cannot be rotated 60° and summed six times because they are not along the lines of symmetry for the rotation. Consequently, if equation (7.1.1) was applied to the far-fields of positions 5 and 7, the values of $U_{tot,5}$ and $U_{tot,7}$ will not account for the whole unit cell centered around position 1. For example, if position 7 in figure 7-3 is rotated 60° it will lie on the other side of position $2a$ and the contribution of position 7 in the region enclosed by positions 3, $2a$ and 1 will be missed. This is similarly the case for position 5. It would be incorrect however to take the the far-field emissions from position 5 in equation (7.1.1) and rotate by 30° 12 times and then summed. This is because 12-fold symmetry will be manifested in the final result of $U_{tot,5}$. This can be explained by the diagram in figure 7-5(a).

From figure 7-5(a), position 5 is located at a distance between the two near neighbouring nanorods as indicated by the black arrows. If position 5 was rotated by 30° to position $5a$, it is assuming the far-field emission pattern has a neighbouring nanorod where there is none. This imaginary nanorod is represented by the fainter dashed circle in figure 7-5(a). Therefore, a mirror operation was used whereby position $5a$ was the reflection of position 5. The far-field emission patterns were summed and input as U_5 in the operation of equation (7.1.1).

The contribution of each dipole to the total result should be considered. For example having too many dipoles in one region will result in the far-field over

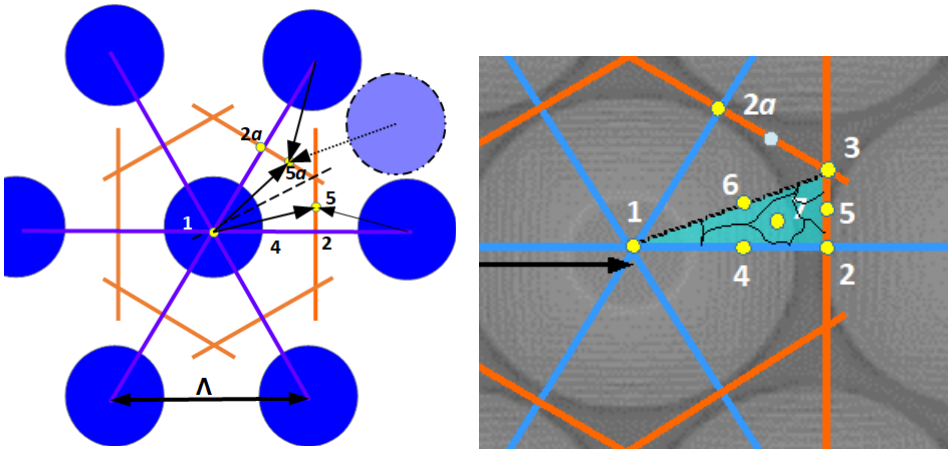

Figure 7-5: *Diagram demonstrating issue of lateral dipole position 5 whose far-field emission pattern cannot be rotated 30° and then summed because it assumes imaginary nanorods as indicated by faint blue dashed circle.*

representing that emission region. In figure 7-5(b) a crude Voronoi diagram was drawn as a way to quantify the contribution from the dipole positions. To a first order approximation, the region sizes are similar.

In the literature, for a vertical structure simulated in [115], seven dipoles were also placed laterally within one period of the array. In [104] the dipoles were placed at positions 1, 2 and 3. Other studies have used a very large number of dipoles evenly distributed: in [105] 25×25 TE emission dipoles and in [109] 1000 dipoles were simulated. The method used in this thesis was intended as a compromise between computational resources and accuracy.

7.1.3 Results

The far-field emission results for the three nanorod samples as a function of the lateral dipole position are now presented. For each of the positions in figure 7-3, the far-fields have been summed over the three vertical dipole positions z_{src} = 190 nm, 250 nm and 300 nm. For every single dipole position (laterally and vertically), an E_x and E_y polarised dipole was separately simulated and summed using equation (6.1.1) in section 6.1.

Nanorod sample, $\Lambda = 800nm$

From figure 7-1, the values $h = 700$ nm, $d_1 = 760$ nm and $d_2 = 280$ nm were modelled for $\Lambda = 800$ nm. Figure 7-6 compares the far-field emission patterns obtained from PL experiment and FDTD simulation for the dipole positions 1 through to 7 in figure 7-3 for emission wavelength, $\lambda = 450$ nm.

From figures 7-6(a-g), very good agreement of the FDTD simulation with experimental PL was observed for emission from several dipole positions. In particular, the far-field emission patterns from dipoles at positions 3,4, 5 and 7 in the respective figures 7-6(c-e) and (g) demonstrated good fits for both azimuths, $\phi = 60°$ and $\phi = 90°$. As shown in figure 7-6(g), the far-field emission from the dipole at position 7 alone provided very good agreement with PL experiment in terms of the overall emission pattern shape. The far-field emission from the dipole at position 1 in figure 7-6(a) showed the least amount of correlation with the experimental PL where the FDTD simulated emission was highly collimated at $\theta = 0°$. This position is the most symmetrical and so it could be the most singular and thus least representative of the far-field emission for this structure. Similarly the far-field emission from the dipole at position 2 displayed collimation in the vertical emission.

In figure 7-6(h), the far-field emission patterns obtained from FDTD for each of the lateral dipole positions 1 to 7, in figures 7-6(a-g), were summed and very good agreement with PL experiment was observed. There is some discrepancy observed for the $\phi = 60°$ slice where the emission in the range of around $\theta = 30° - 40°$ is not as accurately reproduced. This is likely exacerbated by the error in the PL experiment when the sample was aligned along 60°.

Figure 7-7 compares the far-field emission patterns obtained from PL experiment and FDTD simulation for the dipole positions 1 to 7 in figure 7-3(a-g) integrated over the wavelength emission range, 420 nm to 480 nm in 5 nm increments.

From figure 7-7, in terms of overall emission shape, good agreement between the emission patterns obtained from PL experiment and FDTD simulation were observed for the dipole placed at positions 5 and 7 in figures 7-7(e) and 7-7(g) respectively for both azimuth angles, $\phi = 60°$ and $\phi = 90°$. The emission patterns from the dipole placed at position 1 in FDTD simulation similarly displayed strong collimation in the vertical direction that was not observed in the PL ex-

periment.

In figure 7-7(h), the far-field emission pattern was summed over the lateral dipole positions 1 to 7, in figures 7-7(a-g) and integrated over the wavelength emission range, 420 nm to 480 nm in 5 nm increments.

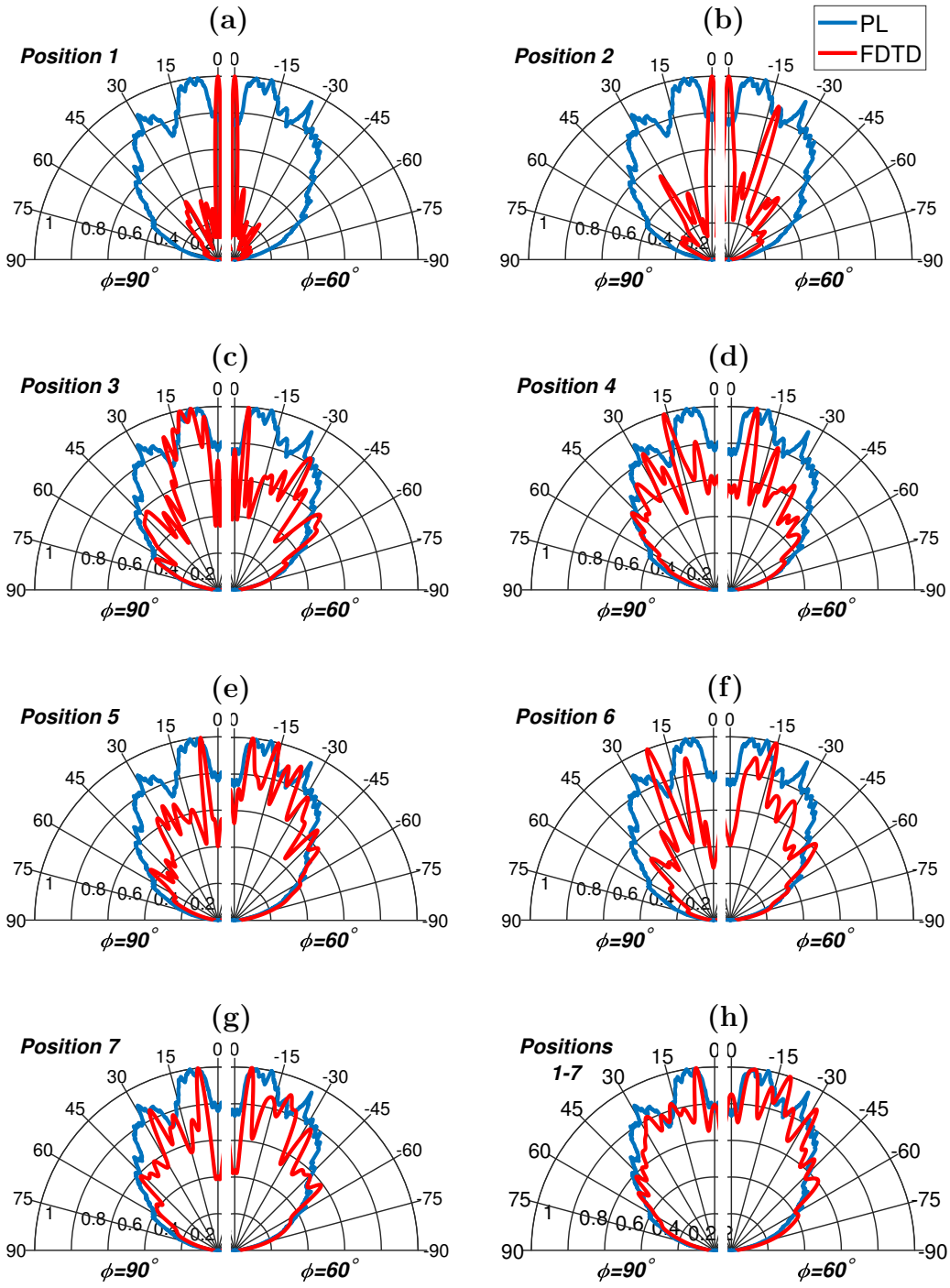

Figure 7-6: *Comparison of far-field emission patterns obtained from PL and FDTD spectrally resolved at 450 nm for fixed azimuth, $\phi = 90°$ and $\phi = 60°$ for nanorod array, $\Lambda = 800$ nm. Far-fields from FDTD were obtained for lateral dipole positions (a) to (g) 1 to 7 and (h) integrated positions 1 to 7.*

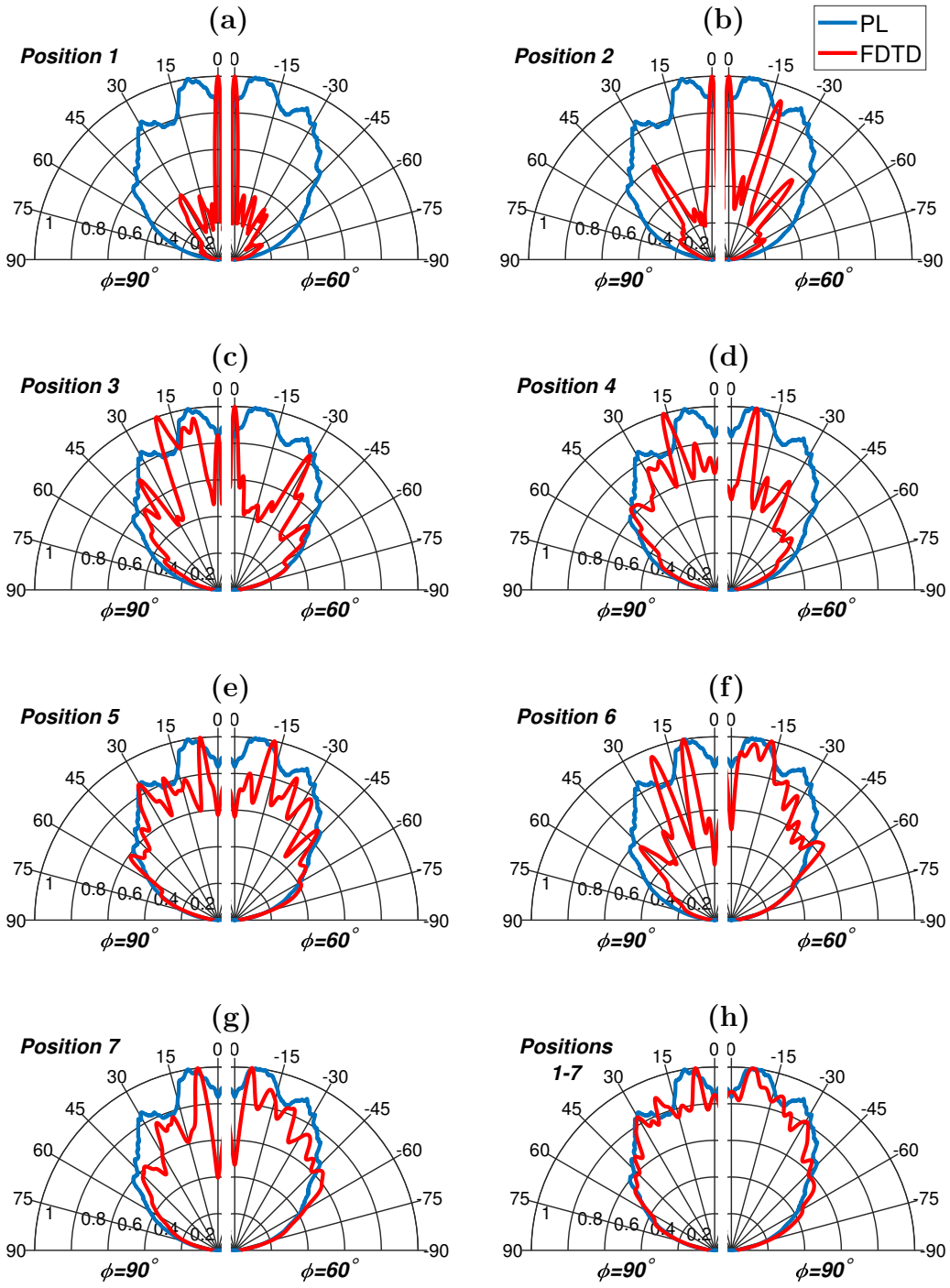

Figure 7-7: *Comparison of far-field emission patterns obtained from PL and FDTD integrated over wavelength emission for fixed azimuth, $\phi = 90°$ and $\phi = 60°$ for for nanorod array, $\Lambda = 800$ nm. Far-fields from FDTD were obtained for lateral dipole positions (a) to (g) 1 to 7 and (h) integrated positions 1 to 7.*

Figure 7-7 shows how each of the emission patterns from the individual dipole positions contributes to specific lobes in the overall emission pattern summed for all of the dipoles. In figure 7-7(h) for the results obtained from PL experiment, there are two high intensity lobes of width around 10° within the ±15° emission cone which contributes to the higher observed directionality. In the FDTD-obtained far-field however, the width of these lobes is around 4°.

The three-dimensional unnormalised hemispherical far-field emission patterns summed for all dipole positions 1 to 7 are shown in figures 7-8(a) and 7-8(b) corresponding to the emission spectrally resolved at 450 nm and integrated over wavelength respectively.

In figure 7-8(a), six-fold symmetry is observed which indicates diffraction from the hexagonal nanorod array. This effect is similarly observed for the integrated wavelength emission in figure 7-8(b) and is more defined near the vertical direction. The intensity is relatively spread out which indicates the angular conditions for constructive interference are not strict, most likely due to the cone-shape of the nanorods causing scattering.

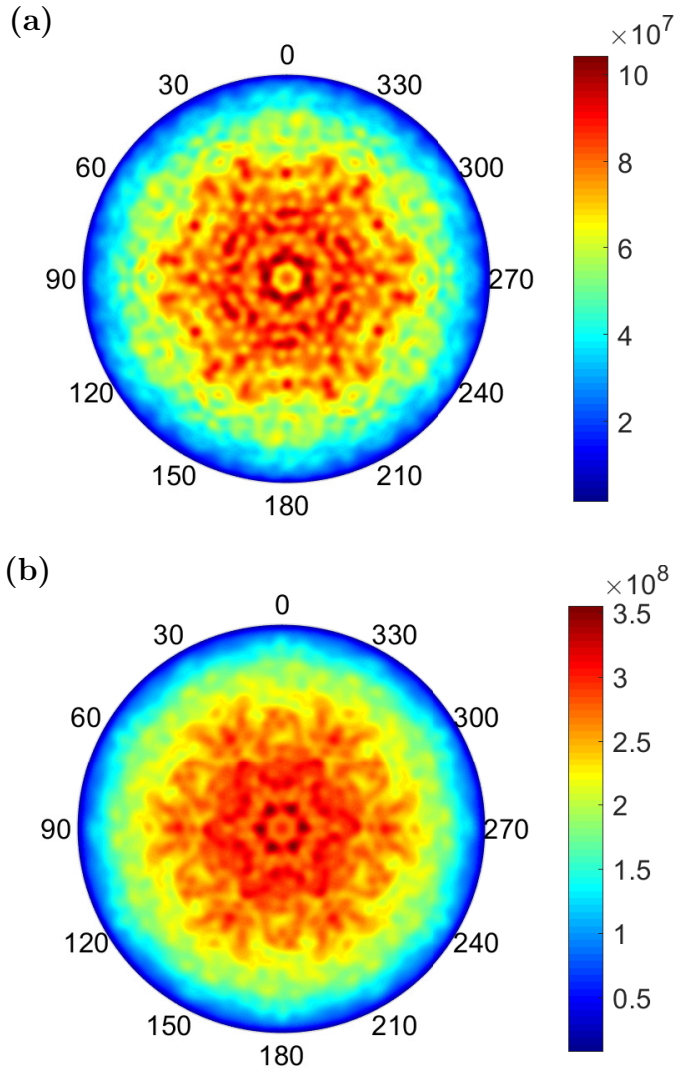

Figure 7-8: *3D unnormalised hemispherical far-field emission patterns spectrally resolved at (a)* 450 *nm and (b) integrated over wavelength for nanorod sample of* $\Lambda = 800$ *nm.*

To observe the light propagation inside the simulated structure, the near-fields were plotted. Figures 7-9(a) and 7-9(b) display the real part of the E_x field distribution for 450 nm wavelength. Figure 7-9(a) is in the xz-plane at $y = 0$ nm i.e., halfway and 7-9(b) is for the xy-plane at $z = z_{nf}$ where the near-fields are collected for the near-to-far-field transform (NFFT). All of the plots are summed for the dipoles at position 7 for $z_{src} = 190$ nm, 250 nm, 300 nm for the E_x-polarised dipoles. The fields from the dipoles at position 7 were taken because the far-field emission appeared to provide the best agreement with the results

obtained from experimental PL in terms of overall emission pattern shape[1].

In figure 7-9(a), the field distribution shows that a large amount of the escaped light was due to scattering from the outside edges of the truncated cone-shaped nanorods. The central nanorod and its neighbour show strong scattering from the top surface. The field intensity is concentrated between $x = 4$ μm and $x = 8$ μm inside the epitaxy and shows that much of the light which escapes is directly from the dipole source and scattered from the central nanorods. Return reflections from the nanorod array rapidly decay, and escape via scattering from the edges of the cone-shaped nanorods. Between adjacent nanorods there is some coupling of the fields near the base of the nanorods because they are closely packed but it appears they decouple further up because of the cone shape. The field intensity drops as one progresses further from the center nanorod. This is shown in figure 7-9(b) where the field distribution has higher relative intensity at the center of the array.

[1]It will be shown later this appeared to be the case for all of the nanorod structures

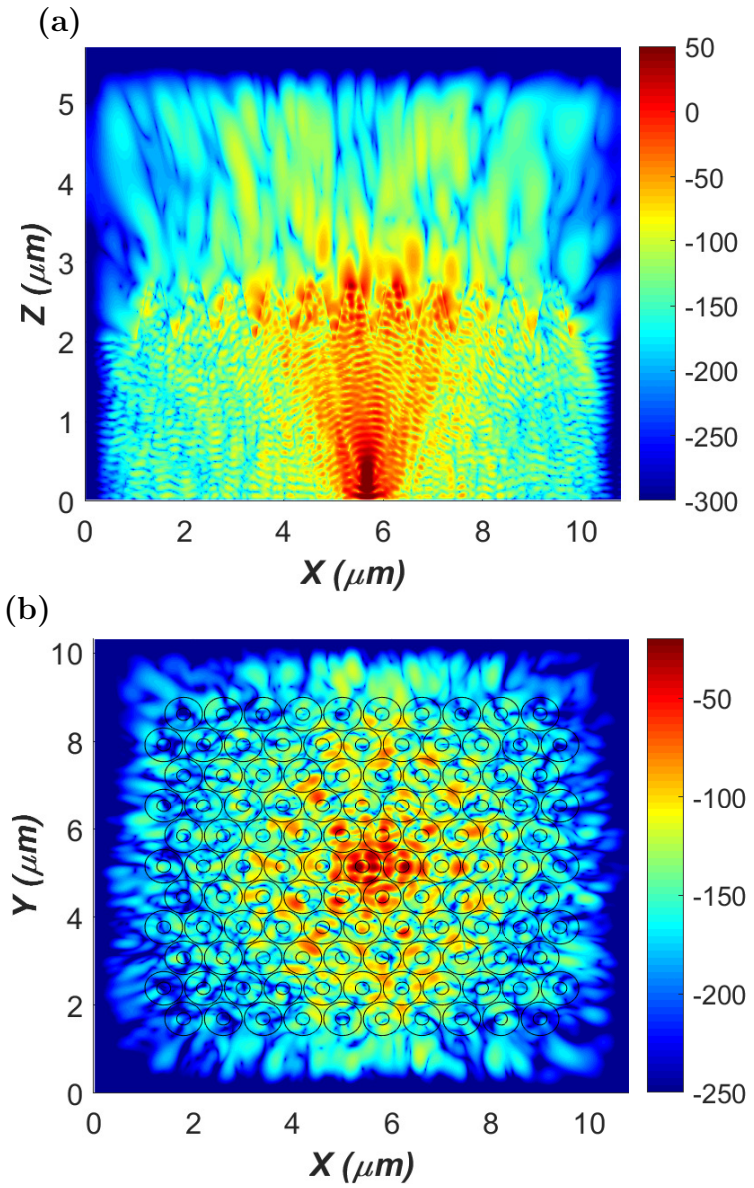

Figure 7-9: *Real part of E_x field distribution for* 450 *nm wavelength of nanorod structure of* $\Lambda = 800$ *nm in (a) xz-plane and (b) xy-plane at* $z = z_{nf}$.

To examine the overall effect of both the E_x and E_y dipoles, the H_z field component is also plotted. Figures 7-10(a) and 7-10(b) display the corresponding real part of the H_z field distribution for 450 nm wavelength. Figure 7-10(a) is in the xz-plane at $y = 0$ nm and figure 7-10(b) is for the xy-plane at $z = z_{nf}$. Similarly all of the plots are summed for the dipoles at position 7 for $z_{src} = 190$ nm, 250 nm, 300 nm for both the E_x- and E_y-polarised dipoles.

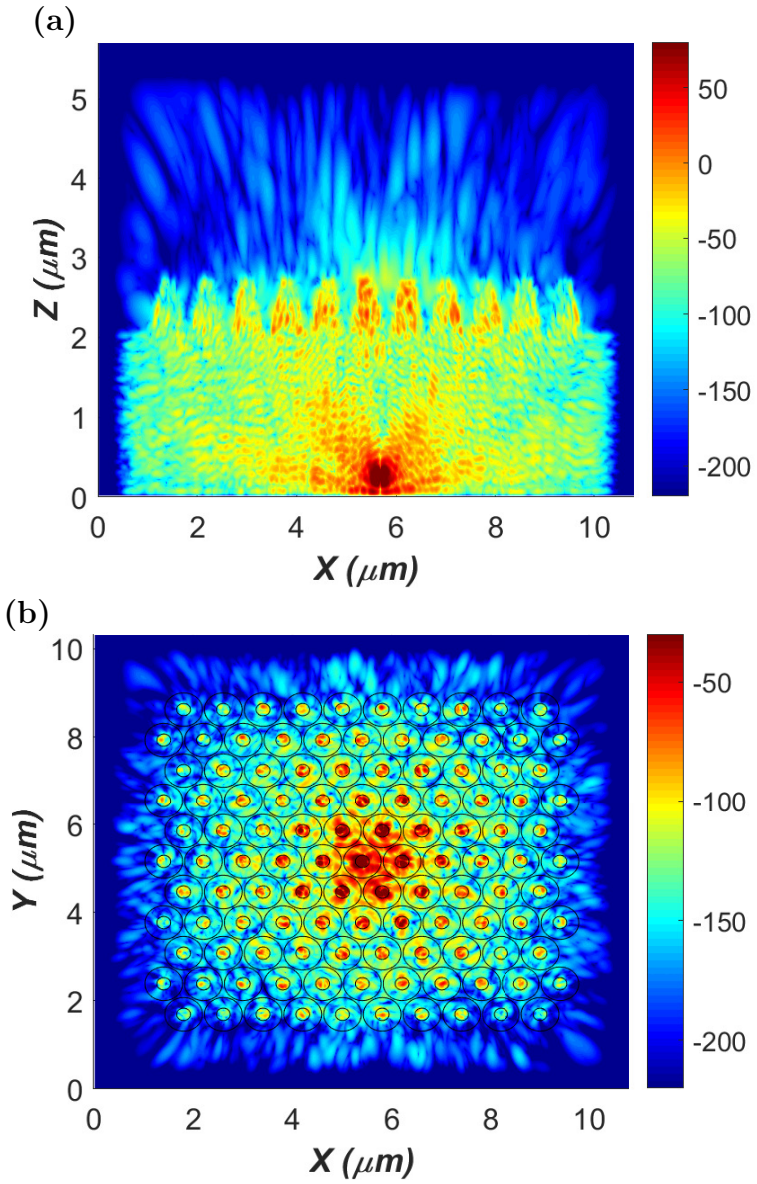

Figure 7-10: *Real part of H_z field distribution for 450 nm wavelength of nanorod structure of $\Lambda = 800$ nm in (a) xz-plane at $y = 0$ nm and (b) xy-plane at $z = z_{nf}$.*

In figure 7-10(a) there is a distinct localisation of the H_z fields inside the center nanorod and it's nearest neighbours. Reflections from the nanorod array can also be seen from the 'rippling' of the fields inside the epitaxy and at the edges of the array, the fields that have not decayed have more intensity on the outside edge of the cones. From figure 7-10(b) there is distinctive localisation of

the H_z field inside the nanorods. These fields inside the center and surrounding nanorods display some symmetric patterns. This indicates these may be modes and therefore waveguiding inside the nanorods for the $\Lambda = 800$ nm structure.

Note about Dipole at Position 1

To a first order approximation, this nanorod structure is a horizontal dipole above a ground plane whose far-field strikes the nanorord array: this could be justified given the distance between the array and the dipole is around 8-10λ. Referring to section 4.1.3, the definition of the array factor for a horizontal dipole above a ground plane has a $\cos(\theta)$ dependence. When the dipole is placed directly under the center nanorod as is the case for position 1 at $\theta = 0$ there may be strong coupling and excitation of guided modes inside the nanorod. To investigate further, a comparison was made of the near-fields for the dipoles at positions 1 and 4: Position 4 was referenced because at this location, the dipole is equivalent to a dipole being positioned at $y = 0$ nm and then shifted from $x = 0$ by 0.25Λ.

Figure 7-11 shows the real part of the E_x field distribution in the xz-plane for $y = 0$ and integrated over the vertical source positions with E_x polarisation at (a) position 1 and (b) position 4.

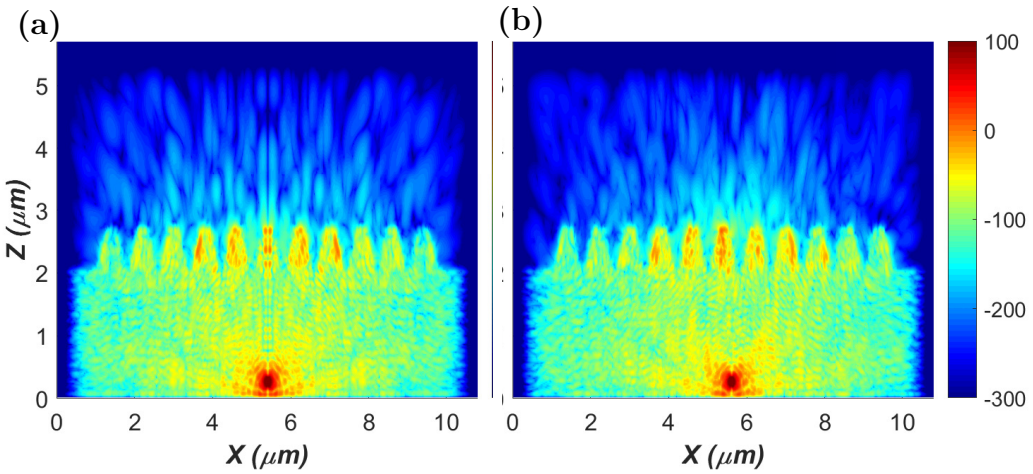

Figure 7-11: *Real part of E_x field distribution for* 450 *nm wavelength of nanorod structure of* $\Lambda = 800$ *nm for dipole at position (a) 1 and (b) 4 in the xz-plane.*

In figure 7-11(a), strong waveguiding is observed inside the center nanorod

which diffracts upwards and outwards. In the far-field emission pattern obtained from FDTD in figure 7-6(a), the emission measured from the dipole at position 1 was highly collimated. This highly directional far-field pattern may be due to a mode inside the nanorod approaching cut-off. When a mode is near cut-off it becomes highly radiative and spread out which would result in the directional emission as per Fourier transform theory. Interestingly in figure 7-11 there also appeared to be a focused standing wave pattern from the dipole directly to the center nanorord. In figure 7-11(b) for the fields due to the dipole at position 4, the field distribution appeared more random and the symmetric field pattern observed for the center nanorod in figure 7-11 is not present.

Figures 7-12(a) and 7-12(b) show the corresponding xy-plane for $z = z_{nf}$ of positions 1 and 4 respectively. Here the real part of the H_z field component was plotted and the fields were integrated over all vertical dipole positions for both E_x and E_y polarisations.

From figure 7-12(a), the centrally positioned dipole results in a highly symmetric near-field distribution, for example the field above the center nanorod has 4 antinodes which indicates a mode pattern. In figure 7-12(b) this symmetry is reduced when the dipole is shifted by $x = 0.5\lambda$. The insets of figures 7-12(a) and 7-12(b) are the corresponding H_z fields inside the center nanorod in the xz-plane. The inset of figure 7-12(a) shows a strong mode pattern or waveguiding inside the nanorod was observed for position 1 which is removed when the dipole is shifted to $x_{src} = 0.25\Lambda$. It was noted that this strong waveguiding effect into the center nanorod for position 1 was observed for all three nanorod samples.

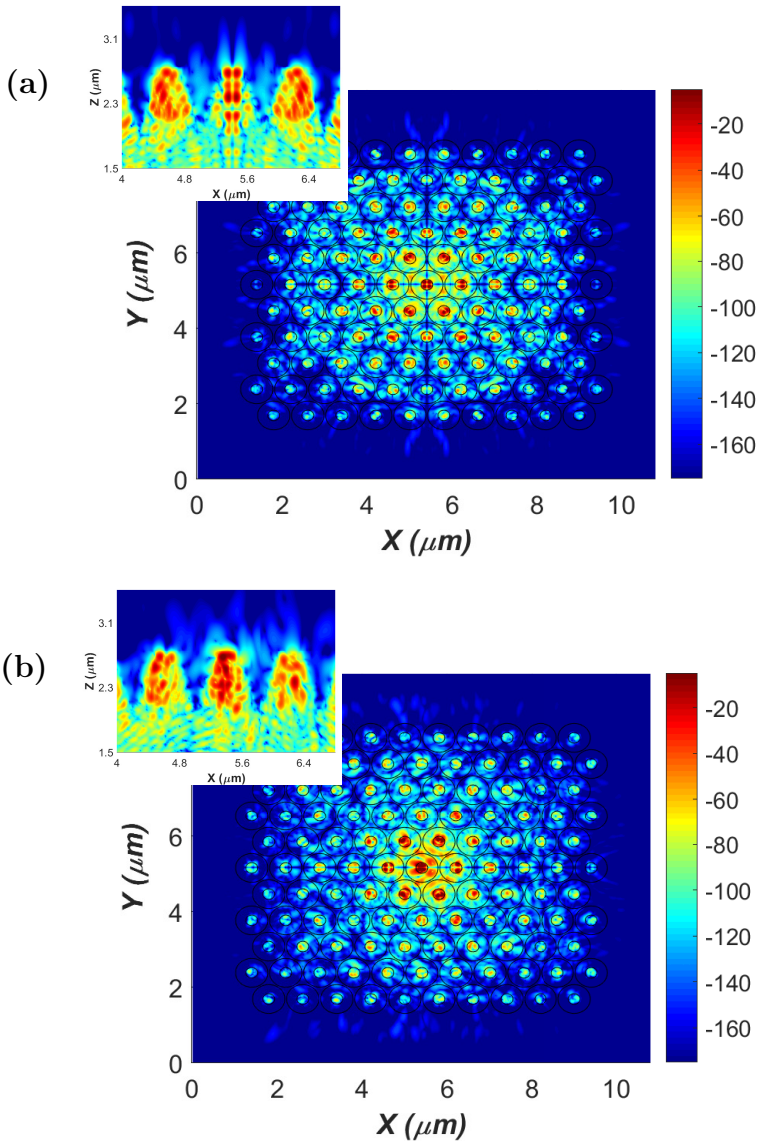

Figure 7-12: *Real part of H_z field distribution for 450 nm wavelength of nanorod structure of $\Lambda = 800$ nm for dipole at position (a) 1 and (b) 4. Main figures are in the xy-plane and insets are in the xz-plane.*

Note about Run-Times and Convergence

It is noted here that run-times for the modelling of nanorods was significantly increased. This was due to the inability to exploit symmetry for several of the dipole positions and the reduced convergence rate which increased for smaller pitch. The latter manifested in the measured decay of the fields oscillating towards the end of the simulation. For a single E_x dipole at position 7 for $\Lambda = 600$

nm, the run time was around 5.8 hours, for $\Lambda = 800$ nm the run time was 4.6 hours. It is noted that the PML is less efficient where the group velocity of waves is smaller which would be more likely to occur for a nanostructure with reduced pitch. Oscillations would be further exacerbated by the lower PEC boundary condition.

Nanorod sample, $\Lambda = 600nm$

From figure 7-1, the values $h = 730$ nm, $d_1 = 600$ nm and $d_2 = 140$ nm were modelled for $\Lambda = 600$ nm. Figure 7-13 compares the far-field emission patterns obtained from PL experiment and FDTD simulation for the dipole positions 1 to 7 in figure 7-3 for emission wavelength, $\lambda = 450$ nm.

In figure 7-13, there is some good agreement between the far-field patterns obtained from PL experiment and FDTD simulations for several dipole positions. The FDTD-obtained far-field as a result of the dipole at position 7 in figure 7-13(g) is in extremely good agreement with PL experiment, particularly for the fixed azimuth angle $\phi = 90°$, with just a discrepancy around 5° in the vertical emission. The far-field emission obtained for the dipole at positions 1 in figure 7-13(a) had little correlation with PL experiment in the angular range $\pm 15°$.

In figure 7-13(h), the far-field emission patterns obtained from FDTD for each of the lateral dipole positions 1 to 7, in figures 7-13(a-g) were summed. The overall emission pattern shape obtained in FDTD is well-emulated with that obtained from PL experiment. There is some disparity for the fixed azimuth angle, $\phi = 60°$ between 17° and 45° in figure 7-13(h) where the peaks occur at the same positions but the intensity is less for the simulated pattern. This was observed for all of the FDTD-obtained far-field emissions from the dipoles at positions 1 to 7 at $\phi = 60°$ where the intensity of the lobes between 15° and 45° was also underestimated.

Figure 7-14 compares the far-field emission patterns obtained from PL experiment and FDTD simulation for the dipole positions 1 to 7 in figure 7-3(a-g) integrated over the wavelength emission range, 420 nm to 480 nm in 5 nm increments.

In figure 7-14 for the integrated emission, there was some reasonable agreement between the far-field emissions obtained for FDTD simulation and PL experiment. The emission pattern from the dipole at position 4 in figure 7-14(d)

showed good correlation in the overall shape of the emission profile with PL results, however the FDTD emission shape was also dominated by strong intensity in the vertical direction. The FDTD-obtained emission pattern in figure 7-14(g) for the dipole at position 7 was also in good agreement with PL-obtained emission, though some of the sharper lobe features in the PL pattern are not captured in the FDTD. This indicates an array made up of more nanorods was required to resolve these.

In figure 7-14(h), the far-field emission pattern was summed over the lateral dipole positions 1 to 7, in figures 7-14(a-g) and integrated over the wavelength emission range, 420 nm to 480 nm in 5 nm increments. Here much of the emission shape obtained in PL could be reproduced in the FDTD however, there was deviation in the vertical profile between 0° and 13° for both $\phi = 60°$ and $\phi = 90°$.

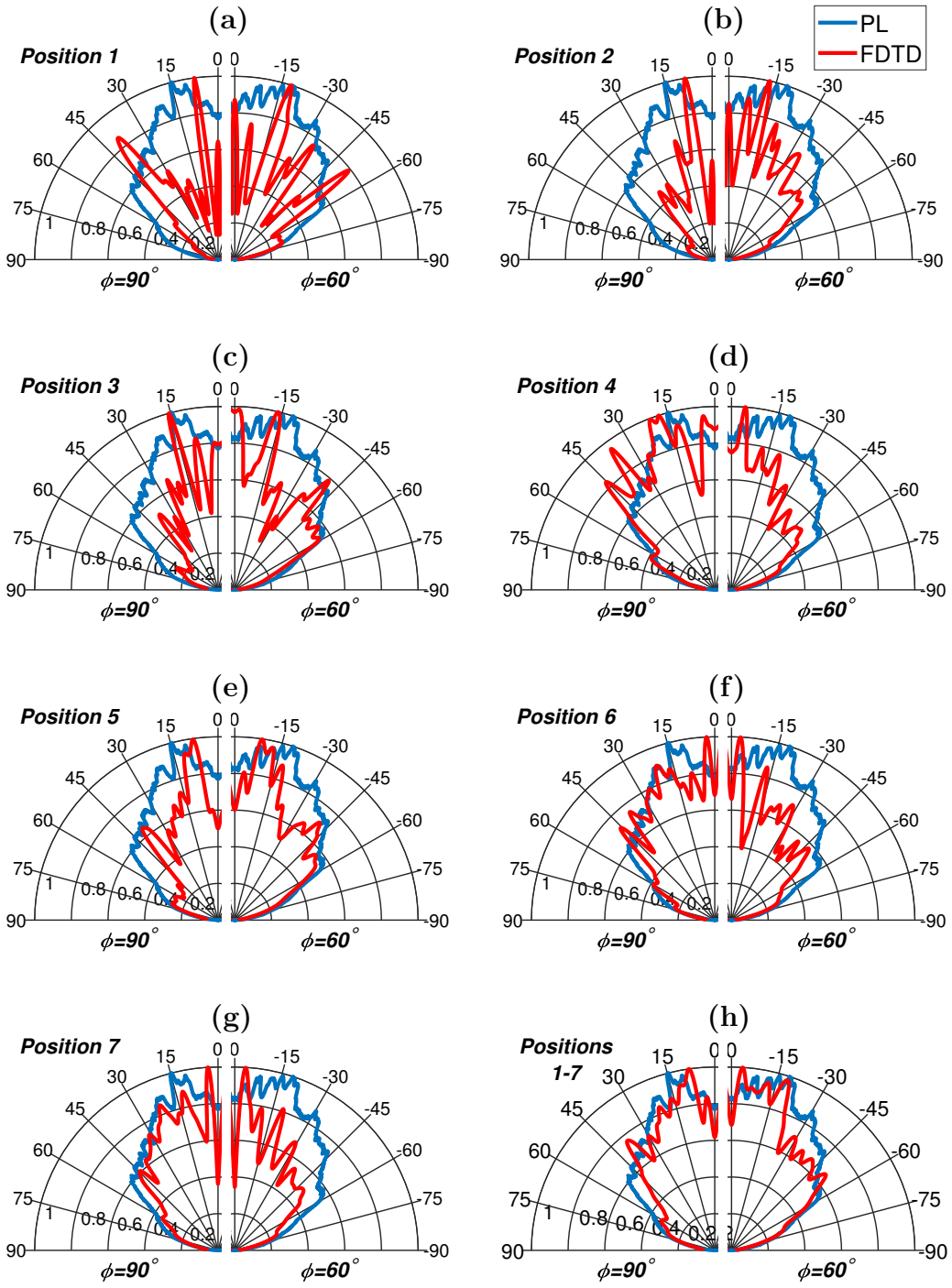

Figure 7-13: *Comparison of far-field emission patterns obtained from PL and FDTD spectrally resolved at 450 nm for fixed azimuth, $\phi = 90°$ and $\phi = 60°$ for nanorod array, $\Lambda = 600$ nm. Far-fields from FDTD were obtained for lateral dipole positions (a) to (g) 1 to 7 and (h) integrated positions 1 to 7.*

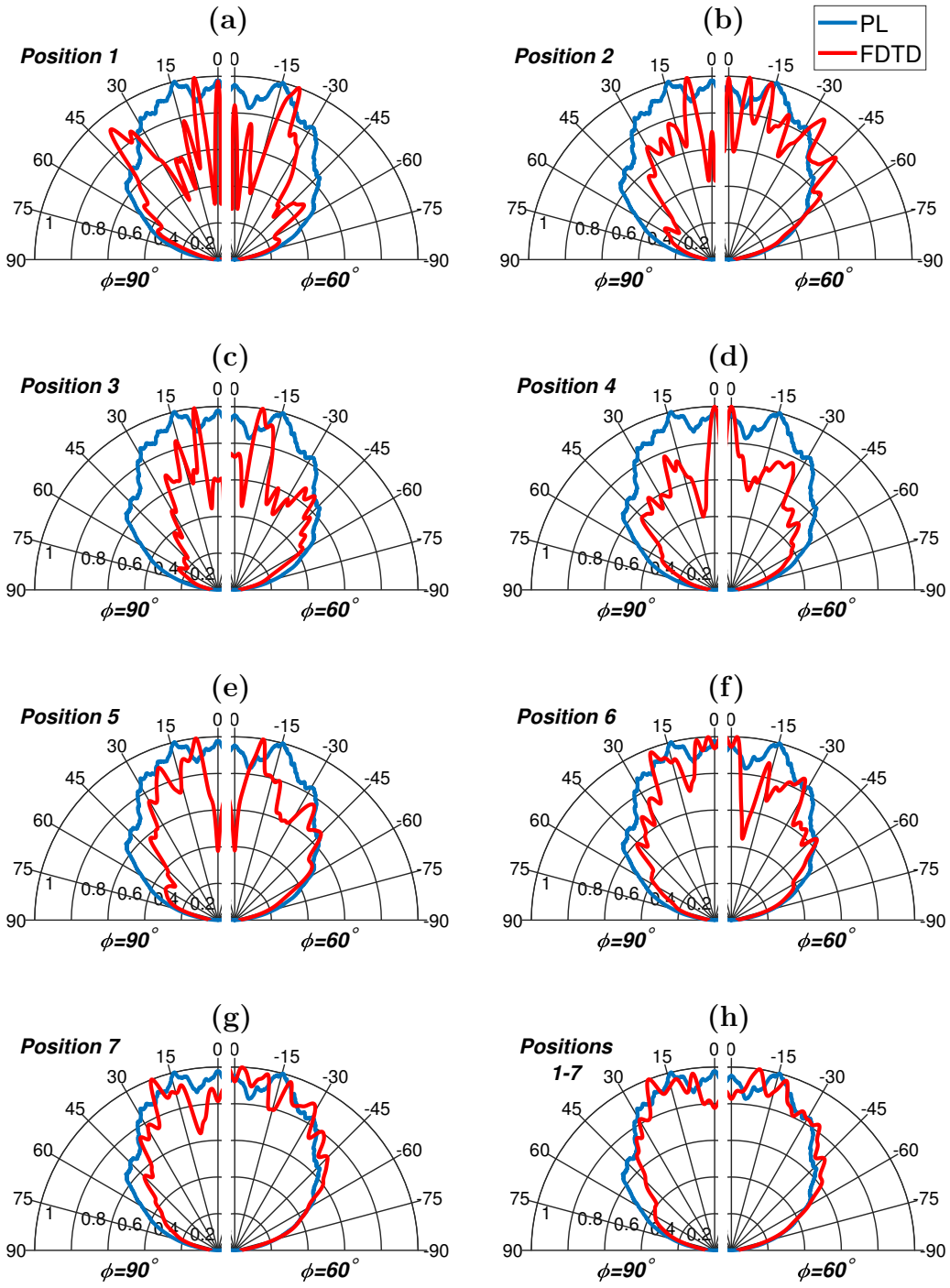

Figure 7-14: *Comparison of far-field emission patterns obtained from PL and FDTD integrated over wavelength emission for fixed azimuth, $\phi = 90°$ and $\phi = 60°$ for for nanorod array, $\Lambda = 600$ nm. Far-fields from FDTD were obtained for lateral dipole positions (a) to (g) 1 to 7 and (h) integrated positions 1 to 7.*

The three-dimensional unnormalised hemispherical far-field emission patterns summed for all dipole positions 1 to 7 are shown in figures 7-15(a) and 7-15(b) corresponding to the far-field emission pattern spectrally resolved at 450 nm and integrated over wavelength respectively.

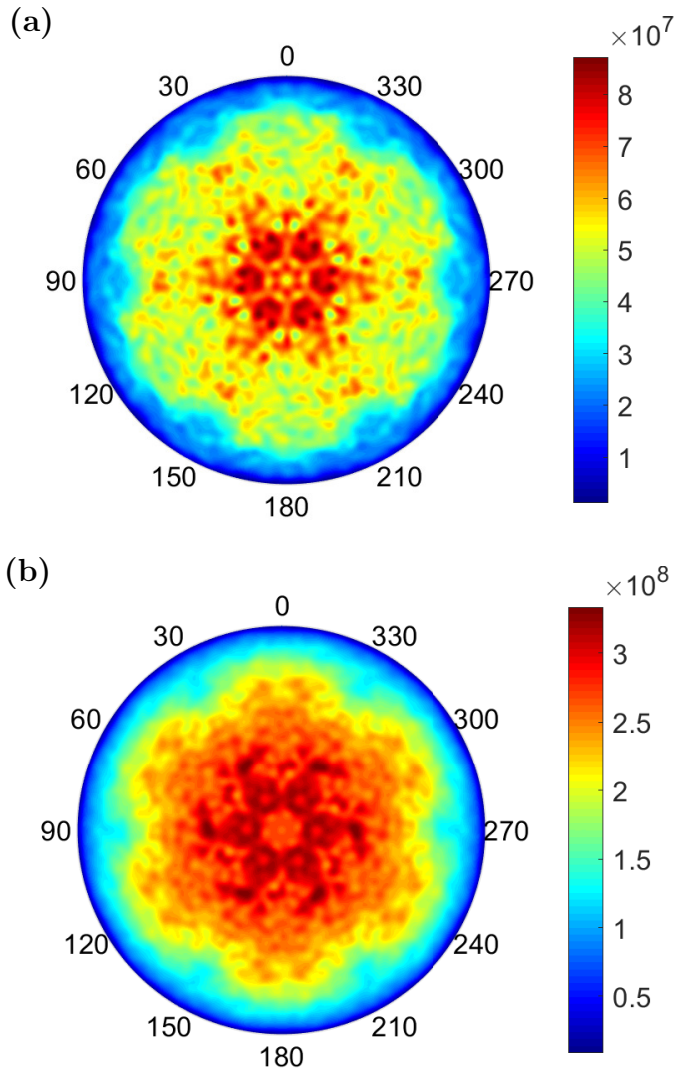

Figure 7-15: *3D unnormalised hemispherical far-field emission patterns spectrally resolved at (a)* 450 *nm and (b) integrated over wavelength for nanorod sample of* $\Lambda = 600$ *nm.*

Similarly to the results obtained for the nanorod sample $\Lambda = 800$ nm in figures 7-8(a) and 7-8(b), six-fold symmetry of the emission pattern is observed. This indicates diffraction as a result of the hexagonal arrangement of the nanorod

array. In figure 7-15(b), the relatively continuous intensity across the emission may be due to scattering off the cone-shaped nanorods.

Figures 7-16(a) and 7-16(b) display the real part of the E_x field distribution for 450 nm wavelength. Figure 7-16(a) is in the xz-plane at $y = 0$ nm and figure 7-16(b) is for the xy-plane at $z = z_{nf}$ where the near-fields are collected for the NFFT. All of the plots are summed for the dipoles at position 7 for $z_{src} = 190$ nm, 250 nm, 300 nm for the E_x-polarised dipoles. The emission from the dipole at position 7 was taken because it was very similar to the emission integrated over all of the dipole positions as demonstrated in figures 7-14(g) and 7-14(h). Furthermore the emission in figure 7-14(h) was a better approximation in the vertical emission direction for $\lambda = 450$ nm.

In figure 7-16(a), the field distribution shows a large amount of the escaped light was due to scattering from the truncated cone-shaped nanorods, similar to the nanorod sample of $\Lambda = 800$ nm in figure 7-9(a). Observation of the centrally-positioned nanorods in figure 7-16(a) appear to show the small top diameter of the nanorod cone resulting in large radiation of the fields from the top of the rods. The majority of the field's intensity is concentrated between $x = 5$ μm and $x = 7$ μm, indicating much of the escaped light is from the dipole emission directly coupling to the array. The scattering of the fields off the edge of the nanorod cones rapidly decays as one progresses further from the center nanorod. This rapid decay is further demonstrated in figure 7-16(b) where there is a large contrast between the intensity of the fields surrounding the central nanorod and further out across the array.

Figures 7-17(a) and 7-17(b) display the real part of the H_z field distribution for 450 nm wavelength. Figure 7-17(a) is in the xz-plane at $y = 0$ nm and figure 7-17(b) is for the xy-plane at $z = z_{nf}$. All of the plots are summed for the dipoles at position 7 for $z_{src} = 190$ nm, 250 nm, 300 nm for both the E_x- and E_y-polarised dipoles.

In figure 7-17(a) the H_z fields are present inside the central nanorod and the surrounding rods. These decay as one progresses to the nanorods at the edge of the array. In figure 7-17(b) for the xy-plane, the fields are localised around the central nanorod and do not couple more than a period. This lack of coupling is likely due to the small top diameter which decouples the fields at the top of the array so the light does not spread.

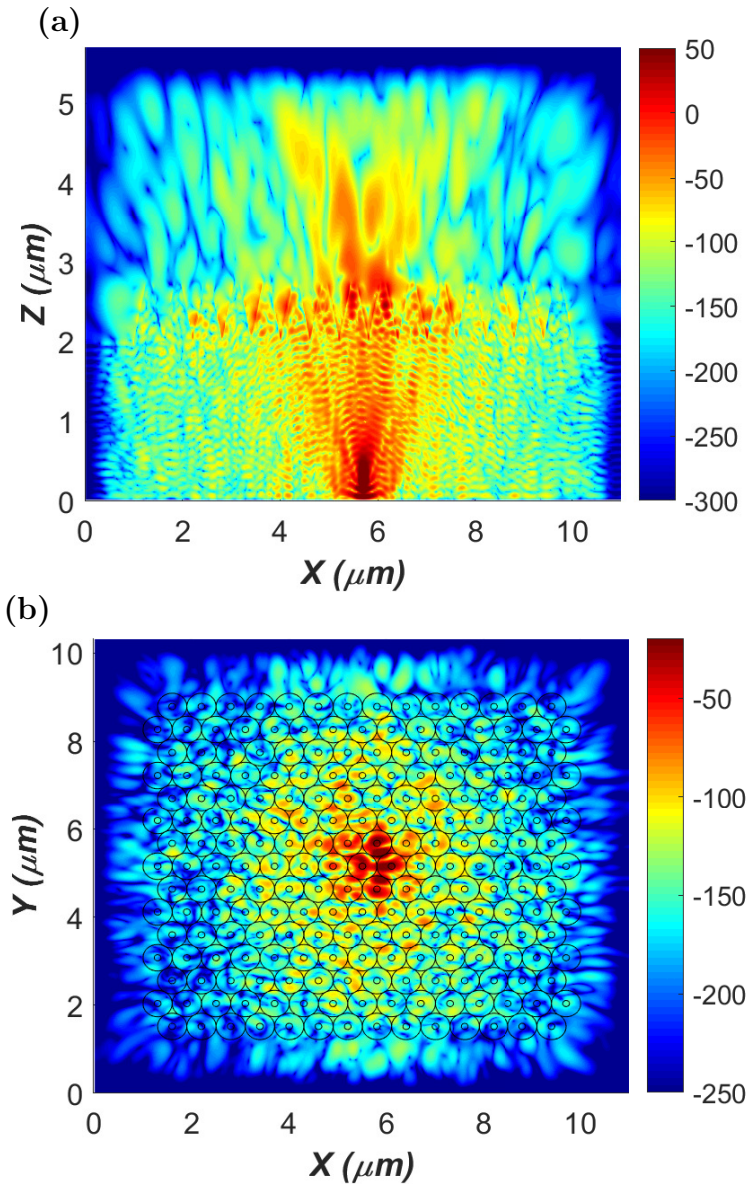

Figure 7-16: *Real part of E_x field distribution for 450 nm wavelength of nanorod structure of $\Lambda = 600$ nm in (a) xz-plane and (b) xy-plane at $z = z_{nf}$.*

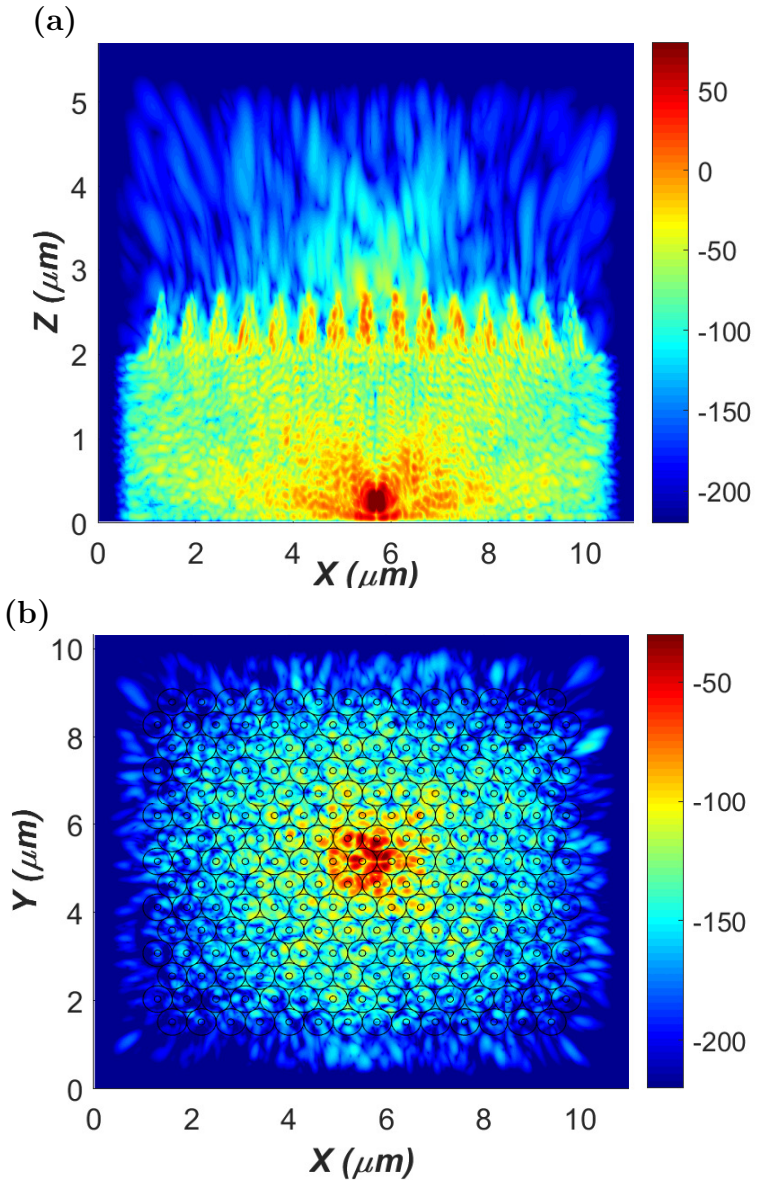

Figure 7-17: *Real part of H_z field distribution for 450 nm wavelength of nanorod structure of $\Lambda = 600$ nm in (a) xz-plane at $y = 0$ nm and (b) xy-plane at $z = z_{nf}$.*

Nanorod sample, $\Lambda = 1200nm$

From figure 7-1, the values $h = 600$ nm, $d_1 = 850$ nm and $d_2 = 360$ nm were modelled for $\Lambda = 1200$ nm. Figure 7-18(a-g) compares the far-field emission patterns obtained from PL experiment and FDTD simulation for the dipole positions 1 to 7 in figure 7-3 for emission wavelength, $\lambda = 450$ nm.

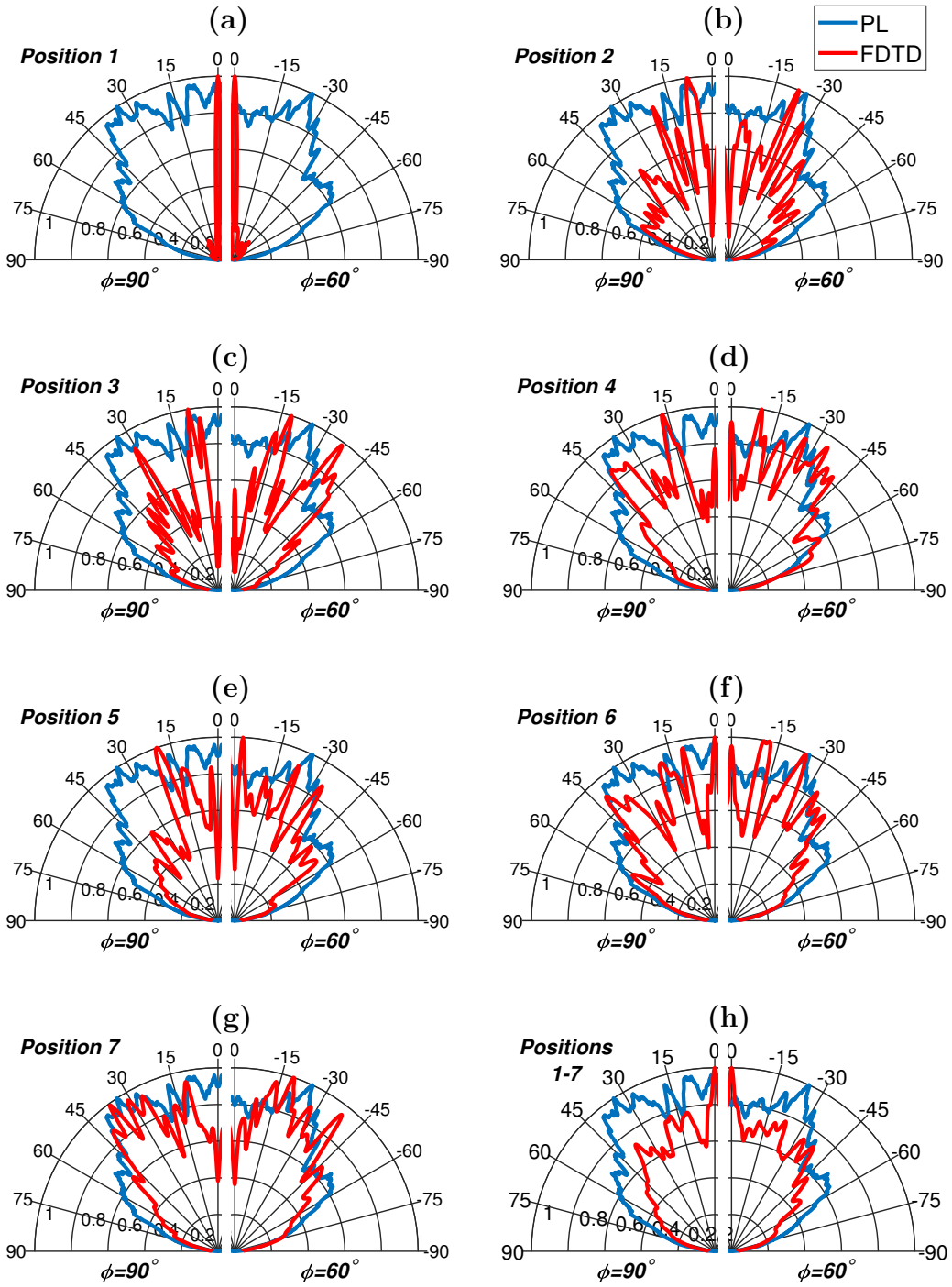

Figure 7-18: *Comparison of far-field emission patterns obtained from PL and FDTD spectrally resolved at 450 nm for fixed azimuth, $\phi = 90°$ and $\phi = 60°$ for nanorod array, $\Lambda = 1200$ nm. Far-fields from FDTD were obtained for lateral dipole positions (a) to (g) 1 to 7 and (h) integrated positions 1 to 7.*

The agreement between the results of experimental PL and FDTD is less pronounced compared to the modelling of the nanorod samples of $\Lambda = 800$ nm and $\Lambda = 600$ nm. In figures 7-18(a-e) the far-field emission patterns obtained for the dipoles at positions 1 to 6 in FDTD do not capture the overall form of the emission pattern obtained from PL in the angular range 25° to 45° at azimuth angle $\phi = 90°$. However, the results of the dipole at position 7 in figure 7-18(g) reproduce this segment very well. The emission from the PL experiment and FDTD simulation are also in reasonable agreement for the azimuth, $\phi = 60°$ in terms of the overall emission shape, although there is a shifted difference of the lobes between 10° and 20° elevation angle range.

In figure 7-18(a) for the FDTD-obtained results from the dipole at position 1, the emission is dominated by an extremely collimated beam which is focused within an angle of less than 1°. This is not observed in the corresponding PL emission pattern. The cause of this collimation is the same cause as that observed for the nanorod sample of $\Lambda = 800$ nm where strong waveguiding inside the nanorod was observed. This is shown in figure 7-19 which displays the real part of the E_x field distribution for 450 nm wavelength in the xz-plane for the dipole at position 1. As can be seen, the mode diffracts strongly from the top of the center nanorod in a focused beam resulting in the collimated emission result in figure 7-18(a).

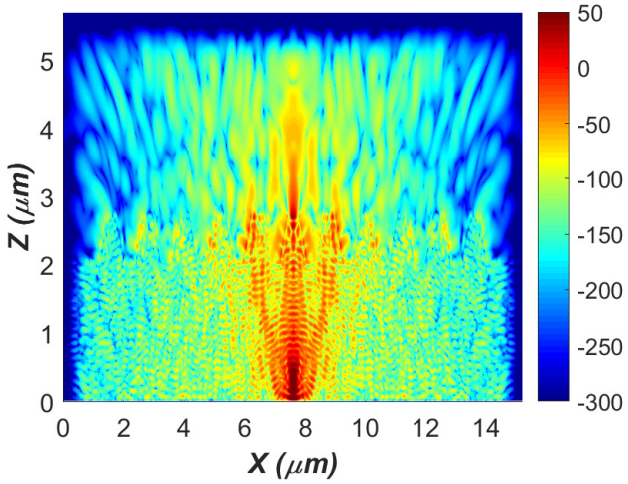

Figure 7-19: *Real part of E_x field distribution for 450 nm wavelength of nanorod structure of $\Lambda = 1200$ nm in xz-plane for dipole at position 1.*

In figure 7-18(h), the far-field emission patterns obtained from FDTD for each of the lateral dipole positions 1 to 7, in figures 7-18(a-g) were summed. In figure 7-18(h) there is some significant discrepancy between the FDTD simulation and PL experiment. This arises from the simulations for the dipoles at positions 1 to 6 producing far-field emissions that could not reproduce the overall pattern shape observed for PL between 25° to 45° for $\phi = 90°$. The emission obtained from the dipole at position 7 in figure 7-18(g) appears to provide a better match with the PL experimental results in comparison in terms of the overall emission shape.

Figure 7-20 compares the far-field emission patterns obtained from PL experiment and FDTD simulation for the dipole positions 1-7 in figure 7-3(a-g) integrated over the wavelength emission range, 420 nm to 480 nm in 5 nm increments.

In figure 7-20(a), the same intense collimation of the emission in the vertical direction was observed. A sharp peak at 0° elevation was also observed in FDTD results obtained for the dipoles at positions 2, 4, and 5 in figures 7-20(b), 7-20(d) and 7-20(e) respectively which was not observed for the results obtained experimentally in PL. Reasonable agreement of the FDTD-obtained far-field patterns with PL results were observed for the simulated dipoles at positions 3, 4, 6 and 7 in figures 7-20(c),7-20(d),7-20(f) and 7-20(g) respectively. In terms of reproducing the overall emission shape, the FDTD-obtained results for the dipole at position 7 appeared to provide the best fit.

In figure 7-20(h), the far-field emission pattern was summed over the lateral dipole positions 1 to 7, in figures 7-20(a-g) and integrated over the wavelength emission range, 420 nm to 480 nm in 5 nm increments. Here, the far-field pattern obtained from the FDTD simulations is dominated by the sharp peak at 0° elevation angle which occurred for several of the dipoles at the different lateral positions. The far-field pattern obtained from the dipole at position 7 in figure 7-20(g) provided a better fit with the results of PL experiment in comparison to figure 7-20(h).

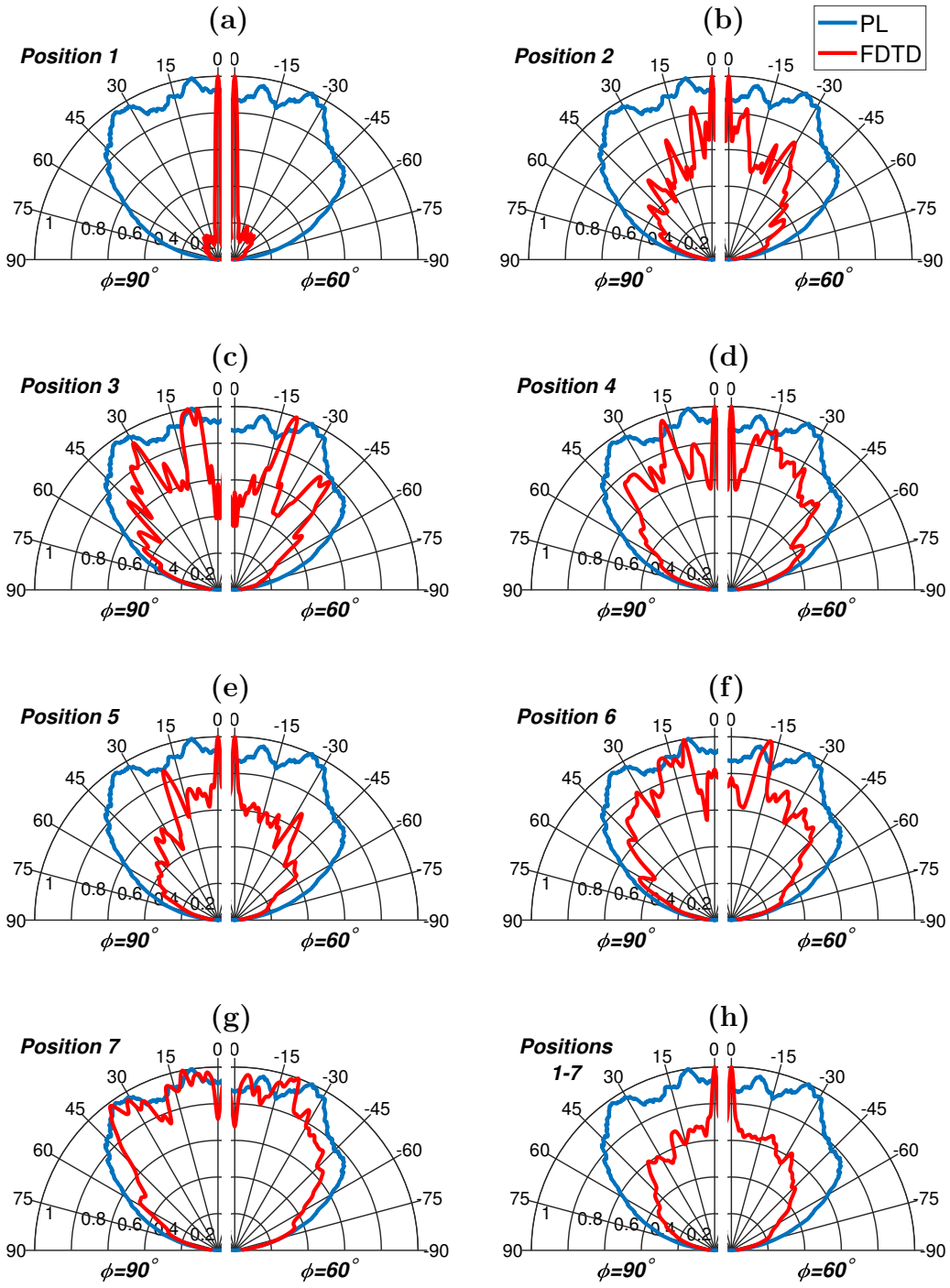

Figure 7-20: *Comparison of far-field emission patterns obtained from PL and FDTD integrated over wavelength emission for fixed azimuth, $\phi = 90°$ and $\phi = 60°$ for for nanorod array, $\Lambda = 1200$ nm. Far-fields from FDTD were obtained for lateral dipole positions (a) to (g) 1 to 7 and (h) integrated positions 1 to 7.*

The three-dimensional unnormalised hemispherical far-field emission patterns summed for all dipole positions 1-7 are shown in figures 7-21(a) and 7-21(b) corresponding to the emission spectrally resolved at 450 nm and integrated over wavelength respectively.

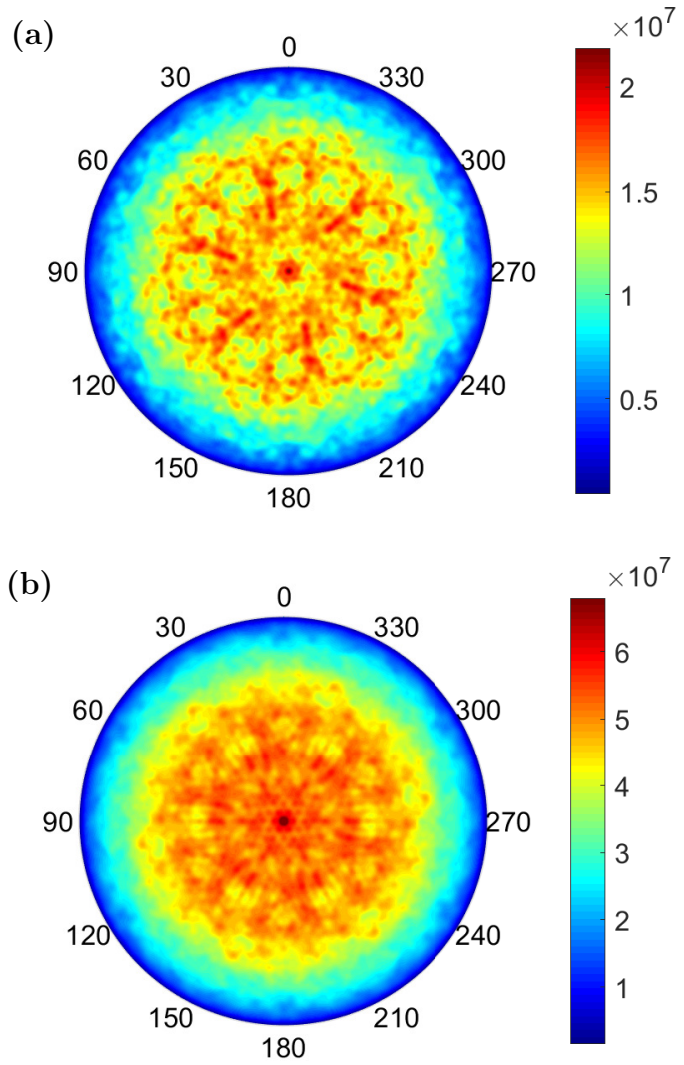

Figure 7-21: *3D unnormalised hemispherical far-field emission patterns spectrally resolved for (a)* 450 *nm and (b) integrated over wavelength for nanorod sample of* $\Lambda = 1200$ *nm.*

In figure 7-21(a), the six-fold symmetry is observed which arises from diffraction of the hexagonal arrangement of the nanorod array. The diffraction pattern is relatively well defined over a broad range of elevation. This is likely due to

the larger pitch resulting in more orders of diffraction. Furthermore, the nanorod array of the structure of $\Lambda = 1200$ nm is not closely packed and the nanorods are separated by straight facets. These facets will likely cause reflection back into the epitaxy and less scattering. The angular conditions for constructive interference will therefore be more limited and this may result in the more well-defined diffraction pattern in figure 7-21(a).

In figure 7-21(b) for the integrated emission, the six-fold diffraction pattern is weaker and the emission is dominated by strongly directional emission focused into a narrow beam in the vertical direction.

Strong collimation of the emission was observed for dipoles placed at several positions other than position 1, namely positions 2, 4 and 5 from figure 7-20 which dominated the emission in figures 7-21(a) and 7-21(b). Taking the far-field results obtained from the dipole at position 5, it was found this intense directionality in the emission occurred at the vertical dipole positions at $z_{src} = 190$ nm and $z_{src} = 300$ nm. For $z_{src} = 190$ nm, the effect was isolated to 455 nm emission wavelength and is shown in figure 7-22 (a) for both azimuth angles $\phi = 90°$ and $\phi = 60°$. The emission for the dipole at position 5 is also presented for 450 nm wavelength in figure 7-22(b) at the same vertical position of the source, $z_{src} = 190$ nm, for comparison. It is observed the intense direction beam effect is removed by shifting the emission 5 nm.

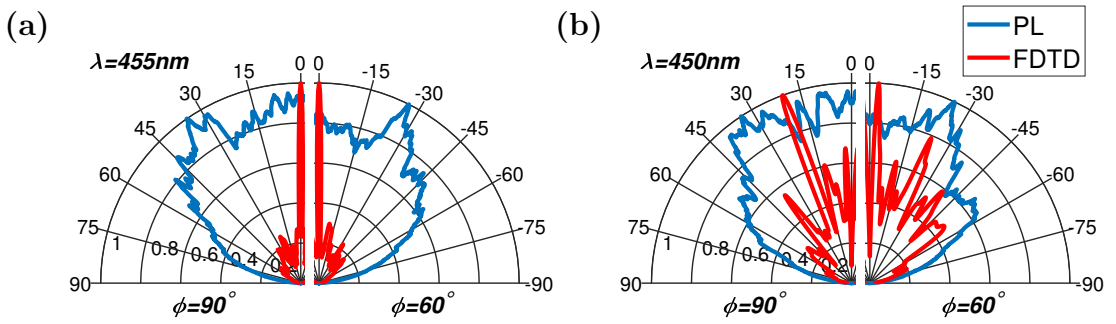

Figure 7-22: *Comparison of far-field emission patterns obtained from PL and FDTD spectrally resolved at (a) 445 nm and (b) 450 nm for fixed azimuth, $\phi = 90°$ and $\phi = 60°$ for nanorod array, $\Lambda = 1200$ nm. Dipole is at position 5 and $z_{src} = 190$ nm.*

To investigate further, the corresponding E_x near-field distributions are plotted in the xz-plane for the wavelengths 445 nm and 450 nm when the dipole is

placed vertically at $z_{src} = 190$ nm and laterally at position 5. These are shown in figures 7-23(a) and 7-23(b) respectively for each wavelength.

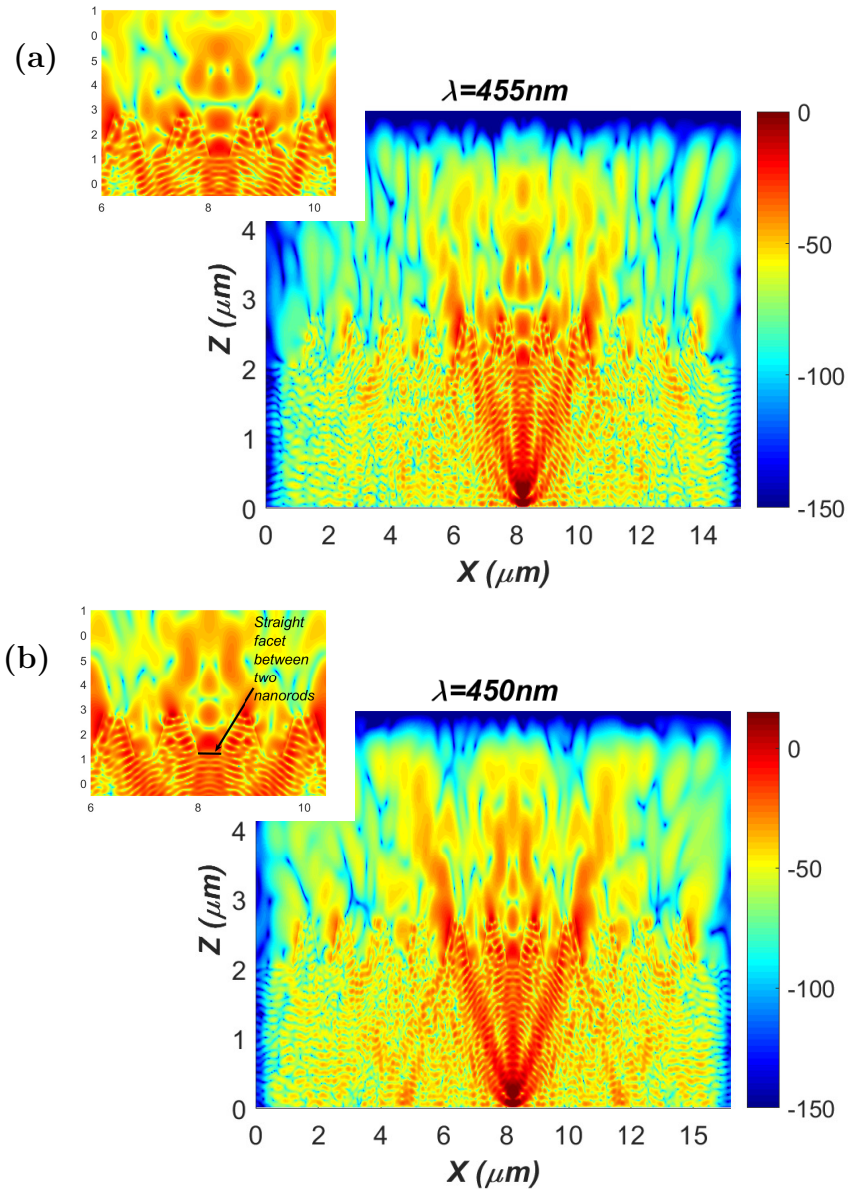

Figure 7-23: *Real part of E_x field distribution for (a) 455 nm and (b) 450 nm wavelength of nanorod structure of $\Lambda = 1200$ nm in xz-plane for dipole at position 5 and srcz $= 190$ nm.*

From figures 7-23(a) and 7-23(b) it is observed that the straight facet joining the two nanorods causes symmetric field patterns between the two nanorods.

This is magnified in the insets of the figures in 7-23. The dipole is placed below halfway between the straight facet and consequently this appears to excite these symmetric field intensities. For 450 nm wavelength, in figure 7-23(b), the field pattern formed above the straight facet between the two nanorods diffracts upwards and outwards. When the wavelength is increased to 455 nm in figure 7-23(a), the fields just above the nanorods break off and the fields just above the facet is coupled with the neighbouring nanorods. Because this field is more spread out in the near-field, it may result in the highly collimated emission in the far-field. Given how sensitive this effect is to a 5 nm wavelength shift, it may not be observed in the PL because of the potential error in the measured height of the nanorods from the SEM imaging used for the FDTD simulation.

From the comparison of the integrated far-field emission patterns in figure 7-20, it was found the emission from the dipole at position 7 reproduced the overall far-field pattern obtained from the PL experiment relatively well. The three-dimensional unnormalised hemispherical far-field emission patterns from the dipole at position 7 are shown in figures 7-24(a) and 7-24(b) corresponding to the emission spectrally resolved at 450 nm and integrated over wavelength respectively.

In figures 7-24(a) and 7-24(b), the far-field emission is concentrated at six lobes azimuthally separated by 30°. These lobes indicate diffraction from the hexagonal array of nanorods and it appears a single order is well diffracted.

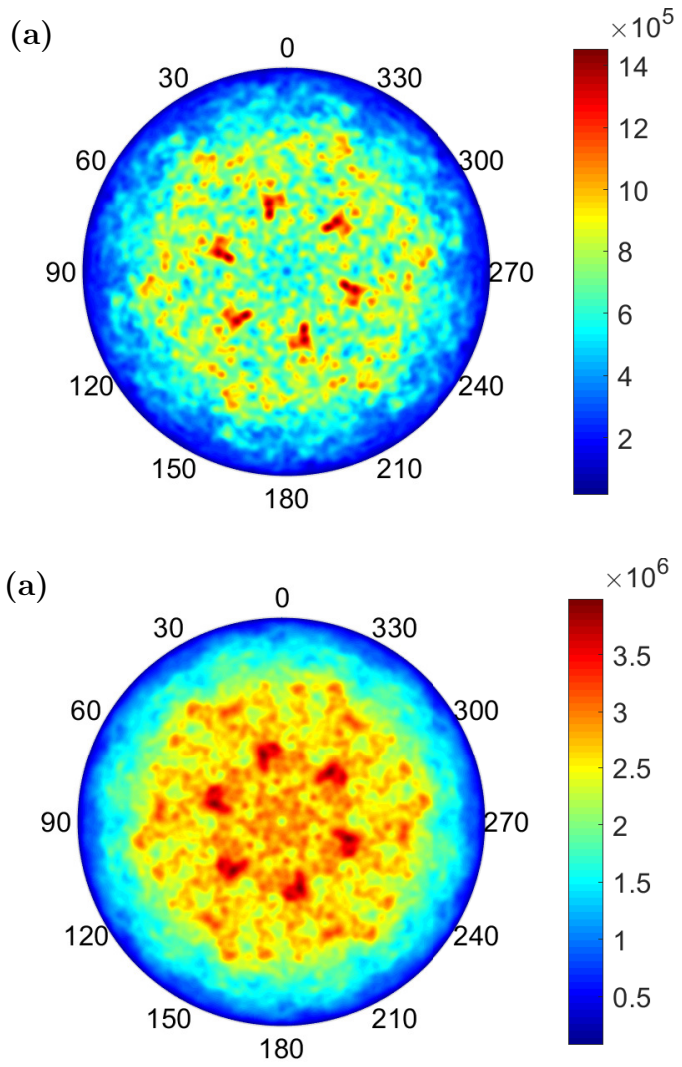

Figure 7-24: *3D unnormalised hemispherical far-field emission patterns spectrally resolved at (a)* 450 *nm and (b) integrated over wavelength for nanorod sample of* $\Lambda = 1200$ *nm.*

Figures 7-25(a) and 7-25(b) display the real part of the E_x field distribution for 450 nm wavelength. Figure 7-16(a) is in the xz-plane at $y = 0$ nm and figure 7-16(b) is for the xy-plane at $z = z_{nf}$ where the near-fields are collected for the NFFT. All of the plots are summed for the dipoles at position 7 for $z_{src} = 190$ nm, 250 nm, 300 nm for the E_x-polarised dipoles. The emission from the dipole at position 7 was taken because it was found to be in good agreement with the results obtained from PL experiment in figures 7-18(g) and 7-20(g). Therefore any features observed in the near-fields indicate what is likely occurring in the

physical samples.

In figure 7-25(a) strong scattering of the fields is observed from one side of the edge of two nanorods indicated by the black arrows. This scattering was observed for all of the emission wavelengths and results in the strong diffraction lobes observed in the three-dimensional far-field emission patterns in figures 7-24(a) and 7-24(b). Return reflections are strongly attenuated and there is light trapping inside the epitaxy represented by the dashed black arrows in figure 7-24(a). The coupling between nanorods across the array is relatively weak due to the larger pitch seperating the nanorods. This is also shown in figure 7-24(b)where the field is localised around the central and a few of the neighbouring nanorods. The scattering from the edge of the cone-shape of the nanorods appears to be only from one side of the cone, which indicates poor interaction of the fields with the nanorod array.

Figures 7-26(a) and 7-26(b) display the real part of the H_z field distribution for 450 nm wavelength. Figure 7-26(a) is in the xz-plane at $y = 0$ nm and figure 7-26(b) is for the xy-plane at $z = z_{nf}$. All of the plots are summed for the dipoles at position 7 for $z_{src} = 190$ nm, 250 nm, 300 nm for both the E_x- and E_y-polarised dipoles.

In figure 7-26(a), the field is localised inside four of the nanorods nearest to the dipole source. As one progresses further across the array, the field is weakly visible along the outer edge of the cone-shape of the nanorods. In figure 7-26(b) there is fringing of the fields indicating points of constructive and destructive interference.

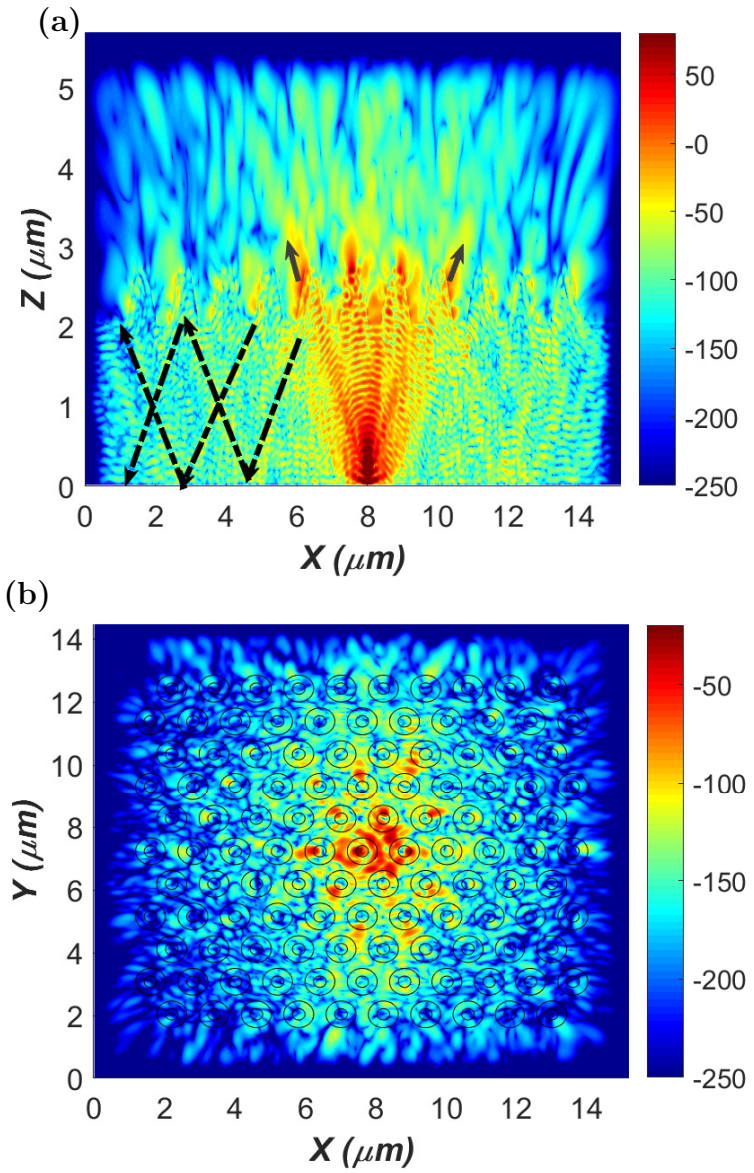

Figure 7-25: *Real part of E_x field distribution for 450 nm wavelength of nanorod structure of $\Lambda = 1200$ nm in (a) xz-plane and (b) xy-plane at $z = z_{nf}$.*

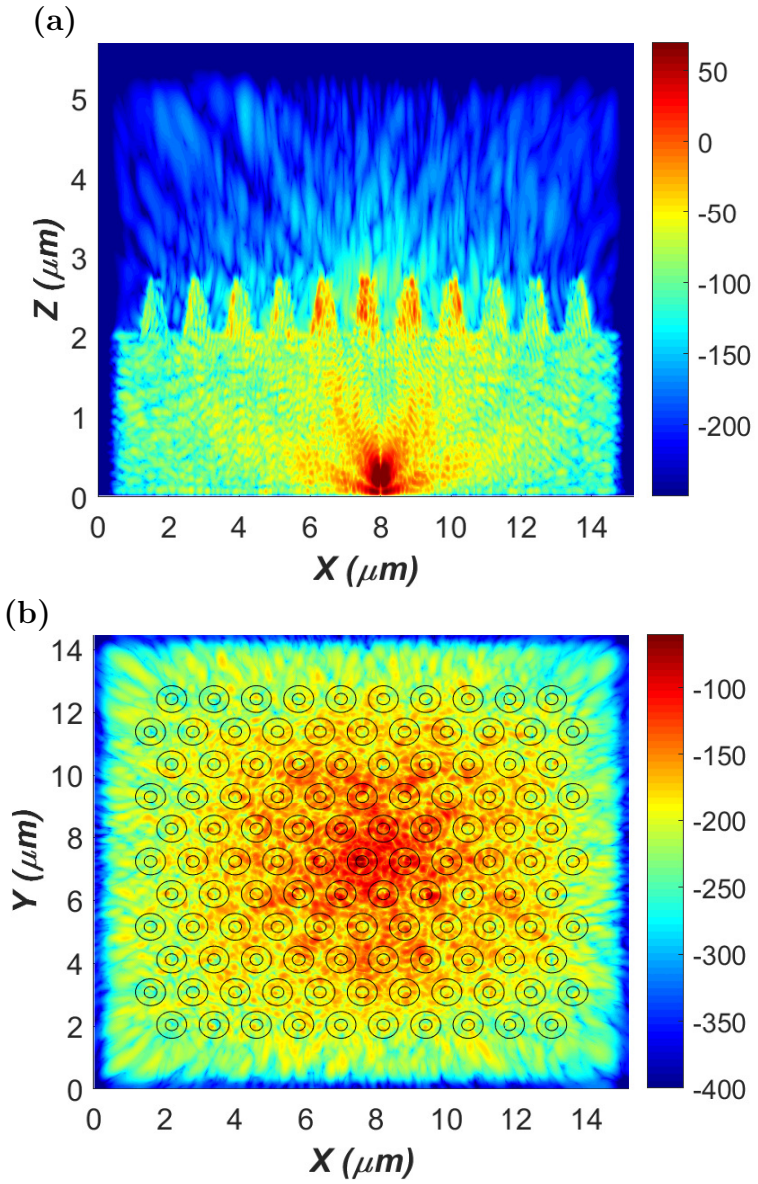

Figure 7-26: *Real part of H_z field distribution for 450 nm wavelength of nanorod structure of $\Lambda = 1200$ nm in (a) xz-plane at $y = 0$ nm and (b) xy-plane at $z = z_{nf}$.*

7.1.4 Discussion

From the angular far-field distributions obtained in FDTD, values of the directionality, D, light extraction efficiency, η_{lee} and enhancement factor, F were calculated using the methods described in chapter 4. Here, the values for the far-

field emission from the dipole at position 7 were taken because of the improved emission profile fit obtained for the nanorod structure of $\Lambda = 1200$ nm. Table 7.1 summarises the directionality values measured for all three nanorod structures using FDTD. The results obtained from experimental PL in chapter 5 have also been included for comparison.

	FDTD		**PL**	
$\Lambda(nm)$	$\boldsymbol{D}$ **($\lambda = 450$ nm)**	***D* (Integrated)**	$\boldsymbol{D_{2D}}$ **($\lambda = 450$ nm)**	$\boldsymbol{D_{2D}}$ ***(Integrated)***
1200	0.77	0.80	0.88	0.88
800	0.99	0.96	1.07	1.07
600	1.04	0.98	1	0.98

Table 7.1: *Summary of directionality values, D and D_{2D}, obtained from FDTD simulations and PL for the three nanorod structures of $\Lambda = 1200$ nm, 800 nm and 600 nm.*

Here the directionality for the FDTD-obtained far-field pattern is defined as the ratio of the normalised emission power of the nanorod structure, P_{ext}, to the normalised emission power of Lambertian emission within $\pm 15°$ elevation cone from the normal and integrated over azimuth, ϕ:

$$D = \frac{\int_0^{360} \int_0^{15} \bar{U}|_{PhC}(\theta, \phi) \sin(\theta)\ \mathrm{d}\phi\, \mathrm{d}\theta}{\int_0^{360} \int_0^{15} \bar{U}|_{pla.}(\theta, \phi) \sin(\theta)\ \mathrm{d}\phi\, \mathrm{d}\theta} \tag{7.1.2}$$

The directionality of the emission obtained from PL experiment is the average value of D measured for each azimuth slice, $\phi = 90°$ and $\phi = 60°$. Because the emission measured from the PL is not integrated over solid angle, directionality is defined over a single elevation segment within $\theta = \pm 15°$ and thus is denoted D_{2D} in table 7.1.

Table 7.2 summarises light extraction efficiency, η_{lee} and the enhancement factors, F, measured for all three nanorod structures using FDTD. The values of F obtained from experimental PL in chapter 5 have also been included for comparison.

	FDTD		PL
$\boldsymbol{\Lambda}(nm)$	$\boldsymbol{\eta_{lee}}$ (%)	$\boldsymbol{F}$	$\boldsymbol{F_{2D}}$
1200	11.9	2.79	8.50
800	16.8	3.93	9.86
600	16.6	3.89	8.78

Table 7.2: *Summary of η_{lee} and enhancement factor values, F and F_{2D}, obtained from FDTD simulations for the three nanorod structures of Λ = 1200 nm, 800 nm and 600 nm.*

The value of η_{lee} was calculated by first obtaining the output power of a single dipole in homogeneous dispersive GaN, P_{in}, and then calculating the extracted power, P_{ext} from the nanorod structure using the near-fields measured at $z = z_{nf}$ as per the method discussed in section 4.2. Light extraction efficiency was calculated from the following equation:

$$\eta_{LEE} = \frac{P_{ext}}{P_{in}} \tag{7.1.3}$$

The enhancement factor, F, was calculated for the FDTD simulated results by dividing the value of η_{lee} of the nanorod structure by that of the planar structure. In section 6.1.3, a value of $\eta_{lee} = 4.27\%$ was obtained for the planar structure simulated in FDTD. The enhancement factor of the emission obtained by PL was calculated by integrating the single azimuth slices over elevation. Therefore this measure of the enhancement is denoted F_{2D}.

An issue arose for the calculation of F and η_{lee} whereby the values were dependent on the lateral size of the computational cell. This is because for a larger lateral size of the nanorod array, higher order guided modes trapped inside the epitaxy will escape and contribute to a larger value of F [158]. For the nanostructures of $\Lambda = 600$ nm and $\Lambda = 800$ nm, due to the similar lateral size, a comparison could be made. However for the nanorod structure of $\Lambda = 1200$ nm where an $N = 11 \times 11$ nanorod array was used, the lateral dimensions were much larger. When N was increased from 7 to 11 the value of η_{lee} increased from 11.9% to 17.0%. To make comparison between all of the nanorod structures, the lateral size of the $\Lambda = 1200$ nm was reduced to a 7×7 nanorod array which is of similar size to the other structures. It is interesting to note that in reference [161], lower

values of η_{lee} were measured and this was stated to be due to the relatively large lateral size compared to the vertical which resulted in more light propagating into the sides of the PML.

In table 7.1, the nanorod structure with $\Lambda = 600$ nm demonstrated the highest directionality in the FDTD simulations. This is in contrast to the experimental PL results where the nanorod structure of $\Lambda = 800$ nm exhibited a higher value of directionality for a single azimuth slice, D_{2D}. In figure 7-7(h) which compares the integrated far-field emission of the structure, $\Lambda = 800$ nm, for the results obtained PL, there are two high intensity lobes of width around 10° within the ±15° emission cone which contributes to the higher observed directionality. In the FDTD-obtained far-field however, the width of these lobes is around 4° and this will result in the value of D being underestimated. It should be noted that similarly for the nanorod structure $\Lambda = 600$ nm, the emission within ±15° in figure 7-14(h) obtained from PL experiment was not as accurately reproduced in the FDTD simulation.

The discrepancies between the FDTD- and PL-obtained far-field patterns are likely due to or at least exacerbated by the non-uniformity of the nanorod dimensions across the physical samples arising from the fabrication process. This non-uniformity is more apparent for smaller pitch nanorod arrays and it is demonstrated in figure 7-27 which compares the nanorod array geometry for $\Lambda = 600$ nm set up in the FDTD simulation in figure 7-27(a) and the corresponding nanorod array of the physical sample in the SEM image in figure 7-27(b). Examples of the non-uniformity in both the spacing between the nanorods and the top diameter are indicated in the SEM image by black arrows and magenta circles respectively. In the FDTD simulation, the nanorods are approximated as identical cones shown in figure 7-27(a). The non-uniformity would result in more scattering which may contribute to the emission within ±15° observed for the measured PL in figure 7-14(h). Because in the FDTD simulations the nanorods are identical and equally spaced, this would result in stricter angular conditions for constructive interference figure 7-14(h).

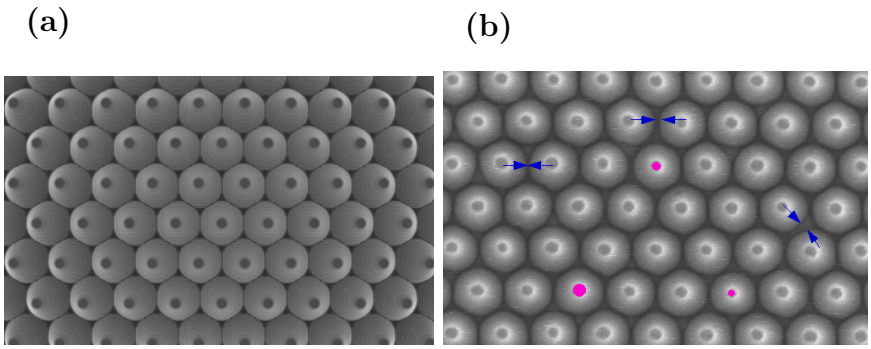

Figure 7-27: *Comparison of nanorod array geometry for structure of* $\Lambda = 600$ *nm of (a) simulated FDTD model and (b) SEM image of physical sample where non-uniformity is indicated by the black arrows and magenta circles.*

From table 7.1, the structure of $\Lambda = 1200$ nm displayed significantly lower directionality. This was also observed in the PL experiments.

From table 7.2, the values of F calculated in FDTD were far smaller in magnitude to those obtained from PL experiment. As was discussed in section 5.2.4, absolute values of the enhancement factor in PL are unreliable because of the in-coupling effect. There is also the issue of the smaller size of the computational cell relative to the physical size of the samples structure used in the PL experiments.

Nevertheless, the trend of F obtained from FDTD for the nanorod samples was similar with those obtained from PL experiment. From table 7.2, the nanorod structure of $\Lambda = 1200$ nm displayed the lowest values of F and η_{lee}. Those obtained for the structures of $\Lambda = 800$ nm and $\Lambda = 600$ nm were relatively similar differing by only a 1% increase for the former structure. Both of these structures displayed values of F a factor of 1.4 larger than the nanorod structure of $\Lambda = 1200$ nm. This indicates the light extraction is highly dependent on the arrays being closely packed to both increase scattering and coupling between the nanorods. This is in agreement with the study in [80] where it was found the reflectivity decreased for complete tiling where the bases of the nanorods touched.

To compare the light propagation mechanisms of the three nanorod structures, the near-fields are re-plotted on the same scale. Figures 7-28(a-c) display the real part of the E_x field distribution for 450 nm wavelength of the structures $\Lambda = 1200$ nm, 800 nm and 600 nm respectively for xz-plane (at $y = 0$ nm). All of the near-field plots are summed for the dipoles at position 7 at $z_{src} = 190$ nm, 250 nm,

300 nm for the E_x-polarised dipoles only.

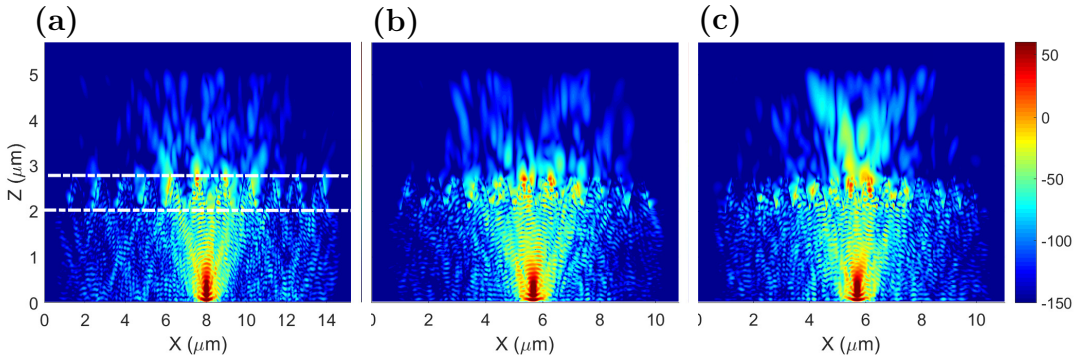

Figure 7-28: *Real part of E_x field distribution for 450 nm wavelength for xz-plane of nanorod structure with (a) $\Lambda = 1200$ nm, (b) $\Lambda = 800$ nm and (c) $\Lambda = 600$ nm.*

From figure 7-28(a), it can be seen for the larger nanorod seperation for the $\Lambda = 1200$ nm structure there is more reflection inside the epitaxy. The other structures in figures 7-28(b) and 7-28(c) show similar field distributions. For the nanorod structure of $\Lambda = 600$ nm in figure 7-28(c), their is a marked 'volcano-like' plume of radiation immediately above the two central nanorods.

To better quantify the field variation differences between the nanorod structures, line slices of the intensity of the field were taken at the top and base of the nanorods as indicated by the dashed lines in figure 7-28(a). These line slices are shown in figure 7-29(a) for the nanorod base position and figure 7-29(b) for the nanorod top position.

In both figures of 7-29, the intensity of the E_x field is generally lower across the nanorod array for the structure of $\Lambda = 1200$ nm, which indicates less coupling of the fields between adjacent nanorods relative to the other two nanorod structures. This lack of coupling manifests as a reduced value of the directionality, D. At the base position in figure 7-29(a), the field variation for both nanorod structures of $\Lambda = 800$ nm and 600 nm are similar. Towards the top of the nanorods in figure 7-29(b), the intensity across the $\Lambda = 600$ nm array is just slightly lower than that across the $\Lambda = 800$ nm array. This may indicate how the small top diameter of the nanorods of the $\Lambda = 600$ nm array act to decouple the fields.

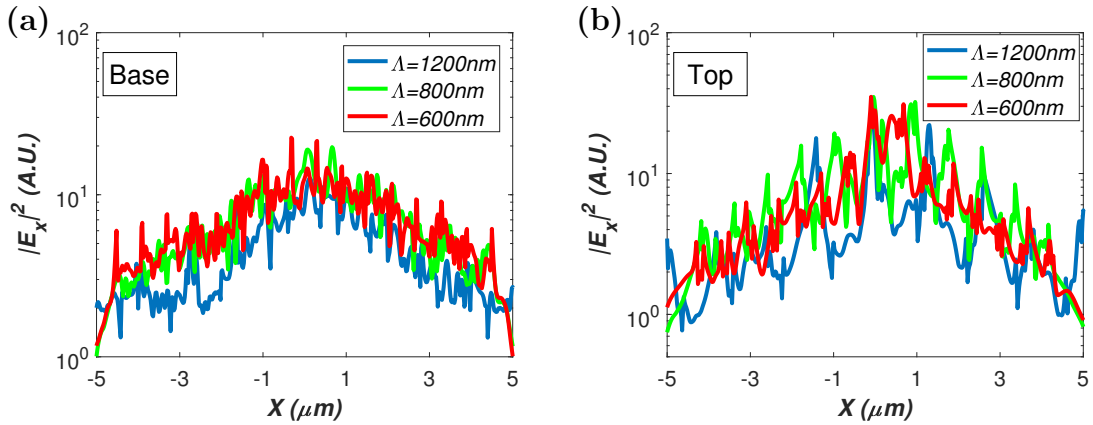

Figure 7-29: *Intensity of E_x field in the xz-plane at vertical positions corresponding to (a) the top of the nanorods and (b) the base of the nanorods as indicated in figure 7-28(a) for the three structures.*

Figures 7-30(a-c) display the real part of the H_z field distribution for 450 nm wavelength of the structures $\Lambda = 1200$ nm, 800 nm and 600 nm respectively for the xz-plane (at $y = 0$ nm). All of the near-field plots are summed for the dipoles at position 7 at $z_{src} = 190$ nm, 250 nm, 300 nm for the E_x-polarised dipoles only. The insets display a close up of the center nanorod and its adjacent neighbour on the right. The scale has been more limited to better isolate any dominant effects inside the nanorods.

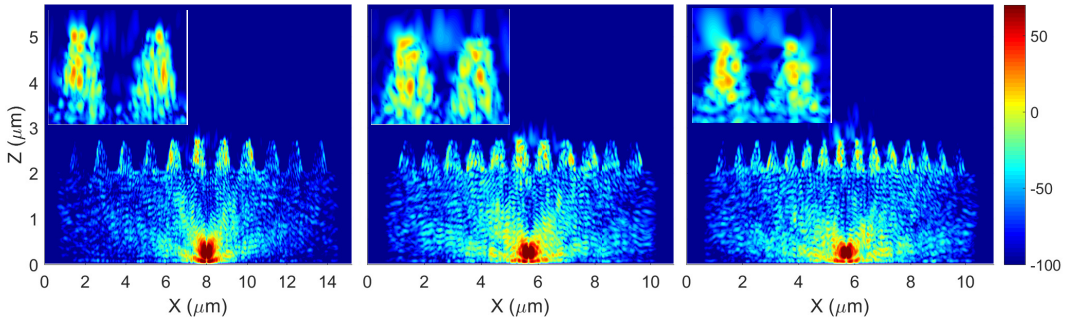

Figure 7-30: *Real part of H_z field distribution for 450 nm wavelength for xz-plane of nanorod structure with (a) $\Lambda = 1200$ nm, (b) $\Lambda = 800$ nm and (c) $\Lambda = 600$ nm. Insets are the corresponding close-ups of the center nanorod and its adjacent neighbour on the right.*

From the figures of 7-30, the intensity of the fields inside the nanorods drops

as one progresses further from the center nanorod. From the insets of figures 7-30(a-c) there are regions of relatively high intensity inside the nanorods. For the $\Lambda = 800$ nm structure, the magnitude of these was larger compared to the other nanostructures: inside the nanorod, the field magnitude ranged from 18 to 30 dB compared with 14 to 18 dB of $\Lambda = 1200$ nm and 15 to 20 dB of $\Lambda = 600$ nm.

Similarly to figure 7-29, line slices of the intensity of the field were taken at the top and base of the nanorods as indicated by the dashed lines in figure 7-28(a). These line slices are shown in figure 7-31(a) for the nanorod base position and figure 7-31(b) for the nanorod top position.

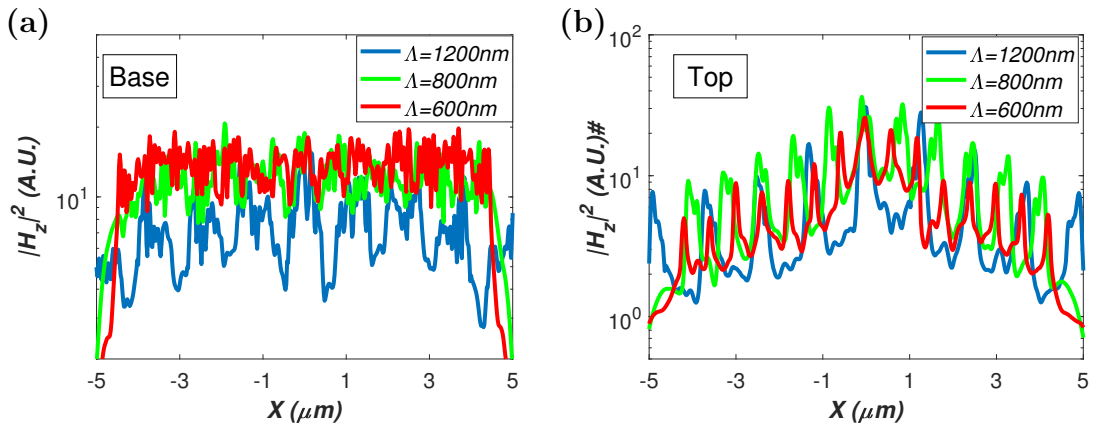

Figure 7-31: *Intensity of H_z field in the xz-plane at vertical positions corresponding to (a) the top of the nanorods and (b) the base of the nanorods as indicated in figure 7-28(a) for the three structures.*

In both figures of 7-31, the intensity of the H_z field is generally lower across the nanorod array with $\Lambda = 1200$ nm. In figure 7-31(a) at the base of the nanorods, the fields are more localised inside the nanorods for the array of $\Lambda = 1200$ nm because they are further apart and the facet seperating them prevents the fields escaping. At the base position in figure 7-31(a), the field variation for both nanorod structures of $\Lambda = 800$ nm and 600 nm are similar. Towards the top of the nanorods in figure 7-29(b), the intensity across the $\Lambda = 800$ nm array is slightly higher than that across the $\Lambda = 600$ nm array.

7.2 Summary

The three nanorod samples identified by pitches, $\Lambda = 1200$ nm, 800 nm and 600 nm were simulated in FDTD using the model developed in chapter 6. The dimensions were obtained from SEM imaging in section 5.1.3. The simulations were performed for seven lateral dipole positions within a unit cell of the hexagonal array and for the three different distances from the reflector to model the positions of the quantum wells (QWs) in the active region. From comparison of the FDTD-obtained far-field emission patterns with those obtained from experimental PL, good agreement was found in terms of reproducing the overall shape of the angular emission. Emission from the dipole at position 7 indicated in figure 7-3 provided the best correlation with PL experiment when considering individual dipoles. The dipole at position 1 was found to result in strong waveguiding effects.

Calculated values of the directionality, D, from FDTD displayed some disagreement with the trend observed in PL experiment between the nanorod structures of $\Lambda = 800$ nm and $\Lambda = 600$ nm. The latter displayed a slightly larger value in FDTD. This discrepancy is likely due to the more non-uniform geometry of the $\Lambda = 600$ nm array across the physical sample as evident in SEM imaging, in addition to the overall error in the measured dimensions used in FDTD. The trend in FDTD simulation and PL experiment were in agreement for the structure of $\Lambda = 1200$ nm which exhibited a significantly lower value of D. For this structure, strong collimation of the emission observed at 0° in the vertical direction. This effect was likely due to some form of standing waves arising from the straight facet which separates the nanorods. The lower value of D for the $\Lambda = 1200$ nm structure was due to reduced coupling between neighbouring nanorods.

The nanorod structures of $\Lambda = 800$ nm and $\Lambda = 600$ nm displayed similar enhancement factors, F and light extraction efficiency values, η_{lee}, the latter value being 16.8% and 16.6% respectively. These were around a factor of 1.4 greater than that of the structure of $\Lambda = 1200$ nm for which $\eta_{lee} = 11.9\%$ was calculated. Good agreement was found in the trend of F between FDTD simulation and PL experiment. The increased enhancement of the nanorod structures compared with the planar was mostly due to scattering from the outside edges of the cones. Light trapping was increased for the $\Lambda = 1200$ nm array because the nanorods

were not closely-packed.

For all three structures, light trapping inside the epitaxy was still observed and the directionality was less or comparable to Lambertian emission. Ideally one would like deeper-etched nanorods to extract the light trapped inside the epitaxy (see section 2.4.4) and a small array pitch, Λ, to increase coupling between adjacent nanorods, thus increasing directionality. Making the nanorods vertical would reduce the scattering dependence and thus improve the control (or predictability) of the directionality. Fabricating and measuring many different nanorod structures is time consuming and uses costly resources. However, using the developed FDTD model it is possible to obtain a reliable prediction of the optical behaviour which will help determine if the more complicated fabrication process is worth any observed increase in performance. This is the subject of the next chapter.

Chapter 8

Changing Parameters of Nanorod Structure.

8.1 Introduction

In the previous chapter it was demonstrated that the shape of the nanorod i.e. the tapering profile or conical shape can strongly impact the LED properties such as the light extraction or directionality.

From the discussion in section 2.4.4, it has been reported that the optimisation of the nanorod configuration, aspect ratio and profile can enhance the LED properties. For example, the light extraction was reportedly increased for larger etch depth because there was greater coupling between the modes inside the epitaxy and the PhC. In section 2.4.4 it was discussed how for thin-film vertical devices that the directivity also increased with etch depth of air holes [16] on thin-film vertical devices. The effect of directionality and light extraction enhancement on pitch and radius in previous work typically required an optimisation whereby the diameter and pitch of the array were varied until a maximum of the LED parameter in question was reached [86]. Theoretically, the more coupled the fields are just above the structure then the more directional the far-field emission should be. Therefore one may assume a nanorod array which is closely packed i.e., large radius and small pitch would be desired, in addition to being more deeply etched into the epitaxy.

Several parameters of the nanorod structures were varied in FDTD simula-

tions to observe the subsequent effect on directionality, D, the light extraction efficiency, η_{lee}, and the enhancement factor, F.

8.2 Varying Nanorod Parameters of Nanorod Structure

The parameters that were investigated were:

(i) Increasing the base radius of the nanorods of structure $\Lambda = 1200\ nm$

(ii) Varying radius of straight nanorods of structure $\Lambda = 600\ nm$

(iii) Varying etch depth of straight nanorods of structure $\Lambda = 600\ nm$

From chapter 7, it was found that the far-field patterns obtained from simulations of the dipole at the lateral position 7 provided the best match, out of all the other positions, with those obtained from experimental PL in terms of reproducing the overall waveform. To save computational time, all subsequent FDTD simulations were run for dipoles at this lateral position only. Three positions of the dipole were set vertically above the reflector to be $z_{src} = 190\ nm$, $250\ nm$. For each of these positions, two separate simulations were run for the E_x- and E_y-polarised dipoles. The far-field radiation patterns, U, were summed for the two polarised dipoles as follows:

$$U = \frac{U_{E_x} + U_{Ey}}{2} \tag{8.2.1}$$

The models developed in chapters 6 and 7 were used to simulate the structures. The near-fields were measured at the vertical distance z_{nf} above the nanorod array and then a near-to-far-field transform (NFFT), discussed in section 4-5 was applied. From the obtained far-field emission patterns, the LED parameters, D, η_{lee} and F were extracted as per the methods discussed in chapter 4.

The directionality, D, was defined within a $\pm 15°$ elevation cone of the normalised emission with respect to normalised Lambertian emission:

$$D = \frac{\int_0^{360}\int_0^{15} \bar{U}|_{PhC}(\theta,\phi)\sin(\theta)\ \mathrm{d}\phi\,\mathrm{d}\theta}{\int_0^{360}\int_0^{15} \bar{U}|_{pla.}(\theta,\phi)\sin(\theta)\ \mathrm{d}\phi\,\mathrm{d}\theta} \tag{8.2.2}$$

The light extraction efficiency, η_{lee} was calculated as the extracted power measured at $z = z_{nf}$ divided by the total power emitted by the dipole:

$$\eta_{lee} = \frac{P_{ext}}{P_{in}} \tag{8.2.3}$$

The enhancement factor, F, is defined as the ratio of η_{lee} for the structure with nanorods to that of the planar structure. From section 6.1.3 this was calculated to be 4.27% and so:

$$F = \frac{\eta_{lee}}{4.27} \tag{8.2.4}$$

The results and discussion for the above list of simulations will now be presented.

8.2.1 Increasing Base Radius

In the last chapter, it was found that the nanorod structure of $\Lambda = 1200$ nm displayed the lowest value of η_{lee}. This is in part due to the limited lateral size of the computational cell, however it was also found that the straight facet between the nanorods caused light trapping inside the epitaxy as shown in figure 8-1(a) where light reflects from the facet. To gain a more quantitative insight of how significant this light trapping effect is, the FDTD simulation of the nanorod structure of $\Lambda = 1200$ nm was repeated for an increased base diameter, $d_1 = 1200$ nm so that the bases of the cones were closely packed. This is shown in figure 8-1(b) where the light is more likely to enter the nanorod and be scattered out.

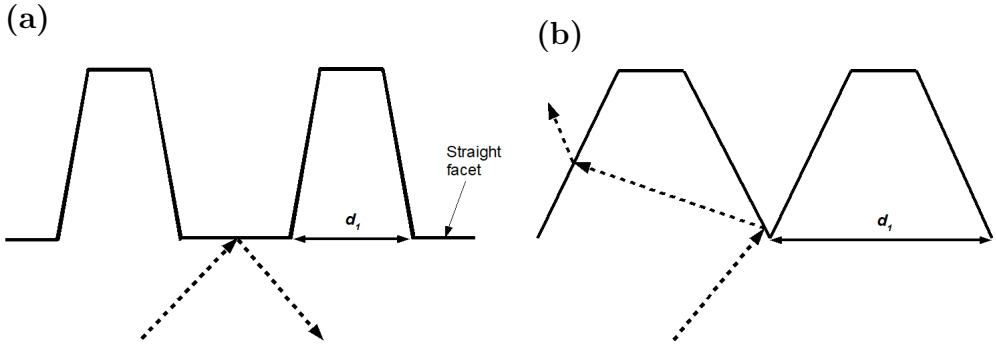

Figure 8-1: *(a) Reflection back into epitaxy from straight facets separating two nanorods. (b) Effect of increasing base diameter, d_1, where ray couples into nanorod and scatters out.*

The FDTD simulations were performed for an 11×11 nanorod array. Figure

8-2(a) displays the normalised far-field emission patterns for $\phi = 90°$ and $\phi = 60°$ spectrally resolved at 450 nm. Figure 8-2(b) shows the corresponding far-field emission patterns integrated over the wavelength emission range, 420 nm to 480 nm in 5 nm increments. The far-field emission patterns for the previous structure of where $d_1 = 850$ nm have been superimposed in dashed blue on the same plots for comparison.

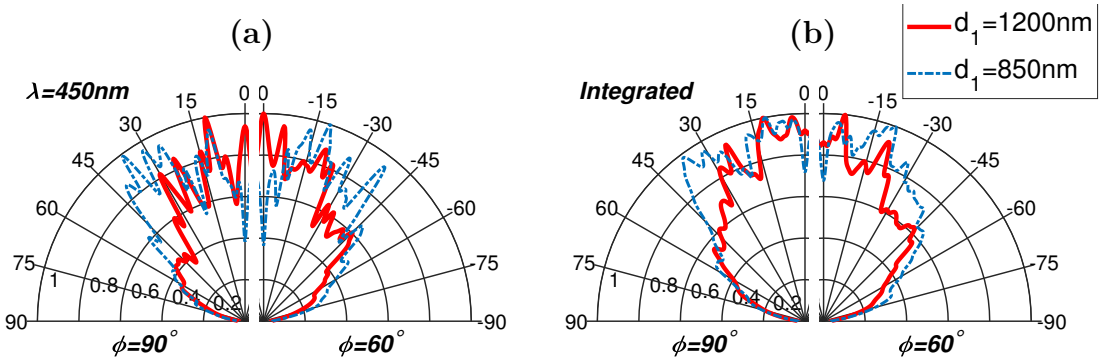

Figure 8-2: *Comparison of far-field emission patterns for the structure of* $\Lambda = 1200$ *nm where base diameter,* d_1 *is* 1200 *nm and* $d_1 = 850$ *nm for (a)* 450 *nm and (b) integrated over wavelength.*

From figure 8-2(a) it is observed that by increasing d_1, the emission intensity is reduced in the side lobes in the range $\pm 30°$ to $\pm 45°$ and larger in the vertical direction, within $\pm 15°$. Similarly this is also observed for the integrated wavelength emission in figure 8-2(b).

The three-dimensional unnormalised hemispherical far-field emission patterns are shown in figures 8-3(a) and 8-3(b) corresponding to the emission spectrally resolved at 450 nm and integrated over the wavelength emission range, 420 nm to 480 nm in 5 nm increments, respectively.

In figures 8-3(a) and 8-2(b), six-fold symmetry is observed, indicating diffraction from the nanorod array arranged in an hexagonal pattern. The emission intensity is concentrated at a ring of lobes spaced 30° apart. This was also observed for the unchanged structure in figure 7-24 in the previous chapter. The difference in figure 8-3 for the increased base diameter, is the lobes are more distributed.

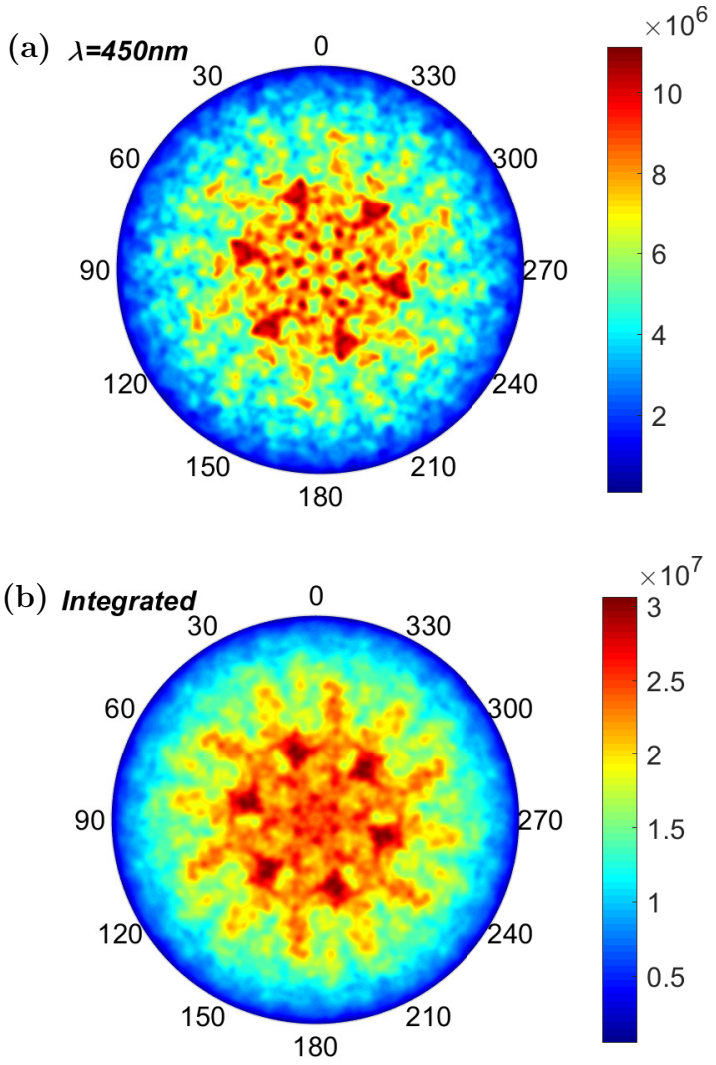

Figure 8-3: *3D unnormalised hemispherical far-field emission patterns spectrally resolved at (a)* 450 *nm and (b) integrated over wavelength for nanorod sample of* $\Lambda = 800$ *nm with* $d_1 = 1200$ *nm.*

Table 8.1 summarises the directionality, D, light extraction efficiency, η_{lee} and enhancement factor, F values. The values obtained for the unchanged structure modelled in chapter 7 have been included for comparison. It is reminded that both sets of values have been obtained from the far-field emission of the dipole at position 7.

d_1(nm)	D ($\lambda = 450nm$)	D ($Integrated$)	η_{lee} (%)	F
1200	1.07	1.01	23.9	5.60
850	0.8	0.89	11.9	2.79

Table 8.1: *Summary of directionality, D, enhancement factor, F and light extraction efficiency, η_{lee}, for nanorod structure of $\Lambda = 600nm$ for $d_1 = 1200$ nm and $d_1 = 850$ nm.*

From table 8.1, by increasing the base diameter, d_1 to 1200 nm, the directionality was increased by a factor of almost 1.4 compared to the original $d_1 = 850$ nm for an emission wavelength of 450 nm. The integrated wavelength emission displayed a 10% increase in directionality. From table 8.1 the larger value of d_1 has doubled the value of η_{lee}. This resulted in a large increase of the enhancement factor from 2.79 to 5.60.

Figures 8-4(a) and 8-4(b) display the real part of the E_x field distribution in the xz-plane for $y = 0$ and integrated over the vertical source positions for (a) $d_1 = 1200$ nm and (b) $d_1 = 850$ nm. Here the fields have been integrated over wavelength to display the overall behaviour inside the structure more clearly.

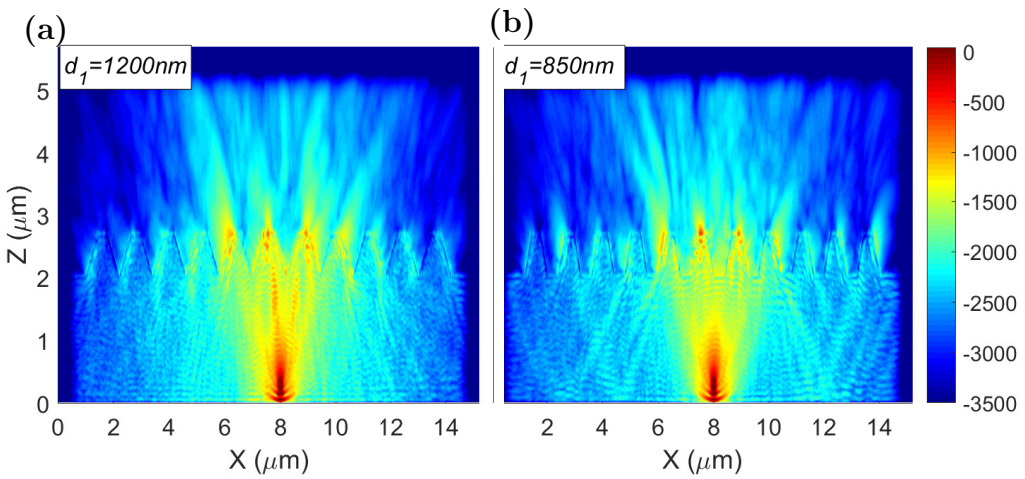

Figure 8-4: *Real part of E_x field distribution for integrated wavelength of nanorod structure of $\Lambda = 1200$ nm in xz-plane with nanorod base diameter, (a) $d_1 = 1200$ nm and (b) $d_1 = 850$ nm.*

For $d_1 = 1200$ nm in figure 8-4(a), a larger amount of light couples directly from the dipole source to the nanorods. This light is immediately radiated out of

the structure which contributes to the increased enhancement and η_{lee}. This is unlike the case of figure 8-4(b) where the light is reflected back and escapes after several bounces, as indicated by the zig-zag pattern of the fields and the higher intensity of fields along the outer edge of the cone-shaped nanorods.

Figures 8-5(a) and 8-5(b) display the real part of the E_x field distribution in the xy-plane for $z = z_{nf}$ and integrated over the vertical source positions (a) $d_1 = 1200$ nm and (b) $d_1 = 850$ nm. The fields have been integrated over the emission spectrum.

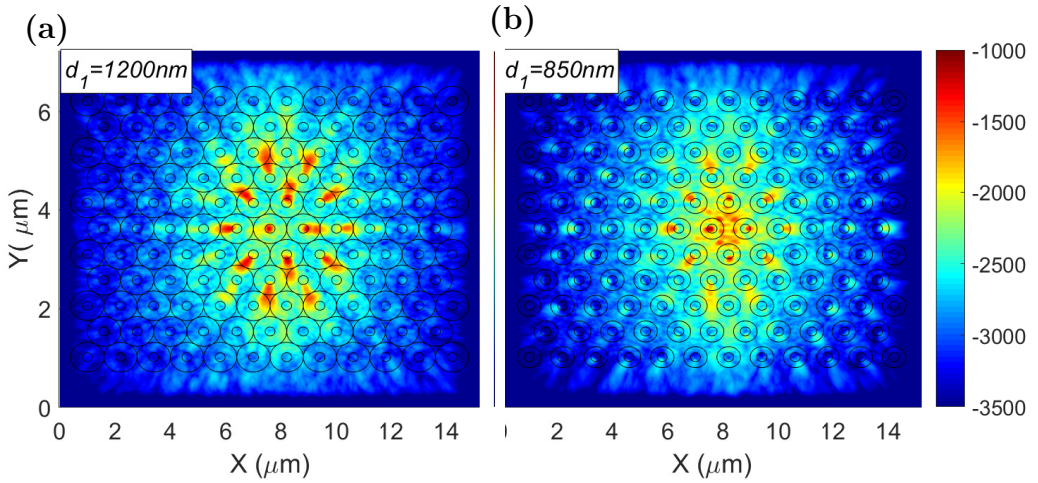

Figure 8-5: *Real part of E_x field distribution for integrated wavelength of nanorod structure of $\Lambda = 1200$ nm in xy-plane with nanorod base diameter, (a) $d_1 = 1200$ nm and (b) $d_1 = 850$ nm.*

In figure 8-5(a) where the rods are touching, the scattering off the outer edge of the cones is much larger in intensity for the increased nanorod base diameter. This is due to the larger direct coupling from the source to the nanorods. Furthermore the fields are more uniform in comparison to the fields across the nanorods of the smaller base diameter, $d_1 = 850$ nm, in figure 8-5(b). This likely is the cause of the observed increase in directionality for the nanorods with $d_1 = 1200$ nm.

8.2.2 Straight Nanorods

The lack of directionality relative to the planar structure was due to scattering from the cone-shape of the nanorods. By using straight nanorods, dominance of the scattering is reduced and thus one has better and more simple control of

the directionality as a function of pitch, radius and height. Taking the nanorod structure of $\Lambda = 600$ nm, the nanorods were made to have a vertical sidewall profile by setting the nanorod base diameter, d_1, to be equal to the top diameter, d_2, as shown in figure 8-6.

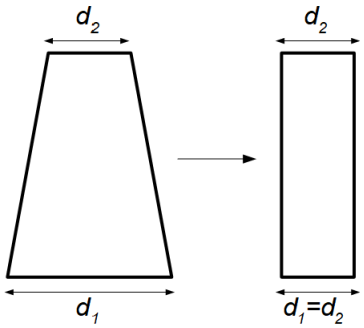

Figure 8-6: *Straightening the nanorods of nanorod structure of* $\Lambda = 600$ *nm.*

The FDTD simulations were performed for a 15×15 nanorod array. Figure 8-7(a) displays the normalised far-field emission patterns for $\phi = 90°$ and $\phi = 60°$ spectrally resolved at 450 nm. Figure 8-7(b) shows the corresponding far-field emission patterns integrated over the wavelength emission range, 420 nm to 480 nm in 5 nm increments. The far-field emission patterns for the previous structure where the nanorods are cone-shaped with $d_1 = 300$ nm have been superimposed in dashed blue on the same plots for comparison.

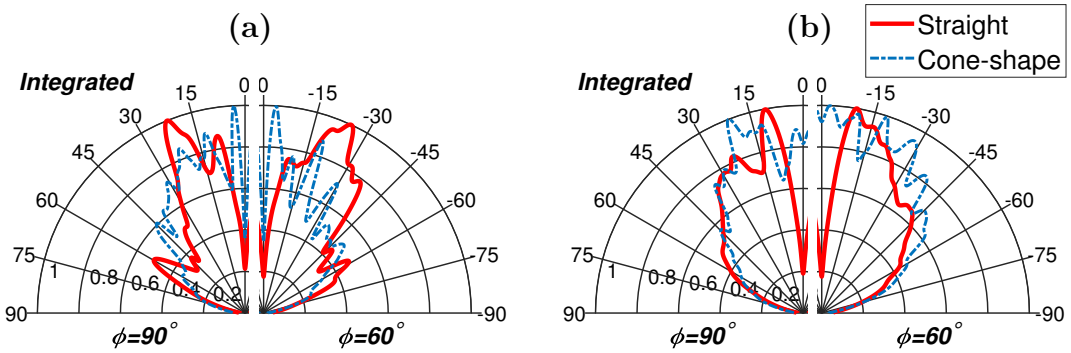

Figure 8-7: *Comparison of far-field emission patterns for the structure of* $\Lambda = 600$ *nm where nanorods are straight and cone-shaped for (a)* 450 *nm and (b) integrated over wavelength.*

In figure 8-7(a), the straight nanorods result in the far-field emission for 450

nm wavelength displaying a drop in intensity in the angular region of ±15°. For the integrated emission in figure 8-7(b), the straight nanorods also result in minimal intensity at at 0° elevation but there are high intensity lobes that fall within ±15° which contribute to the directionality.

The three-dimensional unnormalised hemispherical far-field emission patterns are shown in figures 8-8(a) and 8-8(b) corresponding to the emission spectrally resolved at 450 nm and integrated over emission wavelength respectively.

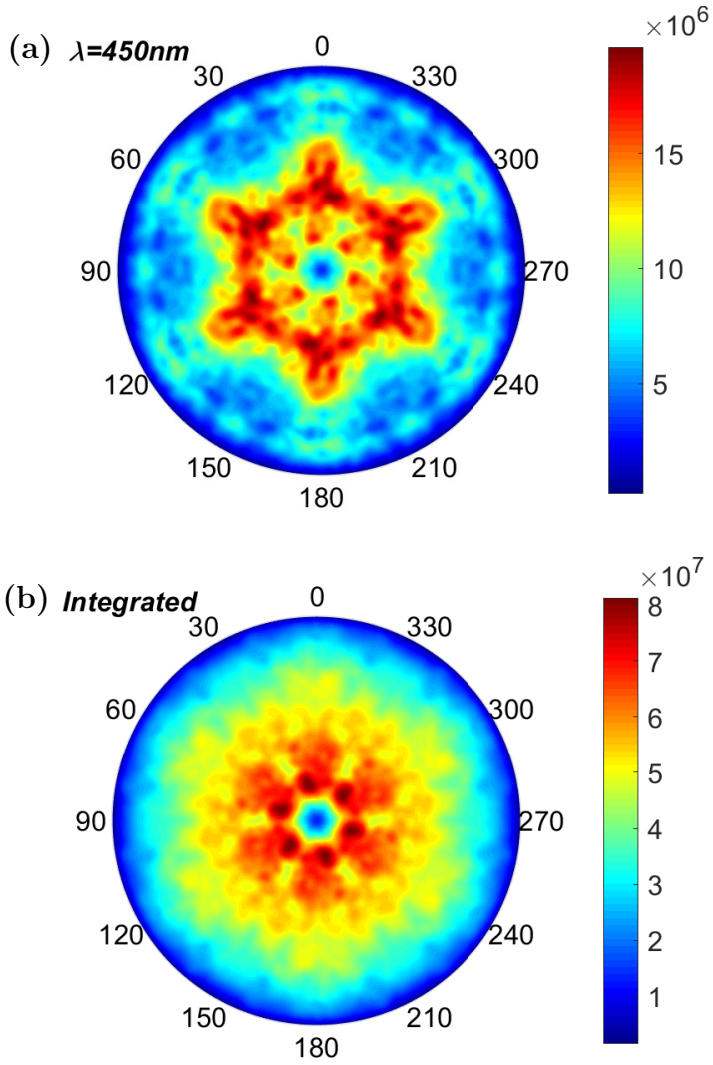

Figure 8-8: *3D unnormalised hemispherical far-field emission patterns spectrally resolved at (a)* 450 *nm and (b) integrated over wavelength for nanorod structure of* $\Lambda = 600$ *nm with* $d_1 = d_2 = 140$ *nm.*

In figures 8-8(a), strong emission intensity is observed within a ring. It is likely the large separation of neighbouring nanorods and their straight shape restrict the allowed conditions for constructive interference. In figure 8-8(b) for the integrated emission, this intense ring is concentrated nearer to 0° elevation, resulting in increased directionality.

Table 8.1 summarises the directionality, D, light extraction efficiency, η_{lee} and enhancement factor, F values. The values obtained for the unchanged structure modelled in chapter 7 have been included for comparison.

$\boldsymbol{d_1, d_2}$(nm)	$\boldsymbol{D}$ ($\lambda = 450nm$)	$\boldsymbol{D}$ (Integrated)	$\boldsymbol{\eta_{lee}}$ (%)	$\boldsymbol{F}$
140, 140 (straight)	0.93	1.01	10.0	2.34
600, 140 (cone)	1.00	0.95	16.6	3.89

Table 8.2: *Summary of directionality, D, enhancement factor, F and light extraction efficiency, η_{lee}, for nanorod structure of $\Lambda = 600nm$ for $d_1 = 140$ nm and $d_1 = 600$ nm.*

From table 8.2, comparison with the cone-shaped nanorod structure shows the directionality is slightly increased for the wavelength-integrated far-field emission when the nanorods are made to have a straight profile. It appears to be reduced however for the far-field emission at 450 nm wavelength. This is due to the strong drop in intensity in the vertical emission direction for the straight nanorods as shown in figure 8-7(a).

The listed values of η_{lee} and F in table 8.2 indicate the light extraction is strongly reduced from straightening the nanorods. From the results in the previous section and those in section 7.1.4, this is due to the straight facets between adjacent nanorods causing light trapping and the lack of scattering. The reduced light extraction indicates that for the straight nanorods, the random nature of the scattering is no longer as dominant.

Figures 8-9(a) and 8-9(b) display the real part of the E_x field distribution in the xz-plane for $y = 0$ and integrated over the vertical source positions for the straight nanorods and the cone-shaped nanorods respectively. The fields have been integrated over wavelength.

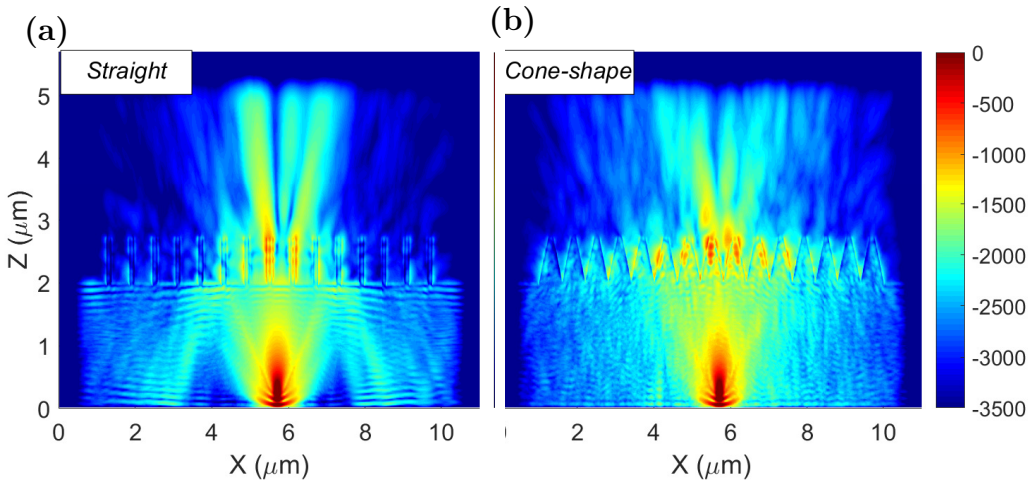

Figure 8-9: *Real part of E_x field distribution for integrated wavelength of nanorod structure of $\Lambda = 600$ nm in xz-plane with (a) straight nanorods of $d_1 = d_2 = 140$ nm and (b) cone-shaped nanorods of $d_1 = 600$ nm and $d_2 = 140$ nm.*

From figure 8-9(a), the straight nanorods result in light trapping due to the straight facets between adjacent rods as indicated by the zig-zag pattern and Fabry-Perot fringing of the field inside the epitaxy. With increasing $+z$ distance from the top of the nanorod array it can be seen that constructive interference of the fields results in three distinctive beams. Compared with the fields in figure 8-9(b), the scattering from the cones results in many constructive interferences. Inside the straight center nanorod of figure 8-9(a) there appears to be a standing wave pattern of the field.

Figures 8-10(a) and 8-10(b) display the real part of the E_x field distribution in the xy-plane for $z = z_{nf}$ and integrated over the vertical source positions for (a) straight nanorods and (b) cone-shaped nanorods.

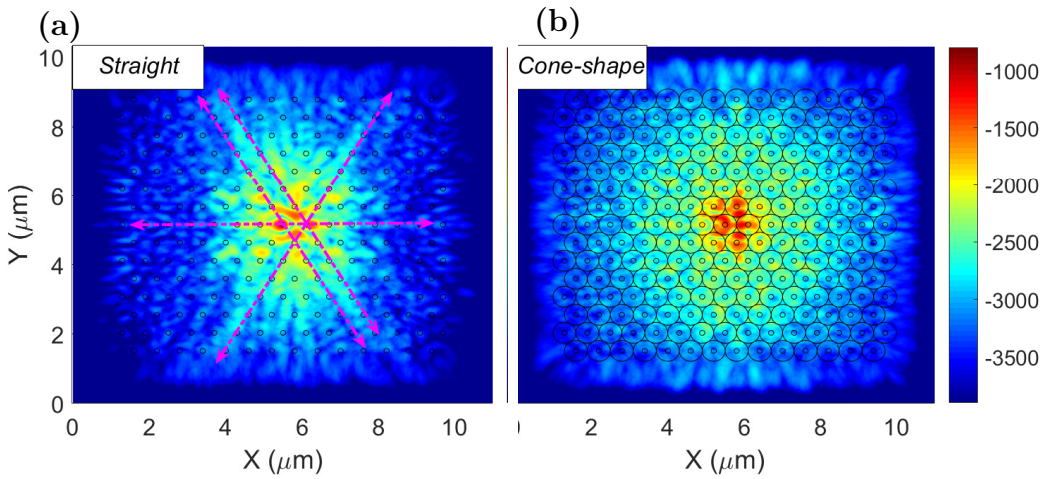

Figure 8-10: *Real part of E_x field distribution for integrated wavelength of nanorod structure of $\Lambda = 600$ nm in xy-plane with (a) straight nanorods of $d_1 = d_2 = 140$ nm and (b) cone-shaped nanorods of $d_1 = 600$ nm and $d_2 = 140$ nm.*

In figure 8-10(a) for the straight nanorods, the interference pattern of the fields arising from diffraction is clearer some examples of which are indicated by dashed-magenta arrows. In figure 8-7(b) the fields are more uniform due to the increased scattering arising from the cone shape of the nanorods.

8.2.3 Varying Diameter of Straight Nanorods

Taking the nanorod structure of $\Lambda = 600$ nm with nanorod diameter, $d_1 = d_2 = r = 140$ nm from the previous section, 8.2.2, the FDTD simulation were repeated whereby the diameter of the nanorods, d, was increased to 300 nm, 400 nm and 500 nm.

Figure 8-11(a) displays the far-field emission patterns for $\phi = 90°$ and $\phi = 60°$ spectrally resolved at 450 nm for $d = 140$ nm, 300 nm, 400 nm and 500 nm. Here, the plots are unnormalised to highlight the enhancement in light extraction.. Figure 8-7(b) shows the corresponding far-field emission patterns integrated over the wavelength emission range, 420 nm to 480 nm in 5 nm increments.

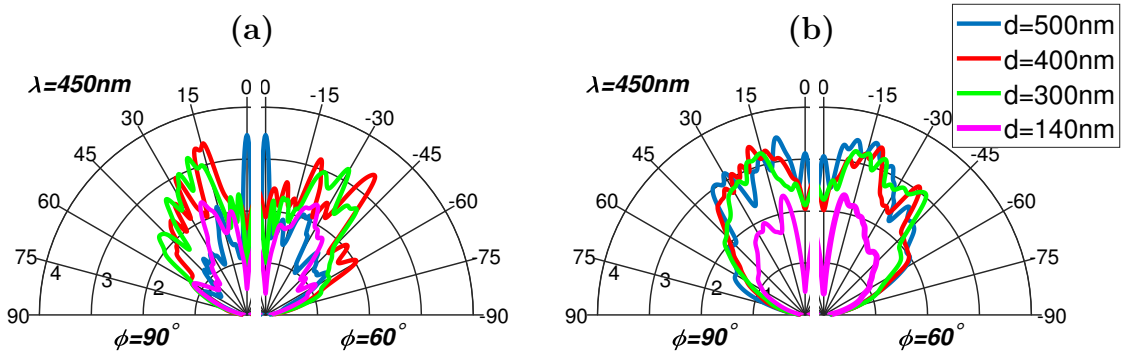

Figure 8-11: *Comparison of unnormalised far-field emission patterns for the structure of* $\Lambda = 600$ *nm where the diameter, d, of straight nanorods is varied for (a)* 450 *nm and (b) integrated over wavelength.*

In figure 8-11(a), some narrow collimation of the emission is observed at 0° elevation when the diameter of the nanorods is increased to 500 nm. The far-field pattern obtained for the nanorod diameter of 140 nm also displays higher intensity lobes at around 3 to 4°. In figure 8-11(b), the integrated wavelength emission patterns are relatively similar between ±10° and ±65° as the diameter of the nanorods is varied. For the vertically-directed emission, the largest and smallest diameter nanorods result have some intensity peaks within ±5° from 0°. It is immediately apparent how more than doubling the diameter, $d = 140$ nm, to $d = 300$ nm of the nanord results in increased emission intensity.

The three-dimensional unnormalised hemispherical far-field emission patterns are shown in figures 8-12(a-c) corresponding to the nanorods of diameter, $d = 300$ nm, 400 nm and 500 nm. These are presented for 450 nm wavelength and where it has been integrated over the emission wavelength.

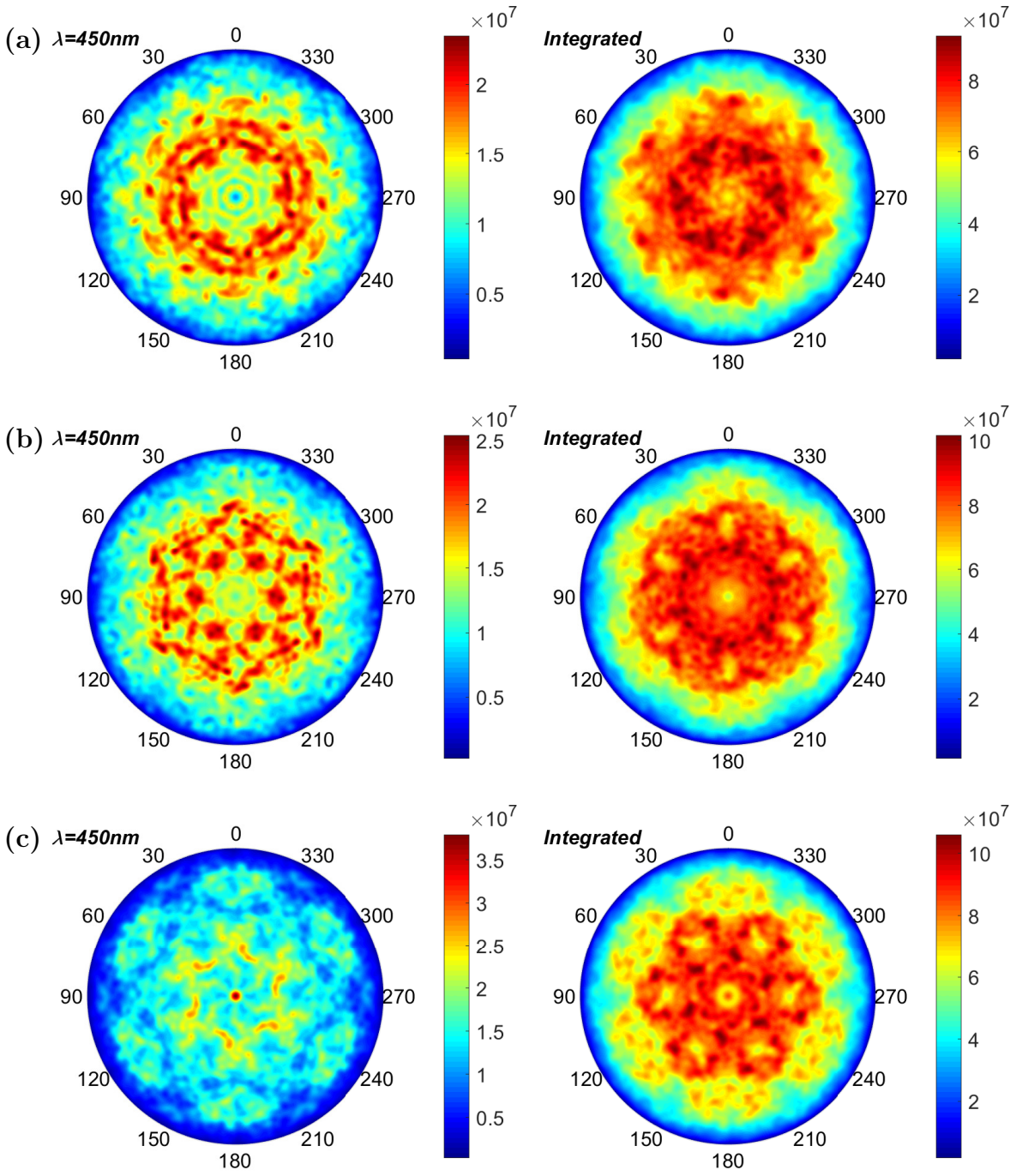

Figure 8-12: *3D unnormalised hemispherical far-field emission patterns spectrally resolved at 450 nm (left) and integrated over wavelength (right) for nanorod structure of $\Lambda = 600$ nm with (a) $d = 300$ nm, (b) $d = 400$ nm and (c) $d = 500$ nm.*

From figures 8-12(a) to 8-12(c), the change in the far-field emission pattern as a function of the nanorod diameter is more apparent where the patterns become quite exotic. In figure 8-12(c), there is a high intensity spike in the vertical direction, which could imply a guided mode of the structure is approaching cut-off or there is strong coupling of the fields across the array due to the large nanorod diameter.

The directionality, D, and enhancement factor, F, are plotted as a function of the nanorod diameter in figures 8-13(a) and 8-13(b) respectively. The values obtained for the structure in the previous section where $d = 140$ nm have been included for comparison.

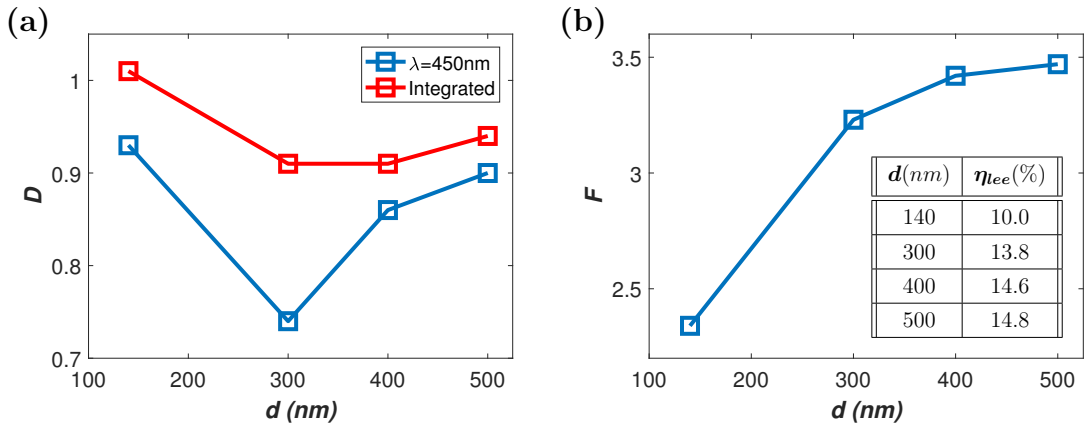

Figure 8-13: *(a) D and (b) F, plotted as a function of nanorod diameter, d, for structure of $\Lambda = 600$ nm with straight nanorods. Table in (b) summarises η_{lee} as a function of d.*

From figure 8-13(a), the directionality drops when the diameter of the nanorods is increased from 140 nm to 300 nm, before it begins to rise when d was increased to 500 nm. This drop may be due to the fields becoming more localised inside the nanorods. As d increases, neighbouring nanorods are closer to each other and these localised fields may be coupling with each other, resulting in the increase in D.

In figure 8-13(b), the enhancement factor was increased significantly by a factor of 1.4 when the nanorod diameter was approximately doubled from 140 nm to 300 nm. Upon increasing the diameter further to $d = 500$ nm, the trend of F begins to level off and no more significant increase in F is observed.

The figures in 8-14 show the real part of the E_x field distribution in the xz-plane for $y = 0$ and the emission from each vertical source position integrated for

(a) $d = 300$ nm, (b) $d = 400$ nm and (c) $d = 500$ nm. Here, all of the fields have been plotted on the same scale for comparison.

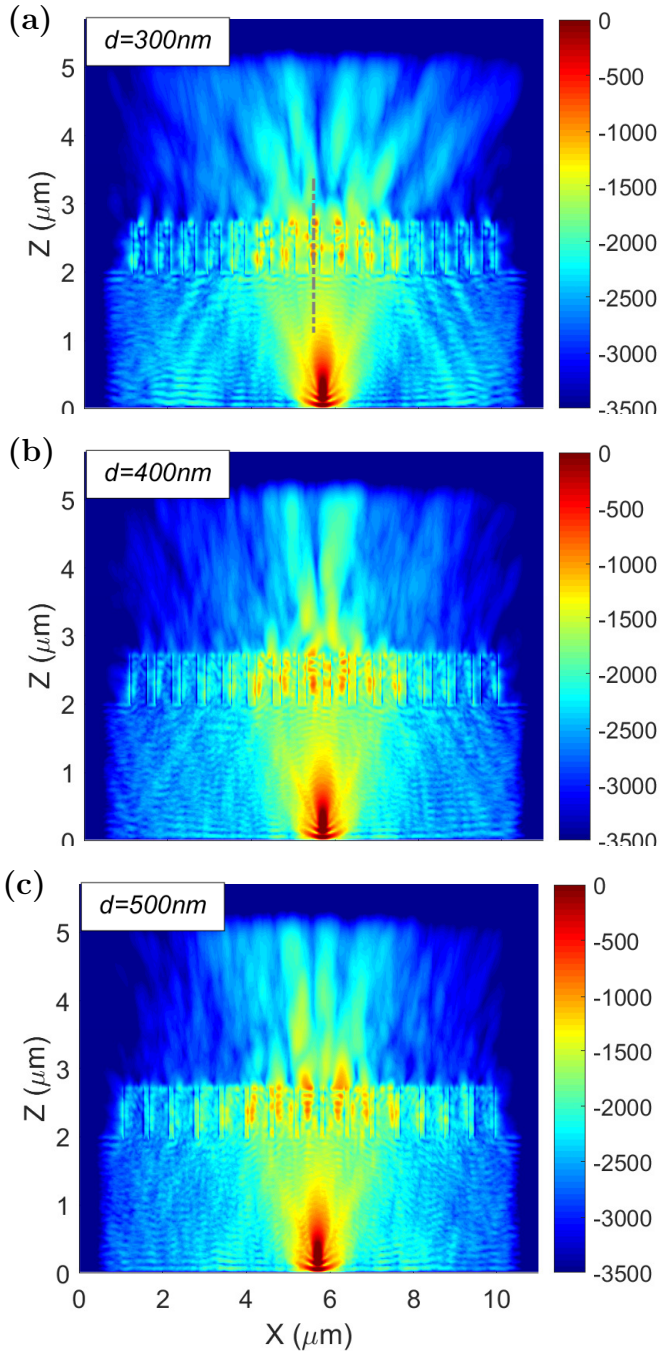

Figure 8-14: *Real part of E_x field distribution for integrated wavelength of nanorod structure of $\Lambda = 600$ nm in xz-plane for (a) $d = 300$ nm, (b) $d = 400$ nm and (c) $d = 500$ nm.*

From figures 8-14(a) to 8-14(c), it can be seen as the diameter is increased, the light trapping inside the epitaxy is significantly reduced because of the reduced reflection from the straight facets separating the nanorods. In figure 8-14(b), there is possible coupling of the fields between the nanorod positioned at the center and it's neighbour. For a nanorod diameter, $d = 500$ nm in figure 8-14(c) the fields at the end of the nanorods are highly radiative which is likely the cause of the more directional light observed in figures 8-11(a) and 8-11(b).

Figure 8-15 displays a line slices of the intensity of the field through one of the nanorods as indicated by the dashed lines in figure 8-14(a).

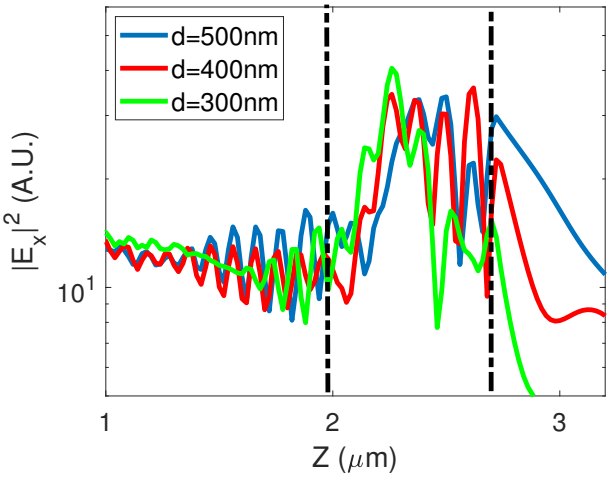

Figure 8-15: *Intensity of E_x field in the xz-plane along line indicated in figure 8-14(a) through nanorod for the three different nanorod diameters.*

The dashed lines in figure 8-15 correspond to the base and top of the nanorod. Inside the nanorod the field oscillates. For the larger nanorod diameter, $d = 500$ nm, the field escapes from the top at a higher intensity.

The figures in 8-16 show the real part of the H_z field distribution in the xz-plane for $y = 0$ and where the emission has been integrated for the vertical source positions for (a) $d = 140$ nm, (b) $d = 300$ nm, (c) $d = 400$ nm and (d) $d = 500$ nm for 450 nm emission wavelength. Similarly, all of the fields have been plotted on the same scale for comparison

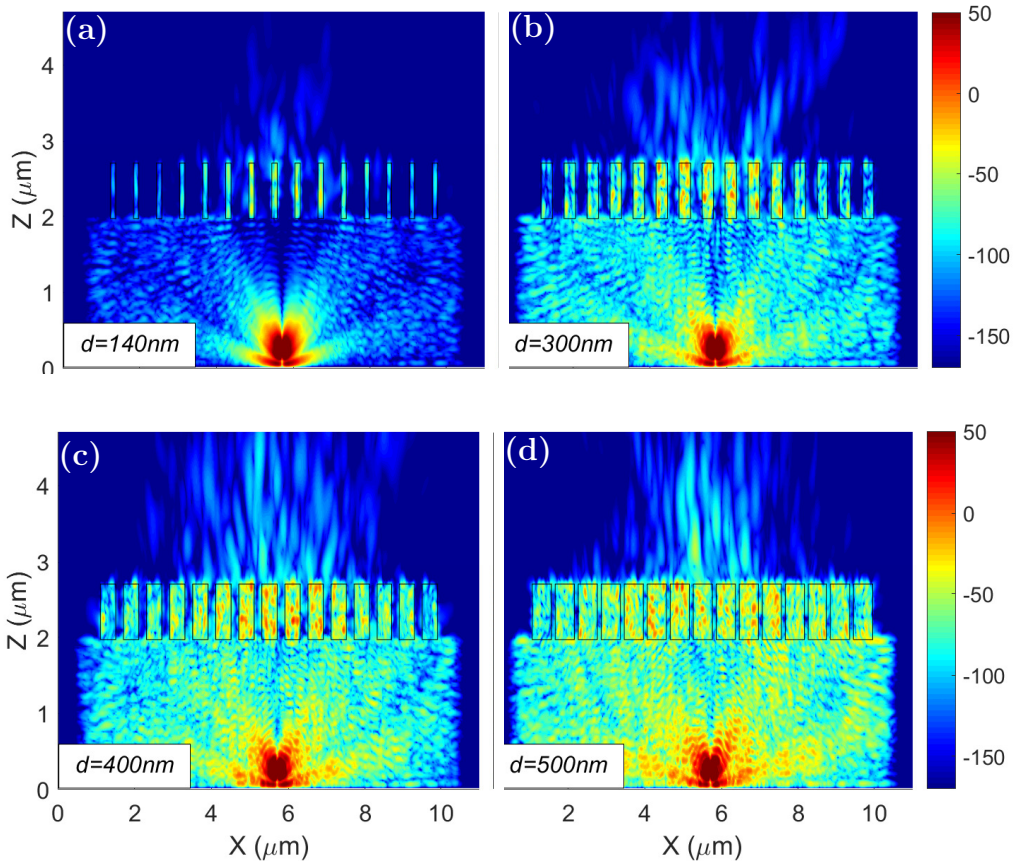

Figure 8-16: *xz-plane near-field distribution of real part of H_z field spectrally resolved at* 450 *nm for nanorod sample of* $\Lambda = 600$ *nm with diameter (a)* $d = 140$ *nm, (b)*$d = 300$ *nm, (c)* $d = 400$ *nm and (d)* $d = 500$ *nm.*

From figures 8-16(a) to 8-16(d) it can be seen that as the nanorod diameter is increased the H_z field component has a larger intensity inside the epitaxy. This may be due to return reflections from the nanorods.

The figures in 8-17 show the real part of the H_z field distribution in the xy-plane for $z = z_{nf}$ spectrally resolved at 450 nm and where the emission has been integrated for the vertical source positions for (a) $d = 140$ nm, (b) $d = 300$ nm, (c) $d = 400$ nm and (d) $d = 500$ nm.

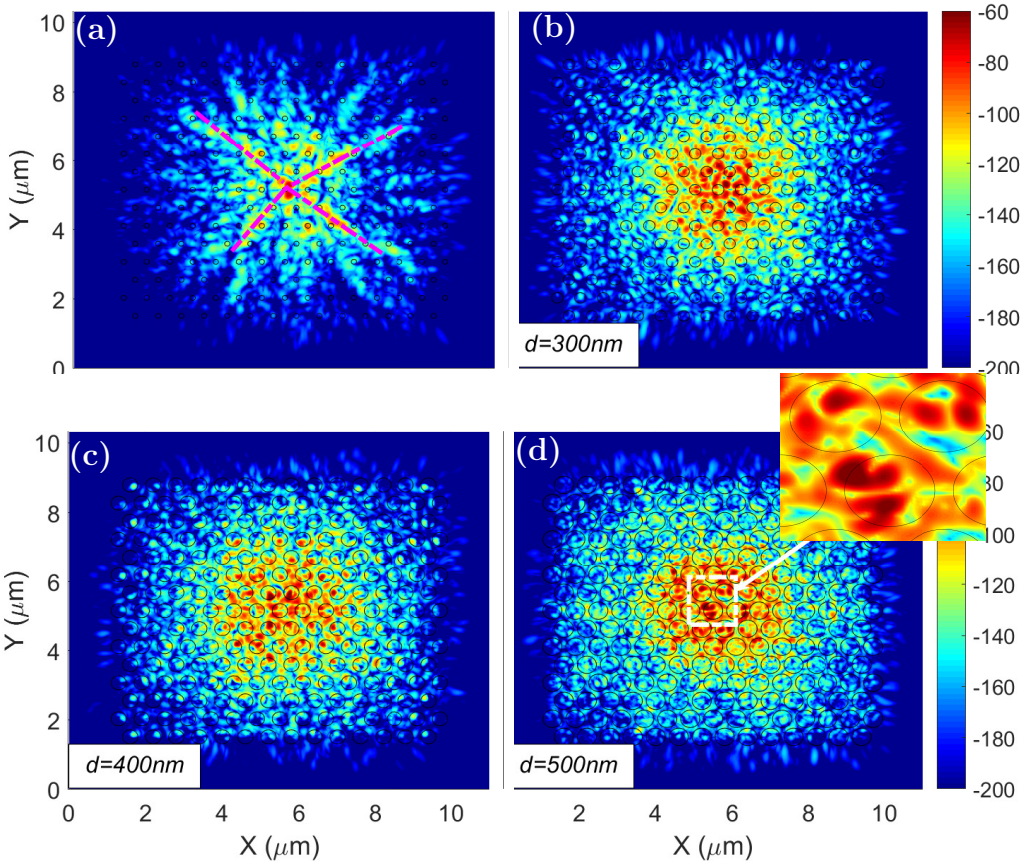

Figure 8-17: *xy-plane near-field distribution of real part of H_z field spectrally resolved at 450 nm for nanorod sample of $\Lambda = 600$ nm with diameter (a) $d = 140$ nm, (b)$d = 300$ nm, (c) $d = 400$ nm and (d) $d = 500$ nm.*

In figure 8-17(a) for $d = 140$ nm, there are distinctive paths of higher field intensity along the array which indicate constructive interference, some of which are indicated by the dashed lines in magenta. When the diameter of the rods is doubled in figure 8-17(b), strong coupling of the fields between nanorods is observed in addition to the formation of fields inside the nanorods. As the diameter of the nanorods is increased further in figures 8-17(c) and 8-17(d), H_z fields appear more localised inside the nanorods. It is possible that guided modes are being supported due to the larger diameter because in figure 8-17 there appear to be some nodes as indicated by the dashed rectangle in white. The inset of figure 8-17(d) provides a magnified view of this effect.

8.2.4 Varying Etch Depth of Straight Nanorods

In the previous section, it was found for the nanorod structure of $\Lambda = 600$ nm, with vertically-shaped nanorods and diameter, $d = 500$ nm exhibited the largest light extraction and relatively more directional emission than most of the other structures considered in this chapter. Here, FDTD simulations were repeated for where the etch depth, h, of the nanorods was increased to 1200 nm and 2000 nm.

Figure 8-18 displays the unnormalised far-field emission patterns for $\phi = 90°$ and $\phi = 60°$ spectrally resolved at 450 nm and integrated over emission wavelength. The far-field emission patterns for the previous structure with nanorod etch depth, $h = 730$ nm has been included for comparison.

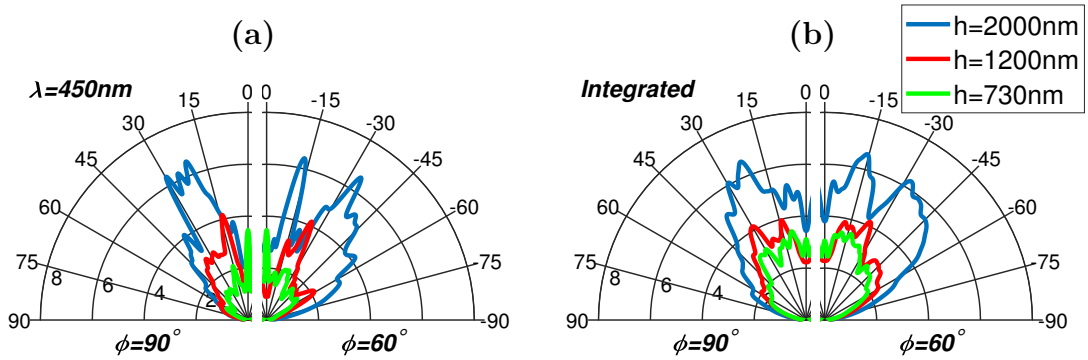

Figure 8-18: *Comparison of unnormalised far-field emission patterns obtained from FDTD of nanorod sample of $\Lambda = 600$ nm for varying etch depth, h, of straight nanorods for fixed azimuth, $\phi = 90°$ and $\phi = 60°$ (a) spectrally resolved at 450nm and (b) integrated over wavelength.*

From figure 8-18 it is immediately apparent that there is a large enhancement for the deepest etch depth, $h = 2000$ nm. This is in agreement with previous work [80]. From figure 8-18(a) the 450 nm wavelength emission far-field patterns become less directional. This is indicated by (i) the overall emission in the angular range $\pm 15°$ to $\pm 30°$ for $\phi = 90°$ shifting outwards as h is increased and (ii) the larger emission intensity in the region $\pm 30°$ to $\pm 60°$ for $h = 2000$ nm for $\phi = 60°$ in figure 8-18(a). This is also observed in figure 8-18(b) for integrated wavelength emission.

The directionality, D, and enhancement factor, F, are plotted as a function of the nanorod etch depth, h, in figures 8-19(a) and 8-19(b) respectively. The values obtained for the structure in the previous section where $h = 730$ nm have been included for comparison.

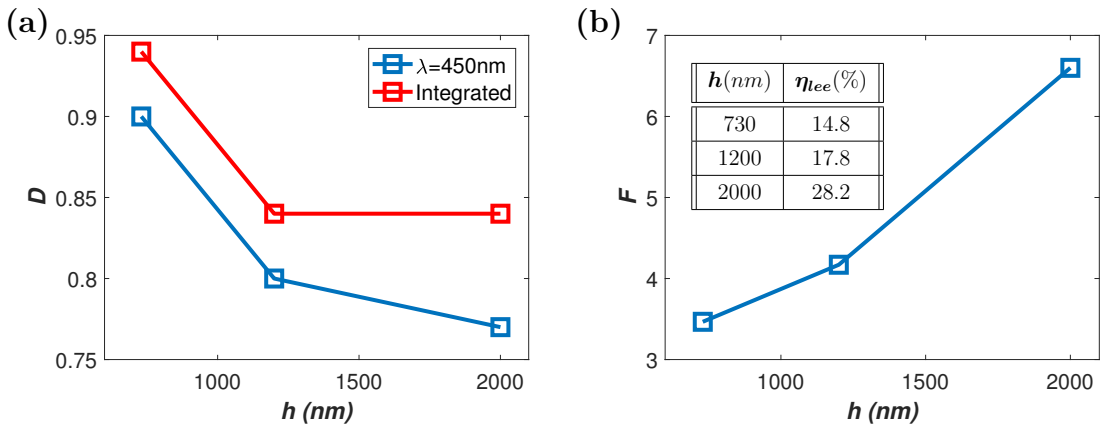

Figure 8-19: *(a) D and (b) F, plotted as a function of nanorod etch depth, h, for structure of $\Lambda = 600$ nm with straight nanorods and $d = 500$ nm. Table in (b) summarises η_{lee} as a function of h.*

From figure 8-19(a) the directionality generally reduces for increasing etch depth. This reduction is likely due to fields becoming localised inside the nanorods. In figure 8-19(b), the enhancement factor increases by a factor of 1.7 as the etch depth is increased from $h = 730$ nm to $h = 2000$ nm. According to previous studies [16] [14] this trend was attributed to low-order guided modes of the epitaxy having increased overlap with the array.

The figures in 8-20 show the real part of the E_x field distribution in the xz-plane for $y = 0$ and integrated for the dipoles at each vertical source position for (a) $h = 1200$ nm and (b) $h = 2000$ nm on the same scale.

In figure 8-20(a) for $h = 1200$ nm fields appear to couple from the dipole source to the nanorods where they are guided and diffract from the top, similar to the behaviour for $h = 730$ nm in figure 8-14(c). For the etch depth of $h = 2000$ nm in figure 8-20(b), the majority of the fields propagate directly from the source into the nanorods where they are guided along the rod as indicated by the zig-zag field intensity. Here the more intense near-fields emitted from the source couple strongly with the array and are highly localised in two adjacent nanorods. The fields are diffracted from the top of the rods and contribute to the increased light extraction observed in figure 8-19(b). This indicates that coupling from the dipole source to the nanorod array plays a large part in increased light extraction. The larger value of the nanorod diameter, d, will likely also increase the coupling to the source.

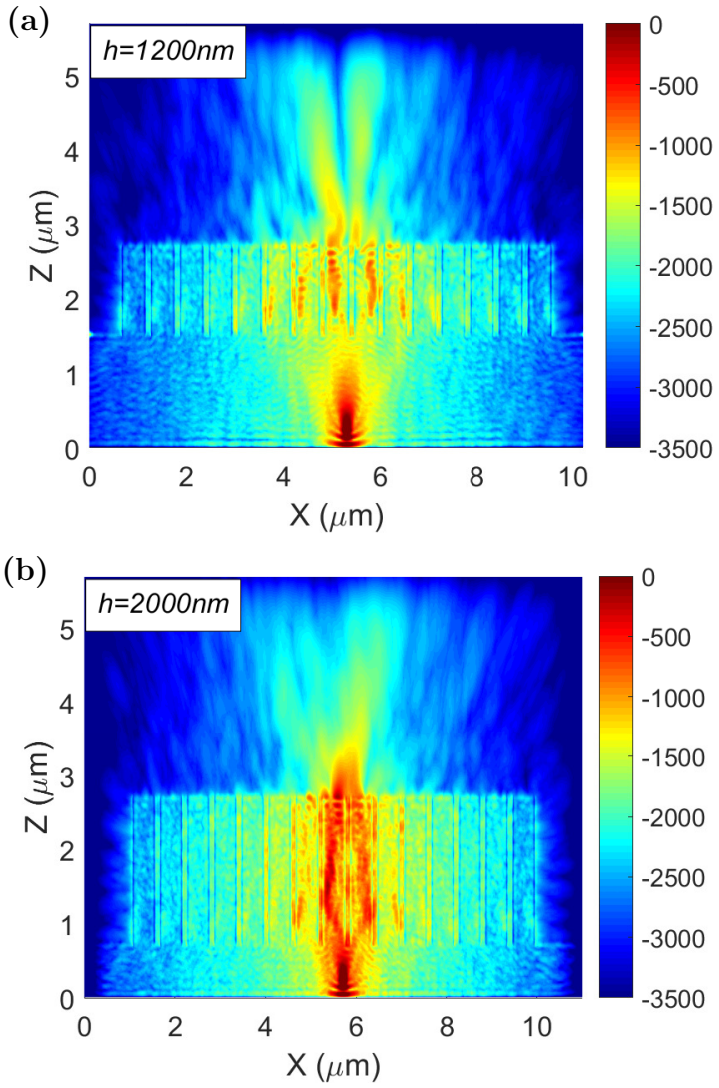

Figure 8-20: *xz-plane near-field distribution of real part of E_x field integrated over wavelength for nanorod sample of $\Lambda = 600$ nm with etch depth (a) $h = 1200$ nm and (b)$h = 2000$ nm.*

The figures in 8-21 show the real part of the E_x field distribution in the xy-plane for $y = 0$ and integrated for each dipole at the vertical source positions for (a) $h = 1200$ nm and (b) $h = 2000$ nm. Here the fields have been integrated over wavelength to display the overall behaviour inside the structure more clearly.

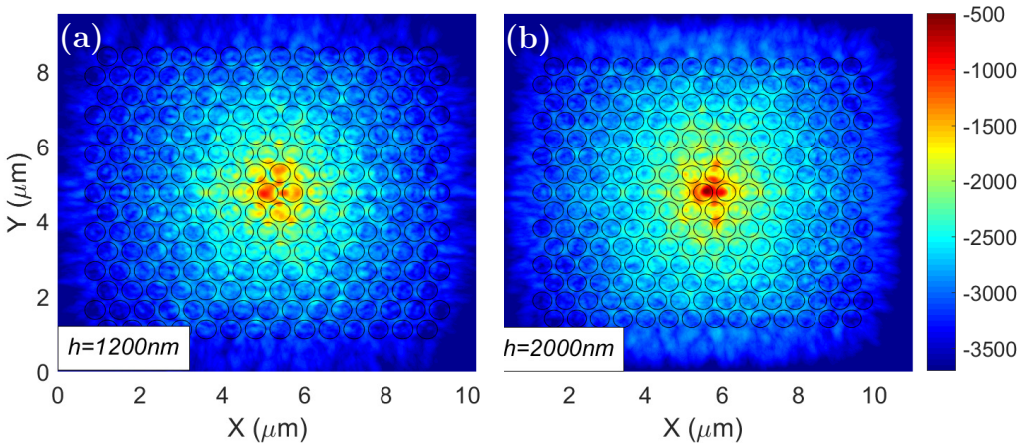

Figure 8-21: *xy-plane near-field distribution of real part of E_x field integrated over wavelength for nanorod sample of $\Lambda = 600$ nm with etch depth (a) $h = 1200$ nm and (b)$h = 2000$ nm.*

Comparison of figures 8-21(a) and 8-21(b) with 8-17(c) shows that as the etch depth is increased, the E_x field is of higher intensity inside the center positioned nanorods: the intensity of the E_x field at the center nanorod measured in figure 8-21(b) was over a factor of two than that measured in figure 8-21(a) for $h = 1200$ nm. The localisation of the fields in the near-field will result in less directional emission in the far-field as is observed in table 8-19(a) and the figures of 8-18. For the studies where increased directionality was observed for increasing etch depth [16], the nanorods were air filled i.e. the arrays were honeycomb-like structures.

It should be considered that modelling the emission for the isolated dipole at position 7 may no longer be as robust for the increased etch depth. It is likely the dipoles at the other positions need to be included for a more accurate representation. This is because the dominant mechanism appears to no longer be simple diffraction and scattering, and is instead the coupling of source fields to nanorods. When the nanorods overlap the near-fields of the dipole, these fields are more varying over a smaller spatial area and lateral dipole position may become more important.

8.3 Summary

In this section, the validated FDTD model developed in chapter 6 was used to vary several geometric parameters of the modelled nanorod arrays to observe the subsequent effects on the light extraction (quantified by F and η_{lee}) and directionality, D. These variations were:

(i) Increasing the base radius of nanorod sample of $\Lambda = 1200$ nm from 425 nm to 600 nm

(ii) Altering the cone-shaped nanorods of nanorod sample $\Lambda = 600$ nm to be straight

(iii) Varying the radius of nanorod sample $\Lambda = 600$ nm

(iv) Varying the etch depth of nanorod sample $\Lambda = 600$ nm

It was found the most practical method of increasing F and D was by increasing the base radius in (i) to alleviate the light trapping from the facets between adjacent nanorods. This doubled the value of F for the nanorod sample of $\Lambda = 1200$ nm and resulted in the largest observed directionality for all of the structures considered in this chapter. Similarly this light trapping mechanism caused the value of η_{lee} to drop from 16.6% to 10% when the nanorods were straightened in (ii) by reducing the base diameter from 600 nm to 140 nm. These observations are in agreement with previous studies whereby reflection was significantly reduced when nanostructures were closely packed [80]. Near-fields showed the large reduction of light extraction observed for the straight nanorods was also due to reduced scattering from the array. However the more directional dependent field intensity demonstrates the potential to control the directionality although further optimisation is required.

The enhancement of the light extraction saturated to $F = 3.5$ when the diameter of nanorods was increased in (iii) to 400 nm and 500 nm for the nanorod structure of $\Lambda = 600$ nm. This saturation was likely due to light trapping from the facets between nanorods. Although the value of D was reduced, it began to increase for the larger diameters, likely due to increased coupling of the fields betweens adjacent nanorods.

In (iv) the directionality reduced with increasing etch depth, h, from $D = 0.9$ to $D = 0.78$ for $h = 730$ nm to $h = 2000$ nm respectively. This was due to the fields being more strongly localised within a few adjacent nanorods as the fields from the dipole source were directly coupled out of the structure. The guiding resulted in the structure of $d = 250$ nm and $h = 2000$ nm displaying the largest enhancement factor of 6.71.

Thus for the largest light extraction of the vertical structure, it is important for direct coupling of the source fields out of the epitaxy with very few reflections back inside the epitaxy. However, for all of the structures considered in this chapter, the value of D was not significantly increased. To improve the directionality, further optimisation is required. Given the many parameters available to vary, this can be a time consuming process using FDTD.

In the next chapter, the conclusions of this thesis will be presented where the robustness and validity of this FDTD will be discussed. Suggestions of future research extending on the work in this thesis will also be presented.

Chapter 9

Conclusion and Future Work

9.1 Conclusion

The core aim of this thesis has been to develop a reliable finite-difference time-domain (FDTD) model of a commercial vertical LED structure with incorporated ordered arrays of nanorods that are intended to enhance the light output. Using this model, some parameters of the nanorod geometry can be varied and their behaviour predicted as quantified by enhancement in light output, directionality and the emission profile.

Given this, it can be stated that the core aim was met with the development of an FDTD model that could reproduce the overall emission profile obtained from experimental photoliminescence (PL) results. The following summarises the key findings from this work:

- PL and FDTD results showed that light extraction increased for the structure implementing nanorods compared to the planar version.
- PL and FDTD results indicated the increase in light extraction for the samples was due to scattering.
- PL and FDTD results showed directionality was not significantly increased for the structures implementing nanorods.
- FDTD showed for some specific wavelengths and symmetric dipole positions, highly collimated directional light could be obtained. This is likely due to guided modes approaching cut-off.

Using this model, FDTD simulations were repeated for the nanorod arrays where the shape, diameter and etch depth of the nanorods was varied. The following were found:

- Increasing base diameter of large pitch cone-shape nanorods provided very effective way to increase light extraction.
- Coupling of the dipole source to the array is a key factor for increased light extraction.
- Light extraction saturated for increasing diameter.
- Directionality decreased for increasing etch depth.
- Largest enhancement of light extraction (6.71) was obtained for structure with largest diameter and etch depth.

Therefore the work in this thesis has shown that one can get increased light extraction from a commercially viable, cost effect vertical LEDs by implementing deep-etched, closely packed nanorod arrays. Indeed, an outcome of this work is that Plessey Semiconductors Ltd. now use a close-packed array of cone-shaped nanorods as the light extraction element in their commerical vertical LEDs. Obtaining a device with more directional emission using such arrays however is yet to be achieved and it would appear to require more optimisation.

Several limitations of the FDTD modelling were identified which impacted the final results. Firstly, the light extraction efficiency, η_{lee}, was highly sensitive to the number of nanorods included in the simulation. Attempts to alleviate this effect by modelling larger arrays would have increased the computation time. Given the large number of simulations required to model the emission region of the LED, this would have become impractical. Furthermore, the limited size of the computational cell limits the spatial angular resolution of the simulated far-field patterns so that sharp peaks in intensity may not be resolved. This means that the FDTD-obtained emission profiles were more suited to reproducing the overall emission pattern and defining the directionality to be in the range $\pm 15^{\circ}$ overestimated the accuracy of the model. It may have been more suitable to define this range to be $\pm 30^{\circ}$.

Some obstacles existed due to the reliance on non-obligatory support from the MEEP forum community. Furthermore, a large amount of post-processing on the FDTD results was required which is in contrast to commercial software such as Lumerical [92] where LED parameters such as light extraction efficiency can be automatically calculated. Such software also has automated features to identify effects such as waveguiding inside structures, again without the need for processing. Consequently, little quantitative information could be provided on the near-field results inside the structures and interpretations could only be made from visual data. There was also insufficient knowledge to properly analyse effects of changing parameters of the array and to further analyse the light propagation mechanisms occurring in the modelled structures.

It is noted in this work that the modelling of the active region was thoroughly investigated by comparison of results with experimental PL. For modelling of the emission of the vertical structure LED, it was shown that a single vertical position in the middle of the active region could not be assumed. However previous work on vertical structures has made this assumption [98, 99, 104, 105]. Furthermore, it was found placing the dipole at a symmetric position resulted in far-field patterns that had a worse match with those obtained from PL. There was also a variation across literature for the number of dipoles placed laterally under the nanorod array from three at symmetric positions [104] to 1000 [109] in FDTD modelling. This work has shown that the overall shape of the emission profile can be well approximated with a single dipole strategically placed laterally. Therefore much time can be saved in future FDTD modelling for similar structures. In addition, there has been a variation of boundary conditions used for modelling the periodic arrays across studies [95, 98, 99, 106, 110]. The work in this thesis provides clarity on such issues and a procedure for optimising the boundary conditions devised.

By identifying how to model the active region and material properties more accurately, this FDTD model can be used as a template or guideline for more accurate simulation of LEDs with nanostructures. Furthermore, this reliable model contributes to accurate modelling of LEDs using free software, thus improving the availability of modelling to a wider range of researchers who may not prefer to invest thousands on a time-limited licence. Having developed much of the post-processing from established techniques, this model has the added advantage of increased flexibility by accessing the source code. This model would be ideal

for one who wanted to extract LED parameters, emission profiles and a general indication of what is occurring inside the devices.

The concept and foundation developed in this thesis for more accurate modelling can be also be extended to complicated and novel devices that are current topics of research.

9.2 Future Work

Suggestions for future research that extend on the work in this thesis will now be presented.

9.2.1 Quasi-Analytic Modelling

The aim of this work would be to develop a quasi-analytic method that could use fewer resources than FDTD. In doing this, one could more quantitatively optimise a structure to get a i.e., more directional far-field emission profile. Here several approximate methods would be developed depending on which effect or structural feature is more dominant.

Firstly an investigation of the vertical waveguiding inside the nanorods of the vertical LED structure would be made. A detailed set-up is discussed in reference [21] but to summarise, the initial general procedure would be follows:

1. Find the field distribution at the entrance of the nanorod or optical fibre.
    - Exploit the relatively large distance between the dipole and nanorods to get dipole's far-field.
    - Initially take single dipole rather than dipole pair formed from ground plane - provides opportunity to look at effect of reflector on the field distribution.
2. Find the coupling between incident fields and guided modes inside the nanorod.
    - Start by using the scalar wave approximation where the mode distri-

bution, Ψ, can be assumed to be nearly transverse i.e.,

$$\nabla^2\Psi = \epsilon_0\mu_0 n^2 \frac{\partial^2\Psi}{\partial t^2}$$

- If the large refractive index step between air and the nanorod cannot be ignored, the Marcatelli approximation could be used to obtain the 2D rectangular modes
  - Repeat overlap calculation of far-field coupling from dipole

3. Extend this to a 2-dipole array i.e. include the effect of the reflector

The results obtained for each iteration would be checked against results from two- and three-dimensional FDTD simulations.

9.2.2 Application to Nano-LEDs with UV emission

A lot of current research is on developing high power LEDs with UV emission [9] because they could replace existing lighting for a huge range of applications such as water treatment and sterilization.

The model and optimisation developed in this thesis could be extended to these devices with incoorporated nanorods arrays and different materials, including the effect of the metal near UV-emission wavelength. UV-LEDs are AlGaN based and contain AlN in the quantum wells (QW) and with increasing Al content, the wavelength of emission reduces. In addition to the shorter wavelength, the polarisation of the excitation becomes more polarised in the direction parallel to the *c*-axis, referred to as TM emission. It has been found in previous work that the use of nanorods for AlGaN-based UV LEDs were particularly effective at extracting this TM-polarised light [175] and so by performing a similar optimisation to that presented in this thesis, the results would be interesting for comparison.

9.2.3 Application to Core Shells

Core shell nanorods are a novel type of structure currently under research. Their layout is shown in figure 9-1 whereby the active region is sandwiched between the *n*-type core and the *p*-type shell. Such structures would experience little strain

and have been demonstrated to provide tunable emission, making them ideal for white light applications [176] [35].

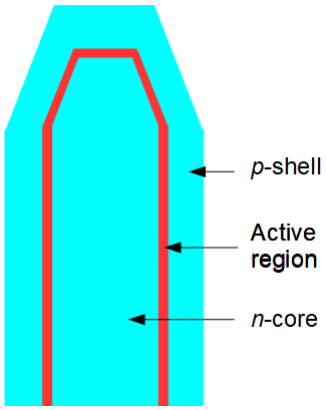

Figure 9-1: *Schematic of core shell nanorod structure.*

Currently, much of the experimental optical characterisation is limited to individual structures and proof of concept. Such structures could be modelled as arrays and their emission profiles predicted using FDTD with the concepts developed in this thesis. For example, to model the active region, it is suggested to run separate simulations for many dipoles along the active region. However careful consideration must be made as to the polarisations of the dipoles along the active region because some of the regions are not grown along the [0001] *c*-axis.

9.3 Summary

The key points of the work in this thesis have been summarised and the concluding remarks stated. A presentation of future research suggestions has been made which involves both further investigation of the work in this thesis and its implementation to a wider range of lighting applications. It has therefore been demonstrated that by meeting the aims set in this thesis, this work can be extended to novel and more complicated LED devices which are currently the subject of much research.

List of Publications

InGaN/GaN nano-LED arrays for etendue-limited applications
S.Fox, S.E.J. O'Kane, S.Lis and D.W.E. Allsopp, physica status solidi (c) 12(4), 2015

Influence of geometry on the directionality of light emission of nanorod array vertical light emitting diodes
S. Fox, S. Lis, S.E.J. O'Kane, D.W.E. Allsopp and J. Sarma, Proceedings of ASDAM 2014, 2014

Conferences

Investigation of Directional Light Emission from InGaN/GaN Vertical Light Emitting Diodes using Ordered Nanorod Arrays
S.A. Fox, S.M. Lis, P.A. Shields, D.J. Wallis, G. Thompson, J. Sarma and D.W.E. Allsopp, UK Nitrides Consortium (UKNC). Cambridge, UK, January 6-7, 2016

Achieving Directional Light Emission from InGaN/GaN Vertical Light Emitting Diodes using Wavelength Scale Photonic Structures
S.A. Fox, S. Lis, P.A. Shields, S. Nigrin, S. Harrington, D.J. Wallis, G. Thompson and D.W.E. Allsopp, 11th International Conference on Nitride Semiconductors, Beijing, China, August 30-September 4, 2015

Influence of geometry on the directionality of light emission of nanorod array vertical light emitting diodes
S. Fox, S. Lis, S.E.J. O'Kane, D.W.E. Allsopp and J. Sarma, 10th International Conference on Advanced Semiconductor Devices and Microsystems (ASDAM), Smolenice Castle, Slovakia, October 20-22, 2014

InGaN/GaN nano-LED arrays for étendue-limited applications
S. Lis, S.E.J. O'Kane, S.A. Fox, C.J. Lewins, Y.D. Zhuang, J. Sarma, P.A. Shields and D.W.E. Allsopp, Spring meeting of European Materials Research Society (EMRS), Lille, France, May 27-30, 2014

Design and fabrication of enhanced lateral growth for dislocation reduction in GaN using nanodashes
E.D. Le Boulbar, J. Priesol, M. Nouf-Allehiani, N.K. Gunaseker, S. Fox, C. Trager-Cowan, A. Satka, D.W.E. Allsopp and P. Shields, Journal of Crystal Growth, 466, pp. 30-38, 2017

Selective etching of n-type GaN in InGaN/GaN quantum disc nanorod arrays using electrode-less photo-electrochemical etching
C.J. Lewins, S.A. Fox, A. Sergejevs, P.A. Shields and D.W.E. Allsopp, UK Nitrides Consortium (UKNC). Cambridge, UK, January 6-7, 2016

Impact of Size and Pitch on the Optical Properties of Ordered Arrays of InGaN/GaN Quantum Disc and Core-Shell Nanowires
D.W.E. Allsopp, I. Girgel, C.J. Lewins, E.D. Le Boulbar, S.E.J. O'Kane, P. M. Coulon, S.M. Lis, S.A. Fox and P.A. Shields, 6th International Conference on Metamaterials, Photonic Crystals and Plasmonics (META'15), New York, USA, Aug 4-7, 2015

Bibliography

[1] "Led scale up," *The Climate Change Group*, August 2015. www.theclimategroup.org/project/led-scale.

[2] I. Navigant Consulting, "Life-cycle assessment of energy and environmental impacts of led lighting products, part i: Review of the life-cycle energy consumption of incandescent, compact fluorescent, and led lamps," 2012.

[3] P. McKenna, "The lighting paradox: Cheaper, efficient leds save energy, and people use more," *inside climate news*, August 2015. https://insideclimatenews.org/news/20082015/lighting-paradox-cheaper-efficient-led-save-energy-use-rises.

[4] N. Yagi, M. Mori, A. Hamamoto, M. Nakano, M. Akutagawa, S. Tachibana, A. Takahashi, T. Ikehara, and Y. Kinouchi, "Sterilization using 365 nm uv-led," in *2007 29th Annual International Conference of the IEEE Engineering in Medicine and Biology Society*, pp. 5841–5844, Aug 2007.

[5] J. R. Biard and G. Pittman, "Semiconductor radiant diode," 12 1962.

[6] S. Nakamura, M. Senoh, and T. Mukai, "P-gan/n-ingan/n-gan double-heterostructure blue-light-emitting diodes," *Japanese Journal of Applied Physics*, vol. 32, no. 1A, p. L8, 1993.

[7] T. Mukai, M. Yamada, and S. Nakamura, "Characteristics of ingan-based uv/blue/green/amber/red light-emitting diodes," *Japanese Journal of Applied Physics*, vol. 38, no. 7R, p. 3976, 1999.

[8] "Nobel prize in physics goes to inventors of blue light-emitting diodes," October 2014. [Online; posted 7-October-2014].

[9] Y. Muramoto, M. Kimura, and S. Nouda, "Development and future of ultraviolet light-emitting diodes: Uv-led will replace the uv lamp," *Semiconductor Science and Technology*, vol. 29, no. 8, p. 084004, 2014.

[10] S. Reineke, M. Thomschke, B. Lüssem, and K. Leo, "White organic light-emitting diodes: Status and perspective," *Rev. Mod. Phys.*, vol. 85, pp. 1245–1293, Jul 2013.

[11] J. Piprek, "Efficiency droop in nitride-based light-emitting diodes," *physica status solidi (a)*, vol. 207, no. 10, pp. 2217–2225, 2010.

[12] A. Minj, D. Cavalcoli, A. Cavallini, P. Gamarra, and M.-A. di Forte Poisson, "Strain distribution and defect analysis in iii-nitrides by dynamical afm analysis," *Nanotechnology*, vol. 24, no. 14, p. 145701, 2013.

[13] W. Alexander, "Requirements on LEDs in etendue limited light engines," *Photonics in Multimedia II*, vol. 7001, pp. 70010F–70010F–10, Apr. 2008.

[14] C. Wiesmann, K. Bergenek, N. Linder, and U. Schwarz, "Photonic crystal LEDs - designing light extraction," *Laser Photonics Review*, vol. 3, no. 3, pp. 262–286, 2009.

[15] P. A. Shields, C. Chan, N. Read, D. W. E. Allsopp, and R. A. Taylor, "Photoluminescence and Electroluminescence in InGaN / GaN Nano-rod Array LEDs Fabricated on a Wafer Scale," *In. Solid-State and Organic Lighting*, vol. 4, pp. 4–5, 2010.

[16] E. Rangel, E. Matioli, Y. Choi, C. Weisbuch, J. Speck, and E. Hu, "Directionality control through selective excitation of low-order guided modes in thin-film InGaN photonic crystal light-emitting diodes," *Applied Physics Letters*, vol. 90, pp. 081104–1–3, 2011.

[17] K. McGroddy, A. David, E. Matioli, M. Iza, S. Nakamura, S. DenBaars, J. S. Speck, C. Weisbuch, and E. L. Hu, "Directional emission control and increased light extraction in gan photonic crystal light emitting diodes," *Applied Physics Letters*, vol. 93, no. 10, 2008.

[18] Y. Kalra and R. Sinha, "Photonic band gap engineering in 2d photonic crystals," *Pramana - Journal of Physics*, vol. 67, no. 6, pp. 1155–1164, 2006.

[19] J. A. E. Wasey and W. L. Barnes, "Efficiency of spontaneous emission from planar microcavities," *Journal of Modern Optics*, vol. 47, no. 4, pp. 725–741, 2000.

[20] *Designing InGaN/GaN nano-LED arrays for etendue-limited applications*, Conference, (Lille, France), 2014.

[21] S. Fox, "The fabrication and characterisation of ingan/gan nano-leds," tech. rep., University of Bath, 08 2013.

[22] E. Schubert, *Light-Emitting Diodes*. Proceedings of SPIE - The International Society for Optical Engineering, Cambridge University Press, 2006.

[23] C. Kittel, *Introduction to Solid State Physics*. Wiley, 2004.

[24] A. Siegman, *Lasers*. University Science Books, 1986.

[25] F. C. Frank, "On Miller-Bravais indices and four-dimensional vectors," *Acta Crystallographica*, vol. 18, pp. 862–866, May 1965.

[26] T. Zhu and R. A. Oliver, "Unintentional doping in gan," *Physical Chemistry Chemistry Physics*, vol. 14, pp. 9558–9573, 2012.

[27] E. Yu, X. Dang, P. Asbeck, S. Lau, and G. Sullivan, "Spontaneous and piezoelectric polarization effects in iii-v nitride heterostructures," *Journal of Vacuum Science Technology B: Microelectronics and Nanometer Structures*, vol. 17, pp. 1742–1749, Jul 1999.

[28] T. Hanada, "Basic properties of zno, gan, and related materials," in *Oxide and Nitride Semiconductors* (T. Yao and S.-K. Hong, eds.), vol. 12 of *Advances in Materials Research*, pp. 1–19, Springer Berlin Heidelberg, 2009.

[29] Y. Song, D. Chen, L. Wang, H. Li, G. Xi, and Y. Jiang, "Splitting of valance subbands in the wurtzite c-plane ingan/gan quantum well structure," *Applied Physics Letters*, vol. 93, no. 16, p. 161910, 2008.

[30] M. I. Dyakonov, *Basics of Semiconductor and Spin Physics*. Berlin, Heidelberg: Springer Berlin Heidelberg, 2008.

[31] H. Lu, T. Yu, G. Yuan, C. Jia, G. Chen, and G. Zhang, "Valence subband coupling effect on polarization of spontaneous emissions from al-rich algan/aln quantum wells," *Opt. Express*, vol. 20, pp. 27384–27392, Dec 2012.

[32] J. Shakya, K. Knabe, K. H. Kim, J. Li, J. Y. Lin, and H. X. Jiang, "Polarization of iii-nitride blue and ultraviolet light-emitting diodes," *Applied Physics Letters*, vol. 86, no. 9, 2005.

[33] Y. Kawakami, Y. Narukawa, K. Omae, S. Fujita, and S. Nakamura, "Dimensionality of excitons in ingan-based light emitting devices," *physica status solidi (a)*, vol. 178, no. 1, pp. 331–336, 2000.

[34] M. Boroditsky and E. Yablonovitch, "Light-emitting diode extraction efficiency," *Light-Emitting Diodes: Research, Manufacturing, and Applications*, vol. 119, apr 1997.

[35] M. Deppner, *Design of Nanorod-LEDs Using Computational Modelling*. Series in microelectronics, Hartung-Gorre, 2013.

[36] A. Laubsch, M. Sabathil, W. Bergbauer, M. Strassburg, H. Lugauer, M. Peter, S. Lutgen, N. Linder, K. Streubel, J. Hader, J. V. Moloney, B. Pasenow, and S. W. Koch, "On the origin of IQE-'droop' in InGaN LEDs," *Physica Status Solidi (C)*, vol. 6, pp. S913–S916, June 2009.

[37] S.-F. Yu, R.-M. Lin, S.-J. Chang, and F.-C. Chu, "Efficiency Droop Characteristics in InGaN-Based Near Ultraviolet-to-Blue Light-Emitting Diodes," *Applied Physics Express*, vol. 5, p. 022102, 2012.

[38] J.-R. Chen, Y.-C. Wu, S.-C. Ling, T.-S. Ko, T.-C. Lu, H.-C. Kuo, Y.-K. Kuo, and S.-C. Wang, "Investigation of wavelength-dependent efficiency droop in InGaN light-emitting diodes," *Applied Physics B*, vol. 98, pp. 779–789, Dec. 2009.

[39] A. Ghatak and K. Thyagarajan, *Optical Electronics*. Cambridge University Press, 1989.

[40] H. Benisty, *Physics of light extraction efficiency in planar microcavity light-emitting diodes*, pp. 393–405. Berlin, Heidelberg: Springer Berlin Heidelberg, 1999.

[41] H. Benisty, H. D. Neve, and C. Weisbuch, "Impact of planar microcavity effects on light extraction-part i: basic concepts and analytical trends," *IEEE Journal of Quantum Electronics*, vol. 34, pp. 1612–1631, Sep 1998.

[42] C. F. Janz and J. N. McMullin, "Spontaneous emission coupling to radiation and guided modes of planar waveguide structures," *IEEE Journal of Quantum Electronics*, vol. 31, pp. 1344–1353, Jul 1995.

[43] G. Harbers and S. Bierhuizen, "Invited Paper: Performance of High Power Light Emitting Diodes in Projection Applications," *SID Symposium Digest of Technical Papers*, vol. 37, no. 2, pp. 2007–2010, 2006.

[44] F. Fournier and J. Rolland, "Design Methodology for High Brightness Projectors," *Journal of Display Technology*, vol. 4, pp. 86–91, Mar. 2008.

[45] S. B. G. Harbers and M. Krames, "Performance of High Power Light Emitting Diodes in Display Illumination Applications," *Journal of Display Technology*, vol. 3, pp. 98–109, June 2007.

[46] J. Wierer, M. Krames, J. Epler, N. Gardner, M. Craford, J. Wendt, J. Simmons, and M. Sigalas, "InGaN/GaN quantum-well heterostructure light-emitting diodes employing photonic crystal structures," *Applied Physics Letters*, vol. 84, no. 19, pp. 3885 – 3887, 2004.

[47] E. Rangel, E. Matioli, H.-T. Chen, Y.-S. Choi, C. Weisbuch, J. S. Speck, and E. L. Hu, "Interplay of cavity thickness and metal absorption in thin-film InGaN photonic crystal light-emitting diodes," *Applied Physics Letters*, vol. 97, no. 6, p. 061118, 2010.

[48] "Beyond sapphire: Led substrates from gan to zno, sic and si," May 2012. [Online; posted 14-May-2012].

[49] M. Weddle, "Manufacturing leds on large diameter substrates: What's the holdup?," February 2013.

[50] J. Chung, K. Ryu, B. Lu, and T. Palacios, "Gan-on-si technology, a new approach for advanced devices in energy and communications," in *Solid-State Device Research Conference (ESSDERC), 2010 Proceedings of the European*, pp. 52–56, Sept 2010.

[51] "Success in research: First gallium-nitride led chips on silicon in pilot stage," January 2013.

[52] D. A. Steigerwald, J. C. Bhat, D. Collins, R. M. Fletcher, M. O. Holcomb, M. J. Ludowise, P. S. Martin, and S. L. Rudaz, "Illumination with solid state lighting technology," *IEEE Journal of Selected Topics in Quantum Electronics*, vol. 8, pp. 310–320, Mar 2002.

[53] "Osram's thin-film led chip technology," December 2003.

[54] Y.-R. Wu, C. Chiu, C.-Y. Chang, P. Yu, and H.-C. Kuo, "Size-Dependent Strain Relaxation and Optical Characteristics of InGaN/GaN Nanorod LEDs," *IEEE Journal of Selected Topics in Quantum Electronics*, vol. 15, no. 4, pp. 1226–1233, 2009.

[55] J. S. Lee, J. Lee, S. Kim, and H. Jeon, "Gan light-emitting diode with deep-angled mesa sidewalls for enhanced light emission in the surface-normal direction," *IEEE Transactions on Electron Devices*, vol. 55, pp. 523–526, Feb 2008.

[56] W. Y. Fu, K. N. Hui, X. H. Wang, K. K. Y. Wong, P. T. Lai, and H. W. Choi, "Geometrical shaping of ingan light-emitting diodes by laser micromachining," *IEEE Photonics Technology Letters*, vol. 21, pp. 1078–1080, Aug 2009.

[57] X. H. Wang, P. T. Lai, and H. W. Choi, "The contribution of sidewall light extraction to efficiencies of polygonal light-emitting diodes shaped with laser micromachining," *Journal of Applied Physics*, vol. 108, no. 2, p. 023110, 2010.

[58] J.-K. Sheu, K.-H. Chang, S.-J. Tu, M.-L. Lee, C.-C. Yang, C.-K. Hsu, and W.-C. Lai, "Ingan light-emitting diodes with oblique sidewall facets formed by selective growth on sio2 patterned gan film," *Opt. Express*, vol. 18, pp. A562–A567, Nov 2010.

[59] X. H. Wang, W. Y. Fu, P. T. Lai, and H. W. Choi, "Evaluation of ingan/gan light-emitting diodes of circular geometry," *Opt. Express*, vol. 17, pp. 22311–22319, Dec 2009.

[60] X. H. Wang, P. T. Lai, and H. W. Choi, "Laser micromachining of optical microstructures with inclined sidewall profile," *Journal of Vacuum Science & Technology B: Microelectronics and Nanometer Structures Processing, Measurement, and Phenomena*, vol. 27, no. 3, pp. 1048–1052, 2009.

[61] T. Fujii, Y. Gao, R. Sharma, E. L. Hu, S. P. DenBaars, and S. Nakamura, "Increase in the extraction efficiency of gan-based light-emitting diodes via surface roughening," *Applied Physics Letters*, vol. 84, no. 6, pp. 855–857, 2004.

[62] R. Windisch, C. Rooman, B. Dutta, A. Knobloch, G. Borghs, G. Dohler, and P. Heremans, "Light-extraction mechanisms in high-efficiency surface-textured light-emitting diodes," *IEEE Journal of Selected Topics in Quantum Electronics*, vol. 8, pp. 248–255, Mar 2002.

[63] A. David, "Surface-roughened light-emitting diodes: An accurate model," *Journal of Display Technology*, vol. 9, pp. 301–316, May 2013.

[64] C. Huh, K.-S. Lee, E.-J. Kang, and S.-J. Park, "Improved light-output and electrical performance of ingan-based light-emitting diode by microroughening of the p-gan surface," *Journal of Applied Physics*, vol. 93, no. 11, pp. 9383–9385, 2003.

[65] T. Fujii, A. David, Y. Gao, M. Iza, S. P. DenBaars, E. L. Hu, C. Weisbuch, and S. Nakamura, "Cone-shaped surface gan-based light-emitting diodes," *physica status solidi (c)*, vol. 2, no. 7, pp. 2836–2840, 2005.

[66] R. Windisch, C. Rooman, S. Meinlschmidt, P. Kiesel, D. Zipperer, G. H. Döhler, B. Dutta, M. Kuijk, G. Borghs, and P. Heremans, "Impact of texture-enhanced transmission on high-efficiency surface-textured light-emitting diodes," *Applied Physics Letters*, vol. 79, no. 15, pp. 2315–2317, 2001.

[67] C. Hums, T. Finger, T. Hempel, J. Christen, and A. Dadger, "Fabry-Perot effects in InGaN/GaN heterostructures on Si-substrate," *Journal of Applied Physics*, vol. 101, no. 033113, pp. 033113–033113–4, 2007.

[68] K. Vahala, "Optical microcavities," *Nature*, vol. 424, no. 6950, pp. 839–846, 2003.

[69] E. Purcell, "Spontaneous emission probabilities at radio frequencies," *Physical Review*, vol. 69, p. 681, 1946.

[70] L. Chen, K. Achouri, E. Kallos, and C. Caloz, "Simultaneous enhancement of light extraction and spontaneous emission using a partially reflecting metasurface cavity," *Phys. Rev. A*, vol. 95, p. 053808, May 2017.

[71] H. De Neve, J. Blondelle, P. Van Daele, P. M. A. Demeester, R. G. Baets, and G. Borghs, "Planar substrate-emitting-microcavity light-emitting diodes with 20

[72] J. J. Wierer, D. A. Kellogg, and N. H. Jr., "Tunnel contact junction native-oxide aperture and mirror vertical-cavity surface-emitting lasers and resonant-cavity light-emitting diodes," *Applied Physics Letters*, vol. 74, no. 7, pp. 926–928, 1999.

[73] M. Rattier, H. Benisty, R. P. Stanley, J. F. Carlin, R. Houdre, U. Oesterle, C. J. M. Smith, C. Weisbuch, and T. F. Krauss, "Toward ultrahigh-efficiency aluminum oxide microcavity light-emitting diodes: guided mode extraction by photonic crystals," *IEEE Journal of Selected Topics in Quantum Electronics*, vol. 8, no. 2, pp. 238–247, 2002.

[74] J. W. Gray, Y. S. Jalili, P. N. Stavrinou, M. Whitehead, G. Parry, A. Joel, R. Robjohn, R. Petrie, S. Hunjan, P. Gong, and G. Duggan, "High-efficiency, low voltage resonant-cavity light-emitting diodes operating around 650 nm," *Electronics Letters*, vol. 36, no. 20, pp. 1730–1731, 2000.

[75] C. L. Tsai, C. T. Yen, W. J. Huang, Z. F. Xu, and S. C. Ko, "Ingan-based resonant-cavity light-emitting diodes fabricated with a $hboxTa_2hboxO_5/hboxSiO_2$ distributed bragg reflector and metal reflector for visible light communications," *Journal of Display Technology*, vol. 9, pp. 365–370, May 2013.

[76] C. Lin, H. Yao, J. Lu, Y. Hsieh, H. Kuo, and S. Wang, "Characteristics of stable emission gan-based resonant-cavity light-emitting diodes," *Journal of Crystal Growth*, vol. 261, no. 2, pp. 359 – 363, 2004. Proceedings of the 11th Biennial (US) Workshop on Organometallic Vapor Phase Epitaxy (OMVPE).

[77] H.-W. Liu, Q. Kan, C.-X. Wang, H.-Y. Hu, X.-S. Xu, and H.-D. Chen, "Light Extraction Enhancement of GaN LED with a Two-Dimensional Photonic Crystal Slab," *Chinese Physics Letters*, vol. 28, p. 054216, May 2011.

[78] T. Oder, K. Kim, J. Lin, and H. Jiang, "III-nitride blue and ultraviolet photonic crystal light emitting diodes," *Applied Physics Letters*, vol. 84, no. 4, pp. 466 – 468, 2004.

[79] J. Shakya, K. Kim, J. Lin, and H. Jiang, "Enhanced light extraction in III-nitride ultraviolet photonic crystal light-emitting diodes," *Applied Physics Letters*, vol. 85, pp. 142–144, July 2004.

[80] A. Deinega, I. Valuev, B. Potapkin, and Y. Lozovik, "Minimizing light reflection from dielectric textured surfaces," *J. Opt. Soc. Am. A*, vol. 28, pp. 770–777, May 2011.

[81] X. Fu, B. Zhang, X. Kang, J. Xu, C. Xiong, and G. Zhang, "Lattice constant effects of photonic crystals on the extraction of guided mode of GaN based light emitting diodes," *Science China Technological Sciences*, vol. 54, pp. 1–5, Dec. 2010.

[82] C. Lai, J. Chi, H. Kuo, H. Yen, C. Lee, C. Chao, W. Yeh, and T. Lu, "Far-field and near-field distribution of gan-based photonic crystal leds with guided mode extraction," *IEEE Journal of Selected Topics in Quantum Electronics*, vol. 15, no. 4, pp. 1234–1241, 2009.

[83] A. David, T. Fujii, R. Sharma, K. McGroddy, S. Nakamura, S. DenBaars, E. Hu, C. Weisbuch, and H. Benisty, "Photonic-crystal GaN light-emitting diodes with tailored guided modes distribution," *Applied Physics Letters*, vol. 88, pp. 061124–1–3, 2006.

[84] A. David, B. Moran, K. McGroddy, E. Matioli, E. Hu, S. DenBaars, S. Nakamura, and C. Weisbuch, "GaN/InGaN light emitting diodes with embedded photonic crystal obtained by lateral epitaxial overgrowth," *Applied Physics Letters*, vol. 92, pp. 113514–1–3, Mar. 2008.

[85] E. Matioli and C. Weisbuch, "Impact of photonic crystals on LED light extraction efficiency: approaches and limits to vertical structure designs," *Journal of Physics D: Applied Physics*, vol. 43, p. 354005, Sept. 2010.

[86] J. J. Wierer, A. David, and M. M. Megens, "Iii-nitride photonic-crystal light-emitting diodes with high extraction efficiency," *Nature Photonics*, vol. 3, no. March, pp. 163–169, 2009.

[87] K. Bergenek, C. Wiesmann, H. Zull, C. Rumbolz, R. Wirth, N. Linder, K. Streubel, and T. Krauss, "Strong High Order Diffraction of Guided Modes in Micro-Cavity Light-Emitting Diodes With Hexagonal Photonic Crystals," *IEEE Journal of Quantum Electronics*, vol. 45, no. 12, pp. 1517 – 1523, 2009.

[88] C. Lai, H. Kuo, C. Chao, P. Yu, and W. Yeh, "Structural effects on highly directional far-field emission patterns of gan-based micro-cavity light-emitting diodes with photonic crystals," *Journal of Lightwave Technology*, vol. 28, no. 19, pp. 2881–2890, 2010.

[89] A. David, T. Fujii, B. Moran, S. Nakamura, S. DenBaars, C. Weisbuch, and H. Benisty, "Photonic crystal laser lift-off GaN light-emitting diodes," *Applied Physics Letters*, vol. 88, pp. 133514–1–3, 2006.

[90] A. Taflove, "Application of the finite-difference time-domain method to sinusoidal steady-state electromagnetic-penetration problems," *IEEE Transactions on Electromagnetic Compatibility*, vol. EMC-22, no. 3, pp. 191–202, 1980.

[91] I. J. Buss, M. J. Cryan, D. Ho, I. Craddock, G. Nash, M. K. Haigh, C. Railton, and J. G. Rarity, "3d modelling of enhanced surface emission by surface roughening," in *Conference on Lasers and Electro-Optics/Quantum Electronics and Laser Science Conference and Photonic Applications Systems Technologies*, p. JWB80, Optical Society of America, 2006.

[92] L. Inc., "Fdtd solutions."

[93] S. Fan, P. Villeneuve, J. Joannopoulos, and E. Schubert, "High Extraction Efficiency of Spontaneous Emission from Slabs of Photonic Crystals," *Physical Review Letters*, vol. 78, pp. 3294–3297, Apr. 1997.

[94] H.-Y. Ryu, J.-K. Hwang, Y.-J. Lee, and Y.-H. Lee, "Enhancement of light extraction from two-dimensional photonic crystal slab structures," *IEEE Journal of Selected Topics in Quantum Electronics*, vol. 8, pp. 231–237, Mar 2002.

[95] H. K. Cho, J. Jang, J.-H. Choi, J. Choi, J. Kim, J. S. Lee, B. Lee, Y. H. Choe, K.-D. Lee, S. H. Kim, K. Lee, S.-K. Kim, and Y.-H. Lee, "Light extraction enhancement from nanoimprinted photonic crystal gan-based blue lighte-mitting diodes," *Opt. Express*, vol. 14, pp. 8654–8660, Sep 2006.

[96] H. Ichikawa and T. Baba, "Efficiency enhancement in a light-emitting diode with a two-dimensional surface grating photonic crystal," *Applied Physics Letters*, vol. 84, no. 4, pp. 457–459, 2004.

[97] W. Choi, Q. Han Park, D. Kim, H. Jeon, C. Sone, and Y. Park, "FDTD Simulation for Light Extraction in a GaN-Based LED," *Journal of the Korean Physical Society*, vol. 49, no. 3, pp. 877–880, 2006.

[98] H. K. Cho, S. K. Kim, D. K. Bae, B. C. Kang, J. S. Lee, and Y. H. Lee, "Laser liftoff gan thin-film photonic crystal gan-based light-emitting diodes," *IEEE Photonics Technology Letters*, vol. 20, pp. 2096–2098, Dec 2008.

[99] S.-K. Kim, H. K. Cho, D. K. Bae, J. S. Lee, H.-G. Park, and Y.-H. Lee, "Efficient gan slab vertical light-emitting diode covered with a patterned high-index layer," *Applied Physics Letters*, vol. 92, no. 24, pp. –, 2008.

[100] M.-A. Tsai, P. Yu, C. L. Chao, C. H. Chiu, H. C. Kuo, T. C. Lu, S. C. Wang, and J. J. Huang, "Beam shaping of gan/ingan vertical-injection light emitting diodes via high-aspect-ratio nanorod arrays," in *Conference on Lasers and Electro-Optics/International Quantum Electronics Conference*, p. CMH5, Optical Society of America, 2009.

[101] M. Charlton, M. Zoorob, and T. Lee, "Photonic quasi-crystal leds: design, modelling, and optimisation," *Proceedings of SPIE. 17th International Conference on Optical Fibre Sensors*, vol. 6486, January 2007. Invited paper.

[102] P. W. Anderson, "Absence of diffusion in certain random lattices," *Physical Review*, vol. 109, pp. 1492–1505, Mar 1958.

[103] Y. Inose, K. Ema, M. Sakai, A. Kikuchi, K. Kishino, and T. Ohtsuki, "Anderson localization of light in two-dimensional random arrays of semiconductor nanocolumns," *AIP Conference Proceedings*, vol. 1566, pp. 548–549, 2013.

[104] Q. Yue, K. Li, F. Kong, J. Zhao, and M. Liu, "Analysis on the effect of amorphous photonic crystals on light extraction efficiency enhancement for gan-based thin-film-flip-chip light-emitting diodes," *Optics Communications*, vol. 367, pp. 72 – 79, 2016.

[105] Z. Xu, L. Cao, Q. Tan, Q. He, and G. Jin, "Enhancement of the light output of light-emitting diode with double photonic crystals," *Optics Communications*, vol. 278, no. 1, pp. 211 – 214, 2007.

[106] D. H. Long, I. K. Hwang, and S. W. Ryu, "Design optimization of photonic crystal structure for improved light extraction of gan led," *IEEE Journal of Selected Topics in Quantum Electronics*, vol. 15, pp. 1257–1263, July 2009.

[107] D.-H. Kim, D. S. Shin, and J. Park, "Enhanced light extraction from gan based light-emitting diodes using a hemispherical nicoo lens," *Opt. Express*, vol. 22, pp. A1071–A1078, Jun 2014.

[108] A. Chutinan, K. Ishihara, T. Asano, M. Fujita, and S. Noda, "Theoretical analysis on light-extraction efficiency of organic light-emitting diodes using {FDTD} and mode-expansion methods," *Organic Electronics*, vol. 6, no. 1, pp. 3 – 9, 2005.

[109] Y.-J. Lee, S.-H. Kim, G.-H. Kim, Y.-H. Lee, S.-H. Cho, Y.-W. Song, Y.-C. Kim, and Y. R. Do, "Far-field radiation of photonic crystal organic light-emitting diode," *Opt. Express*, vol. 13, pp. 5864–5870, Jul 2005.

[110] P. Zhao and H. Zhao, "Analysis of light extraction efficiency enhancement for thin-film-flip-chip ingan quantum wells light-emitting diodes with gan micro-domes," *Opt. Express*, vol. 20, pp. A765–A776, Sep 2012.

[111] P. Zhao, L. Han, and H. Zhao, "Light extraction efficiency enhancement for ingan quantum wells light-emitting diodes with gan micro-domes," vol. 8641, pp. 864117–864117–6, 2013.

[112] P. Zhao, L. Han, M. R. McGoogan, and H. Zhao, "Analysis of tm mode light extraction efficiency enhancement for deep ultraviolet algan quantum wells light-emitting diodes with iii-nitride micro-domes," *Opt. Mater. Express*, vol. 2, pp. 1397–1406, Oct 2012.

[113] P. Zhu, G. Liu, J. Zhang, and N. Tansu, "FDTD Analysis on Extraction Efficiency of GaN Light-Emitting Diodes With Microsphere Arrays," *Journal of Display Technology*, vol. 9, no. 5, pp. 317–323, 2013.

[114] X. Wang, K. Li, F. Kong, and Z. Zhang, "Light extraction enhancement analysis of gan-based led with surface spherical crown array," in *2012 12th International Conference on Numerical Simulation of Optoelectronic Devices (NUSOD)*, pp. 31–32, Aug 2012.

[115] P. Zhu and N. Tansu, "Effect of packing density and packing geometry on light extraction of iii-nitride light-emitting diodes with microsphere arrays," *Photon. Res.*, vol. 3, pp. 184–191, Aug 2015.

[116] K. Huang, N. Gao, C. Wang, X. Chen, J. Li, S. Li, X. Yang, and J. Kang, "Top- and bottom-emission-enhanced electroluminescence of deep-uv light-emitting diodes induced by localised surface plasmons," *Scientific Reports*, vol. 4, no. 4380, 2014.

[117] J.-S. Park, J.-H. Kim, J.-Y. Kim, D.-H. Kim, J.-Y. Na, S.-K. Kim, D. Kang, and T.-Y. Seong, "Formation of an indium tin oxide nanodot/Ag nanowire electrode as a current spreader for near ultraviolet AlGaN-based light-emitting diodes," *Nanotechnology*, vol. 28, no. 4, 2016.

[118] Y. Leem, N. Kim, W. Lim, S. Kim, and S. Park, "Enhanced optical output power of ingan/gan vertical light-emitting diodes by zno nanorods on plasma-treated n-face gan," *Nanoscale*, vol. 6, no. 10187, 2014.

[119] E. Yablonovitch, "Photonic band-gap structures," *Journal of the Optical Society of America B*, vol. 410, no. 2, pp. 283 – 295, 1993.

[120] C. Chan, K. Ho, and C. Soukoulis, "Photonic Band Gaps in Experimentally Realizable Periodic Dielectric Structures," *Europhysics Letters*, vol. 16, no. 6, p. 563, 1991.

[121] D. Cassagne, C. Jouanin, and D. Bertho, "Hexagonal photonic-band-gap structures," *Physical Review B*, vol. 53, pp. 7134–7142, Mar 1996.

[122] Z.-Y. Li, J. Wang, and B.-Y. Gu, "Creation of partial band gaps in anisotropic photonic-band-gap structures," *Physical Review B*, vol. 58, pp. 3721–3729, Aug 1998.

[123] Z.-Y. Li, B.-Y. Gu, and G.-Z. Yang, "Large absolute band gap in 2d anisotropic photonic crystals," *Physical Review Letters*, vol. 81, pp. 2574–2577, Sep 1998.

[124] B. Gralak and M. de Dood, "Theoretical study of photonic band gaps in woodpile crystals," *Physical Review E*, vol. 67, no. 066601, pp. 066601–1–18, 2003.

[125] S. Fan, J. D. Joannopoulos, J. N. Winn, A. Devenyi, J. C. Chen, and R. D. Meade, "Guided and defect modes in periodic dielectric waveguides," *Journal of the Optical Society of America B*, vol. 12, pp. 1267–1272, Jul 1995.

[126] Y. Li, N.-F. Bai, M.-D. Zhang, and X.-H. Sun, "Fdtd based analysis for electromagnetic band gap structure and defect mode of 2d metallic photonic crystals," vol. 2, pp. 906–909 Vol. 2, Aug 2005.

[127] D. Popescue and P. Sterian, "Fdtd analysis of photonic crystals with square and hexagonal symmetry," *Journal of Advanced Research in Physics*, vol. 2, no. 021105, 2011.

[128] T. Kim, B. Liu, R. Smith, M. Athanasiou, Y. Gong, and T. Wang, "Coherent nanocavity structures for enhancement in internal quantum efficiency of iii-nitride multiple quantum wells," *Applied Physics Letters*, vol. 104, no. 16, p. 161108, 2014.

[129] A. Taflove and S. Hagness, *Computational Electrodynamics: The Finite-difference Time-domain Method*. Artech House antennas and propagation library, Artech House, 2005.

[130] K. S. Yee, "Numerical solution of initial boundary value problems involving maxwell's equations in isotropic media," *IEEE Trans. Antennas and Propagation*, pp. 302–307, 1966.

[131] R. Courant, K. Friedrichs, and H. Lewy, "Über die partiellen differenzengleichungen der mathematischen physik," *Mathematische Annalen*, vol. 100, no. 1, pp. 32–74, 1928.

[132] R. Courant, K. Friedrichs, and H. Lewy, "On the partial difference equations of mathematical physics," *IBM J. Res. Dev.*, vol. 11, pp. 215–234, Mar. 1967.

[133] J.-P. Berenger, "A perfectly matched layer for the absorption of electromagnetic waves," *Journal of Computational Physics*, vol. 114, no. 2, pp. 185 – 200, 1994.

[134] S. G. Johnson, "Notes on Perfectly Matched Layers (PMLs)." MIT course notes, 5223630, 2010.

[135] Z. S. Sacks, D. M. Kingsland, R. Lee, and J.-F. Lee, "A perfectly matched anisotropic absorber for use as an absorbing boundary condition," *IEEE Transactions on Antennas and Propagation*, vol. 43, pp. 1460–1463, Dec 1995.

[136] S. Gedney, "An anisotropic pml absorbing media for the fdtd simulation of fields in lossy and dispersive media," *Electromagnetics*, vol. 16, no. 4, pp. 399–415, 1996.

[137] R. Rumpf, "Em analysis using fdtd ee5303, lecture notes: The perfectly matched layer (pml) (lecture 13)," September 2016.

[138] X. L. Travassos, S. L. Avila, D. Prescott, A. Nicolas, and L. Krahenbuhl, "Optimal configurations for perfectly matched layers in fdtd simulations," *IEEE Transactions on Magnetics*, vol. 42, pp. 563–566, April 2006.

[139] A. F. Oskooi, L. Zhang, Y. Avniel, and S. G. Johnson, "The failure of perfectly matched layers, and towards their redemption by adiabatic absorbers," *Opt. Express*, vol. 16, pp. 11376–11392, Jul 2008.

[140] C.-L. Li, C.-W. Liu, and S.-H. Chen, "Optimization of a pml absorber's conductivity profile using fdtd," *Microwave and Optical Technology Letters*, vol. 37, no. 5, pp. 380–383, 2003.

[141] S. G. Johnson, "Coordinate transformation and invariance in electromagnetism: notes for the course 18.369 at mit.." online at http://math.mit.edu/ stevenj/18.369/coordinate-transform.pdf," 2007.

[142] W. C. Chew and W. H. Weedon, "A 3d perfectly matched medium from modified maxwell's equations with stretched coordinates," *Microwave and Optical Technology Letters*, vol. 7, no. 13, pp. 599–604, 1994.

[143] F. L. Teixeira and W. C. Chew, "General closed-form pml constitutive tensors to match arbitrary bianisotropic and dispersive linear media," *IEEE Microwave and Guided Wave Letters*, vol. 8, pp. 223–225, Jun 1998.

[144] A. Deinega and I. Valuev, "Long-time behavior of {PML} absorbing boundaries for layered periodic structures," *Computer Physics Communications*, vol. 182, no. 1, pp. 149 – 151, 2011. Computer Physics Communications Special Edition for Conference on Computational Physics Kaohsiung, Taiwan, Dec 15-19, 2009.

[145] B. Lombardet, L. Dunbar, R. Ferrini, and R. Houdré, "Fourier analysis of Bloch wave propagation in photonic crystals," *Journal of Optical Society of America B*, vol. 22, no. 6, pp. 1179 – 1190, 2005.

[146] R. D. M. John D. Joannopoulos, Steven G. Johnson, Joshua N. Winn, *Photonic Crystals: Moulding the Flow of Light*. Princeton University Press, 2 ed., 2008.

[147] T. Kashiwa and I. Fukai, "A treatment by the fd-td method of the dispersive characteristics associated with electronic polarization," *Microwave and Optical Technology Letters*, vol. 3, no. 6, pp. 203–205, 1990.

[148] R. M. Joseph, S. C. Hagness, and A. Taflove, "Direct time integration of maxwell's equations in linear dispersive media with absorption for scattering and propagation of femtosecond electromagnetic pulses," *Opt. Lett.*, vol. 16, pp. 1412–1414, Sep 1991.

[149] A. Oskooi, D. Roundy, M. Ibanescu, P. Bernel, J. Joannopoulos, and S. Johnson, "Meep: A flexible free-software package for electromagnetic simulations by the FDTD method," *Computer Physics Communications*, vol. 181, pp. 687–702, Mar. 2010.

[150] MATLAB, *version 8.5 (R2015a)*. Natick, Massachusetts: The MathWorks Inc., 2015.

[151] J. Jackson, *Classical Electrodynamics*. Wiley, 3 ed., 1999.

[152] U. Trottenberg, C. Oosterlee, and A. Schuller, *Multigrid*. Elsevier Science, 2000.

[153] A. Farjadpour, D. Roundy, A. Rodriguez, M. Ibanescu, P. Bermel, J. D. Joannopoulos, S. G. Johnson, and G. W. Burr, "Improving accuracy by subpixel smoothing in the finite-difference time domain," *Opt. Lett.*, vol. 31, pp. 2972–2974, Oct 2006.

[154] V. A. Mandelshtam and H. Taylor, "Harmonic inversion of time signals and its applications," *The Journal of Chemical Physics*, vol. 107, no. 17, pp. 6756–6769, 1997.

[155] T. Tao, T. Zhi, B. Liu, M. Li, Z. Zhuang, J. Dai, Y. Li, F. Jiang, W. Luo, Z. Xie, D. Chen, P. Chen, Z. Li, Z. Zou, R. Zhang, and Y. Zheng, "Significant improvements in ingan/gan nano-photoelectrodes for hydrogen generation by structure and polarization optimization," *Scientific Reports*, vol. 6, no. 20218, 2016.

[156] C. Balanis, *Antenna Theory: Analysis and Design*. Wiley, 2012.

[157] S. Orfanidis, *Electromagnetic Waves and Antennas*. Rutgers University, 2014.

[158] C. Wiesmann, *Nano-structured LEDs - Light Extraction Mechanisms and Applications*. Universitatsverlag Regensburg, 2009.

[159] J. Schmidt, *Numerical Simulation of Optical Wave Propagation With Examples in MATLAB*. Press Monograph, SPIE Press, 2010.

[160] P. Zhao, *Analysis of Light Extraction Efficiency Enhancement for Deep Ulatraviolet and Visible Light-Emitting Diodes with III-Nitride Micro-Domes*. PhD thesis, Electrical Engineering and Computer Science Department, Case Western Reserve University, 1 2013.

[161] S. Jiang, Y. Feng, Z. Chen, L. Zhang, X. Jiang, Q. Jiao, J. Li, Y. Chen, D. Li, L. Liu, T. Yu, B. Shen, and G. Zhang, "Study on light extraction from gan-based green light-emitting diodes using anodic aluminum oxide pattern and nanoimprint lithography," *Scientific Reports*, vol. 6, no. 21573, 2016.

[162] M.-Y. Ryu, G. G. Shim, P. W. Yu, E. Oh, C. Sone, O. Nam, and Y. Park, "Optical properties of ingan/gan double quantum wells with varying well thickness," *Solid State Communications*, vol. 120, no. 12, pp. 509 – 514, 2001.

[163] J. H. Zhu, S. M. Zhang, H. Wang, D. G. Zhao, J. J. Zhu, Z. S. Liu, D. S. Jiang, Y. X. Qiu, and H. Yang, "The investigation on carrier distribution in ingan/gan multiple quantum well layers," *Journal of Applied Physics*, vol. 109, no. 9, p. 093117, 2011.

[164] C.-F. Lai, J.-Y. Chi, H.-C. Kuo, H.-H. Yen, C.-E. Lee, C.-H. Chao, H.-T. Hsueh, and W.-Y. Yeh, "Far-field of gan film-transferred green light-emitting diodes with two-dimensional photonic crystals," *Opt. Express*, vol. 17, pp. 8795–8804, May 2009.

[165] H.-Y. Ryu, K.-S. Jeon, M.-G. Kang, Y. Choi, and J.-S. Lee, "Dependence of efficiencies in gan-based vertical blue light-emitting diodes on the thickness and doping concentration of the n-gan layer," *Opt. Express*, vol. 21, pp. A190–A200, Jan 2013.

[166] A. S. Barker and M. Ilegems, "Infrared lattice vibrations and free-electron dispersion in gan," *Phys. Rev. B*, vol. 7, pp. 743–750, Jan 1973.

[167] K. Takeuchi, S. Adachi, and K. Ohtsuka, "Optical properties of algan alloys," *Journal of Applied Physics*, vol. 107, no. 2, pp. 1–11, 2010.

[168] J. Pastrnak and L. Roskovcova, "Refraction index measurements on aln single crystals," *physica status solidi (b)*, vol. 14, no. 1, pp. K5–K8, 1966.

[169] S. Shokhovets, R. Goldhahn, G. Gobsch, S. Piekh, R. Lantier, A. Rizzi, V. Lebedev, and W. Richter, "Determination of the anisotropic dielectric function for wurtzite aln and gan by spectroscopic ellipsometry," *Journal of Applied Physics*, vol. 94, no. 1, pp. 307–312, 2003.

[170] A. D. Rakić, A. B. Djurišić, J. M. Elazar, and M. L. Majewski, "Optical properties of metallic films for vertical-cavity optoelectronic devices," *Applied Optics*, vol. 37, pp. 5271–5283, Aug 1998.

[171] E. Becache, P. G. Petropoulos, and S. D. Gedney, "On the long-time behavior of unsplit perfectly matched layers," *IEEE Transactions on Antennas and Propagation*, vol. 52, pp. 1335–1342, May 2004.

[172] S. Abarbanel, D. Gottlieb, and J. S. Hesthaven, "Long time behavior of the perfectly matched layer equations in computational electromagnetics," *Journal of Scientific Computing*, vol. 17, Dec 2002.

[173] J. De Moerloose and D. De Zutter, "Poynting's theorem for the finite-difference–time-domain method," *Microwave and Optical Technology Letters*, vol. 8, no. 5, pp. 257–260, 1995.

[174] A. Henderson, *ParaView Guide, A Parallel Visualization Application*. Sandia National Labs: Kitware Inc, 2007.

[175] H.-Y. Ryu, "Large enhancement of light extraction efficiency in algan-based nanorod ultraviolet light-emitting diode structures," *Nanoscale Research Letters*, vol. 9, p. 58, Feb 2014.

[176] F. Qian, S. Gradecak, Y. Li, C.-Y. Wen, and C. M. Lieber, "Core/multishell nanowire heterostructures as multicolor, high-efficiency light-emitting diodes.," *Nano letters*, vol. 5, pp. 2287–91, Nov. 2005.